Instituto de Física Teórica
UAM-CSIC

Universidad Autónoma de Madrid

Universidad Autónoma de Madrid

Departamento de Física Teórica
Instituto de Física Teórica UAM-CSIC

Sampling the $\mu\nu$SSM in the light of experimental data

Memoria de Tesis Doctoral realizada por

Essodjolo KPATCHA

presentada ante el Departamento de Física Teórica
de la Universidad Autónoma de Madrid
para optar al título de **Doctor en Física Teórica**.

Tesis dirigida por el **Prof. Carlos Muñoz López**

October 7, 2019

This thesis is based on the following articles:

Sampling the $\mu\nu$SSM for displaced decays of the tau left sneutrino LSP at the LHC
E. Kpatcha, I. Lara, D.E. López-Fogliani, C. Muñoz, N. Nagata, H. Otono and R. Ruiz de Austri
To be published in EPJC, arXiv:1907.02092 [hep-ph]

Impact of Higgs physics on the parameter space of the $\mu\nu$SSM
E. Kpatcha, D.E. López-Fogliani, C. Muñoz and R. Ruiz De Austri
To be published in EPJC

Explaining muon anomalous $(g-2)$ in the $\mu\nu$SSM
E. Kpatcha, I. Lara, D.E. López-Fogliani, C. Muñoz and N. Nagata
To be published in EPJC

Contents

Resumen

Las características de las señales del bosón escalar descubierto por las Colaboraciones ATLAS y CMS, en el Gran Colisionador de Hadrones (LHC) en 2012, indican que esta resonancia es compatible con las expectativas para el bosón de Higgs del Modelo Estándar (SM) de la física de partículas. Por lo tanto, esta partícula representa la última evidencia que faltaba a favor del SM, para explicar las partículas elementales conocidas y sus interacciones. Sin embargo, hay cuestiones relevantes que no se pueden responder en el marco teórico del SM, como por ejemplo el origen del potencial de Higgs que produce la ruptura de la simetría electrodébil (EWSB), la solución del problema de las jerarquías, el origen de las masas y ángulos de mezcla de los neutrinos, la naturaleza de la materia oscura (DM), la solución al problema CP de las interacciones fuertes, el origen de la asimetría entre la materia y la anti-materia, o cómo acomodar la interacción gravitacional.

Desde el punto de vista teórico, se han propuesto muchas teorías para abordar estas cuestiones. Aunque la motivación para cada una de ellas puede diferir, el factor común para la mayoría es que el contenido de partículas del SM tiene que aumentarse y se espera que las nuevas partículas aparezcan a escalas no muy alejadas de la escala Electrodébil (EW).

Entre un puñado de teorías elegibles más allá del Modelo Estándar (BSM), la Supersimetría (SUSY) a la escala EW ha recibido una gran atención durante un largo período de tiempo, tanto desde la perspectiva teórica como experimental. SUSY es una simetría que proporciona una conexión entre fermiones y bosones, de tal manera que para cada partícula del SM existe una compañera supersimétrica (también llamada *sparticle*) con los mismos números cuánticos pero con media unidad menos de espín. Así, el principio supersimétrico permite que cada bosón (fermión) del SM tenga una compañera supersimétrica que es un fermión (bosón). Como consecuencia, SUSY predice un gran número de nuevas partículas que podrían ser descubiertas en el LHC o en la próxima generación de colisionadores. Sin embargo, no se ha detectado todavía ninguna partícula supersimétrica, a pesar de las numerosas búsquedas y de los tremendos esfuerzos de las colaboraciones

experimentales. Por tanto, los espacios de parámetros de los modelos supersimétricos parecen reducirse considerablemente. Se deduce entonces que es crucial llevar a cabo estudios exhaustivos de la situación actual de los distintos modelos.

En esta tesis, consideramos el 'μ from ν' Supersymmetric Standard Model ($\mu\nu$SSM) como el modelo teórico a analizar. Además de las ventajas habituales de los modelos supersimétricos, el $\mu\nu$SSM, a través de la presencia de tres familias de supercampos de *neutrinos right-handed* puede resolver simultáneamente el problema μ del *Minimal Supersymmetric Standard Model* (MSSM), así como el problema ν, siendo capaz de reproducir correctamente las masas de los neutrinos y sus ángulos de mezcla. También puede propocionar un buen candidato a DM, el gravitino.

En los modelos supersimétricos, la presencia de términos que violan los números bariónico y leptónico predice una desintegración demasiado rápida del proton y usualmente se utiliza la simetría de paridad R para prohibir que los mismos aparezcan en el Lagrangiano. Esta estrategia da lugar a modelos que conservan la paridad R (RPC), tales como el MSSM. Por el contrario, el $\mu\nu$SSM es un modelo en el que la paridad R se viola (RPV) debido a nuevos acoplamientos que involucran a los *neutrinos right-handed*, los cuales violan por tanto el número leptónico (siendo inofensivos para el desintegración del proton) Como la partícula supersimétrica más ligera (LSP) no es por tanto estable en el $\mu\nu$SSM, se generan nuevas señasles en los colisionadores, tales como la producción de vértices desplazados, multileptones o nuevos canales de desintegración.

El objetivo de esta tesis es estudiar a fondo el espacio de parámetros del $\mu\nu$SSM a la luz de los datos experimentales actuales, utilizando un método muy potente basado en el análisis de datos y probabilidad. En concreto, estudiamos las regiones viables que son compatibles con los datos del Higgs y de las oscilaciones de neutrinos, así como con una clase de observables de sabor. Por un lado, analizamos aquellas regiones que pueden ser exploradas en el funcionamiento actual y futuro del LHC a través del sector extendido de Higgs del $\mu\nu$SSM, que en general consiste en dos dobletes de Higgs mezclados con las tres familias de sneutrinos. Después, aplicamos esta estrategia para estudiar la compatibilidad del *sneutrino left* como un candidato interesante a LSP en el $\mu\nu$SSM, con las búsquedas actuales de dileptones desplazados. Por otro lado, también analizamos las regiones que pueden explicar un viejo rompecabezas del SM, a saber, la desviación del valor medido del momento magnético anómalo del muón con respecto a la predicción teórica.

Summary

The properties and signal rates of the scalar boson discovered by ATLAS and CMS Collaborations at the Large Hadron Collider (LHC) in 2012 indicate that this resonance is compatible with the expectations for the Higgs boson of the Standard Model (SM) of particle physics. Hence, this particle represents the last piece of evidence in favour of the SM in explaining the known elementary particles and their interactions. However, there are relevant questions that cannot be answered in the theoretical framework of the SM, such as for example the origin of the Higgs potential producing the electroweak symmetry breaking (EWSB), the solution of the hierarchy problem, the origin of neutrino masses and mixing angles, the nature of dark matter (DM), the solution to the strong CP problem, the origin of matter anti-matter asymmetry, or how to accommodate the gravitational interaction.

From the theoretical viewpoint, many theories have been proposed to address some of these questions. Even though the motivation for each theory might differ, the common point for most of them is that the SM particle content has to be extended and that the new particles are expected to show up at scales not too far from the electroweak (EW) scale.

Among a handful of eligible theories beyond the standard model (BSM), EW Supersymmetry (SUSY) has received extensive attention from both theoretical and experimental perspectives over a long period of time. SUSY is a symmetry that provides a connection between fermions and bosons in such a way that for each SM particle there exists a supersymmetric partner (also called sparticle) with the same set of quantum numbers but a half integer spin difference. Thus, SUSY principle allows every SM boson (fermion) to have a supersymmetric partner that is a fermion (boson). As a consequence, SUSY predicts a large number of new particles that could be discovered at the LHC or at the next generation of colliders. Nevertheless, no sparticle has been detected yet despite numerous searches and tremendous efforts of the experimental collaborations. Therefore, the parameter spaces of SUSY models seem to be shrinking considerably. It appears then

crucial to conduct thorough studies of the current situation for the different models.

In this thesis, we consider the 'μ from ν' Supersymmetric Standard Model ($\mu\nu$SSM) as the theoretical model to be analyzed. In addition to the usual advantages of SUSY models, the $\mu\nu$SSM, through the presence of three families of right-handed neutrino superfields can simultaneously solve the μ-problem of the Minimal Supersymmetric Standard Model (MSSM), as well as the ν-problem, being able to reproduce the correct neutrino masses and mixing angles. It can also provide a good candidate for DM, the gravitino.

In SUSY models, the presence of baryon- and lepton-number violating terms predicts too fast proton decay, and usually the R-parity symmetry is used to forbid these terms from appearing in the Lagrangian. This strategy gives rise to the so-called R-parity conserving (RPC) models, such as the MSSM. On the contrary, the $\mu\nu$SSM is an R-parity violating (RPV) model due to the presence of new couplings involving right-handed neutrinos, and therefore violating lepton number (harmless for proton decay). Then, since the lightest supersymmetric particle (LSP) is no longer stable in the $\mu\nu$SSM, it leads to novel signatures at colliders, such as the production of displaced vertices, multileptons or new decay chains.

The goal of this thesis is to thoroughly study the parameter space of the $\mu\nu$SSM in the light of current experimental data, using a powerful likelihood data-driven method. In particular, we study the viable regions compatible with current neutrino oscillations and Higgs data, as well as a class of flavor observables. On the one hand, we analyze those regions that can be explored at the current and future runs of the LHC via the extended Higgs sector of the $\mu\nu$SSM, which in general consists of two Higgs doublets mixed with the three families of sneutrinos. Then, we apply this strategy to study the compatibility of the left sneutrino as an interesting LSP candidate in the $\mu\nu$SSM, with current displaced dilepton searches. On the other hand, we also analyze the regions that can explain a long standing puzzle of the SM, namely, the deviation of the measurement of the anomalous magnetic moment of the muon with respect to the theoretical prediction.

Chapter 1

Introduction/Introducción

The properties and signal rates of the scalar boson discovered by ATLAS [1] and CMS Collaborations [2] at the Large Hadron Collider (LHC) in 2012 indicate that this resonance is compatible with the expectations for the Higgs boson of the Standard Model (SM) of particle physics. Hence, this particle represents the last piece of evidence in favour of the SM in explaining the known elementary particles and their interactions. However, there are relevant questions that cannot be answered in the theoretical framework of the SM, such as for example the origin of the Higgs potential producing the electroweak symmetry breaking (EWSB), the solution of the hierarchy problem, the origin of neutrino masses and mixing angles, the nature of dark matter (DM), the solution to the strong CP problem, the origin of matter anti-matter asymmetry, or how to accommodate the gravitational interaction.

From the theoretical viewpoint, many theories have been proposed to address some of these questions. Even though the motivation for each theory might differ, the common point for most of them is that the SM particle content has to be extended and that the new particles are expected to show up at scales not too far from the electroweak (EW) scale.

Among a handful of eligible theories beyond the standard model (BSM), EW Supersymmetry (SUSY) [3–7] has received extensive attention from both theoretical and experimental perspectives over a long period of time. SUSY is a symmetry that provides a connection between fermions and bosons in such a way that for each SM particle there exists a supersymmetric partner (also called sparticle) with the same set of quantum numbers but a half integer spin difference. Thus, SUSY principle allows every SM boson (fermion) to have a supersymmetric partner that is a fermion (boson). As a consequence,

SUSY predicts a large number of new particles that could be discovered at the LHC or at the next generation of colliders. Nevertheless, no sparticle has been detected yet despite numerous searches and tremendous efforts of the experimental collaborations. Therefore, the parameter spaces of SUSY models seem to be shrinking considerably. It appears then crucial to conduct thorough studies of the current situation for the different models.

In this thesis, we consider the 'μ from ν' Supersymmetric Standard Model ($\mu\nu$SSM) [8] as the theoretical model to be analyzed. In addition to the usual advantages of SUSY models, the $\mu\nu$SSM, through the presence of three families of right-handed neutrino superfields can simultaneously solve the μ-problem [9] of the Minimal Supersymmetric Standard Model (MSSM) [4,6,7], as well as the ν-problem, being able to reproduce the correct neutrino masses and mixing angles [10–13]. It can also provide a good candidate for DM, the gravitino.

In SUSY models, the presence of baryon- and lepton-number violating terms predicts too fast proton decay, and usually the R-parity symmetry is used to forbid these terms from appearing in the Lagrangian. This strategy gives rise to the so-called R-parity conserving (RPC) [14–18] models, such as the MSSM. On the contrary, the $\mu\nu$SSM is an R-parity violating (RPV) model [19] due to the presence of new couplings involving right-handed neutrinos, and therefore violating lepton number (harmless for proton decay). Then, since the lightest supersymmetric particle (LSP) is no longer stable in the $\mu\nu$SSM, it leads to novel signatures at colliders, such as the production of displaced vertices, multileptons or new decay chains.

The goal of this thesis is to thoroughly study the parameter space of the $\mu\nu$SSM in the light of current experimental data, using a powerful likelihood data-driven method. In particular, we study the viable regions compatible with current neutrino oscillations and Higgs data, as well as a class of flavor observables. On the one hand, we analyze those regions that can be explored at the current and future runs of the LHC via the extended Higgs sector of the $\mu\nu$SSM, which in general consists of two Higgs doublets mixed with the three families of sneutrinos. Then, we apply this strategy to study the compatibility of the left sneutrino as an interesting LSP candidate [20, 21] in the $\mu\nu$SSM, with current displaced dilepton searches. On the other hand, we also analyze the regions that can explain a long standing puzzle of the SM, namely, the deviation of the measurement of the anomalous magnetic moment of the muon with respect to the theoretical prediction.

This work is organized as follows: In Chapter 2, we briefly describe the MSSM and discuss some of its limitations. Chapter 3 is devoted to describe the $\mu\nu$SSM, its main

features and the extended Higgs sector of the model are presented. In Chapter 4, we describe the methodology employed in our analyses. In particular, the sampling method and likelihoods used are introduced. Using this methodology, in Chapter 5 we sample the $\mu\nu$SSM to study the impact of Higgs physics on its parameter space. We identify all possible viable regions that are compatible with the latest LHC data, with some complementary data from LEP and Tevatron, as well as a class of flavor observables such as B decays and μ decays. In Chapter 6, we recast the result of the ATLAS 8-TeV displaced dilepton search from long-lived particles, in order to obtain the potential limits on the parameter space for the tau left sneutrino LSP in the $\mu\nu$SSM with a mass in the range $45 - 100$ GeV. In particular, we sample the $\mu\nu$SSM to explore the regions of the parameter space that lead to tau left sneutrino as the LSP, and to find those that can be probed using the displaced dilepton signal at current and future runs of the LHC. In Chapter 7, we analyze the parameter space of the model that can explain the measurement of the anomalous magnetic moment of muon. Within the model it is possible to produce light supersymmetric particles that are still consistent with experimental exclusion limits, and that can contribute to solve this challenging puzzle of the SM. Finally, in Chapter 8 the main results obtained are summarized, and the future prospects are outlined.

Introducción

Las características de las señales del bosón escalar descubierto por las Colaboraciones ATLAS [1] y CMS [2], en el Gran Colisionador de Hadrones (LHC) en 2012, indican que esta resonancia es compatible con las expectativas para el bosón de Higgs del Modelo Estándar (SM) de la física de partículas. Por lo tanto, esta partícula representa la última evidencia que faltaba a favor del SM, para explicar las partículas elementales conocidas y sus interacciones. Sin embargo, hay cuestiones relevantes que no se pueden responder en el marco teórico del SM, como por ejemplo el origen del potencial de Higgs que produce la ruptura de la simetría electrodébil (EWSB), la solución del problema de las jerarquías, el origen de las masas y ángulos de mezcla de los neutrinos, la naturaleza de la materia oscura (DM), la solución al problema CP de las interacciones fuertes, el origen de la asimetría entre la materia y la anti-materia, o cómo acomodar la interacción gravitacional.

Desde el punto de vista teórico, se han propuesto muchas teorías para abordar estas cuestiones. Aunque la motivación para cada una de ellas puede diferir, el factor común para la mayoría es que el contenido de partículas del SM tiene que aumentarse y se espera

que las nuevas partículas aparezcan a escalas no muy alejadas de la escala Electrodébil (EW).

Entre un puñado de teorías elegibles más allá del Modelo Estándar (BSM), la Supersimetría (SUSY) a la escala EW [3–7] ha recibido una gran atención durante un largo período de tiempo, tanto desde la perspectiva teórica como experimental. SUSY es una simetría que proporciona una conexión entre fermiones y bosones, de tal manera que para cada partícula del SM existe una compañera supersimétrica (también llamada *sparticle*) con los mismos números cuánticos pero con media unidad menos de espín. Así, el principio supersimétrico permite que cada bosón (fermión) del SM tenga una compañera supersimétrica que es un fermión (bosón). Como consecuencia, SUSY predice un gran número de nuevas partículas que podrían ser descubiertas en el LHC o en la próxima generación de colisionadores. Sin embargo, no se ha detectado todavía ninguna partícula supersimétrica, a pesar de las numerosas búsquedas y de los tremendos esfuerzos de las colaboraciones experimentales. Por tanto, los espacios de parámetros de los modelos supersimétricos parecen reducirse considerablemente. Se deduce entonces que es crucial llevar a cabo estudios exhaustivos de la situación actual de los distintos modelos.

En esta tesis, consideramos el 'μ from ν' Supersymmetric Standard Model ($\mu\nu$SSM) [8] como el modelo teórico a analizar. Además de las ventajas habituales de los modelos supersimétricos, el $\mu\nu$SSM, a través de la presencia de tres familias de supercampos de *neutrinos right-handed* puede resolver simultáneamente el problema μ [9] del *Minimal Supersymmetric Standard Model* (MSSM) [4, 6, 7], así como el problema ν, siendo capaz de reproducir correctamente las masas de los neutrinos y sus ángulos de mezcla [10–13]. También puede propocionar un buen candidato a DM, el gravitino.

En los modelos supersimétricos, la presencia de términos que violan los números bariónico y leptónico predice una desintegración demasiado rápida del proton y usualmente se utiliza la simetría de paridad R para prohibir que los mismos aparezcan en el Lagrangiano. Esta estrategia da lugar a modelos que conservan la paridad R (RPC) [14–18], tales como el MSSM. Por el contrario, el $\mu\nu$SSM es un modelo en el que la paridad R se viola (RPV) [19] debido a nuevos acoplamientos que involucran a los *neutrinos right-handed*, los cuales violan por tanto el número leptónico (siendo inofensivos para el desintegración del proton) Como la partícula supersimétrica más ligera (LSP) no es por tanto estable en el $\mu\nu$SSM, se generan nuevas señasles en los colisionadores, tales como la producción de vértices desplazados, multileptones o nuevos canales de desintegración.

El objetivo de esta tesis es estudiar a fondo el espacio de parámetros del $\mu\nu$SSM a

la luz de los datos experimentales actuales, utilizando un método muy potente basado en el análisis de datos y probabilidad. En concreto, estudiamos las regiones viables que son compatibles con los datos del Higgs y de las oscilaciones de neutrinos, así como con una clase de observables de sabor. Por un lado, analizamos aquellas regiones que pueden ser exploradas en el funcionamiento actual y futuro del LHC a través del sector extendido de Higgs del $\mu\nu$SSM, que en general consiste en dos dobletes de Higgs mezclados con las tres familias de sneutrinos. Después, aplicamos esta estrategia para estudiar la compatibilidad del *sneutrino left* como un candidato interesante a LSP [20, 21] en el $\mu\nu$SSM, con las búsquedas actuales de dileptones desplazados. Por otro lado, también analizamos las regiones que pueden explicar un viejo rompecabezas del SM, a saber, la desviación del valor medido del momento magnético anómalo del muón con respecto a la predicción teórica.

La tesis está organizada como sigue. En el Capítulo 2 describimos brevemente el MSSM y discutimos algunas de sus limitaciones. En el Capítulo 3 describimos el modelo $\mu\nu$SSM, presentando sus principales características y su sector de Higgs extendido. El capítulo 4 está dedicado a la descripción de la metodología que empleamos para nuestros análisis. Describimos el método de muestreo y los datos utilizados. Usando esta metodología, en el Capítulo 5 muestreamos el $\mu\nu$SSM para estudiar el impacto de la física del Higgs sobre su espacio de parámetros. Identificamos todas las regiones viables posibles que son compatibles con los últimos datos del LHC, teniendo en cuenta también otros datos del LEP y del Tevatron, así como una clase de observables de sabor como las desintegracion del B y el muon. En el Capítulo 6, reinterpretamos el resultado de la búsqueda de dileptones desplazados en ATLAS a 8-TeV originados en la desintegración de partículas de una vida media grande, para obtener los límites potenciales sobre el espacio de parámetros del *sneutrino tauónico left* como LSP en el $\mu\nu$SSM, con masa en el rango $45 - 100$ GeV. En concreto, muestreamos el $\mu\nu$SSM para explorar las regiones del espacio de parámetros que conducen al *sneutrino tauónico left* como LSP y para encontrar aquellas que puedan ser probadas usando la señal de dileptones desplazados en el funcionamiento actual y futuro del LHC. En el Capítulo 7, analizamos el espacio de parámetros del modelo que puede explicar el valor medido del momento magnético anómalo del muón. Dentro del modelo es posible producir partículas supersimétricas ligeras que son consistentes con los límites de exclusión experimental y que pueden contribuir por tanto a resolver este enorme rompecabezas del SM. Por último, en el Capítulo 8, resumimos los principales resultados obtenidos y esbozamos las perspectivas de futuro.

Chapter 2

Beyond the Standard Model

The SM of particles physics remains so far the most successful framework to explain the known elementary particles and their interactions. Considerable credence has further been given to it following the discovery in 2012 by the ATLAS [1] and CMS Collaborations [2] at the LHC of a new scalar resonance with properties similar to the SM predictions. Nevertheless, there are credible indications that the SM is not the ultimate theory and physics BSM must be present.

From the theoretical viewpoint, one of the relevant arguments in this sense is the existence of the hierarchy problem [22–24]. This is a problem that concerns the hierarchy between the electroweak scale and the Planck scale at which gravitational interactions are relevant. It is associated with the presence of an elementary scalar in the SM. Unlike the fermions and the gauge bosons, whose masses are finite because they are protected by the chiral and gauge symmetries, respectively, the scalar mass is unprotected. In a general quantum field theory like the SM, where an elementary scalar is present, the mass of the latter would be naturally at the scale of the cutoff of the theory up to which it remains valid. Thus, if the SM were the final theory the Higgs mass would be naturally of the order of the Planck scale. Therefore, the SM lacks a well-motivated explanation for the value of the mass of the scalar particle ~ 125 GeV, if the new physics is much above the electroweak scale.

Another argument in favor of physics BSM, from the experimental perspective, is the ν-problem, i.e. the evidence of non-zero masses and mixing angles of neutrinos [25, 26]. These results have been established by numerous collaborations, such as the atmospheric neutrino experiments SuperKamiokande [27] and SNO [28], the solar neutrino experiments [29–31] and the reactor experiments [32–36]. These observations are BSM frame-

work where, by construction, the light active neutrinos are exactly massless. Also, by construction, the SM does not include the gravitational interaction. Moreover, the evidence for DM [37–40] cannot be explained within the SM. Other arguments in favor of physics BSM include for example the strong CP problem, or the explanation of the baryon asymmetry of the Universe.

SUSY [3–7] has been the most studied of all the eligible candidates for physics BSM. It is a symmetry that provides a connection between fermions and bosons in such a way that for each SM particle there exists a supersymmetric partner with the same set of quantum numbers but a half integer spin difference. In addition, unlike in the SM where one Higgs doublet is enough, SUSY requires two Higgs doublets for the consistency of the theory and for giving masses to the up and down type fermions. As already mentioned, SUSY principle allows every SM boson and fermion to have a supersymmetric partner that is a fermion and boson respectively. In an exact SUSY, the masses of supersymmetric partners would be identical to their corresponding SM partners. However, none of the SUSY partners have been discovered, thus they must be heavier than their corresponding SM partners. By construction, SUSY solves several shortcomings of the SM, for instance, the hierarchy problem cancelling the quadratic divergences [7]. Also, assuming RPC [14–18] the LSP becomes stable and thereby provides a natural candidate for DM. Even in the case of RPV [19], it is possible to accommodate a decaying gravitino DM with a lifetime longer than the age of the Universe [41, 42]. Moreover, local SUSY is a theory of (super)gravity and therefore includes the gravitational interaction [43].

The simplest realization of SUSY, the MSSM [4, 6, 7], is briefly described in the next sections, as well as the issue of R-parity, the μ-problem and the ν-problem.

2.1 The MSSM

The MSSM particle content consists of the two-Higgs-doublet extension of the SM plus the corresponding SUSY partners. The Higgses and sparticles are shown in Table 2.1, together with their quantum numbers. The superpotential of the MSSM is written as

$$\begin{aligned} W_{\text{MSSM}} = & \quad \varepsilon_{ab} \left(Y_{e_{ij}} \hat{H}_d^a \hat{L}_i^b \hat{e}_j^c + Y_{d_{ij}} \hat{H}_d^a \hat{Q}_i^b \hat{d}_j^c + Y_{u_{ij}} \hat{H}_u^b \hat{Q}_i^a \hat{u}_j^c \right) \\ & - \varepsilon_{ab}\, \mu \hat{H}_u^b \hat{H}_d^a, \end{aligned} \tag{2.1}$$

where $\hat{Q}_i = (\hat{u}_i, \hat{d}_i)$, $\hat{L}_i = (\hat{\nu}_i, \hat{e}_i)$, $\hat{H}_d = (\hat{H}_d^0, \hat{H}_d^-)$, $\hat{H}_u = (\hat{H}_u^+, \hat{H}_u^0)$ are $SU(2)_L$ doublet superfields, and a, b are $SU(2)_L$ indices with ϵ_{ab} the totally antisymmetric tensor $\epsilon_{12} = 1$. The first three terms of Eq. (2.1) are related to quark and charged lepton Yukawa

	Spin	Gauge eigenstates	$SU(3)_c$	$SU(2)_L$	$U(1)_Y$
Squarks	0	$\widetilde{Q}_i$, $\widetilde{u}_{iR}$, $\widetilde{d}_{iR}$	3, 3, 3	2, 1, 1	1/6, 2/3, −1/3
Sleptons	0	$\widetilde{L}_i$, $\widetilde{e}_{iR}$	1, 1	2, 1	−1/2, −1
Higgses	0	H_d, H_u	1, 1	2, 2	−1/2, 1/2
Higgsinos	1/2	$\widetilde{H}_d$, $\widetilde{H}_u$	1, 1	2, 2	−1/2, 1/2
Gauginos	1/2	$\widetilde{W}_\mu$, $\widetilde{B}_\mu$, $\widetilde{g}$	1, 1, 8	3, 1, 1	0, 0, 0

Table 2.1: Sparticle and Higgs content of the MSSM, with $i = 1, 2, 3$ a family index.

interactions. The fourth term, i.e. the so-called μ-term, is the only dimensionful in superpotential.

In an exact SUSY, the SM particles and their SUSY partners would have the same masses and, therefore, should have already been discovered at colliders. SUSY partners must be therefore heavier then their SM counterparts. As a consequence, SUSY must be (softly) broken. The soft SUSY-breaking Lagrangian of the MSSM is given by [4, 6, 7]

$$\begin{aligned}
-\mathcal{L}^{\text{soft}}_{\text{MSSM}} = \quad & \epsilon_{ab}\left(T_{e_{ij}} H_d^a \widetilde{L}_{iL}^b \widetilde{e}_{jR}^* + T_{d_{ij}} H_d^a \widetilde{Q}_{iL}^b \widetilde{d}_{jR}^* + T_{u_{ij}} H_u^b \widetilde{Q}_{iL}^a \widetilde{u}_{jR}^* + \text{h.c}\right) \\
- \quad & \epsilon_{ab}\left(b H_u^b H_d^u + \text{h.c}\right) \\
+ \quad & \left(m^2_{\widetilde{Q}_L}\right)_{ij} \widetilde{Q}^*_{iL}\widetilde{Q}_{jL} + \left(m^2_{\widetilde{u}_R}\right)_{ij} \widetilde{u}^*_{iR}\widetilde{u}_{jR} + \left(m^2_{\widetilde{d}_R}\right)_{ij} \widetilde{d}^*_{iR}\widetilde{d}_{jR} + \left(m^2_{\widetilde{L}}\right)_{ij} \widetilde{L}^*_{iL}\widetilde{L}_{jL} \\
+ \quad & \left(m^2_{\widetilde{e}_R}\right)_{ij} \widetilde{e}^*_{iR}\widetilde{e}_{jR} + m^2_{H_d} H_d^{a^*} H_d^a + m^2_{H_u} H_u^{a^*} H_u^a \\
+ \quad & \frac{1}{2}\left(M_3\ \widetilde{g}\widetilde{g} + M_2\ \widetilde{W}\widetilde{W} + M_1\ \widetilde{B}^0\widetilde{B}^0 + \text{h.c}\right).
\end{aligned} \tag{2.2}$$

The trilinear terms in the first line are in correspondence with the trilinear couplings of the superpotential. The bilinear term in the second line is in correspondence with the μ-term. The terms in the third and fourth lines are the squared sfermion masses and Higgs masses. Finally, the parameters $M_{1,2,3}$ are the Majorana masses of the gluino, wino and bino fields.

The EWSB of the MSSM occurs when the neutral components of the two Higgs doublets, H_u^0 and H_d^0, acquire non-zero vacuum expectation values (VEVs) v_u and v_d, respectively, generating mass terms for quarks and charged leptons. After the EWSB, the gauge eigenstates mix forming the mass eigenstates. In particular, in the Higgs sector which is specially interesting for our analysis, the two neutral higgsinos mix with the two neutral gauginos giving rise to the four neutralinos. Similarly, charged gauginos mix with charged

higgsinos giving rise to the two charginos. Concerning Higgses, of the eight states, three of them are swallowed by the SM gauge bosons to become massive, while the other five give rise to two scalar Higgses, one pseudoscalar Higgs and two charged Higgses.

2.2 R-parity

The superpotential of the MSSM given in Eq. (2.1) is not the most general one. In fact, the most general (gauge invariant and renormalizable) superpotential of the MSSM must include in addition [19]:

$$W_{\rm RPV} = \epsilon_{ab}\left(\lambda_{ijk}\hat{L}_i^a\hat{L}_j^b\hat{e}_k^c + \lambda'_{ijk}\hat{L}_i^a\hat{Q}_j^b\hat{d}_k^c + \mu_i\hat{L}_i^a\hat{H}_d^b\right) + \lambda''_{ijk}\hat{u}_i^c\hat{d}_j^c\hat{d}_k^c\,, \tag{2.3}$$

where the terms in brackets, and the last term, violate lepton and baryon number, respectively. However, the simultaneous presence of the second and fourth term produces fast proton decay. To forbid this situation, R-parity was introduced [14–18] implying that all the SM particles have quantum number $R_p = 1$ while their superpartners have $R_p = -1$. One of the crucial consequences is that SUSY particles must be produced in pairs and, therefore, the LSP is stable and, hence, a good candidate for DM.

Nevertheless, invoking RPV to avoid the problem of proton decay is clearly too stringent, since then the other couplings λ_{ijk} and μ_i in the superpotential (2.3), which are harmless for proton decay, would also be forbidden. As discussed recently in detail in Ref. [44], λ''_{ijk} can be naturally forbidden, for example through Z_3 Baryon-parity or stringy selection rules.

2.3 The μ-problem

The μ-term in the second line of Eq. (2.1), is the only coupling in the superpotential with dimension of mass. Given that this term is purely supersymmetric, the scale of μ is expected to be of the same order as the scale at which SUSY remains preserved, typically the Planck scale. However, μ also contributes to the EWSB, and therefore to the mass of the Z:

$$\frac{1}{2}M_Z^2 = \frac{m_{H_d}^2 - m_{H_u}^2\tan^2\beta}{\tan^2\beta - 1} - \mu^2. \tag{2.4}$$

For soft masses of the order of the TeV scale, the measured value of $M_Z = 91.1876$ GeV [45] indicates that the scale of μ should be also around the TeV. This is the so-called μ-problem [9], the origin of μ and why it is much smaller than the Planck scale. The μ-term cannot be set to zero because then $v_d = 0$ giving rise to massless down-type fermions

and charged leptons. Besides, if $\mu = 0$, $W_{\rm MSSM}$ would have a global U(1) symmetry leading to a Goldstone boson after EWSB [46, 47]. In addition, $\mu \gtrsim 100$ GeV is necessary if we want to fulfill the RPC lower bound on chargino masses from LEP [45].

A solution to the μ problem is present in the gauge singlet extension of the MSSM, the so-called Next-to-MSSM (NMSSM) [48,49] where the bilinear $\mu\hat{H}_u\hat{H}_d$ term is replaced by $\lambda\hat{S}\hat{H}_u\hat{H}_d$, with the superfield $\hat{S}$ a singlet under the SM gauge group. After EWSB, an effective μ-term, with $\mu = \lambda s$, is generated with s the vacuum expectation value of the scalar S.

2.4 The ν-problem

The minimal way of generating massive neutrinos in the MSSM is by allowing RPV interaction terms in the Lagrangian [19]. In particular, the third type of terms in Eq. (2.3), $\mu_i\hat{L}_i\hat{H}_d$, added to the superpotential of the MSSM constitute the Bilinear R-parity Violating (BRpV) model, which generates neutrino masses through the mixing of the left-handed neutrinos with the neutralinos. However, because of the structure of the mass matrix, only one neutrino is massive at tree level while the remaining masses must appear through loops corrections. In addition, this type of terms generates other μ problems since the μ_i have to be very small $\lesssim 10^{-4}$ GeV, if one wants to reproduce the smallness of neutrino masses.

For the trilinear R-parity Violating (TRpV) models, the terms proportional to λ_{ijk} and λ'_{ijk}, or to λ''_{ijk}, in Eq. (2.3), are added to the superpotential of the MSSM. In this case, all light active neutrino masses are generated at loop level.

In sum, there exist SUSY models that can either solve the μ-problem or accommodate massive neutrinos. A simultaneous solution to both, μ- and ν-problem is possible in another singlet extension of the MSSM, once one allows RPV terms in the Lagrangian. This is the case of the so-called $\mu\nu$SSM, where three families of right-handed neutrino superfields are introduced for these tasks, as we will discuss in the next chapter.

Chapter 3

The $\mu\nu$SSM

In the previous chapter, we introduced the minimal realization of a SUSY model, the MSSM, and briefly presented several arguments as motivations to extend its framework. In this chapter, we introduce one of the extensions of the MSSM that provides a solution to the μ problem, and, simultaneously, an answer to the origin of neutrinos masses and mixing angles. This model is known as the 'μ from ν' Supersymmetric Standard Model ($\mu\nu$SSM) [8]. As we will discuss in detail below, in the $\mu\nu$SSM the presence of trilinear terms in the superpotential involving three families of right-handed neutrino superfields $\hat{\nu}^c_i$, with $i = 1, 2, 3$, is crucial to relate the origin of the μ-term to the origin of neutrino masses and mixing angles.

3.1 The superpotential and soft terms

The simplest superpotential of the $\mu\nu$SSM [8,20,50] with three right-handed neutrinos is the following:

$$\begin{aligned} W = & \sum_{a,b}\sum_{i,j}\epsilon_{ab}\left(Y_{e_{ij}}\,\hat{H}^a_d\,\hat{L}^b_i\,\hat{e}^c_j + Y_{d_{ij}}\,\hat{H}^a_d\,\hat{Q}^b_i\,\hat{d}^c_j + Y_{u_{ij}}\,\hat{H}^b_u\,\hat{Q}^a\,\hat{u}^c_j\right) \\ & + \sum_{a,b}\sum_{i,j}\epsilon_{ab}\left(Y_{\nu_{ij}}\,\hat{H}^b_u\,\hat{L}^a_i\,\hat{\nu}^c_j - \lambda_i\,\hat{\nu}^c_i\,\hat{H}^b_u\hat{H}^a_d\right) + \sum_{i,j,k}\frac{1}{3}\kappa_{ijk}\hat{\nu}^c_i\hat{\nu}^c_j\hat{\nu}^c_k\,, \end{aligned} \tag{3.1}$$

with $a, b = 1, 2$ $SU(2)_L$ indices with ϵ_{ab} the totally antisymmetric tensor $\epsilon_{12} = 1$, and $i, j, k = 1, 2, 3$ the usual family indices of the SM.

The three terms in the first line of the superpotential are the usual Dirac Yukawa couplings for quarks and charged leptons of the MSSM. The three terms in the third line are characteristic of the $\mu\nu$SSM. In particular, the first one contains the Dirac Yukawa couplings for neutrinos, and the last two generate dynamically the μ term and

Majorana masses for neutrinos, respectively. The simultaneous presence of these terms in Eq. (3.1) makes it impossible to assign R-parity charges consistently to the right-handed neutrinos (ν_{iR}), thus producing explicit RPV (harmless for proton decay). Note nevertheless, that in the limit of neutrino Yukawa couplings $Y_{\nu_{ij}} \to 0$, $\hat{\nu}_i^c$ can be identified in the superpotential as pure singlet superfields without lepton number, similar to the singlet of the NMSSM [49], and therefore R parity is restored. Thus, Y_ν are the parameters which control the amount of RPV in the $\mu\nu$SSM, and as a consequence this violation is small since the size of $Y_\nu \lesssim 10^{-6}$ is determined by the electroweak-scale seesaw of the $\mu\nu$SSM [8, 50].

Working in the framework of a typical low-energy SUSY, the Lagrangian containing the soft SUSY-breaking terms related to the superpotential in Eq. (3.1) is given by:

$$
\begin{aligned}
-\mathcal{L}_{\text{soft}} = \quad & \sum_{a,b}\sum_{i,j} \epsilon_{ab} \left(T_{e_{ij}}\, H_d^a\, \widetilde{L}_{iL}^b\, \widetilde{e}_{jR}^* + T_{d_{ij}}\, H_d^a\, \widetilde{Q}_{iL}^b\, \widetilde{d}_{jR}^* + T_{u_{ij}}\, H_u^b \widetilde{Q}_{iL}^a \widetilde{u}_{jR}^* + \text{h.c.} \right) \\
+ \quad & \sum_{a,b}\sum_{i,j} \epsilon_{ab} \left(T_{\nu_{ij}}\, H_u^b\, \widetilde{L}_{iL}^a \widetilde{\nu}_{jR}^* - T_{\lambda_i}\, \widetilde{\nu}_{iR}^*\, H_d^a H_u^b \ + \text{h.c.} \right) \\
+ \quad & \sum_{i,j,k} \left(\frac{1}{3} T_{\kappa_{ijk}}\, \widetilde{\nu}_{iR}^* \widetilde{\nu}_{jR}^* \widetilde{\nu}_{kR}^* \ + \text{h.c.} \right) \\
+ \quad & \sum_{a,b}\sum_{i,j} \Big[\left(m_{\widetilde{Q}_L}^2 \right)_{ij} \widetilde{Q}_{iL}^{a*} \widetilde{Q}_{jL}^a + \left(m_{\widetilde{u}_R}^2 \right)_{ij} \widetilde{u}_{iR}^* \widetilde{u}_{jR} + \left(m_{\widetilde{d}_R}^2 \right)_{ij} \widetilde{d}_{iR}^* \widetilde{d}_{jR} \\
+ \quad & \left(m_{\widetilde{L}_L}^2 \right)_{ij} \widetilde{L}_{iL}^{a*} \widetilde{L}_{jL}^a + \left(m_{\widetilde{\nu}_R}^2 \right)_{ij} \widetilde{\nu}_{iR}^* \widetilde{\nu}_{jR} + \left(m_{\widetilde{e}_R}^2 \right)_{ij} \widetilde{e}_{iR}^* \widetilde{e}_{jR} \Big] \\
+ \quad & \sum_a \left(m_{H_d}^2 H_d^{a*} H_d^a + m_{H_u}^2 H_u^{a*} H_u^a \right) \\
+ \quad & \frac{1}{2} \left(M_3\, \widetilde{g}\, \widetilde{g} + M_2\, \widetilde{W}\, \widetilde{W} + M_1\, \widetilde{B}^0\, \widetilde{B}^0 + \text{h.c.} \right) \ ,
\end{aligned}
\tag{3.2}
$$

The trilinear parameters $T_{d,e,u}$, T_ν, T_λ and T_κ are in correspondence with the trilinear couplings of the superpotential. If we follow the assumption based on the breaking of supergravity that all the trilinear parameters are proportional to their corresponding couplings in the superpotential [51], we can write

$$
T_{e_{ij}} = A_{e_{ij}} Y_{e_{ij}} \ , \ T_{d_{ij}} = A_{d_{ij}} Y_{d_{ij}} \ , \ T_{u_{ij}} = A_{u_{ij}} Y_{u_{ij}} \ , \tag{3.3}
$$

$$
T_{\nu_{ij}} = A_{\nu_{ij}} Y_{\nu_{ij}} \ , \ T_{\lambda_i} = A_{\lambda_i} \lambda_i \ , \ T_{\kappa_{ijk}} = A_{\kappa_{ijk}} \kappa_{ijk} \ , \tag{3.4}
$$

and the parameters A substitute the T as the most representative. We will use both type of parameters in our discussions. It is worth noticing here that we do not use the summation convention on repeated indices throughout this work, unless explicitly specified.

3.2 The scalar potential and EWSB

Together with the corresponding soft SUSY-breaking terms, the F and D terms give rise to the following tree-level neutral scalar potential:

$$V^{(0)} = V_{\rm soft} + V_F + V_D \ , \tag{3.5}$$

with

$$\begin{aligned} V_{\rm soft} = & \sum_{i,j,k} \left(T_{\nu_{ij}} \, H_u^0 \, \widetilde{\nu}_{iL} \, \widetilde{\nu}_{jR}^* - T_{\lambda_i} \, \widetilde{\nu}_{iR}^* \, H_d^0 H_u^0 + \frac{1}{3} T_{\kappa_{ijk}} \, \widetilde{\nu}_{iR}^* \widetilde{\nu}_{jR}^* \widetilde{\nu}_{kR}^* \ + \text{h.c.} \right) \\ + & \sum_{i,j} \left[\left(m^2_{\widetilde{L}_L} \right)_{ij} \widetilde{\nu}_{iL}^* \widetilde{\nu}_{jL} + \left(m^2_{\widetilde{\nu}_R} \right)_{ij} \widetilde{\nu}_{iR}^* \widetilde{\nu}_{jR} \right] + m^2_{H_d} H_d^{0*} H_d^0 + m^2_{H_u} H_u^{0*} H_u^0 \ , \end{aligned} \tag{3.6}$$

$$\begin{aligned} V_F = & \sum_{i,j,k,l,m} \Big(\lambda_j \lambda_j^* H_d^0 H_d^{0^*} H_u^0 H_u^{0^*} + \lambda_i \lambda_j^* \tilde{\nu}_{iR}^* \tilde{\nu}_{jR} H_d^0 H_d^{0*} + \lambda_i \lambda_j^* \tilde{\nu}_{iR}^* \tilde{\nu}_{jR} H_u^0 H_u^{0*} \\ + & \kappa_{ijk} \kappa^*_{ljm} \tilde{\nu}^*_{iR} \tilde{\nu}_{lR} \tilde{\nu}^*_{kR} \tilde{\nu}_{mR} - \Big(\kappa_{ijk} \lambda_j^* \tilde{\nu}^*_{iR} \tilde{\nu}^*_{kR} H_d^{0*} H_u^{0*} - Y_{\nu_{ij}} \kappa^*_{ljk} \tilde{\nu}_{iL} \tilde{\nu}_{lR} \tilde{\nu}_{kR} H_u^0 \\ + & Y_{\nu_{ij}} \lambda_j^* \tilde{\nu}_{iL} H_d^{0*} H_u^{0*} H_u^0 + Y^*_{\nu_{ij}} \lambda_k \tilde{\nu}^*_{iL} \tilde{\nu}_{jR} \tilde{\nu}^*_{kR} H_d^0 + \text{h.c.} \Big) \\ + & Y_{\nu_{ij}} Y^*_{\nu_{ik}} \tilde{\nu}^*_{jR} \tilde{\nu}_{kR} H_u^0 H_u^{0*} + Y_{\nu_{ij}} Y^*_{\nu_{lk}} \tilde{\nu}_{iL} \tilde{\nu}^*_{lL} \tilde{\nu}^*_{jR} \tilde{\nu}_{kR} + Y_{\nu_{ji}} Y^*_{\nu_{ki}} \tilde{\nu}_{jL} \tilde{\nu}^*_{kL} H_u^0 H_u^{0*} \Big) \ , \end{aligned} \tag{3.7}$$

$$V_D = \frac{1}{8} \left(g^2 + g'^2 \right) \left(\sum_i \widetilde{\nu}_{iL} \widetilde{\nu}_{iL}^* + H_d^0 H_d^{0*} - H_u^0 H_u^{0*} \right)^2 . \tag{3.8}$$

The EW gauge couplings are estimated at the m_Z scale by $e = g \sin\theta_W = g' \cos\theta_W$. Since only dimensionless trilinear couplings are present in the superpotential, the EWSB is determined by the soft terms of the scalar potential. Thus all known particle physics phenomenology can be reproduced in the $\mu\nu$SSM with one scale, the about 1 TeV scale of the soft terms, avoiding the introduction of'ad-hoc' high-energy scales. With the choice of CP conservation, one can define the neutral scalars as:

$$H_d^0 = \frac{1}{\sqrt{2}} \left(H_d^{\mathcal{R}} + v_d + i \ H_d^{\mathcal{I}} \right) , \tag{3.9}$$

$$H_u^0 = \frac{1}{\sqrt{2}} \left(H_u^{\mathcal{R}} + v_u + i \ H_u^{\mathcal{I}} \right) , \tag{3.10}$$

$$\widetilde{\nu}_{iR} = \frac{1}{\sqrt{2}} \left(\widetilde{\nu}_{iR}^{\mathcal{R}} + v_{iR} + i \ \widetilde{\nu}_{iR}^{\mathcal{I}} \right) , \tag{3.11}$$

$$\widetilde{\nu}_{iL} = \frac{1}{\sqrt{2}} \left(\widetilde{\nu}_{iL}^{\mathcal{R}} + v_{iL} + i \ \widetilde{\nu}_{iL}^{\mathcal{I}} \right) , \tag{3.12}$$

in such a way that after the EWSB they develop the real VEVs

$$\langle H_d^0\rangle = \frac{v_d}{\sqrt{2}}\,, \quad \langle H_u^0\rangle = \frac{v_u}{\sqrt{2}}\,, \quad \langle \widetilde{\nu}_{iR}\rangle = \frac{v_{iR}}{\sqrt{2}}\,, \quad \langle \widetilde{\nu}_{iL}\rangle = \frac{v_{iL}}{\sqrt{2}}\,. \tag{3.13}$$

The eight minimization conditions with respect to v_d, v_u, v_{iR} and v_{iL} can then be written as:

$$\begin{aligned} m_{H_d}^2 &= -\frac{1}{8}\left(g^2+g'^2\right)\left(v_{iL}v_{iL}+v_d^2-v_u^2\right)-\frac{1}{2}\lambda_i\lambda_j v_{iR}v_{jR}-\frac{1}{2}\lambda_i\lambda_i v_u^2 \\ &\quad +v_{iR}\tan\beta\left(\frac{1}{\sqrt{2}}T_{\lambda_i}+\frac{1}{2}\lambda_j\kappa_{ijk}v_{kR}\right)+Y_{\nu_{ij}}\frac{v_{iL}}{2v_d}\left(\lambda_k v_{kR}v_{jR}+\lambda_j v_u^2\right) \\ &\quad -\frac{\sqrt{2}}{v_d}V_{v_d}^{(n)}, \end{aligned} \tag{3.14}$$

$$\begin{aligned} m_{H_u}^2 &= \frac{1}{8}\left(g^2+g'^2\right)\left(v_{iL}v_{iL}+v_d^2-v_u^2\right)-\frac{1}{2}\lambda_i\lambda_j v_{iR}v_{jR}-\frac{1}{2}\lambda_j\lambda_j v_d^2 \\ &\quad +\lambda_j Y_{\nu_{ij}}v_{iL}v_d-\frac{1}{2}Y_{\nu_{ij}}Y_{\nu_{ik}}v_{kR}v_{jR}-\frac{1}{2}Y_{\nu_{ij}}Y_{\nu_{kj}}v_{iL}v_{kL} \\ &\quad +\frac{v_{iR}}{\tan\beta}\left(\frac{1}{\sqrt{2}}T_{\lambda_i}+\frac{1}{2}\lambda_j\kappa_{ijk}v_{kR}\right)-\frac{v_{iL}}{v_u}\left(\frac{1}{\sqrt{2}}T_{\nu_{ij}}v_{jR}+\frac{1}{2}Y_{\nu_{ij}}\kappa_{ljk}v_{lR}v_{kR}\right) \\ &\quad -\frac{\sqrt{2}}{v_u}V_{v_u}^{(n)}\,, \end{aligned} \tag{3.15}$$

$$\begin{aligned} (m_{\widetilde{\nu}_R}^2)_{ij}v_{jR} &= \frac{1}{\sqrt{2}}\left(-T_{\nu_{ji}}v_{jL}v_u+T_{\lambda_i}v_uv_d-T_{\kappa_{ijk}}v_{jR}v_{kR}\right)-\frac{1}{2}\lambda_i\lambda_j\left(v_u^2+v_d^2\right)v_{jR}+\lambda_j\kappa_{ijk}v_dv_uv_{kR} \\ &\quad -\kappa_{lim}\kappa_{ljk}v_{mR}v_{jR}v_{kR}+\frac{1}{2}Y_{\nu_{ji}}\lambda_k v_{jL}v_{kR}v_d+\frac{1}{2}Y_{\nu_{kj}}\lambda_i v_d v_{kL}v_{jR}-Y_{\nu_{jk}}\kappa_{ikl}v_uv_{jL}v_{lR} \\ &\quad -\frac{1}{2}Y_{\nu_{ji}}Y_{\nu_{lk}}v_{jL}v_{lL}v_{kR}-\frac{1}{2}Y_{\nu_{ki}}Y_{\nu_{kj}}v_u^2v_{jR}\;-\;V_{v_{iR}}^{(n)}\,, \end{aligned} \tag{3.16}$$

$$\begin{aligned} (m_{\widetilde{L}_L}^2)_{ij}v_{jL} &= -\frac{1}{8}\left(g^2+g'^2\right)\left(v_{jL}v_{jL}+v_d^2-v_u^2\right)v_{iL}-\frac{1}{\sqrt{2}}T_{\nu_{ij}}v_uv_{jR}+\frac{1}{2}Y_{\nu_{ij}}\lambda_k v_dv_{jR}v_{kR} \\ &\quad +\frac{1}{2}Y_{\nu_{ij}}\lambda_j v_u^2v_d-\frac{1}{2}Y_{\nu_{il}}\kappa_{ljk}v_uv_{jR}v_{kR}-\frac{1}{2}Y_{\nu_{ij}}Y_{\nu_{lk}}v_{lL}v_{jR}v_{kR}-\frac{1}{2}Y_{\nu_{ik}}Y_{\nu_{jk}}v_u^2v_{jL} \\ &\quad -V_{v_{iL}}^{(n)}\,, \end{aligned} \tag{3.17}$$

where $\tan\beta \equiv \frac{v_u}{v_d}$, $V_\theta^{(n)} \equiv \partial V^{(n)}/\partial x$ with $x = v_d$, v_u, v_{iR}, v_{iL}, and $V^{(n)}$ represents the n-loop radiative correction to the potential, $V = V^{(0)}+V^{(n)}$. Note that here the summation convention on repeated indices is used for simplicity. The scale at which the EWSB conditions are imposed is $M_{EWSB} = \sqrt{m_{\tilde{t}_l}m_{\tilde{t}_h}}$, where $m_{\tilde{t}_l}$ and $m_{\tilde{t}_h}$ correspond to the lightest and heaviest stop mass eigenvalues, respectively, measured at M_{EWSB}.

After the successful EWSB, several crucial terms are effectively generated in the $\mu\nu$SSM. Note from Eq. (3.16) that the VEVs of the right sneutrinos are naturally of

the order of the EWSB scale

$$\frac{v_{iR}}{\sqrt{2}} \approx 1 \text{ TeV} , \tag{3.18}$$

implying that the μ problem of the MSSM [9] is solved, thanks to the presence of the 5^{th} term in the superpotential above which generates an effective μ term with

$$\mu = \sum_i \lambda_i \frac{v_{iR}}{\sqrt{2}} . \tag{3.19}$$

In addition, the 6^{th} term in the superpotential generates effective Majorana masses for the right-handed neutrinos

$$\mathcal{M}_{ij} = \sum_\kappa 2\kappa_{ijk} \frac{v_{kR}}{\sqrt{2}} , \tag{3.20}$$

and, as a consequence, we can implement naturally a (generalized) electroweak-scale seesaw in the $\mu\nu$SSM which includes the neutralinos, asking for neutrino Yukawa couplings of the order of the electron Yukawa coupling or smaller (see the first two terms of Eqs. (3.32) and (3.36) below) [8, 50, 52–55]:

$$Y_{\nu_{ij}} \lesssim 10^{-6} . \tag{3.21}$$

This means that, we work with Dirac masses for neutrinos of the order of

$$m_{\mathcal{D}_{ij}} = Y_{\nu_{ij}} \frac{v_u}{\sqrt{2}} \lesssim 10^{-4} \text{ GeV} , \tag{3.22}$$

and that, no 'ad hoc' high-energy scales (larger than a TeV) are necessary to reproduce experimentally consistent neutrino masses. It is worth pointing out in this context that, the VEVs of the left sneutrinos are much smaller than the other VEVs. This is because of the small value of Y_ν. We can see in this respect that in Eq. (3.17), $v_{iL} \to 0$ as $Y_{\nu_{ij}} \to 0$. It is then easy to estimate the values of VEVs as $v_{iL} \lesssim m_{\mathcal{D}}$ [8], thus:

$$\frac{v_{iL}}{\sqrt{2}} \lesssim 10^{-4} \text{ GeV} . \tag{3.23}$$

This result allows that the seesaw of the $\mu\nu$SSM works properly, since the third term $\sim v_L^2/M$ in Eqs. (3.32) and (3.36) below, is of the same order as the first two. Finally, the 4^{th} term in the superpotential generates effective bilinear RPV couplings

$$\mu_i = \sum_i Y_{\nu_{ij}} \frac{v_{jR}}{\sqrt{2}} , \tag{3.24}$$

as those constituting the BRpV.

In sum, the superpotential of the $\mu\nu$SSM serves both the purposes of solving the μ

problem and generating non-zero neutrino masses and mixing solving the ν problem. As a consequence of the new terms introduced in the superpotential to solve these challenges, R-parity is explicitly broken, with its breaking controlled by the small Yukawa couplings for neutrinos, i.e. R-parity is restored for $Y_{\nu_{ij}} \to 0$.

3.3 The parameter space

Given the structure of the scalar potential, the free parameters in the neutral scalar sector of the $\mu\nu$SSM at the low scale M_{EWSB} are therefore: λ_i, κ_{ijk}, $Y_{\nu_{ij}}$, $m^2_{H_d}$, $m^2_{H_u}$, $m^2_{\widetilde{\nu}_{ij}}$, $m^2_{\widetilde{L}_{ij}}$, T_{λ_i}, $T_{\kappa_{ijk}}$ and $T_{\nu_{ij}}$. Using diagonal sfermion mass matrices, in order to avoid the strong upper bounds upon the intergenerational scalar mixing (see e.g. Ref. [56]), from the eight minimization conditions with respect to v_d, v_u, v_{iR} and v_{iL} one can eliminate the above soft masses in favor of the VEVs. In addition, using $\tan\beta$ and the SM Higgs VEV, $v^2 = v_d^2 + v_u^2 + \sum_i v_{iL}^2 = 4m_Z^2/(g^2 + g'^2) \approx (246\ \text{GeV})^2$, one can determine the SUSY Higgs VEVs, v_d and v_u. Since $v_{iL} \ll v_d, v_u$, one has $v_d \approx v/\sqrt{\tan^2\beta + 1}$. Besides, we can use diagonal neutrino Yukawa couplings, since data on neutrino physics can easily be reproduced at tree level in the $\mu\nu$SSM with such structure, as we will discuss below. Finally, assuming for simplicity that the off-diagonal elements of κ_{ijk} and soft trilinear parameters T vanish, we are left with the following set of variables as independent parameters in the neutral scalar sector:

$$\lambda_i,\ \kappa_i,\ Y_{\nu_i},\ \tan\beta,\ v_{iL},\ v_{iR},\ T_{\lambda_i},\ T_{\kappa_i},\ T_{\nu_i}, \tag{3.25}$$

where $\kappa_i \equiv \kappa_{iii}$, $Y_{\nu_i} \equiv Y_{\nu_{ii}}$, $T_{\nu_i} \equiv T_{\nu_{ii}}$ and $T_{\kappa_i} \equiv T_{\kappa_{iii}}$. Note that now the Majorana and Dirac mass matrices for neutrinos are diagonal, with the non-vanishing entries given respectively by

$$\mathcal{M}_i = 2\kappa_i \frac{v_{iR}}{\sqrt{2}}. \tag{3.26}$$

$$m_{\mathcal{D}_i} = Y_{\nu_i} \frac{v_u}{\sqrt{2}} \tag{3.27}$$

The rest of (soft) parameters of the model, namely the following gaugino masses, scalar masses, and trilinear parameters:

$$M_1,\ M_2,\ M_3,\ m_{\tilde{Q}_{iL}},\ m_{\tilde{u}_{iR}},\ m_{\tilde{d}_{iR}},\ m_{\tilde{e}_{iR}},\ T_{u_i},\ T_{d_i},\ T_{e_i}, \tag{3.28}$$

are also taken as free parameters and specified at low scale.

A further sensible simplification that we will also use in the next sections when nec-

essary, is to assume universality of the parameters in Eq. (3.25) with the exception of those connected directly with neutrino physics such as Y_{ν_i} and v_{iL}, that must be non-universal to generate correct neutrino masses and mixing angles. Neither we will impose universality for T_{ν_i}, since they are connected with sneutrino physics as we will discuss in the next section, and a hierarchy of masses in that sector can be phenomenologically interesting [57]. We are then left with the following set of low-energy free parameters:

$$\lambda,\, \kappa,\, Y_{\nu_i},\, \tan\beta,\, v_{iL},\, v_R,\, T_\lambda,\, T_\kappa,\, T_{\nu_i}, \tag{3.29}$$

where $\lambda \equiv \lambda_i$, $\kappa \equiv \kappa_i$, $v_R \equiv v_{iR}$, $T_\lambda \equiv T_{\lambda_i}$ and $T_\kappa \equiv T_{\kappa_i}$. In this case, the three non-vanishing Majorana masses are equal $\mathcal{M}_i = \mathcal{M}$, with

$$\mathcal{M} = 2\kappa\frac{v_R}{\sqrt{2}}, \tag{3.30}$$

and the μ-term is given by

$$\mu = 3\lambda\frac{v_R}{\sqrt{2}}. \tag{3.31}$$

3.4 The spectrum

The presence of new couplings and sneutrino VEVs in the $\mu\nu$SSM induce new mixing of states [8, 50]. In this section we review the particle spectrum of the model.

Neutral scalar sector: The right and left sneutrinos are mixed with the Higgs doublets. The real components of these eight states give rise to eight CP-even scalar eigenstates. In a similar way, after rotating away the neutral Goldstone boson, the imaginary parts of these eight states give rise to seven CP-odd scalar eigenstates. The corresponding mass matrices are given in Appendices A.1.1 and A.1.2, respectively. On the other hand, the couplings among left sneutrinos and Higgses occur through $Y_{\nu_{ij}}$ or v_{iL}. These are constrained to be small from the smallness of measured neutrino masses and hence left sneutrinos remain practically decoupled from Higgses. The right sneutrinos, nevertheless, couple through λ_i. The latter, being in general $\mathcal{O}(1)$ couplings, can generate significant singlet-doublet mixing in the $\mu\nu$SSM.

Charged scalar sector: The charged Higgses mix with the three families of left and righ charged sleptons. After rotating away the charged Goldstone boson, one gets seven charged eigenstates. Basically, the charged Higgs and the charged sleptons remain practically decoupled because they couple through tiny $Y_{\nu_{ij}}$. Their mass matrix is given in Appendix A.1.3.

Squarks: The squark mass matrices in the $\mu\nu$SSM include new terms with respect to the MSSM, but they are proportional either to $Y_{\nu_{ij}}$ or v_{iL} and hence have small effect in the determination of squark masses. Thus, the squarks eigenstates of the $\mu\nu$SSM coincide basically with those of the MSSM scenario. Novel differences, nonetheless, can appear in the decay cascades in the presence of RPV and additional states. The mass matrices can be found in Appendices A.1.4 and A.1.5.

Neutral fermions: MSSM neutralinos mix with the three generations of left- and right-handed neutrinos to form a 10×10 flavour matrix. Of the ten eigenstates, the three light-most states overlap with the light neutrinos, ν_L. We will discuss this issue in more detail in the next subsection. The mass matrix is given in Appendix A.2.1.

Charged fermions: MSSM Charginos mix with the charged leptons in the $\mu\nu$SSM, giving rise to five chargino eigenstates. Nevertheless, these mixings are suppressed by the smallness of $Y_{\nu_{ij}}$ and v_{iL} and, basically the three lighter charginos coincide with the charged leptons. The corresponding mass matrix can be found in Appendix A.2.2.

3.5 The neutrino sector

We have discussed in Section 3.2, that effective Majorana masses for right-handed neutrinos of the order of the EWSB scale are dynamically generated in the $\mu\nu$SSM (see Eq. (3.20)). In addition, in Section 3.4, we have seen that the MSSM neutralinos mix with the left- and right-handed neutrinos giving rise to the 10×10 neutral fermion ('neutrino') mass matrix shown in Eq. (A.63), which has the structure of a generalized electroweak-scale seesaw. Because of this structure, data on neutrino physics [10–13] can easily be reproduced at tree level [8,50,52–55], even with diagonal Yukawa couplings [52,54]. Qualitatively, we can understand this in the following way. First of all, the three neutrino masses are going to be very small since the entries of the first three rows (and columns) of the neutrino matrix are much smaller than the rest of the entries. The latter are of the order of the electroweak scale, whereas the former are of the order of the Dirac masses for neutrinos (see Eq. (3.22)) [8,50]. Second, from this matrix one can obtain a simplified formula for the effective mixing mass matrix of the light neutrinos [54]:

$$\begin{aligned}(m_\nu)_{ij} &= \frac{m_{\mathcal{D}_i} m_{\mathcal{D}_j}}{3\mathcal{M}}(1-3\delta_{ij}) - \frac{(v_{iL}/\sqrt{2})(v_{jL}/\sqrt{2})}{2M^{\text{eff}}} \\ &- \frac{m_{\mathcal{D}_i} m_{\mathcal{D}_j}}{2M^{\text{eff}}} \frac{1}{3\lambda \tan\beta}\left(\frac{v_{iL}/\sqrt{2}}{m_{\mathcal{D}_i}} + \frac{v_{jL}/\sqrt{2}}{m_{\mathcal{D}_j}} + \frac{1}{3\lambda\tan\beta}\right),\end{aligned} \tag{3.32}$$

where

$$M^{\rm eff} \equiv M - \frac{\left(v/\sqrt{2}\right)^2}{2\mu\left(\mathcal{M}\frac{v_R}{\sqrt{2}} + 2\lambda\left(\frac{v}{\sqrt{2}}\right)^2 \frac{\tan\beta}{1+\tan^2\beta}\right)}\left[2\mathcal{M}\frac{v_R}{\sqrt{2}}\frac{\tan\beta}{1+\tan^2\beta} + \lambda\left(\frac{v}{\sqrt{2}}\right)^2\right], \quad (3.33)$$

with

$$\frac{1}{M} = \frac{g'^2}{M_1} + \frac{g^2}{M_2}. \quad (3.34)$$

Here is assumed $\lambda_i = \lambda$, $v_{iR} = v_R$, and $\kappa_i = \kappa$, as in Eq. (3.29). The first term of Eq. (3.32) is generated through the mixing of ν_{iL} with ν_{iR}-Higgsinos, and the other two also include the mixing with the gauginos. These are the so-called ν_R-Higgsino seesaw and gaugino seesaw, respectively [54].

Using this approximate formula it is easy to understand how diagonal Yukawas can give rise to off-diagonal entries in the mass matrix. The key points are clearly the extra contributions with respect to the ordinary seesaw, given by the pieces which are not proportional to δ_{ij}.

We are then left in general with the following subset of variables of Eqs. (3.25) and (3.28) as independent parameters in the neutrino sector:

$$\lambda_i,\ \kappa_i,\ Y_{\nu_i}, \tan\beta,\ v_{iL},\ v_{iR},\ M, \quad (3.35)$$

In the numerical analyses, it will be enough for our purposes to consider the sign convention where all these parameters are positive.

Under several assumptions, the formula for $(m_\nu)_{ij}$ can be further simplified. Notice first that the third term is inversely proportional to $\tan\beta$, and therefore negligible in the limit of large or even moderate $\tan\beta$ provided that λ is not too small. Besides, the first piece inside the brackets in the second term of Eq. (3.33) is also negligible in this limit, and for typical values of the parameters involved in the seesaw also the second piece, thus $M^{\rm eff} \sim M$. Under these assumptions, the second term for $(m_\nu)_{ij}$ is generated only through the mixing of left-handed neutrinos with gauginos. Therefore, we arrive to a very simple formula where only the first two terms survive with $M^{\rm eff} = M$ in Eq. (3.33), i.e.

$$(m_\nu)_{ij} \;=\; \frac{m_{\mathcal{D}_i} m_{\mathcal{D}_j}}{3\mathcal{M}}(1 - 3\delta_{ij}) - \frac{(v_{iL}/\sqrt{2})(v_{jL}/\sqrt{2})}{2M}, \quad (3.36)$$

that can be used to understand easily the seesaw mechanism in the $\mu\nu$SSM in a qualitative way. From this discussion, it is clear that Y_{ν_i}, v_{iL} and M are crucial parameters to

determine the neutrino physics.

As we can understand from these equations, neutrino physics in the $\mu\nu$SSM is closely related to the parameters and VEVs of the model, since the values chosen for them must reproduce current data on neutrino masses and mixing angles. For example, for the typical values of the parameters and VEVs in Eqs. (3.18), (3.21) and (3.23), neutrino masses $\lesssim 0.1$ eV as expected, can easily be reproduced.

Let us finally point out that all these results in the $\mu\nu$SSM give a kind of answer to the question of why the mixing angles are so different in the quark and lepton sectors. Basically, because no generalized seesaw exists for the quarks.

3.6 The Higgs sector

As we discussed in Section 3.4, neutral Higgses are mixed with left and right sneutrinos, giving rise to 8×8 ('Higgs') mass matrices for scalar and pseudoscalar states. Nevertheless, we also noticed that in the 8×8 mass matrices, the 5×5 Higgs-right sneutrino submatrix is almost decoupled from the 3×3 left sneutrino submatrix due to the very small values of $Y_{\nu_{ij}}$ and v_{iL} in the off-diagonal entries [50,52]. Thus we can focus in the next subsection on the analysis of the Higgs-right sneutrino submatrix to accommodate the SM-like Higgs in the $\mu\nu$SSM. We will show how to disentangle the Higgs doublets from the rigth sneutrino states. As the left sneutrinos, the charged Higgs sector of the model is also not relevant for accommodating the SM-like Higgs, nevertheless we will briefly review it for completeness at the end.

3.6.1 The SM-like Higgs

We focus here on the analysis of the Higgs-right sneutrino submatrix to accommodate the SM-like Higgs in the $\mu\nu$SSM. The scalar and pseudoscalar mass submatrices are shown in Appendix B using the parameters of Eq. (3.25). Through the mixing with the right sneutrinos, which appears through λ_i, the tree-level mass of the lightest doublet-like Higgs receives an extra contribution with respecto to the MSSM. We want to emphasize that this analysis has a notable similarity with that of the NMSSM (although in the NMSSM one has only one singlet), however RPV and an enhanced particle content offer a novel and unconventional phenomenology for the Higgs-right sneutrino sector of the $\mu\nu$SSM [50, 52, 53, 58–64]. Taking into account all the contributions, the mass of the

SM-like Higgs in the $\mu\nu$SSM can be schematically written as [50, 62]:

$$m_h^2 = m_{0h}^2 + \Delta_{\text{mixing}} + \Delta_{\text{loop}}, \tag{3.37}$$

where

$$m_{0h}^2 = m_Z^2 \cos^2 2\beta + \left(\frac{v}{\sqrt{2}}\right)^2 \boldsymbol{\lambda}^2 \sin^2 2\beta \tag{3.38}$$

corresponds to neglect the mixing of the SM-like Higgs with the other states in the mass squared matrix, Δ_{mixing} encodes those mixing effects lowering (raising) the mass if it mixes with heavier (lighter) states, and Δ_{loop} refers to the radiative corrections. Note that m_{0h}^2 contains two terms, where the first is characteristic of the MSSM and the second of the $\mu\nu$SSM with

$$\boldsymbol{\lambda} \equiv \left(\sum_i \lambda_i^2\right)^{1/2} = \sqrt{3}\ \lambda, \tag{3.39}$$

where the last equality is obtained if one assumes universality of the parameters $\lambda_i = \lambda$.

We can write m_{0h}^2 in a more elucidate form for our discussion below as

$$m_{0h}^2 = m_Z^2 \left\{ \left(\frac{1-\tan^2\beta}{1+\tan^2\beta}\right)^2 + 14.5\ \boldsymbol{\lambda}^2 \left(\frac{\tan\beta}{1+\tan^2\beta}\right)^2 \right\}, \tag{3.40}$$

where we see straightforwardly that the second term grows with small $\tan\beta$ and large $\boldsymbol{\lambda}$. In the case of the MSSM this term is absent, hence the maximum possible tree-level mass is about m_Z for $\tan\beta \gg 1$ and, consequently, a contribution from loops is essential to reach the target of a SM-like Higgs in the mass region around 125 GeV. This contribution is basically determined by the soft parameters $T_{u_3}, m_{\widetilde{u}_{3R}}$ and $m_{\widetilde{Q}_{3L}}$. On the contrary, in the $\mu\nu$SSM one can reach this mass solely with the tree-level contribution for large values of $\boldsymbol{\lambda}$ [50]. Following the work of Ref. [62], we choose for this analysis three regions in $\boldsymbol{\lambda}$ values. In particular, for convenience of the discussion of Section 5.4, where the last equality of Eq. (3.39) is used, our regions are:

(a) Small to moderate ($0.01 \leq \boldsymbol{\lambda}/\sqrt{3} < 0.2$)
In this range, the maximum value of m_{0h} using Eq. (3.40) with $\boldsymbol{\lambda}/\sqrt{3} = 0.2$ goes as ≈ 78.9 GeV for $\tan\beta = 2$, which is ≈ 18 GeV more compared to a similar situation in the MSSM. It is thus essential to have additional contributions to raise m_{0h}^2 up to around 125 GeV. A possible source of extra tree-level mass can arise when the right sneutrino-like states are lighter compared to the lightest doublet-like Higgs. In this situation, the later

feels a push away effect from the former states characterized by $\Delta_{\rm mixing} > 0$, pushing m_h a bit further towards 125 GeV. Unfortunately, for most of this range of $\boldsymbol{\lambda}$ values, away from the upper end, the push-up effect is normally small owing to the small singlet-doublet mixing which is driven by λ_i (see Eq. (A.7) of Appendix) [50, 59]. The additional contribution to accommodate the 125 GeV doublet-like Higgs is coming then from loop effects. The situation is practically similar to that of the MSSM, where large masses for the third-generation squarks and/or a large trilinear A-term are essential [65–67]. A small trilinear A_{u_3}-term is possible only by decoupling the scalars to at least 5 TeV [67]. A light third generation squark, especially a stop, is natural in the so-called maximal mixing scenario [68], where $|X_{u_3}/m_{\widetilde{Q}_{3L}}| \approx \sqrt{6}$ with $X_{u_3} \equiv A_{u_3} - \mu/\tan\beta$.

These issues indicate that the novel signatures from SUSY particles (e.g., from a light stop or sbottom) are less generic in this region of $\boldsymbol{\lambda}$. Nevertheless, novel differences are feasible for Higgs decay phenomenology, especially in the presence of singlet-like lighter states [53, 58–64].

(b) Moderate to large ($0.2 \leq \boldsymbol{\lambda}/\sqrt{3} < 0.5$)
For this range of $\boldsymbol{\lambda}$ values, m_{0h} can go beyond m_Z, especially for $\tan\beta \lesssim 5$ and $\boldsymbol{\lambda}/\sqrt{3} \gtrsim 0.29$. For example with $\boldsymbol{\lambda}/\sqrt{3} \approx 0.4$, $\tan\beta = 2$ (5) gives $m_{0h} \sim 112$ (96) using Eq. (3.40). This is $\approx$ 100% (14%) enhancement compared to the MSSM scenario with the same $\tan\beta$. Note that this value $\boldsymbol{\lambda} \approx 0.7$ ($\lambda \approx 0.4$) is the maximum possible value of $\boldsymbol{\lambda}$ maintaining its perturbative nature up to the scale of a grand unified theory (GUT), $M_{\rm GUT} \sim 10^{16}$ GeV. As discussed in Ref. [50], using the renormalization group equations (RGEs) for λ and κ between $M_{\rm GUT}$ and the low scale $\sim$ 1 TeV, neglecting the contributions from the top and gauge couplings, one can arrive straightforwardly to the simple formula: $2.35\ \kappa^2 + 1.54\ \boldsymbol{\lambda}^2 \lesssim 1$. This gives the bound $\boldsymbol{\lambda} \lesssim 0.8$, similar but slightly larger than the one of 0.7 mentioned before. Nevertheless, one should expect a final bound slightly stronger when all contributions to the RGEs are taken into account. The numerical analysis indicates that a better approximate formula is

$$2.77\ \kappa^2 + 2\ \boldsymbol{\lambda}^2 \lesssim 1, \tag{3.41}$$

which produces the bounds $\boldsymbol{\lambda} \lesssim 0.7$ and $\kappa \lesssim 0.6$.

For this region of $\boldsymbol{\lambda}$ the singlet-doublet mixing is no longer negligible as we will see in the next subsection, particularly as $\boldsymbol{\lambda}/\sqrt{3} \to 0.4$. Thus, a state lighter than 125 GeV with the leading singlet composition appears difficult without a certain degree of tuning of the other parameters, e.g. κ_i, v_{iR}, T_{κ_i}, T_{λ_i}, etc. In this situation, the extra contribution to

the tree-level value of m_h is favourable through a push-up action from the singlet states compared to small to moderate $\boldsymbol{\lambda}$ scenario. Once again a contribution from the loops is needed to reach the 125 GeV target. However, depending on the values of $\boldsymbol{\lambda}$ and $\tan\beta$ the requirement sometime is much softer compared to small to moderate $\boldsymbol{\lambda}$ scenario. Thus the necessity of very heavy third-generation squarks and/or large trilinear soft-SUSY breaking term may not be so essential for this region [65]. It is also worth noticing that the naturalness is therefore improved with respect to the MSSM or smaller values of $\boldsymbol{\lambda}$.

When $\boldsymbol{\lambda}/\sqrt{3} \to 0.5$, m_{0h} as evaluated from Eq. (3.40) can be larger than 125 GeV. For example, for the upper bound of this range $\boldsymbol{\lambda}/\sqrt{3} = 0.5$, $\tan\beta = 2$ gives $m_{0h} \sim 132$ GeV. In this case we have to relax the idea of perturbativity up to the GUT scale, as we will discuss below.

(c) Large $\boldsymbol{\lambda}$ $(0.5 \leq \boldsymbol{\lambda}/\sqrt{3} < 1.2)$

Assuming e.g. a scale of new physics around 10^{11} GeV, and following similar analytical arguments as above using the RGEs, the perturbative limit gives approximately $1.48\ \kappa^2 + 0.96\ \boldsymbol{\lambda}^2 \lesssim 1$ producing the bounds $\boldsymbol{\lambda} \lesssim 1$ and $\kappa \lesssim 0.82$. For $\boldsymbol{\lambda}$, taking into account the contributions from the top and gauge couplings to the RGEs as above, one can find numerically [50] the final bound $\boldsymbol{\lambda} \lesssim 0.88$, i.e. $\boldsymbol{\lambda}/\sqrt{3} \lesssim 0.5$.

Pushing the scale of new physics further below to 10 TeV, the approximate analytical analysis gives the perturbative limit

$$0.25\ \kappa^2 + 0.14\ \boldsymbol{\lambda}^2 \lesssim 1, \tag{3.42}$$

producing now the bounds $\boldsymbol{\lambda} \lesssim 2.6$ (i.e. $\boldsymbol{\lambda}/\sqrt{3} \lesssim 1.5$) and $\kappa \lesssim 2$. Given that the full numerical analysis produces typically stronger bounds, we will use $\boldsymbol{\lambda}/\sqrt{3} \lesssim 1.2$ in our scan of Sec. 5.4. A similar scenario in the context of the NMSSM has been popularised as λ-SUSY [69]. The constraint in this case [70] is slightly different than ours because of the presence of only one singlet.

In this region of $\boldsymbol{\lambda}$ values, m_{0h} as evaluated from Eq. (3.40) can remain well above 125 GeV even up to $\tan\beta \sim 8$ for $\boldsymbol{\lambda}/\sqrt{3} \sim 1.2$. For $\boldsymbol{\lambda}/\sqrt{3} = 0.58$, m_{0h} for $\tan\beta = 2$, 5 and 10 is estimated as ~ 150 GeV, 108 GeV and ~ 96 GeV, respectively. With $\boldsymbol{\lambda}/\sqrt{3} = 1.2$ these numbers increase further, for example, ~ 113 GeV when $\tan\beta = 10$. The requirement of an extra contribution to reach the target of 125 GeV is thus rather small and even negative in this corner of the parameter space unless $\tan\beta$ goes beyond 10 or 15 depending on the values of $\boldsymbol{\lambda}$. A singlet-like state lighter than 125 GeV is difficult in this corner of the parameter space due to the large singlet-doublet mixing. In fact even if one manages to

get a scalar lighter than 125 GeV with parameter tuning, a push-up action can produce a sizable effect to push the mass of the lightest doublet-like state beyond 125 GeV, especially for $\tan\beta \lesssim 10$ taking $\boldsymbol{\lambda}/\sqrt{3} = 1.2$. Moreover, a huge doublet component makes these light states hardly experimentally acceptable. In this region of the parameter space a heavy singlet-like sector is more favourable which can push m_h down towards 125 GeV, due to $\Delta_{\text{mixing}} < 0$. In addition, for such a large $\boldsymbol{\lambda}$ value, new loop effects from the right sneutrinos proportional to $\boldsymbol{\lambda}^2$ can also give a sizeable negative contribution [71, 72]. A set of very heavy singlet-like states, even with non-negligible doublet composition is also experimentally less constrained.

It is needless to mention that the amount of the loop correction is much smaller in this region compared to the two previous scenarios. Following the above discussion for large values of $\boldsymbol{\lambda}$, this region of the parameter space also favours third-generation squarks lighter than 1 TeV, which can be produced with enhanced cross sections and can lead to novel signatures of this model with RPV at the LHC, even when the singlet-like states remain heavier, as stated earlier.

In Sec. 5.4, we will analyze these $\boldsymbol{\lambda}$ regions using three scans, and we will check how much room is left for new physics in the $\mu\nu$SSM in the light of the current precise measurements of the SM-like Higgs properties. Let us now study the right sneutrino-like sector which, as pointed out before, is crucial to determine the properties of the SM-like Higgs in the $\mu\nu$SSM.

3.6.2 The right sneutrino-like states

From the scalar and pseudoscalar mass submatrices in Appendix B, it is clear that κ_i and T_{κ_i} are crucial parameters to determine the masses of the singlet-like states, originating from the self-interactions. The remaining parameters λ_i and T_{λ_i} (A_{λ_i} assuming the supergravity relation $T_{\lambda_i} = \lambda_i A_{\lambda_i}$ of Eq. (3.4)) not only appear in the said interactions, but also control the mixing between the singlet and the doublet states and hence, contribute in determining the mass scale. Note that the contributions of the parameters T_{ν_i} are negligible assuming $T_{\nu_i} = Y_{\nu_i} A_{\nu_i}$, given the small values of neutrino Yukawas. We conclude, taking also into account the discussion below Eq. (3.40), that the relevant independent low-energy parameters in the Higgs-right sneutrino sector are the following subset of parameters of Eqs. (3.25) and (3.28):

$$\lambda_i,\ \kappa_i, \tan\beta,\ v_{iR},\ T_{\kappa_i},\ T_{\lambda_i}, T_{u_3},\ m_{\widetilde{u}_{3R}},\ m_{\widetilde{Q}_{3L}}. \tag{3.43}$$

In the limit of vanishingly small λ_i (considering simultaneously very large v_{iR} in the case that we require the lighter chargino mass bound of RPC SUSY $\mu \gtrsim 100$ GeV), not only the off-diagonal entries of the right sneutrino submatrices (B.6) and (B.12) are negligible, but also the off-diagonal entries (B.4), (B.5) and (B.10), (B.11) of the Higgs-right sneutrino matrices. As a consequence of the latter, the singlet states are decoupled from the doublets. It is thus apparent, that λ_i are undoubtedly the most relevant parameters for the analysis of these states. Another aspect of the parameters λ_i, namely to yield additional contributions to the tree-level SM-like Higgs mass has already been discussed in the previous subsection. Thus, one can write the right sneutrino masses as:

$$m^2_{\widetilde{\nu}^{\mathcal{R}}_{iR}} = \left(\frac{T_{\kappa_i}}{\kappa_i} + 2\mathcal{M}_i\right)\frac{\mathcal{M}_i}{2}, \tag{3.44}$$

$$m^2_{\widetilde{\nu}^{\mathcal{I}}_{iR}} = -\frac{3}{2}\frac{T_{\kappa_i}}{\kappa_i}\mathcal{M}_i, \tag{3.45}$$

where in the case of supergravity, we can use the relation $T_{\kappa_i}/\kappa_i = A_{\kappa_i}$. In addition, in this limit, $\mathcal{M}_i$ coincide approximately with the masses of the right-handed neutrinos, since they are decoupled from the other entries of the neutralino mass matrix:

$$m_{\nu_{iR}} = \mathcal{M}_i. \tag{3.46}$$

With the sign convention adopted in Section 3.5, $\mathcal{M}_i > 0$, and from Eq. (3.45) we deduce that negative values for T_{κ_i} (or A_{κ_i}) are necessary in order to avoid tachyonic pseudoscalars. Using also that equation, we can write (3.44) as

$$m^2_{\widetilde{\nu}^{\mathcal{R}}_{iR}} = \mathcal{M}_i^2 - \frac{1}{3}m^2_{\widetilde{\nu}^{\mathcal{I}}_{iR}}. \tag{3.47}$$

Thus, the simultaneus presence of non-tachyonic scalars and pseudoscalars implies that [62]

$$m_{\widetilde{\nu}^{\mathcal{I}}_{iR}} < \sqrt{3}\mathcal{M}_i, \tag{3.48}$$

$$m_{\widetilde{\nu}^{\mathcal{R}}_{iR}} < \mathcal{M}_i. \tag{3.49}$$

Hence, light scalars/pseudoscalar states are assured when light neutralinos (i.e. basically the product $\kappa_i v_{iR}$) are present. From Eq. (3.44) we also see that the absence of tachyons implies the condition

$$\frac{-T_{\kappa_i}}{\kappa_i} < 2\mathcal{M}_i, \tag{3.50}$$

and therefore the value of T_{κ_i}/κ_i and the product $\kappa_i v_{iR}$ have to be chosen appropriately to fulfill it. Also from that equation we see that singlet scalars lighter than the SM-like Higgs can be obtained when

$$2\mathcal{M}_i - \frac{2m^2_{\rm Higgs}}{\mathcal{M}_i} < \frac{-T_{\kappa_i}}{\kappa_i}. \tag{3.51}$$

Thus, for a given value of $\mathcal{M}_i$, only a narrow range of values of $-T_{\kappa_i}/\kappa_i$ is able to fulfill simultaneously both conditions (3.50) and (3.51). We will come back to this issue in Section 5.4.

On the other hand, even in a region of small to moderate λ_i, to obtain approximate analytical formulas for tree-level scalar and pseudoscalar masses turn out to be rather complicated due to the index structure of the parameters involved. As discussed in detail in Ref. [62], the expressions for their masses can be simplified in the limit of complete degeneracy in all relevant parameters as in Eq. (3.29), i.e. when $\lambda_i = \lambda$ ($\lambda = \boldsymbol{\lambda}/\sqrt{3}$ as defined in Eq. (3.39)), $\kappa_i = \kappa, v_{iR} = v_R, T_{\kappa_i} = T_\kappa, T_{\lambda_i} = T_\lambda$. In this case, the 3×3 scalar and pseudoscalar mass submatrices in Eqs (B.6) and (B.12) have the form

$$\begin{pmatrix} a & b & b \\ b & a & b \\ b & b & a \end{pmatrix}, \tag{3.52}$$

with the three eigenvalues given by $a - b$, $a - b$ and $a + 2b$. Then, it was shown that for both, scalars and pseudoscalars, the two mass eigenstates corresponding to the first two eigenvalues $a - b$ get decoupled and remain as pure singlet-like states without any doublet contamination. Using the values of a and b from Appendix B, and neglecting T_ν under the supergravity assumption of being proportional to the small Y_ν, one obtains the following degenerate masses:

$$m^2_{\widetilde{\nu}^{\mathcal{R}}_{1,2R}} = \left(\frac{T_\kappa}{\kappa} + 2\mathcal{M}\right)\frac{\mathcal{M}}{2} + 3\lambda^2\left(\frac{v}{\sqrt{2}}\right)^2\left(\frac{1}{\mu}\frac{T_\lambda}{\lambda}\frac{\tan\beta}{1+\tan^2\beta} - 1\right), \tag{3.53}$$

$$m^2_{\widetilde{\nu}^{\mathcal{I}}_{1,2R}} = -\frac{3}{2}\frac{T_\kappa}{\kappa}\mathcal{M} + 3\lambda^2\left(\frac{v}{\sqrt{2}}\right)^2\left[\left(\frac{1}{\mu}\frac{T_\lambda}{\lambda} + \frac{4}{3}\frac{\kappa}{\lambda}\right)\frac{\tan\beta}{1+\tan^2\beta} - 1\right], \tag{3.54}$$

where now μ is defined in Eq. (3.31), and the Majorana mass is given in Eq. (3.30) corresponding approximately, also, to two pure right-handed neutrino states decoupled from the rest of the neutralinos:

$$m_{\nu_{1,2R}} = \mathcal{M}. \tag{3.55}$$

The degeneracy of these states can be broken by introducing mild splittings in κ_i values [59, 62], as it is obvious e.g. from Eqs. (3.44), (3.45) and (3.46). One thing to highlight is that, the first term of Eq. (3.53) is like the one of Eq. (3.44) in the case of universality, and therefore a condition similar to (3.50) is welcome to avoid tachyons in the scalar spectrum. Nevertheless, depending on the values chosen for the input parameters, the second term in (3.53) can be positive, relaxing this condition. The latter is especially true for large values of λ.

The mass eigenstate corresponding to the third eigenvalue, namely the one which goes as $a + 2b$, however mixes with the doublet-like states, and eventually its mass appears with a complicated form. In the case of the pseudoscalar this is given by

$$m^2_{\widetilde{\nu}^{\mathcal{I}}_{3R}} = -\frac{3}{2}\frac{T_\kappa}{\kappa}\mathcal{M} + 9\lambda\kappa \left(\frac{v}{\sqrt{2}}\right)^2 \frac{T_\lambda/\lambda}{\frac{T_\lambda}{\lambda}+\frac{\mathcal{M}}{2}} \frac{\tan\beta}{1+\tan^2\beta}. \tag{3.56}$$

In the case of the scalar, $m^2_{\widetilde{\nu}^{\mathcal{R}}_{3R}}$ appears with a much complicated form that can be found in Ref. [62]. Similarly, the third right-handed neutrino-like state mixes with the other MSSM-like neutralinos, and its mass is given by

$$m_{\nu_{3R}} = \mathcal{M} - \frac{\lambda^2}{2\mu}\left(\frac{v}{\sqrt{2}}\right)^2 \left[\frac{1+\tan^2\beta}{\tan\beta} - \frac{4M\mu}{\left(v/\sqrt{2}\right)^2}\right]\left[\frac{1+\tan^2\beta}{\tan\beta}\frac{M\mu}{\left(v/\sqrt{2}\right)^2} - 1\right]^{-1}, \tag{3.57}$$

where M is defined in Eq. (3.34).

Depending on the input parameters chosen, the two degenerate states can be heavier or lighter than the third state. For example, for the pseudoscalars we see that the second term in Eq. (3.56) is always positive whereas the second term in Eq. (3.54) can be positive (larger or smaller than the previous one) or even negative.

It is also worthy to note that, for further small λ values (i.e. $\lesssim 0.01$) or in the limit of a vanishingly small λ, these formulas take simpler forms, and the three states are degenerate:

$$m^2_{\widetilde{\nu}^{\mathcal{R}}_{iR}} = \left(\frac{T_\kappa}{\kappa} + 2\mathcal{M}\right)\frac{\mathcal{M}}{2}, \tag{3.58}$$

$$m^2_{\widetilde{\nu}^{\mathcal{I}}_{iR}} = -\frac{3}{2}\frac{T_\kappa}{\kappa}\mathcal{M}, \tag{3.59}$$

$$m_{\nu_{iR}} = \mathcal{M}. \tag{3.60}$$

As expected, they coincide with Eqs. (3.44), (3.45), and (3.46), respectively, when written for universal parameters.

Other simple formulas can be obtained in the limit of $\tan\beta \to \infty$, where

$$m^2_{\widetilde{\nu}^{\mathcal{R}}_{1,2R}} = \left(\frac{T_\kappa}{\kappa} + 2\mathcal{M}\right)\frac{\mathcal{M}}{2} - 3\lambda^2\left(\frac{v}{\sqrt{2}}\right)^2, \tag{3.61}$$

$$m^2_{\widetilde{\nu}^{\mathcal{I}}_{1,2R}} = -\frac{3}{2}\frac{T_\kappa}{\kappa}\mathcal{M} - 3\lambda^2\left(\frac{v}{\sqrt{2}}\right)^2, \tag{3.62}$$

and

$$m^2_{\widetilde{\nu}^{\mathcal{R}}_{3R}} = \left(\frac{T_\kappa}{\kappa} + 2\mathcal{M}\right)\frac{\mathcal{M}}{2} - 3\lambda^2\left(\frac{v}{\sqrt{2}}\right)^2\left(\frac{2\mu}{m_Z}\right)^2, \tag{3.63}$$

$$m^2_{\widetilde{\nu}^{\mathcal{I}}_{3R}} = -\frac{3}{2}\frac{T_\kappa}{\kappa}\mathcal{M}, \tag{3.64}$$

whereas for the righ-handed neutrinos one obtains

$$m_{\nu_{1,2R}} = \mathcal{M}, \tag{3.65}$$

$$m_{\nu_{3R}} = \mathcal{M} - \frac{\lambda^2}{2\mu^2 M}\left(\frac{v}{\sqrt{2}}\right)^4. \tag{3.66}$$

It is evident from this result that unless λ is small to moderate, it is in general hard to accommodate a complete non-tachyonic light spectrum (i.e. $\lesssim m_{\text{Higgs}}/2$) for both the scalars and pseudoscalars in the limit of large $\tan\beta$ without a parameter tuning. In addition, this limit is severely constrained from diverse experimental results. This is because the BRs for some low-energy processes (e.g. $B^0_s \to \mu^+\mu^-$), depending on the other relevant parameters are sensitive to the high powers of $\tan\beta$ and thus, can produce large BRs for these processes in an experimentally unnacceptable way. The other limit, i.e. small $\tan\beta$, on the contrary, is useful from the viewpoint of raising the mass of the lightest doublet-like scalar towards 125 GeV, specially for moderate to large λ values . However, as shown in the discussion of Eqs. (3.53), (3.54) and (3.56), not all the mass formulas for the light states are simple structured in this region and a numerical analysis is convenient.

3.6.3 The left sneutrino states

The behaviour of the left sneutrino states is very different from the one of the right sneutrino states, since the former is tightly associated to neutrino physics.

As discussed in the previous subsection, the 3×3 scalar and pseudoscalar left sneutrino submatrices are decoupled from the 5×5 Higgs-right sneutrino sumatrices. Besides, their off-diagonal entries are negligible compared to the diagonal ones, since they are suppressed by terms proportional to $Y^2_{\nu_{ij}}$ and v^2_{iL}. As a consequence, the mass squared eigenvalues correspond to the diagonal entries, and in this approximation both states also have degenerate masses. Using the minimization equations for v_{iL}, we can write their tree-level values as [20, 50, 52, 64]

$$m^2_{\widetilde{\nu}^{\mathcal{R}}_{iL}} = m^2_{\widetilde{\nu}^{\mathcal{I}}_{iL}} = \frac{m_{\mathcal{D}_i}}{v_{iL}/\sqrt{2}}\frac{v_{iR}}{\sqrt{2}}\left[\frac{-T_{\nu_i}}{Y_{\nu_i}} - \frac{\mathcal{M}_i}{2} + \frac{\mu}{\tan\beta} + \lambda_i\frac{\left(v/\sqrt{2}\right)^2}{v_{iR}/\sqrt{2}}\frac{\tan\beta}{1+\tan^2\beta}\right]. \quad (3.67)$$

Therefore, in addition to the parameters of Eq. (3.35) relevant for neutrino physics, the

$$T_{\nu_i} \quad (3.68)$$

are relevant parameters for the study of left sneutrino masses. The fourth term in Eq. (3.67) can usually be neglected as long as $v_{iR} \gg v$ and/or λ_i is small, and we can write then

$$m^2_{\widetilde{\nu}^{\mathcal{R}}_{iL}} = m^2_{\widetilde{\nu}^{\mathcal{I}}_{iL}} \approx \frac{m_{\mathcal{D}_i}}{v_{iL}/\sqrt{2}}\frac{v_{iR}}{\sqrt{2}}\left(\frac{-T_{\nu_i}}{Y_{\nu_i}} - \frac{\mathcal{M}_i}{2} + \frac{\mu}{\tan\beta}\right). \quad (3.69)$$

In the limit of moderate/large $\tan\beta$, one can also neglect the third term. Under these approximations, the condition for non-tachyonic left sneutrinos can be written as an upper bound on the Majorana masses

$$\frac{\mathcal{M}_i}{2} \lesssim \frac{-T_{\nu_i}}{Y_{\nu_i}}, \quad (3.70)$$

Given our sign convention of positive Majorana mass, we will use negative values for T_{ν_i} in our numerical analyses.

Going back to Eq. (3.67), we see clearly why left sneutrinos are special in the $\mu\nu$SSM with respect to other SUSY models. Given that their masses are determined by the minimization equations with respect to v_i, they depend not only on left sneutrino VEVs but also on neutrino Yukawas, *unlike right sneutrinos* and, as a consequence, neutrino physics is very relevant for them.

Considering the normal ordering for the neutrino mass spectrum, which is nowadays favored by the analyses of neutrino data [10–13], and taking advantage of the dominance of the gaugino seesaw for some of the three neutrino families, representative solutions for

neutrino/sneutrino physics using diagonal neutrino Yukawas were summarized in Ref. [57]. Different hierarchies among the generations of left sneutrinos are possible, using different hierarchies among Y_{ν_i} (and also v_{iL}).

There is enough freedom in the parameter space of the $\mu\nu$SSM in order to get heavy as well as light left sneutrinos from Eq. (3.67), and the latter scenario with the left sneutrino as the lightest supersymmetry particle (LSP) was considered in Refs. [20, 21, 57]. Due to the doublet nature of the left sneutrino, masses smaller than half of the mass of the SM-like Higgs were found to be forbidden [57] to avoid dominant decay of the latter into sneutrino pairs, leading to an inconsistency with Higgs data. Let us finally remark that in those works negative values for T_{u_3} were used, in order to avoid too light left sneutrinos due to loop corrections. Although we are not specially interested in light sneutrinos in this work, we will maintain the same sign convention in what follows. To use positive values for T_{u_3} would have not modify our results, since their effect on the SM-like Higgs mass is similar.

3.6.4 The charged scalars

The charged scalars have a 8×8 ('charged Higgs') mass matrix. Similar to the neutral Higgs mass matrices where some sectors are decoupled, the 2×2 charged Higgs submatrix is decoupled from the 6×6 slepton submatrix. Thus, as in the MSSM, the mass of the charged Higgs $H^\pm$ is similar to the one of the doublet-like neutral pseudoscalar A, specially when the latter is not very mixed with the right sneutrinos. In this case, both masses are also similar to the one of the heavy doublet-like neutral Higgs H.

Concerning the 6×6 submatrix, the right sleptons are decoupled from the left ones, since the mixing terms are suppressed by the electron-type Yukawa couplings or v_{iL}. Then, the masses of right and left sleptons are basically determined by their corresponding soft terms, $m^2_{\tilde{e}_{iR}}$ and $m^2_{\tilde{L}_i}$, respectively. Although the left sleptons are in the same $SU(2)$ doublet as the left sneutrinos, they are a little heavier than the latter mainly due to the mass splitting produced by the D-term contribution, $-m_W^2\cos2\beta$.

3.7 Collider phenomenology

Concerning collider signals, RPV in the $\mu\nu$SSM leads to novel signatures such as displaced final states that are practically free from SM backgrounds, and detectable at the LHC with dedicated analyses. Also, the enlarged particle spectrum discussed in Section 3.4 could induce new decay chains rendering very rich and diverse the collider

phenomenology of the model. New final states such as multileptons can also be produced, etc. In this section we summarize previous studies of collider phenomenology in the $\mu\nu$SSM.

In Refs. [52, 53, 60, 62], the decay properties of the LSP assumed to be the lightest neutralino were calculated, and the parameter regions where the displaced decays of the neutralino could be observed with the LHC detectors were identified.

In Refs. [59, 62], the signatures produced via two-body decays of the SM-like Higgs into new lighter states were explored. This is motivated by the fact that light neutralinos and neutral scalars with leading singlino and singlet composition, respectively, are possible in the $\mu\nu$SSM. Thus, a pair produced light neutralinos depending on the associated decay length can give rise to displaced multi-leptons/taus/jets/photons with small/moderate missing transverse energy (MET). Also, the SM-like Higgs decaying to a pair of scalars/pseudoscalars can produce final states with prompt multi-leptons/taus/jets/photons. Related to this, recently, in Refs. [63, 64], in addition to perform the complete one-loop renormalization of the neutral scalar sector of the $\mu\nu$SSM, interesting benchmark points (BPs) with right sneutrinos lighter than the standard model-like Higgs boson were studied. In the same spirit as above, the presence of these light states can produce non-standard on-shell decays of $W^{\pm}$ and Z bosons leading to prompt or displaced multileptons/tau jets/jets/photons in the final states [61].

In Ref. [20], the relevant signals expected at the LHC for a left sneutrino as the LSP were studied. The sneutrinos are pair produced via a virtual W, Z or γ in the s channel. From the prompt decay of a pair of left sneutrinos LSP of any family, a significant diphoton signal plus MET from neutrinos can be present in the mass range $118-132$ GeV, with 13 TeV center-of-mass energy and integrated luminosity of 100 fb^{-1}. In addition, in the case of a pair of tau left sneutrinos LSPs, given the large value of the tau Yukawa coupling diphoton plus leptons and/or multileptons can appear. It was found that, the number of expected events for the multilepton signal, together with properly adopted search strategies, is sufficient to give a significant evidence for a sneutrino of mass in the range 130 - 310 GeV, even with the integrated luminosity of 20 fb^{-1}. In the case of the signal producing diphoton plus leptons, an integrated luminosity of 100 fb^{-1} is needed to give a significant evidence in the mass range 95 - 145 GeV. Moreover, in the framework of the $\mu\nu$SSM with one generation of right-handed neutrino superfields, displaced dilepton signal expected at the LHC for a tau left sneutrino as the LSP with a mass in the range 45 - 100 GeV was addressed in [21]. The predictions of this scenario were compared with

the ATLAS search [73] for long-lived particles using displaced lepton pairs at 8 TeV. The prospects for the 13 TeV LHC searches we also discussed, as well as optimizations of the trigger requirements used.

Finally, in Ref. [74] final states with multi-lepton signal plus MET expected at the LHC were studied for a bino-like neutralino as the LSP, when the left sneutrino is the next-to-LSP (NLSP) and hence a suitable source of binos. The comparison with LHC searches for electroweak superpartners through chargino-neutralino production [75, 76], allowed to exclude a small region of bino (sneutrino) masses $110 - 150$ $(110 - 160)$ GeV.

3.8 Dark matter

The evidence for non-baryonic cold DM in the Universe is confirmed by numerous observations from galactic to cosmological scales, and hence is one of the most compelling and striking evidence for physics BSM.

In RPV models, although the LSP is no longer stable, candidates for DM exist. The lightest neutralino or sneutrino have very short lifetimes and can not be accounted as DM candidates. Nevertheless, the case of gravitino LSP as DM is possible because its decay is suppressed both by the smallness of the gravitational interaction and by the RPV parameters determined by the neutrino Yukawa couplings $Y_{\nu_{ij}}$. As a consequence, its lifetime can be much longer than the age of the Universe. Indeed, due to the mixing of the photino with the left-handed neutrinos, the gravitino is able to decay into a photon and a neutrino [41] and its lifetime is given by

$$\tau_{3/2} \simeq 3.8 \times 10^{27} \text{ s } \left(\frac{|U_{\widetilde{\gamma}\nu_i}|^2}{10^{-16}}\right)^{-1} \left(\frac{m_{3/2}}{10 \text{ GeV}}\right)^{-3}. \tag{3.71}$$

where $|U_{\widetilde{\gamma}\nu_i}|^2$ is the photino content of the neutrino. Searches for gamma-ray lines, as well as smooth spectral signatures, from gravitino dark matter in the $\mu\nu$SSM using Fermi-LAT data have been carried out in Refs. [77–80].

Note that the case of gravitino LSP does not alter the collider phenomenology of the remaining sparticles. For example, the neutralino partial decay length into gravitino and photon is [59]

$$c\,\tau_{\tilde{\chi}^0}^{3/2} \sim 80 \text{ km } \left(\frac{m_{3/2}}{10 \text{ keV}}\right)^2 \left(\frac{m_{\tilde{\chi}_4^0}}{50 \text{ GeV}}\right)^{-5}. \tag{3.72}$$

where $m_{3/2}$ is the gravitino mass. It can easily be seen that, in order to have a significant decay to gravitinos, the mass of the latter must be very small, less than about 10 keV.

That is, for gravitino mass larger than 10 keV, the decay width of neutralino into gravitino and photon is much smaller than the decay widths into SM particles.

Chapter 4

Methodology for scanning the $\mu\nu$SSM

We have detailedly presented the main characteristics of the $\mu\nu$SSM in the previous chapter. We have described the parameter space that we want to thoroughly study in the light of given experimental data. Now we want to present the methodology that we will use for achieving this goal.

The objective is to use a probabilistic method to find all possible regions of the parameter space that are compatible with a given set of experimental data. Although we do not intend to make a statistical interpretation of the results, this approach is well motivated given the large amount of available experimental data.

Concerning the probabilistic methodologies, there are two main classes: the *frequentist* and the *Bayesian* approaches depending on the interpretation of the notion of probability. Let us point out that both methods can be used for the parameter estimation as well as model selection. In model selection, different models are compared and the one that describes best the data is chosen while in the parameter estimation, which is our case, a set of parameters of a given model are estimated in the light of given experimental data. Nevertheless, in the frequentist approach the probability is interpreted in terms of frequency at which an observation occurs from a repeatable experiment in the limit of an infinite or very large number of identical tests. The usual problem with this kind of approach is that infinite number or identical experiments are not possible to realize. On the contrary, in the Bayesian approach, the probability measures a degree of plausibility and is interpreted as a measure of our belief in an outcome given a prior knowledge. Thus, with the increasing amount of available experimental data, Bayesian inference methods appear very suitable

in accessing viable regions of the parameter space of a given theoretical model, and, in this thesis, this method is employed.

In this Chapter, we summarize the algorithm that we will use for sampling the $\mu\nu$SSM in our studies.

4.1 Sampling method: Multinest

The Bayesian inference provides a convenient approach to the inference of a given set of parameters $\Theta = (\Theta_i)_{i=1,\,d} \equiv (\Theta_1, \ldots, \Theta_N)$, where N is the number of parameters, in a given model and for data D. It relies on the Bayes' theorem which states that

$$p(\Theta|\mathrm{D}) = \frac{p(\mathrm{D}|\Theta) \times \pi(\Theta)}{p(\mathrm{D})}\,. \tag{4.1}$$

The quantity $p(\Theta|\mathrm{D})$ is the posterior probability density function (we will call it the posterior henceforth) of the model parameters, and it summarizes the state of knowledge on the parameters after the data has been observed. In the Bayesian approach, the N–dimensional posterior distribution describing the left hand side of Eq.(4.1) represents the Bayesian inference of the parameter values. Note that the inference about an individual parameter Θ_i is given by the marginalized posterior distribution $p(\Theta_i|\mathrm{D})$ and can be obtained by integrating $p(\Theta|\mathrm{D})$ over all other parameters Θ_j for $j \neq i$.

The quantity $p(\mathrm{D}|\Theta)$ as function of Θ for fixed D is the likelihood and will be denoted henceforth as $\mathcal{L}(\Theta)$. The likelihood provides the information encoded in the data. We will describe $\mathcal{L}(\Theta_i)$ associated to each observable in each study presented in this thesis in subsequent chapters.

The $\pi(\Theta)$ and $p(\mathrm{D})$ are respectively the prior probability density function that supplies the knowledge about the values of the parameters Θ_i before observing the data, and the evidence or model likelihood which is the factor required to normalize the posterior over the domain of model parameters. In general, the parameters Θ_i can be correlated. Nevertheless, if the model parameters under consideration are independent and uncorrelated, the prior $\pi(\Theta)$ is separable and can be written as:

$$\pi(\Theta) = \prod_{i=1}^{N} \pi(\Theta_i)\,. \tag{4.2}$$

One usual problem with Bayesian approaches is that the posterior can strongly depend on the choice of priors. See for example [81] where it was analyzed how the impact of the choice of priors may influence the statistical conclusions of the preferred values

of the parameter space of the Constrained MSSM. This happens when data set used is not constraining enough so as to remove the dependence on the type of the priors. Alternatively, it can be understood as if we have a lot of data, the likelihood from that is going to overpower any information contained in the priors. In this context we note that, on the one hand, a *log* prior gives equal weights to all decades for the parameter and thus is a scale invariant prior. At input level, a log prior means that the concerned input parameter is in log scale. On the other hand, for a *flat* prior the concerned parameter is in linear scale and thus is not scale invariant. An increase in the order of magnitude on the parameter implies an increase in the weight. Thus the choice of the type of priors is very important for an efficient Bayesian analysis.

After introducing the basic concepts of Bayesian analysis, we turn now our attention on the sampling algorithm. For instance, we will use `Multinest` for the sampling purpose. A complete and detailed description of `Multinest` can be found in Refs. [82,83], nevertheless, we are going to summarize it subsequently.

`Multinest` is a data driven algorithm that is based on the Nested Sampling (NS) [84, 85] method and it presents a number of advantages with respect to the latter because it is efficient for multi-modal posterior distributions with pronounced curving and degeneracies. The NS is a Monte Carlo method that is aimed for an efficient calculation of the Bayesian evidence but allows for an inference of posterior distribution. The main purpose of the NS is the evaluation of the evidence $\mathcal{Z}$ and as stated above, it is the quantity that normalizes the posterior distribution. It can hence be written as

$$\mathcal{Z} = \int \mathcal{L}(\Theta) \times \pi(\Theta) \mathrm{d}^N\Theta \,, \quad \mathrm{d}^N\Theta = \prod_{i=1}^{N} \mathrm{d}\Theta_i \,. \tag{4.3}$$

This is a multi-dimensional integral and its numerical implementation is a hard and tedious task, even for small dimensional parameter space. However, NS avoids this situation by finding contours of iso-likelihoods within the prior volume and transforming the $N-$dimensional problem of Eq.(4.3) into a one$-$dimensional integral. If V denotes the prior volume such that $\mathrm{d}V = \pi(\Theta)\mathrm{d}^N\Theta$ then the prior volume defined by the likelihood $\mathcal{L}(\Theta) > \alpha$ can be written as

$$V(\alpha) = \int_{\mathcal{L}(\Theta)>\alpha} \pi(\Theta)\mathrm{d}^N\Theta \,. \tag{4.4}$$

The evidence of Eq. (4.3) can be rewritten as

$$\mathcal{Z} = \int_0^1 \mathcal{L}(V)\mathrm{d}V\,, \tag{4.5}$$

where $\mathcal{L}(V)$ is given by the inverse of Eq. (4.4), *i.e.* $\mathcal{L}(V(\alpha)) \equiv \alpha$ and represents the likelihood enclosing the volume V. Thus the evidence can be approximated numerically if for a given sequence of values V_k one can calculate $\mathcal{L}(V_k)$ such that

$$\mathcal{Z} \approx \sum_k w_k \mathcal{L}(V_k)\,, \tag{4.6}$$

where, using the trapezium rule,

$$w_k = \frac{1}{2}(V_{k-1} - V_k). \tag{4.7}$$

Concerning the evaluation of Eq.(4.6), the NS algorithm progresses via iterations. From the full prior in the parameter space of the model, it constructs a set of samples from the posterior in order to estimate how compatible with data is a given region in parameter space with respect to others.

(1) As a starting point of the iterations, the counter j is set to 0 and M *live* samples (also called *active* samples) are uniformly sampled from the full prior $\pi(\Theta)$ volume such that the initial prior volume V_0 equals 1. Then, these samples are sorted in order of their likelihood and the sample with the smallest likelihood $\mathcal{L}_0$ is removed from the set of live samples and replaced by a new sample drawn from the prior but with the constraint that the new point has a likelihood $\mathcal{L} > \mathcal{L}_0$.

(2) At every subsequent j^{th} iteration, the actions performed in (1) are repeated in such a way that the lowest likelihood point $\mathcal{L}_j$ is discarded in the set of live points and replaced with a new one with $\mathcal{L} > \mathcal{L}_j$. The corresponding prior volume enclosed by the iso-likelihood contour shrinks down as $V_j = t_j V_{j-1}$ where t_j is the largest of the fractions of the volume enclosed by the likelihood of each live point and it follows $\Pr(t) = Mt^{M-1}$ distribution. Noticing that $V_j = V_0 \prod_{i=1}^{j} t_i$ (notice $V_0 = 1$) and that the mean value of $\log t_i$ is $-1/M$ and that each of them is independent, the prior volume at iteration j can be taken to $V_j = \exp(-j/M)$. Using these steps, the evidence can be calculated numerically and once this is done, the posterior importance weight is attributed to each live sample as well as all the discarded (removed) points such that

$$p_j = \frac{w_j \mathcal{L}_j}{\mathcal{Z}}\,. \tag{4.8}$$

(3) Stopping condition is satisfied once the precision on the evidence is smaller than a user-defined value $\log(\mathcal{Z}_0)$ in log-evidence scheme. At each iteration, the precision $\mathcal{Z}_j^{\rm tol}$ is determined by

$$\mathcal{Z}_j^{\rm tol} = \mathcal{L}_j^{\rm max} V_j \,. \tag{4.9}$$

where $\mathcal{L}_j^{\rm max}$ is the maximum likelihood in the set of active samples at $j^{\rm th}$ iteration. Hence at a given iteration, if $\log(\mathcal{L}_j^{\rm max}) < \log(\mathcal{Z}_0)$ then it exits and the algorithm returns to (2) with $j \to j+1$

The convenience of `Multinest` resides on how it draws the samples with likelihood $\mathcal{L} > \mathcal{L}_j$ compared with conventional NS algorithms [84]. In NS, as the prior volume shrinks down, it could become difficult to draw new points with the constraint on likelihood and as a result, the acceptance rate of the new points would become more and more small and new points are constructed within the intersection of the domain of integration and this ellipsoidal boundary. Multinest identifies all possible clusters of live points and for each cluster, the points are divided into sub-clusters. Then, ellipsoids are constructed for each sub-cluster and the new sample is drawn uniformly from the region of the intersection of these ellipsoids. In other words, at each iteration of the nested sampling process, the full set of M active points is partitioned and ellipsoidal bounds constructed allowing to automatically accommodate elongated curving degeneracies, while maintaining high efficiency.

In sum, the progress of the MultiNest algorithm is controlled by two main parameters: the number of live points M and the maximum efficiency f. The number of live points M should be large enough that, in the initial sampling from the full prior volume, there is a high probability that at least one point is in the 'basin of attraction' of each mode of the posterior. In later iterations, live points will then tend to populate these modes. M must always be larger than the dimension of the parameter space and also should be sufficiently higher so that all the regions of the parameter space are sampled adequately. The maximum efficiency f controls the sampling volume X_i at the i^{th} iteration, which is equal to the sum of the volumes of the ellipsoids enclosing the live point set, such that $X_i \geq V_i f$ where V_i is the prior volume at the i^{th} iteration of MultiNest algorithm and $X_i \geq V_i f$ in the case when at the i^{th} iteration, no set of ellipsoids enclosing the M live points can be found such that the sum of their volumes, X_i, is smaller than the prior volume, V_i. Also note that the tolerance that defines the stopping criteria is also important and has to be provided at the input. In this thesis, unless explicitly mentioned

the number of live points M is 2000 and the maximum efficiency f, is set to 1. Also, the `Multinest` terminates when $\mathcal{Z}_j^{\rm tol}$ of Eq.(4.9) is no longer changing the final evidence estimate by the user-defined value, here 0.5 in log-evidence.

4.2 Scanning the $\mu\nu$SSM

Based on Multinest described in Section 4.1, we developed a code that allows to find possible regions of the parameter space that are compatible with a given experimental data set. Concretely, the code allows to perform scans on subsets of the parameters of the model. At first, MultiNest samples the points within the prior volume by estimating the input parameters of the model for the scan. Once this step is completed, the full set of parameters of the model are then used to calculate the spectrum, and to compute the likelihood associated to each experimental data. All the likelihoods are then collected in the combined likelihood $\mathcal{L}_{\rm tot}$. The schematic description of the program we used is displayed in Fig. 4.1.

In the subsequent subsections, we discuss the computation of the spectrum as well as the likelihood functions and the observables used.

4.3 Computation of the spectrum

For the computation of the spectrum, we use SARAH [86] to generate a `SPheno` [87, 88] version for our model. SPheno stands for Supersymmetric Phenomenology and is a program that computes particles and sparticles masses and mixing, decays widths, cross sections, branching ratios and low energy observables. Then, we interface SPheno with MultiNest. Each spectrum is required to fulfill the physicality constraint that consists to check the presence of tachyonic eigenstates. The samples that fail this constraint are discarded. For the points that pass this constraint, the likelihood associated to each experimental data is computed and collected in the combined likelihood. Note that for computing the spectrum, the complete set of parameters of the model are used as input.

4.4 Computation of the likelihood

Concerning the likelihoods, we use three types of functions. The first class of function we use are related to the observables for which the data are provided as best fit or central value and uncertainties. In this case, the likelihood is a Gaussian,

$$\mathcal{L} = \exp\left[-\frac{(x-x_0)^2}{2\sigma_T^2}\right], \tag{4.10}$$

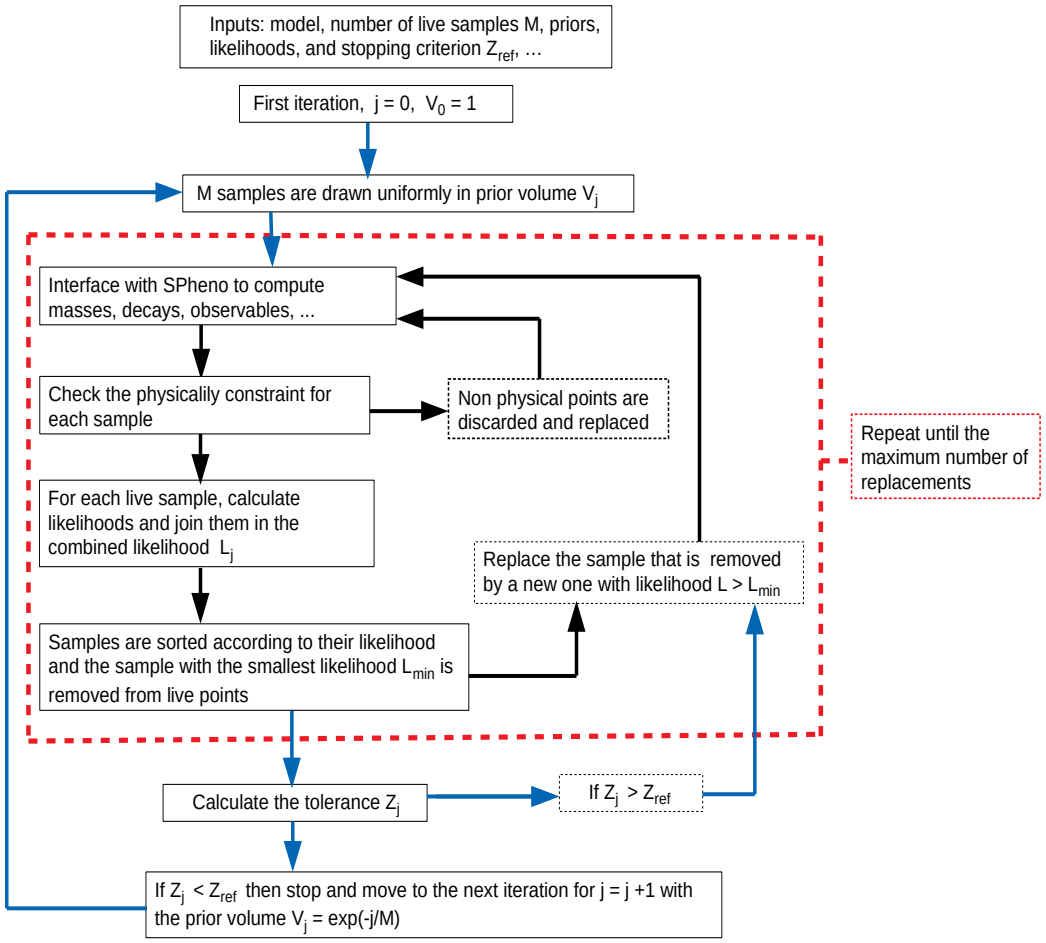

Figure 4.1: Schematic map of the algorithm.

where x_0 is the experimental central value for the observable x, $\sigma_T^2 = \sigma^2 + \tau^2$ with σ and τ being respectively the experimental and theoretical uncertainties on the observable x.

The second class of functions concerns the observable for which the constraint is set as lower or upper limit, for example the lower bound on chargino mass. The corresponding likelihood function is defined as

$$\mathcal{L}(x) = \frac{\sigma}{\sigma_T}[1 - K(D(x))] \exp\left[-\frac{(x - x_0)^2 p}{2\sigma_T^2}\right] + \frac{1}{\tau} K((x - x_0)p), \qquad (4.11)$$

Parameters	$\sin^2\theta_{12}$	$\sin^2\theta_{13}$	$\sin^2\theta_{23}$	δm^2 / 10^{-5} (eV^2)	Δm^2 / 10^{-3} (eV^2)
μ_{exp}	0.297	0.0215	0.425	7.37	2.525
σ_{exp}	0.017	0.0007	0.021	0.17	0.042

Table 4.1: Neutrino data used in the sampling of the $\mu\nu$SSM for the analysis of the $\widetilde{\nu}_\tau$ as LSP in Section 6.5.

where

$$D(x) = \frac{\sigma}{\tau}\left(\frac{(x_0 - x)p}{\sigma_T}\right), \; K(a) = \frac{1}{2}\text{erfc}\Big(\frac{a}{\sqrt{2}}\Big). \tag{4.12}$$

erfc is the complementary error function.

The last class of likelihood function we use is the step function. In this case, the likelihood is fixed on one hand for the points which satisfy the limit, and on the other for those which fail. In this case, the values of likelihoods are chosen to penalize, in the combined likelihood, the points that do not satisfy the corresponding experimental data.

Concerning the uncertainties, the experimental ones are provided with the data while the theoretical ones are unknown and therefore, unless explicitly mentioned, are taken to be zero. The observables together with the associated experimental data used are described subsequently.

4.4.1 Neutrino observables

To impose neutrino physics in sampling the $\mu\nu$SSM for the analysis of $\widetilde{\nu}_\tau$ as LSP in Section 6.5, we used the results for normal hierarchy (NO) from Ref. [10] summarized in Table 4.1, where $\delta m^2 = m_2^2 - m_1^2$ and $\Delta m^2 = m_3^2 - (m_2^2 + m_1^2)/2$. Nevertheless, while we were doing the scan, we updated neutrino observables from a new neutrino global fit analysis [13] summarized in Table 4.2, where $\Delta m_{ij}^2 = m_i^2 - m_j^2$. For the work in Section 7.3, concerning the sampling to explain the discrepancy between the SM prediction of the anomalous magnetic moment of the muon and the experimental value, we already used Ref. [13]. For each of the observables listed in the neutrino sector, the likelihood function is a Gaussian (see Eq. (4.10)) centered at the mean value μ_{exp} and with width σ_{exp}. Concerning the cosmological upper bound on the sum of the masses of the light active neutrinos given by $\sum m_{\nu_i} < 0.12$ eV [89], even though we did not include it directly in the total likelihood, we imposed it on the viable points obtained.

Parameters	$\sin^2\theta_{12}$	$\sin^2\theta_{13}$	$\sin^2\theta_{23}$	Δm^2_{21} / 10^{-5} (eV^2)	Δm^2_{31} / 10^{-3} (eV^2)
μ_{exp}	0.310	0.02241	0.580	7.39	2.525
σ_{exp}	0.012	0.00065	0.017	0.20	0.032

Table 4.2: Neutrino data used in the sampling of the $\mu\nu$SSM for the analysis of the anomalous magnetic moment of the muon in Section 7.3

4.4.2 Higgs observables

Before the discovery of the SM-like Higgs boson, the negative searches of Higgs signals at the Tevatron, LEP and LHC, were transformed into exclusion limits that must be used to constrain any model. Its discovery at the LHC added crucial constraints that must be taken into account in those exclusion limits. We have considered all these constraints in the analysis of the $\mu\nu$SSM, where the Higgs sector is extended with respect to the MSSM as discussed in Section 3.6. For constraining the predictions in that sector of the model, we interfaced `HiggsBounds` v5.3.2 [90,91] with MultiNest. First, several theoretical predictions in the Higgs sector (using a ± 3 GeV theoretical uncertainty on the SM-like Higgs boson) are provided to determine which process has the highest exclusion power, according to the list of expected limits from LEP and Tevatron. Once the process with the highest statistical sensitivity is identified, the predicted production cross section of scalars and pseudoscalars multiplied by the BRs are compared with the limits set by these experiments. Then, whether the corresponding point of the parameter under consideration is allowed or not at 95% confidence level is indicated. In constructing the likelihood from HiggsBounds constraints, the likelihood function is taken to be a step function. Namely, it is set to one for points for which Higgs physics is realized, and zero otherwise. Finally, in order to address whether a given Higgs scalar of the $\mu\nu$SSM is in agreement with the signal observed by ATLAS and CMS, we interfaced `HiggsSignals` v2.2.3 [92, 93] with MultiNest. A χ^2 measure is used to quantitatively determine the compatibility of the $\mu\nu$SSM prediction with the measured signal strength and mass. The experimental data used are those of the LHC with some complements from Tevatron. The details of the likelihood evaluation can be found in Refs. [92, 93].

4.4.3 B decays

$b \to s\gamma$ is a flavour changing neutral current (FCNC) process, and hence it is forbidden at tree level in the SM. However, its occurs at leading order through loop diagrams. Thus, the effects of new physics (in the loops) on the rate of this process can be constrained by precision measurements. In the combined likelihood, we used the average value of $(3.55 \pm 0.24) \times 10^{-4}$ provided in Ref. [94]. Notice that the likelihood function is also a Gaussian (see Eq. (4.10)). Similarly to the previous process, $B_s \to \mu^+\mu^-$ and $B_d \to \mu^+\mu^-$ are also forbidden at tree level in the SM but occur radiatively. In the likelihood for these observables (4.10), we used the combined results of LHCb and CMS [95], $\mathrm{BR}(B_s \to \mu^+\mu^-) = (2.9 \pm 0.7) \times 10^{-9}$ and $\mathrm{BR}(B_d \to \mu^+\mu^-) = (3.6 \pm 1.6) \times 10^{-10}$. Concerning the theoretical uncertainties for each of these observables we take $\tau = 10\%$ of the corresponding best fit value. We denote by $\mathcal{L}_{\text{B physics}}$ the likelihood from $b \to s\gamma$, $B_s \to \mu^+\mu^-$ and $B_d \to \mu^+\mu^-$.

4.4.4 μ decays

We also included in the joint likelihood the constraint from $\mathrm{BR}(\mu \to e\gamma) < 5.7 \times 10^{-13}$ and $\mathrm{BR}(\mu \to eee) < 1.0 \times 10^{-12}$. For each of these observables we defined the likelihood as a step function. As explained before, if a point is in agreement with the data, the likelihood $\mathcal{L}_{\mu\text{ decay}}$ is set to 1 otherwise to 0.

4.4.5 Anomalous magnetic moment of the muon

In the studies conducted in Chapters 5 and 6, we did not try to explain the interesting but not conclusive 3.5σ discrepancy between the measurement and the SM prediction of the anomalous magnetic moment of the muon, $\Delta a_\mu = a_\mu^{\text{exp}} - a_\mu^{\text{SM}} = (26.8 \pm 6.3 \pm 4.3) \times 10^{-10}$ [96]. The reason is that we decouple the rest of the SUSY spectrum with respect to the tau left sneutrino mass, and hence we do not expect a large SUSY contribution over the SM value. Nevertheless, we check for the points fulfilling all constraints discussed in Sections 5.4 and 6.7, whether the extra contribution a_μ^{SUSY} is within the SM uncertainty. On the other hand, the main goal of the analysis of Chapter 7 is to explain this discrepancy, and therefore, we included in the joint likelihood the constraint from Δa_μ. We denote by $\mathcal{L}_{a_\mu}$ the likelihood for this observable.

4.4.6 Chargino mass bound

In RPC SUSY, the lower bound on the lightest chargino mass depends on the spectrum of the model [96, 97]. Although in the $\mu\nu$SSM there is RPV and therefore this constraint does not apply automatically, to compute $\mathcal{L}_{m_{\widetilde{\chi}^{\pm}}}$, we have chosen a conservative limit of $m_{\widetilde{\chi}_1^{\pm}} > 92$ GeV with the theoretical uncertainty $\tau = 5\%$ of the chargino mass.

Chapter 5

Impact of Higgs physics on the parameter space of the $\mu\nu$SSM

In Section 3.6 of Chapter 3, we extensively described the Higgs sector of the $\mu\nu$SSM. We showed that the SM-like Higgs is mainly mixed with the three right sneutrinos, giving rise to an interesting phenomenology. Then, in Chapter 4 we presented a powerful approach that allows to scan given subsets of the parameter space of a given model. In this chapter, which is based on our work of Ref. [98], we will apply this approach to find the viable regions of the parameter space of the Higgs sector of the $\mu\nu$SSM, in the light of the existing Higgs data.

5.1 Introduction

The measurements of the properties and signal rates of the discovered scalar boson at the LHC [1,2], indicate that it is compatible with the expectations of the SM. Besides, no hints for new physics have been detected yet despite of numerous searches and tremendous efforts of the experimental collaborations. As a consequence, extensions of the SM such as low-energy SUSY are being severely constrained, namely the parameter space of SUSY models is shrinking considerably. This renders the detailed analyses of Higgs properties, signal rates and couplings to SM particles very important, as well as the search for new particles.

Concerning Higgs physics, various works, using different methods, have been dedicated to the study of the parameter space of SUSY models in the light of a given set experimental data, and vast regions have been explored such as for example in the NMSSM [72,99–103]. In this work, we use the powerful likelihood data-driven method described in Chapter 4

for sampling the Higgs sector of the $\mu\nu$SSM. Since three families of right-handed neutrino superfields are present in the model in order to solve the μ problem and simultaneously reproduce neutrino physics, the new couplings and sneutrino VEVs produce a substantial mixing among the three right sneutrinos and the SM-like Higgs. Although an analysis of this sector was performed in Ref. [50], finding viable regions that avoid false minima and tachyons, as well as fulfill the Landau pole constraint, it was carried out prior the discovery of the SM-like Higgs boson, and therefore the issue of reproducing Higgs data was still missing. In Ref. [62], this issue was taking into account to perform an analytical estimate of all the new two-body decays for the SM-like Higgs in the presence of light scalars, pseudoscalars and neutralinos. More recently, in Refs. [63, 64], in addition to perform the complete one-loop renormalization of the neutral scalar sector of the $\mu\nu$SSM, interesting benchmark points (BPs) with right sneutrinos lighter than the standard model-like Higgs boson were studied.

Given the increasing data including the properties of the SM-like Higgs and the exclusion lines provided by the combined 7-, 8- and 13-TeV searches at the LHC, and also by other results such as flavor observables, it appears relevant to re-investigate the $\mu\nu$SSM parameter space to simultaneously accommodate this new scalar and its properties, the exclusion limits and to explore the phenomenological consequences respecting various experimental results. To carry this out, the likelihood data-driven method used in our analysis presents advantages over traditional ones such as those based on random grid scans or chi-square methods, since it is much more efficient in the computational effort required to explore a parameter space. Also, since it uses a Bayesian approach, it allows to take easily into account all relevant sources of uncertainties in the likelihood. In addition, given the accumulation of data from various experimental collaborations, this method provides a convenient approach to qualitatively explore beyond standard models compared to simplified methods.

The chapter is organized as follows. The Higgs sector was studied in detail in Sec. 3.6 of Chapter 3, where the mixing among neutral Higgs doublets and right and left sneutrinos was explained, paying special attention to accommodate the correct mass of the SM-like Higgs, depending on the values of the couplings λ among right sneutrinos and Higgses, and the masses of the right sneutrinos. Subsequently, in Chapter 4 we discussed the strategy to employ in order to perform scans searching for points of the parameter space of our scenario compatible with current experimental data on Higgs physics, as well as flavor observables. We will use this strategy in the next Section 5.2, where the methodology that

we will employ to search for viable points of the parameter space is described. The input parameters used and the results of the scans will be presented in Sections 5.3 and 5.4, respectively, and applied to show that there are large viable regions of the parameter space of the $\mu\nu$SSM. Our conclusions are left for Section 5.5. Finally, figures and BPs are given in the Appendices. In Appendix C, results from the $\lambda - \kappa$ plane are shown for different values of the other parameters, using several figures for each scan performed. In Appendix D, several BPs showing interesting characteristics of the model are given.

5.2 Sampling the $\mu\nu$SSM for Higgs physics

In this section we will describe the methodology that we will employ to search for points of our parameter space that are compatible with the latest experimental data of Higgs physics In addition, we will demand the compatibility with some flavor observables. To this end, we will perform scans on the parameter space of the model, with the input parameters optimally chosen. For the sampling of the $\mu\nu$SSM we will employ the method described in Chapter 4. The goal is to find regions of the parameter space of the model that are compatible with a given experimental data. For it we have constructed the joint likelihood function:

$$\mathcal{L}_{\rm tot}^{\rm Higgs} = \mathcal{L}_{\rm Higgs} \times \mathcal{L}_{\rm B\ physics} \times \mathcal{L}_{\mu\ \rm decay} \times \mathcal{L}_{m_{\widetilde{\chi}^{\pm}}}, \tag{5.1}$$

where $\mathcal{L}_{\rm Higgs}$, $\mathcal{L}_{\rm B\ physics}$, $\mathcal{L}_{\mu\ \rm decay}$, and $\mathcal{L}_{m_{\widetilde{\chi}^{\pm}}}$ are defined in Section 4.4. We recall that we condition that each point is required not to have tachyonic eigenstates. For the points that pass this constraint, we compute the likelihood associated to each experimental data set and for each sample all the likelihoods are collected in the joint likelihood $\mathcal{L}_{\rm tot}^{\rm Higgs}$.

5.3 Input parameters

In order to efficiently scan for Higgs physics in the $\mu\nu$SSM, it is important to identify first the parameters to be used, and optimize their number and their ranges of values. In Sect. 3.6, we found that the relevant parameters are those in Eq. (3.43). However, to perform scans over 19 parameters we would have to run `Multinest` a extremely long time making the task very computer resources demanding. The analysis can be nevertheless much simplified assuming universality of the parameters as we did in the discussion below Eq. (3.51), without significantly modifying the conclusions. In addition, we will also assume in the scans for the sake of simplicity $m_{\tilde{Q}_{3L}} = m_{\tilde{u}_{3R}}$. Thus, we will perform scans

over the 8 parameters

$$\lambda,\ \kappa,\ \tan\beta,\ v_R,\ T_\kappa,\ T_\lambda,\ T_{u_3},\ m_{\tilde{Q}_{3L}} = m_{\tilde{u}_3}, \tag{5.2}$$

as shown in Table 5.1. We will use log priors (in logarithmic scale) for all of the parameters, except for $\tan\beta$ which is taken to be a flat prior (in linear scale). Let us point out, nevertheless, that we do not assume exact universality of κ_i, to avoid an artificial degeneracy in the masses of the two scalars/pseudoscalars (and two neutralinos) which appear in the spectrum without doublet contamination (see the discussion in Subsection 3.6.2). Thus we take

$$\kappa_3 = 1.04\kappa_1,\ \kappa_2 = 1.02\kappa_1,\ \kappa_1 = \kappa, \tag{5.3}$$

and scan over κ.

For the choice of the scans, we will choose the ranges of $\boldsymbol{\lambda}$ ($\equiv \sqrt{3}\lambda$) discussed in Section 3.6 for convenience of the discussion. In particular, S_1 corresponds to small/moderate values with $0.01 \leq \lambda < 0.2$, S_2 to moderate/large values with $0.2 \leq \lambda < 0.5$, and finally S_3 to large values $0.5 \leq \lambda < 1.2$. For each scan, the same ranges for the other parameters are considered. In particular, the upper bound of κ has been motivated in the discussion of Subsection 3.6.1 by relaxing the idea of perturbativity up to the GUT scale, pushing the scale of new physics further below to 10 TeV (see Eq. (3.42)). Concerning the range of v_R, the lower and upper bounds allow to have reasonable Majorana masses for right-handed neutrinos, $\mathcal{M}_i = 2k_i v_R/\sqrt{2}$ (see Eq. (3.26)), even when κ_i are very large or very small, respectively. The ranges of T_λ and T_κ are also natural following the supergravity framework of Eq. (3.4). The lower bound on $m_{\widetilde{Q}_{3L}}$ of 200 GeV is chosen to avoid too light stops/sbottoms, and the upper bound of 2 TeV is enough not to introduce too large soft masses and therefore too heavy squarks. With this range of $m_{\widetilde{Q}_{3L}}$, we take the upper bound of $-T_{u_3}$ at 5 TeV to be able to reproduce in the small λ limit the usual maximal mixing scenario when $m_{\widetilde{Q}_{3L}} \sim 2$ TeV.

The rest of the parameters of the model, which are less relevant for the analysis, are fixed as shown in Table 5.2. For squarks, and right sleptons we choose a typical value of 1000 GeV. Note that the rest of soft masses for Higgses, right sneutrinos and left sleptons, are fixed by the minimization conditions, as discussed in Section 3.2. The relations among gaugino masses $M_{1,2,3}$ are inspired by GUTs. As for the other trilinear parameters, the values of T_{d_3} and T_{e_3} have been chosen taking into account the supergravity relations and the corresponding Yukawa couplings. Finally, the parameters Y_{ν_i}, v_{iL}, and T_{ν_i} are mainly

Scan 1 (S_1)	**Scan 2** (S_2)	**Scan 3** (S_3)
$0.01 \leq \lambda < 0.2$	$0.2 \leq \lambda < 0.5$	$0.5 \leq \lambda < 1.2$
$0.01 \leq \kappa \leq 2$		
$1 \leq \tan\beta \leq 40$		
$100 \leq v_R/\sqrt{2} \leq 7000$		
$0 < T_\lambda \leq 500$		
$0 < -T_\kappa \leq 500$		
$0 < -T_{u_3} \leq 5000$		
$200 \leq m_{\widetilde{Q}_{3L}} = m_{\widetilde{u}_{3R}} \leq 2000$		

Table 5.1: Range of low-energy values of the input parameters in Eq. (5.2) that are varied in the three scans, where $\tan\beta$ is a flat prior whereas the others are log priors. The VEVs v_R, and the soft parameters T_λ, T_κ, T_{u_3}, $m_{\tilde{Q}_{3L}} = m_{\tilde{u}_{3R}}$ are given in GeV.

Scan 1 (S_1)	**Scan 2** (S_2)	**Scan 3** (S_3)
$m_{\widetilde{Q}_{1,2L}} = m_{\widetilde{u}_{1.2R}} = m_{\widetilde{d}_{1.2,3R}} = m_{\widetilde{e}_{1,2,3R}} = 1000$		
$T_{u_{1,2}} = T_{d_{1,2}} = T_{e_{1,2}} = 0,\ T_{e_3} = 40,\ T_{d_3} = 100$		
$-T_{\nu_{1,2}} = 10^{-3},\ -T_{\nu_3} = 3 \times 10^{-4}$		
$M_1 = \frac{M_2}{2} = \frac{M_3}{3} = 900$		
$Y_{\nu_1} = 2 \times 10^{-7},\ Y_{\nu_2} = 4 \times 10^{-7},\ Y_{\nu_3} = 0.5 \times 10^{-7}$		
$v_{1L} = 1.5 \times 10^{-4},\ v_{2L} = 4 \times 10^{-4},\ v_{3L} = 5.5 \times 10^{-4}$		

Table 5.2: Low-energy values of the input parameters that are fixed in the three scans. The VEVs v_{iL} and the soft parameters $T_{u,d,e}$, $m_{\widetilde{Q},\widetilde{u},\widetilde{d},\widetilde{e}}$, $M_{1,2,3}$ are given in GeV.

determined by neutrino and sneutrino physics (see Eqs. (3.32) and (3.67)).

Since reproducing neutrino data is an important asset of the $\mu\nu$SSM, a few words on the subject are worth it. As explained in Chapter 3, how the model reproduces the correct neutrino masses and mixing angles has been intensively addressed in the literature [52,54,55,57,80]. Although the parameters in Eq. (3.35), λ_i, κ_i, v_{iR}, $\tan\beta$, Y_{ν_i}, v_{iL} and M, are important for neutrino physics, the most crucial of them are Y_{ν_i}, v_{iL} and M, and they are essentially decoupled from the parameters in Eq. (3.43) controlling Higgs physics. Thus, for a suitable choice of λ_i, κ_i, v_{iR} and $\tan\beta$ reproducing Higgs physics,

there is still enough freedom to reproduce in addition neutrino data by playing with Y_{ν_i}, v_{iL} and M, as shown in Ref. [57] and we will discuss in Chapter 6. As a consequence, we will not scan over the parameters Y_{ν_i}, v_{iL}, M_1, M_2 in order to relax our already demanding computing task, and since it is not going to affect our results. For our purposes, it will be sufficient to choose these parameters mimicking the type of solutions of neutrino physics with normal ordering found in Ref. [57], imposing only the cosmological upper bound on the sum of the masses of the light active neutrinos given by $\sum m_{\nu_i} < 0.12$ [89].

The same comment applies to the parameters T_{ν_i} in Eq. (3.68), which are only relevant to determine the left sneutrino masses, and therefore we fix them to mimic also the left sneutrino physics of Ref. [57]. In that work, it was easy for $M > 0$ to find solutions with the gaugino seesaw as the dominant one for the third family. In this case, v_{3L} determines the corresponding neutrino mass and Y_{ν_3} can be small. On the other hand, the normal ordering for neutrinos determines that the first family dominates the lightest mass eigenstate implying that $Y_{\nu_1} < Y_{\nu_2}$ and $v_1 < v_2, v_3$, with both ν_R-Higgsino and gaugino seesaws contributing significantly to the masses of the first and second family. Taking also into account that the composition of these two families in the second mass eigenstate is similar, we expect $v_2 \sim v_3$. Concerning left sneutrino physics, a light tau left sneutrino was required in Ref. [57] implying $-T_{\nu_3} < -T_{\nu_2} = -T_{\nu_1}$. This pattern of hierarchies for Y_{ν_i}, v_{iL}, and T_{ν_i} are used in Table 5.2.

5.4 Results

By using the methods described in the previous section, we evaluate now the constraints on the parameter space of the $\mu\nu$SSM using the 7-, 8- and 13-TeV LHC data.

To find regions consistent with experimental observations we have performed about 160 million of spectrum evaluations in total and the total amount of computer required for this was approximately 1110 CPU years.

To carry this analysis out, we first demand Higgs physics to be fulfilled. As already mentioned in Section 4.4, we use `HiggsBounds` and `HiggsSignals` to take into account the constraints from the LHC data, as well as those from LEP and Tevatron. In particular, we require that the p-value derived by `HiggsSignals` be larger than 5%. It is worth noticing here that, with the help of Vevacious [104], we have also checked that the EWSB vacua corresponding to the previous allowed points are viable. Then, we select points that lie within $\pm 3\sigma$ from $b \to s\gamma$, $B_s \to \mu^+\mu^-$, and $B_d \to \mu^+\mu^-$. In the third step, the points that pass these cuts are required to also satisfy the upper limits of $\mu \to e\gamma$ and $\mu \to eee$,

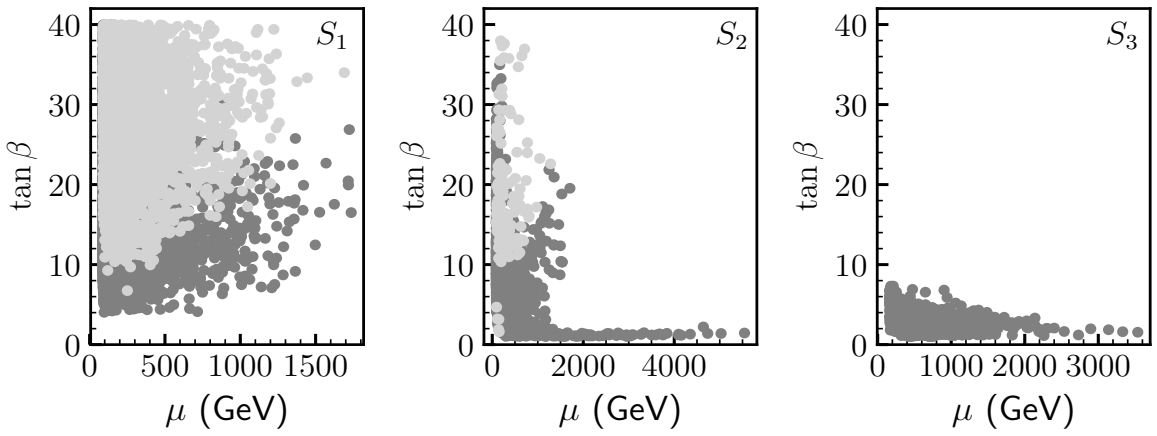

Figure 5.1: Constraints from $b \to s\gamma$ in the $\tan\beta - \mu$ plane, for scans $S_{1,2,3}$. The grey (light-grey) color corresponds to points of the parameter space that are (are not) compatible with the BR($b \to s\gamma$).

and the lower bound on the chargino mass inspired in RPC SUSY. At last we require all the points that passed the above set of cuts to satisfy the cosmological upper bound on the sum of the masses of the light active neutrinos.

As we will explain below, after imposing the relevant constraints from Higgs physics, only $b \to s\gamma$ and (less importantly) the bound on neutrino masses put further constraints on the parameter space of the $\mu\nu$SSM. For completeness, although we have not tried to explain the discrepancy between the measurement of the muon anomalous magnetic moment and the SM prediction, we will also comment on the corners of the parameter space with SUSY contributions larger than the SM uncertainty, and possible improvements in this direction.

b$\to$ sγ

The BR($b \to s\gamma$) puts some constraints on the parameters space of the $\mu\nu$SSM, as shown in Fig. 5.1. There we show the constraints from $b \to s\gamma$ for all points of the parameter space fulfilling Higgs physics. For instance, in our setup this BR can be too small in certain regions of the parameter space. Note nevertheless that there are light-grey points (forbidden) on top of grey points (allowed), thus due to the several free parameters of the model we cannot say that concrete values of $\tan\beta$ and μ are always forbidden. We must check this constraint point by point. Forbidden points occur for small to moderate values of λ, such as in S_1 and S_2, when $\tan\beta$ can be large while $M_{\widetilde{Q}_{3L}}$ can be small. As is well known, the most important contributions to the BR($b \to s\gamma$) come from chargino

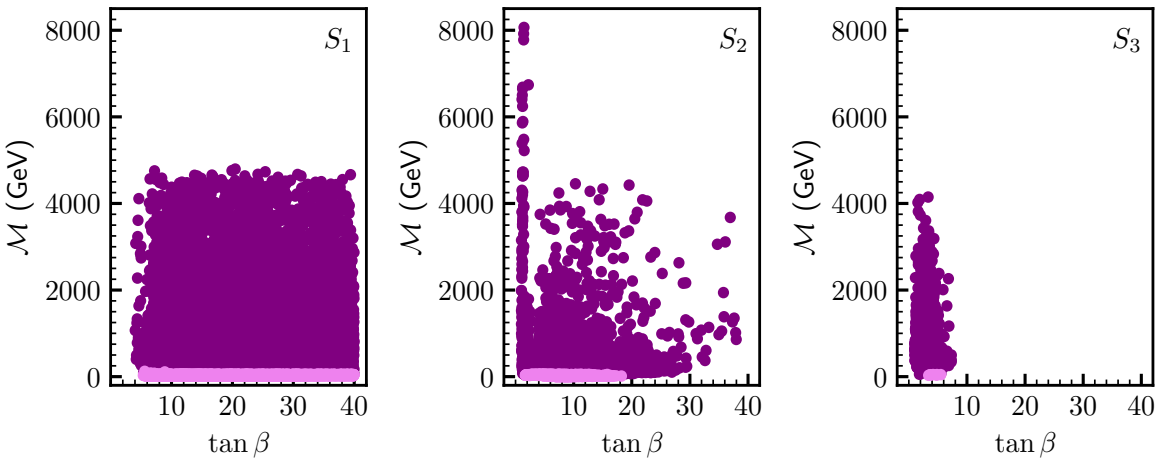

Figure 5.2: Constraints from $\sum m_{\nu_i} < 0.12$ eV in the $\mathcal{M} - \tan\beta$ plane, for scans $S_{1,2,3}$. The purple (light-purple) color corresponds to points of the parameter space that are (are not) compatible with the cosmological upper bound on the sum of the masses of the light active neutrinos.

and charged Higgs mediated processes. On the one hand, the charged Higgs contribution always tends to increase the SM value while that of the charginos depends on the sign of M_2, T_{u_3} and μ, where in our case $\mu = 3\lambda v_R/\sqrt{2}$. Since we are working with $M_2, \mu > 0$ and $T_{u_3} < 0$, the contribution from charginos in the loops acts destructively. Also for light sparticles (here charginos, charged Higgs and stops) and/or large $\tan\beta$ the effects can be large. This is actually what happens in our cases. For small/moderate λ, large $\tan\beta$ favors increasing this effect. In the regime of destructive contribution involving light stops (when $M_{\widetilde{Q}_{3L}}$ becomes small) and light Higgsinos (winos are moderately heavy since we fix M_2 to 1800 GeV), this effect is large and suppresses the BR($b \to s\gamma$). Note that for S_3 this does not occur. The reason is that large values of $\tan\beta$ are not needed, as we will see in detail in the next subsection, and in addition moderate values come together with relatively large values of $M_{\widetilde{Q}_{3L}}$.

Sum of neutrino masses

In Fig. 5.2, we show the constraints on the parameter space fulfilling Higgs physics imposed by the requirement $\sum m_{\nu_i} < 0.12$ eV in the $\mathcal{M}-\tan\beta$ plane, with $\mathcal{M} = 2\kappa\, v_R/\sqrt{2}$. We find that the sum of the masses of the three light neutrinos can exceed this upper bound when the Majoranna masses are small. This can be qualitatively explained using Eq. (3.32) with the approximations discussed below Eq. (3.35). Then, the gaugino seesaw contributions to neutrino masses given by the second term in Eq.(3.32), with $M^{\text{eff}} = M$, is fixed in our

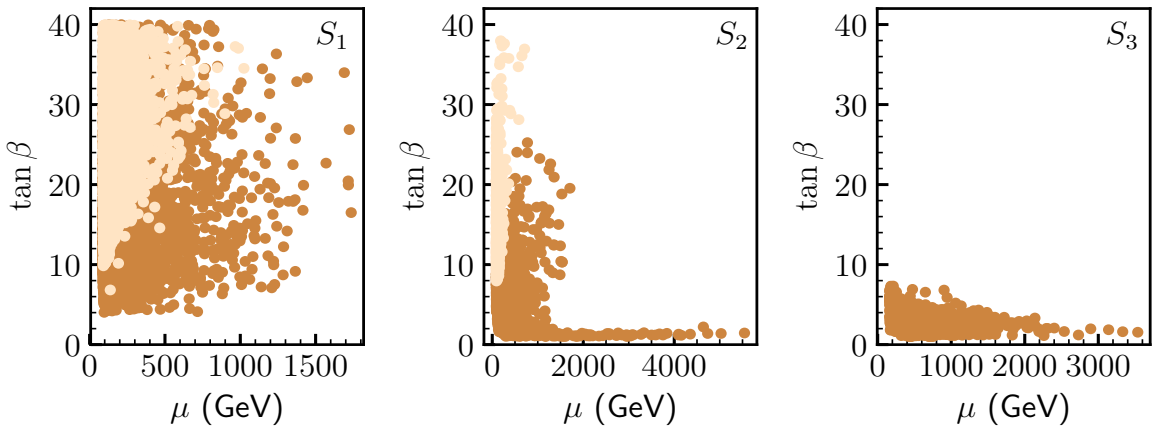

Figure 5.3: Points of the parameter space in the $\tan\beta - \mu$ plane for scans $S_{1,2,3}$ with brown (light-brown) color have (have not) $a_\mu^{\rm SUSY}$ within $\pm 1\,\sigma$ of SM $a_\mu^{\rm SM}$ uncertainty,

scans. Using the values of Table 5.2 for v_{iL} and obtaining $M = 2640.45$ GeV from the values of $M_{1,2}$, we can compute these contributions to the diagonal entries of the mass matrix $(m_\nu)_{ii}$, which turn out to be in absolute value 0.002, 0.015, and 0.0286 eV for $i = 1, 2, 3$, respectively. This indicates that for sizable ν_R-Higgsino seesaw, i.e. the first term in Eq. (3.32), the mass of the heaviest neutrino can easily be made too large. This occurs when $\mathcal{M}$ is small. For example, for $\tan\beta = 10$ and $\mathcal{M} = 30$ GeV the ν_R-Higgsino seesaw contribution to the diagonal entries is in absolute value around 0.027, 0.108, and 0.0017 eV, respectively, and added to the gaugino seesaw at least one neutrino mass would be larger than 0.12 eV. Actually, in our scenarios the effect of $\tan\beta$ is not very relevant, and the size of $\mathcal{M}$ is the most important one. In particular, as shown in Fig. 5.2, in scans S_1, S_2, and S_3, for $\mathcal{M}$ below 123, 52, and 51 GeV, respectively, we find points excluded by the cosmological upper bound on neutrino masses.

Muon anomalous magnetic moment

SUSY contributions to the anomalous moment of muon, $a_\mu^{\rm SUSY}$, can be large in the presence of light muon sneutrino and charginos or light neutralino and smuons. We found in our scans S_1, S_2 and S_3 that $a_\mu^{\rm SUSY}$ is smaller than 16.96×10^{-10}, 16.83×10^{-10}, and 3.7×10^{-10}, respectively. Thus, although none of the points of the parameter space is compatible at $\pm1\sigma$ with $\Delta a_\mu = a_\mu^{\rm exp} - a_\mu^{\rm SM} = (26.8\pm6.3\pm4.3)\times10^{-10}$, in some regions $a_\mu^{\rm SUSY}$ is larger than the uncertainty of the SM value. In Fig. 5.3, we show in brown (light-brown) color the points of the parameter space fulfilling Higgs physics where $a_\mu^{\rm SUSY}$ is (is not) within $\pm1\,\sigma$ of the quadrature sum of the uncertainties of $a_\mu^{\rm SM} = (11659182.3\pm0.1\pm3.4\pm2.6)\times10^{-10}$ [96].

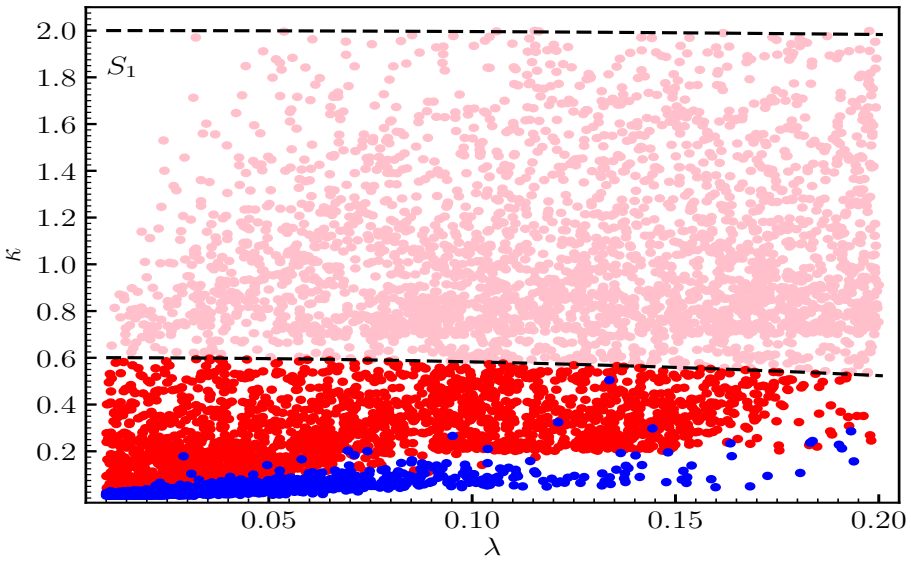

Figure 5.4: Viable points of the parameter space for S_1 in the $\kappa - \lambda$ plane. The red and light-red (blue) colours represent cases where the SM-like Higgs is (is not) the lightest scalar. All red and blue points below the lower black dashed line fulfill the perturbativity condition up to GUT scale of Eq. (3.41). Light-red points below the upper black dashed line fulfill the perturbativity condition up to 10 TeV of Eq. (3.42).

The largest contributions to $a_\mu^{\rm SUSY}$ are found for small μ and large $\tan\beta$. In our scenarios. since bino- and wino-like (neutralino or chargino) eigenstates are heavy (in our scans $M_2 = 2M_1 = 1800$ GeV) the contributions involving them are suppressed. On the other hand, although the Higgsino-like eigenstates can be light when μ is relatively small, their contributions can be diluted by the small Yukawa coupling of the muon. However, when $\tan\beta$ is very large this effect can be important. A way of explaining the discrepancy between $a_\mu^{\rm exp}$ and $a_\mu^{\rm SUSY}$ is to try to lower the muon left sneutrino mass, which in these scans is generically large given the input parameters chosen for neutrino physics. Changing the latter we could obtain smaller masses, and we leave the analysis of this possibility for Chapter 7.

5.4.1 Viable regions of the parameter space

Once $b \to s\gamma$, and mainly Higgs physics, have determined the parameter space that is viable in the $\mu\nu$SSM, we will discuss it in detail. For that, we will follow Subsection 5.3 about the choice of the three relevant scans.

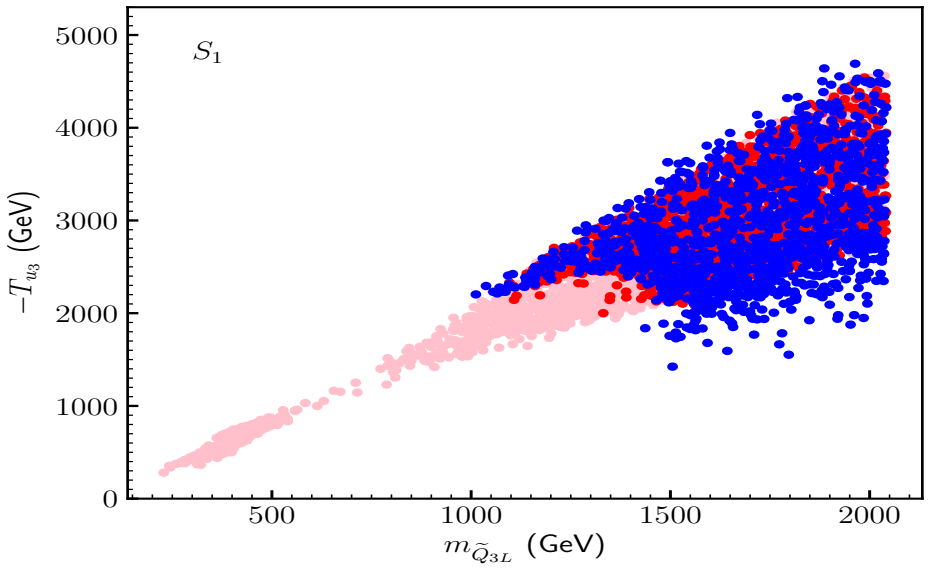

Figure 5.5: Viable points of the parameter space for S_1 in the $-T_{u_3}$ versus $m_{\widetilde{Q}_{3L}}$ plane. The color code is the same as in Fig. 5.4.

5.4.1.1 *Scan 1* $(0.01 \leq \lambda < 0.2)$

Let us concentrate first on the analysis of the results for Scan 1 (S_1). We show in Fig. 5.4 the viable points of the parameter space in the $\kappa - \lambda$ plane. The red points represent cases where the SM-like Higgs boson is the lightest scalar. All of them fulfill perturbativity up to the GUT scale, and therefore $\kappa \lesssim 0.7$. For the light-red points the SM-like Higgs boson is also the lightest scalar, but we have relaxed the perturbativity condition up to 10 TeV and therefore $0.7 \lesssim \kappa \lesssim 2$. On the contrary, the blue points represent cases where the SM-like Higgs boson is not the lightest scalar. This figure can be considered as the summary of results for this scan. Let us now discuss them in detail.

As shown in the figure, we find viable solutions in almost the entire $\kappa-\lambda$ plane analyzed in S_1. The only small (white) region that becomes forbidden corresponds to very small values of λ and very large (non-perturbative up to the GUT scale) values of κ. This can be understood taking into account that we are asking to all the points to fulfill the chargino mass lower bound of RPC SUSY, which corresponds to condition $\mu = 3\lambda v_R/\sqrt{2} \gtrsim 100$ GeV. Thus for a small λ, a large v_R is needed (see also Fig. C.1 in Appendix C). However, this gives rise to a large value of $\mathcal{M} = 2\kappa v_R/\sqrt{2}$ and, as a consequence, the condition in Eq. (3.70) to avoid tachyonic left sneutrinos cannot be fulfilled for any value of κ. In particular, combining both conditions we can write $\frac{100\ \text{GeV}}{3\lambda} \lesssim \frac{v_R}{\sqrt{2}} \lesssim \frac{-T_{\nu_i}/Y_{\nu_i}}{\kappa}$, which cannot always be fulfilled. This is the case for the muon left sneutrino whose ratio

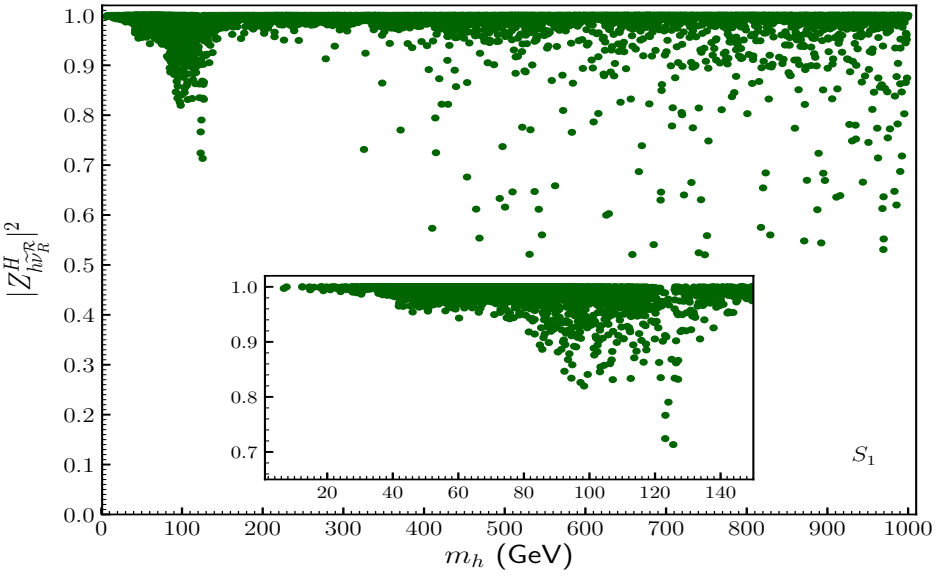

Figure 5.6: The singlet component $\sum_i |Z^H_{h\widetilde{\nu}^{\mathcal{R}}_{iR}}|^2$ of the singlet-like scalars h versus their masses, for S_1. We only show here viable points with scalar masses smaller than 1000 GeV. In the lower part we zoom in the low-mass region.

$-T_{\nu_2}/Y_{\nu_2} = 2500$ GeV is the smallest of the three families, as can be deduced from Table 5.2. For example, $\lambda = 0.01$ implies $v_R/\sqrt{2} \gtrsim 3300$ GeV, and then it is straighforward to see that $\kappa \lesssim 0.75$ to avoid tachyons. Let us point out nevertheless, that this forbidden tachyonic region in Fig. 5.4 turns out to be an artifact of our simplified assumption about the neutrino (sneutrino) pattern in order to relax the demanding computing task, as discussed in Subsection 5.3. Simply breaking the degeneracy between T_{ν_1} and T_{ν_2}, taking a larger value for T_{ν_2}, we would recover this region as viable.

Going back to the values of v_R in Fig. C.1, it is worth noticing that for large λ and/or large κ they are bounded, $v_R/\sqrt{2} \lesssim 2000$ GeV. The reason is that for those points, to increase the value of v_R would increase the mixing term $m^2_{H_u^{\mathcal{R}} H_d^{\mathcal{R}}}$ in Eq. (A.5) of Appendix B, decreasing therefore the SM-like Higgs mass, and eventually leading to the appearance of a negative eigenvalue. Note in this sense that the diagonal term $m^2_{H_u^{\mathcal{R}} H_u^{\mathcal{R}}}$ ($m^2_{H_d^{\mathcal{R}} H_d^{\mathcal{R}}}$) in Eq. (A.4) (Eq. (A.3)) is small (large) for the large values of $\tan\beta$ present in this scan, as we will discuss below (see Fig. C.2). The mixing terms with singlet-like right sneutrinos also increase with the value of v_R, as can be seen in Eqs (A.7) and (A.6), but much less than the above between Higgses, since the former go like v_R whereas the latter as v_R^2. As we can see in those equations, the value of T_λ is also important to determine the mixing among states. In Fig. C.3, we see that in most of the regions T_λ has an upper bound of

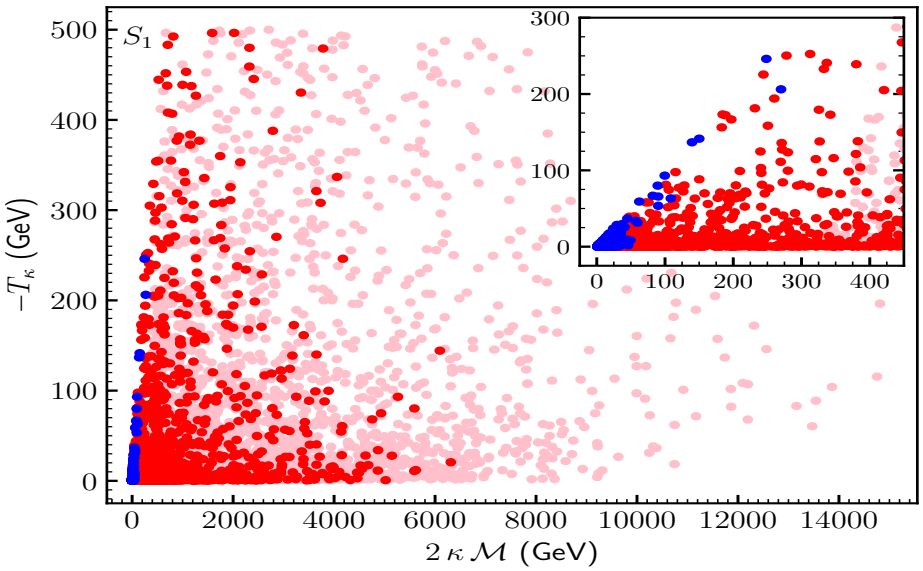

Figure 5.7: Viable points of the parameter space for S_1 in the $-T_\kappa$ versus $2\kappa\mathcal{M}$ plane. The color code is the same as in Fig. 5.4. In the upper right we zoom in the region with blue points.

around 200 GeV, and only for the lower right region with large λ, but small (perturbative up to the GUT scale) κ, it can reach up to 500 GeV. In the region to the left of the latter, although the values of κ are also small, v_R is large as discussed above, and smaller T_λ is favoured. On the other hand, assuming the supergravity relation $A_\lambda = T_\lambda/\lambda$, one can check that in most of the regions A_λ has the upper bound of around 2 TeV, as shown in Fig. C.4.

Concerning the values of $\tan\beta$, we find in S_1 that $\tan\beta > 4$. Such a lower bound is expected in order to maximize the tree-level SM-like Higgs mass for small/moderate values of λ, as discussed in Subsect. 3.6.1. We can see in Fig. C.2 that large values of $\tan\beta$ are welcome for this task, similarly to the MSSM. Given the small singlet-doublet mixing, significant loop contributions are the main source to increase the tree-level mass of the SM-like Higgs. The values of the masses of the third-generation squarks and trilinear soft term necessary to generate the large loop corrections are shown in Fig. 5.5. The white region in the upper left side is excluded by the mass of the SM-like Higgs or by the existence of tachyons when $-T_{u_3}$ is much larger than $m_{\widetilde{Q}_{3L}}$. For the allowed regions, we can see first that for κ perturbative up to 10 TeV (light-red points) the values of $-T_{u_3} \lesssim 2000$ GeV and $m_{\widetilde{Q}_{3L}} \lesssim 1000$ GeV are highly correlated. Given the large value of κ, the push-down effect in these light-red points makes necessary the maximal mixing

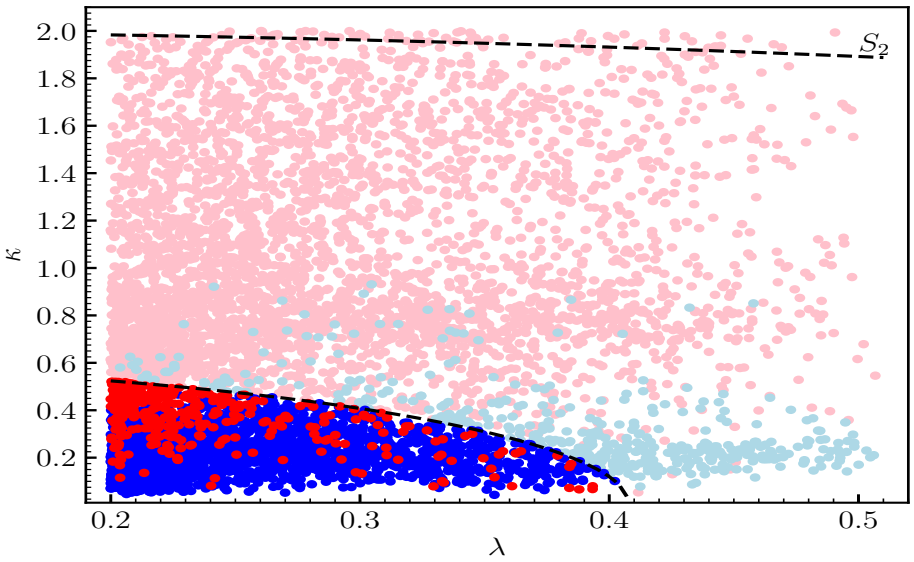

Figure 5.8: Viable points of the parameter space for S_2 in the $\kappa - \lambda$ plane. The red and light-red (blue and light-blue) colours represent cases where the SM-like Higgs is (is not) the lightest scalar. All red and blue points below the lower black dashed line fulfill the perturbativity condition up to GUT scale of Eq. (3.41). Light-red and light-blue points below the upper black dashed line fulfill the perturbativity condition up to 10 TeV of Eq. (3.42).

scenario to cancel it, bringing the mass of the SM-like Higgs to the correct value. For the red points, where κ is smaller, the push-down effect is not so large and the maximal mixing scenario can be relaxed. We can see that the lower right side of Fig. 5.5 becomes populated. The same argument applies to the blue points (note that most of them are on top of red points), but now for the push-up effect which is also small. In Figs. C.5 and C.6 of Appendix C, we show in the $\kappa - \lambda$ plane the values of $m_{\widetilde{Q}_{3L}}$ and $-T_{u_3}$, respectively. As discussed, smaller values of these parameters are needed in the perturbative region up to 10 TeV.

Let us now discuss in more detail the (narrow) region with blue points. For small values of λ, the first term of Eq. (3.53) is a good approximation for right sneutrino masses. Clearly, unless one makes a tuning between the two pieces in that term, T_κ/κ and $2\mathcal{M} = 4\kappa v_R/\sqrt{2}$, one needs these two quantities to be small in order to obtain right sneutrinos lighter than the SM-like Higgs. Now, since v_R is typically large in this scan compared to the SM-like Higgs mass, small values of κ are necessary for this task. This is what we observe in the blue region of Fig. 5.4, where $\kappa \lesssim 0.2$. There we also see that for larger values of λ, larger values of κ are allowed, because the values of v_R decrease with

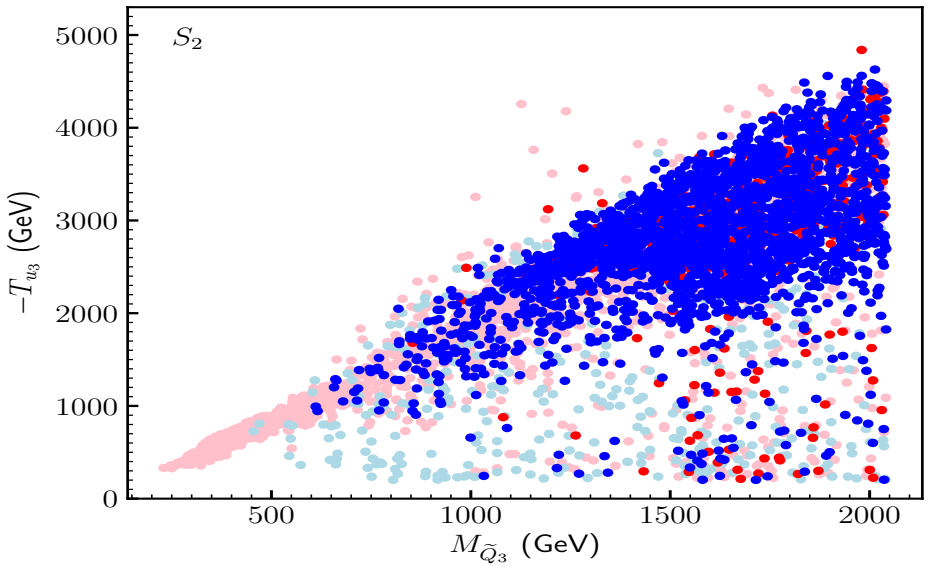

Figure 5.9: Viable points of the parameter space for S_2 in the $-T_{u_3}$ versus $m_{\widetilde{Q}_{3L}}$ plane. The color code is the same as in Fig. 5.8.

λ as shown in Fig. C.1. The correlation between the above two pieces for the blue points is also obvious from Eqs. (3.50) and (3.51). We show explicitly this effect in Fig. 5.7, where basically the line $-T_\kappa = 2\kappa\mathcal{M}$ separates the tachyonic (white) region from the non-tachyonic one with blue and red points, i.e. $-T_\kappa < 2\kappa\mathcal{M}$. Blue points have to be close to the line since they have to fulfill in addition the approximate condition (3.51). In Fig. C.7 of the Appendix, we show the different values of $-T_\kappa$ in the $\kappa - \lambda$ plane. As we can see, for the small values of κ corresponding to the blue region of Fig. 5.4, the values of $-T_\kappa$ are typically small. For larger values of κ corresponding to the regions with red and light-red points of Fig. 5.4, i.e. with right sneutrino masses larger than the SM-like Higgs mass, the tachyonic region can be avoided even with large values of $-T_\kappa$ (up to the upper bound of 500 GeV imposed in the scan), as shown in the figure. We show for completeness in Fig. C.8 the different values of the supergravity parameter $A_\kappa = T_\kappa/\kappa$ in the $\kappa - \lambda$ plane. Due to this relation, values of $-A_\kappa$ as large as around 2.9 TeV can be obtained in regions with small κ. Larger values of $-A_\kappa$ are not possible because the condition $-A_\kappa < 2\mathcal{M}$ cannot be fulfilled since v_R is bounded, and therefore tachyons would appear.

Finally, it is worth noticing that about half of the blue points correspond to cases where the singlet-like scalars have masses $\lesssim m_{\rm Higgs}/2$. As can be seen in Fig. 5.6, most of these states are almost pure singlets and therefore do not affect the Higgs decays,

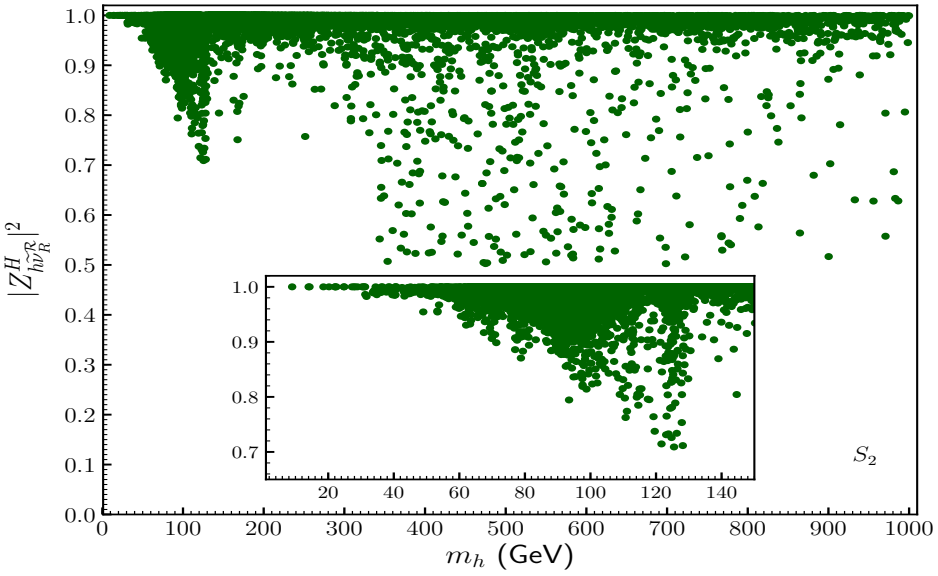

Figure 5.10: The singlet component $\sum_i |Z^H_{h\widetilde{\nu}^{\mathcal{R}}_{iR}}|^2$ of the singlet-like scalars h versus their masses, for S_2. We only show here viable points with scalar masses smaller than 1000 GeV. In the lower part we zoom in the low-mass region.

surviving as viable points.

The presence of light scalars (h_i), pseudoscalars (A_i) and neutralinos ($\widetilde{\chi}^0_i$) such that $m_{h_i} + m_{A_j} < M_Z$, $m_{\widetilde{\chi}^0_i} + m_{\widetilde{\chi}^0_j} < M_Z$ or $m_{\widetilde{\chi}^0_i} + m_{\widetilde{\chi}^\pm_j} < M_W$ (here $\widetilde{\chi}^\pm_j = e,\, \mu,\, \tau$) opens up new on-shell decay modes for the Z and W bosons. The possible signs of new physics from these new decay modes in the $\mu\nu$SSM have been studied in Ref. [61].

On the other hand, when the masses of the singlet-like states are close to 125 GeV, it is possible to find solutions with a larger doublet composition. Actually, for each point of the parameter space only one of the three states has this property, given our assumption of almost degenerate κ's implying that there is always two almost pure singlets. For these solutions, if the SM-like Higgs and the right sneutrino with significant doublet composition have masses within the mass resolution of the experiment, they will have their signal rates superimposed, and both will contribute to the resonance observed at 125 GeV [93]. In this scan, about 0.4% of the phenomenologically viable points found have singlet-like states with masses close to 125 GeV We show in Table D.1 a BP (S1-ss1) with these properties. There we see that the right sneutrino h_4 has a large composition of $H^{\mathcal{R}}_u$ (28.62%), whereas h_1 and h_2 are very pure singlets with dominant compositions $\widetilde{\nu}^{\mathcal{R}}_{eR}$ and $\widetilde{\nu}^{\mathcal{R}}_{\mu R}$, respectively, and not contributing therefore to the superposition of Higgs-like states. As expected, the right sneutrinos are very little mixed among themselves given that λ is small and therefore

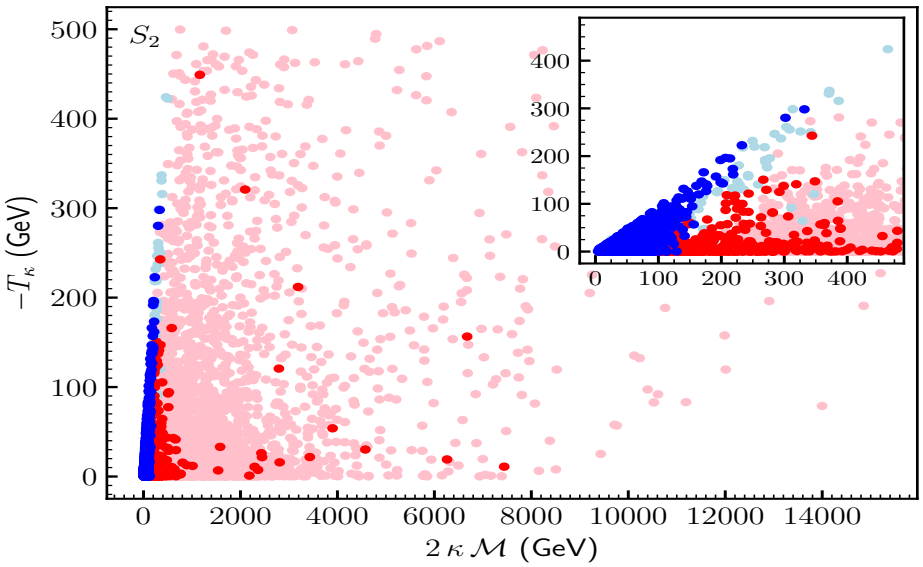

Figure 5.11: Viable points of the parameter space for S_2 in the $-T_\kappa$ versus $2\kappa\mathcal{M}$ plane. The color code is the same as in Fig. 5.8. In the upper right we zoom in the region with blue points.

the off-diagonal terms in Eq. (B.6) are negligible.

5.4.1.2 *Scan 2* ($0.2 \leq \lambda < 0.5$)

Fig. 5.8 summarizes our results for Scan 2 (S_2). In this case, we find viable solutions in the entire $\kappa - \lambda$ plane, since now $\lambda \geq 0.2$ and therefore the chargino mass lower bound can be fulfilled with low values of v_R, being safe from tachyonic left sneutrinos. In fact, we see in Fig. C.9 that in most of the regions $v_R/\sqrt{2} \lesssim 1000$ GeV. This bound, in order to avoid a too large mixing term $m^2_{H_u^{\mathcal{R}} H_d^{\mathcal{R}}}$, is smaller than for S_1 because now we are working with moderate/large values of λ. Concerning the value of T_λ, in Fig. C.11 we see that in regions with large κ this value has an upper bound of around 200 GeV, whereas for lower values of κ the mixing term is smaller and larger values of T_λ are allowed (up to the upper bound of 500 GeV imposed in the scan). Assuming the supergravity relation $A_\lambda = T_\lambda/\lambda$, we see in Fig. C.12 that given the moderate/large values of λ for this scan, the upper bound for A_λ is typically smaller than for S_1 in all regions, with a maximum value of around 2.5 TeV.

Concerning $\tan\beta$, since λ is larger than in S_1 we find that smaller values are favoured to maximize the tree-level SM-like Higgs mass, as shown in Fig. C.10 of Appendix. In addition, as a consequence of the moderate/large λ, the singlet-doublet mixing is larger

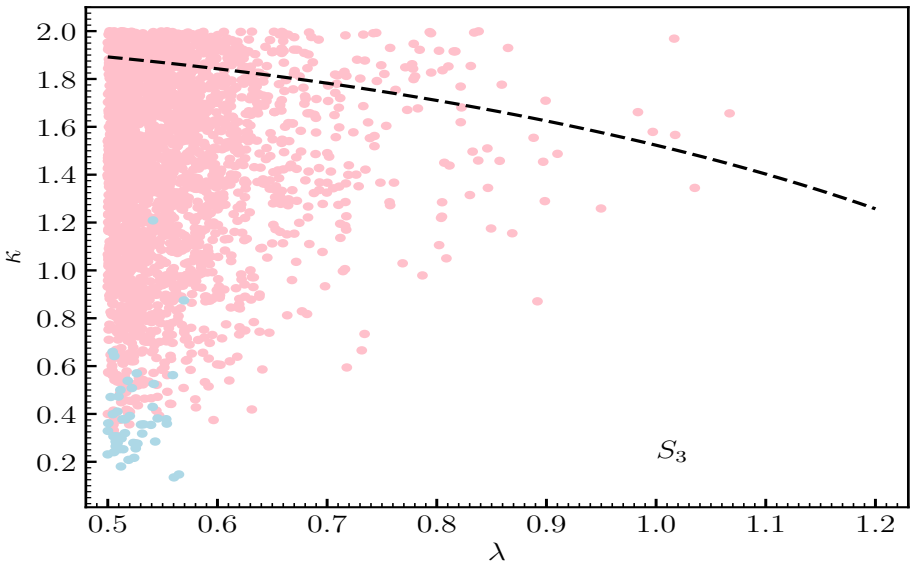

Figure 5.12: Viable points of the parameter space for S_3 in the $\kappa - \lambda$ plane. The light-red (light-blue) colour represents cases where the SM-like Higgs is (is not) the lightest scalar. All light-red and light-blue points below the black dashed line fulfill the perturbativity condition up to 10 TeV of Eq. (3.42).

and therefore the push-up effect for the blue points helps to increase the tree-level mass. All these effects together produce that the loop contributions to increase the tree-level mass of the SM-like Higgs can be relaxed. One can observed this comparing Fig. 5.9 and Figs. C.13 and C.14 with the corresponding ones of S_1.

Related to the above discussion, is the fact that in the perturbative region up to the GUT scale is more easy to find blue than red points. The push-down effect of the latter makes for them more difficult to reach the correct mass of the SM-like Higgs. Note also that blue points with all values κ are present, since v_R is now smaller than for S_1.

In Tables D.2 and D.3 of Appendix D, we show two BPs corresponding to the red region of Fig. 5.8. They have different singlet-like scalar masses, around 230 and 600 GeV respectively, mainly due to the different values of v_R. For the BP S2-R1 in Table D.2, the right sneutrinos $h_{2,3,4}$ are significantly mixed among themselves because of the moderate/large value of λ, and h_4 is the one having a significant composition of $H_u^{\mathcal{R}}$ (10.29%). The SM-like Higgs with a composition of $H_d^{\mathcal{R}}$ of 19.36% is phenomenologically viable because $\tan\beta$ is as small as 2.31. The same occurs for the BP S2-R2 in Table D.3, where now the SM-like Higgs composition of $H_d^{\mathcal{R}}$ is larger, 46.66%, but $\tan\beta$ is smaller, 1.08. For this BP the mixing among singlets is larger, but no one has a significant composition

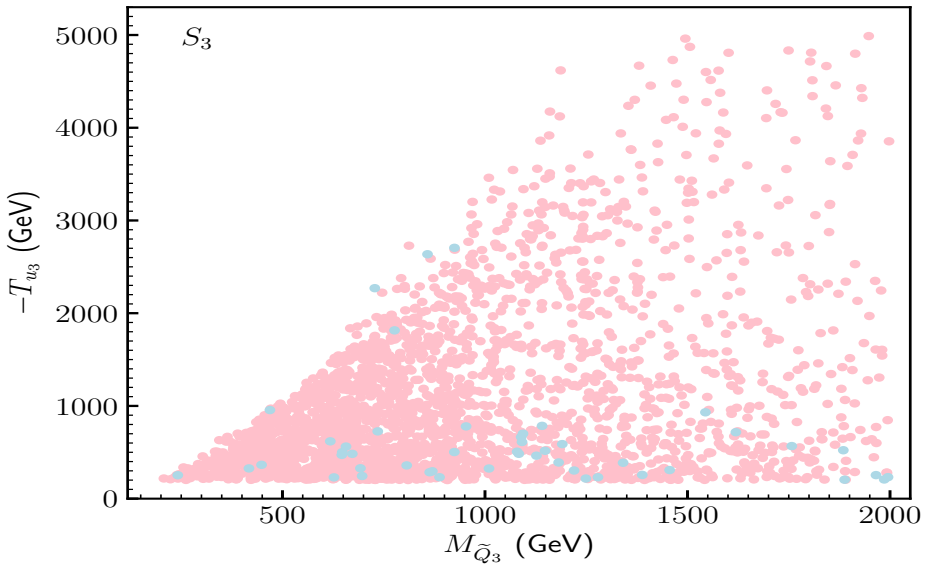

Figure 5.13: Viable points of the parameter space for S_3 in the $-T_{u_3}$ versus $m_{\widetilde{Q}_{3L}}$ plane. The color code is the same as in Fig. 5.12.

of $H_u^{\mathcal{R}}$ given their larger masses. In Fig. 5.10, we show the singlet component of the singlet-like scalars. As for S_1, we find for large masses scalars with a very large doublet composition.

The correlation discussed for S_1 in Fig. 5.7 is relaxed in this new scan, again because of the larger values of λ, as discussed below Eq. (3.55). We show this in Fig. 5.11. In Figs. C.15 and C.16 of the Appendix, we can see the different values of $-T_\kappa$ and $A_\kappa = T_\kappa/\kappa$, respectively, in the $\kappa - \lambda$ plane. In the perturbative region up to the GUT scale, except for areas with κ close to its upper bound, T_κ is typically small to avoid tachyonic right sneutrinos because v_R is small. As a consequence, in the case of supergravity A_κ is also typically small in this region. In this scan, also part of the blue points correspond to cases where the singlet-like scalars have masses $\lesssim m_{\rm Higgs}/2$.

Concerning solutions with singlet-like states with masses close to 125 GeV, about 5% of the phenomenologically viable points found in this scan are of this type. However, not all of them have a significant doublet composition as to have their signals superimposed with that of the SM-like Higgs. We show in Table D.4 the BP S2-ss1 as an example of this situation. As we can see, the right sneutrino h_4 has the largest doublet composition of $H_u^{\mathcal{R}}$ (3.77%) and $H_d^{\mathcal{R}}$ (2.65%), but insufficient as to contribute significantly to the Higgs signals. Unlike the BP S1-ss1 of S_1, now the three sneutrinos are very mixed because of the larger value of λ. It is worth noticing that for this BP the Majorana mass is small,

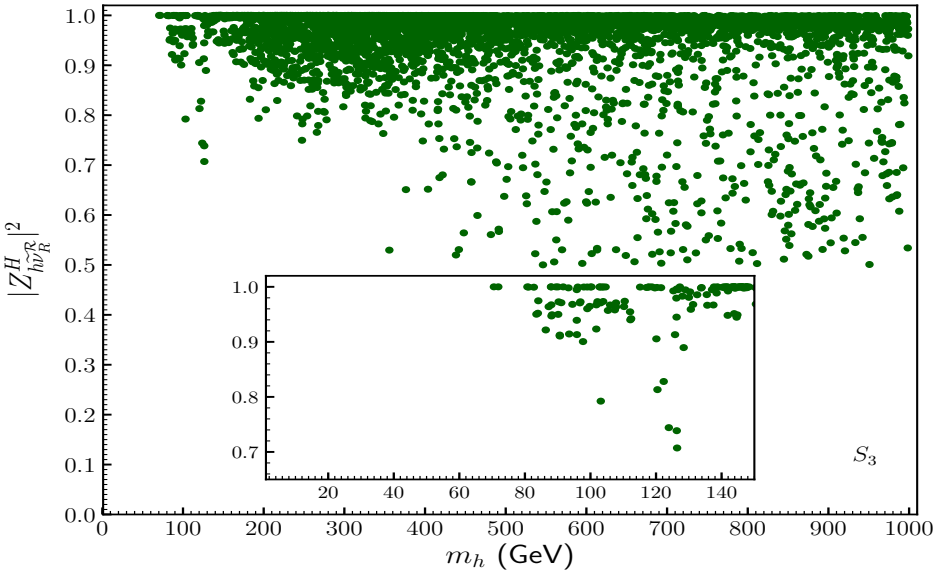

Figure 5.14: The singlet component $\sum_i |Z^H_{h\widetilde{\nu}^{\mathcal{R}}_{iR}}|^2$ of the singlet-like scalars h versus their masses, for S_3. We only show here viable points with scalar masses smaller than 1000 GeV. In the lower part we zoom in the low-mass region.

$\mathcal{M} = 55.8$ GeV, giving rise to two almost degenerate right-handed neutrinos of masses 55.9 and 57.2 GeV, and one heavier of mass 76.7 GeV. As a consequence, the decay channel right sneutrino to two neutralinos (with dominant right-handed neutrino composition) opens, giving the most important contribution to the BRs.

5.4.1.3 *Scan 3* ($0.5 \leq \lambda < 1.2$)

The results for Scan 3 (S_3) are summarized in Fig. 5.12. In this case with so large values of λ, the white region in the lower right is forbidden because of the too large mixing term $m^2_{H^{\mathcal{R}}_u H^{\mathcal{R}}_d}$ producing tachyons. To avoid that situation, in most of the allowed regions the right sneutrino VEVs take small values, $v_R/\sqrt{2} \lesssim 500$ GeV, as shown in Fig. C.17. These small values imply that $\kappa \gtrsim 0.2$ to avoid tachyonic right sneutrinos. We show in Fig. C.19 the value of the corresponding T_λ, whereas in Fig. C.20 the supergravity parameter A_λ is shown.

In Fig. C.18 we show $\tan\beta$ which, given the large value of λ, can take smaller values than in S_2. This region of the parameter space also favours light third generation squarks, as shown in Fig. 5.13 (see also Figs. C.21 and C.22).

As discussed in Section 3.6.1, the push-down effect (together with negative loop corrections) of a heavy singlet-like sector is more favourable to reproduce the SM-like Higgs

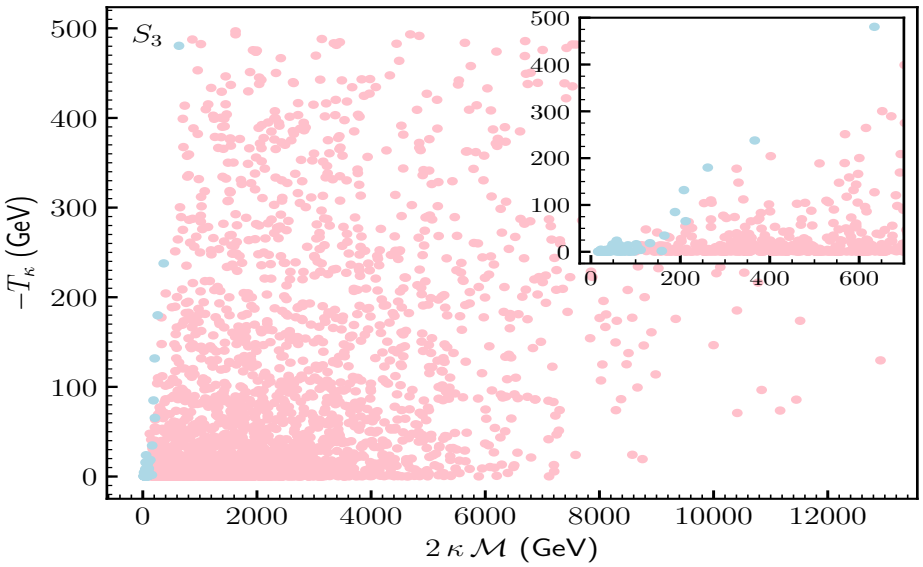

Figure 5.15: Viable points of the parameter space for S_3 in the $-T_\kappa$ versus $2\kappa\mathcal{M}$ plane. The color code is the same as in Fig. 5.12. In the upper right we zoom in the region with light-blue points.

mass. In Fig. 5.14, we show the singlet component of the singlet-like scalars. As for the other scans, scalars with large masses and with a very large doublet composition can also be present.

Although more difficult than in previous scans, we are also able to find in S_3 solutions with light singlet-like scalars (light-blue region). However, as we can see in Fig. 5.14, no solutions with masses $\lesssim m_{\rm Higgs}/2$ are present. In Fig. 5.15, we show the correlation that is necessary to find these points, and in Figs. C.23 and C.24 we show the different values of $-T_\kappa$ and $A_\kappa = T_\kappa/\kappa$, respectively, en the $\kappa - \lambda$ plane. The upper bound for A_κ is around 500 GeV in this case, but this is an artifact of our scan. If we had allowed in S_3 values of T_κ up to 1 TeV, then the upper bound for A_κ would have been around 1 TeV.

In this scan, solutions with singlet-like states with masses close to 125 GeV are more rare. Only about 0.2% of the phenomenologically viable points found are of this type. We show in Table D.5 the BP S3-ss1 as an example. As we can see, the right sneutrino h_1 has the largest doublet composition of $H_u^{\mathcal{R}}$ (1.42%) and $H_d^{\mathcal{R}}$ (4.78%), but its mass if far away from 125 GeV. For this BP also the Majorana mass is small as for S2-ss1, $\mathcal{M} = 50.3$ GeV, and there are three neutralinos dominantly right-handed neutrinos with masses of that order, 50.7, 51.8 and 64.8 GeV. As a consequence, the decay channel right sneutrino to two right-handed neutrinos opens for h_2 and h_3 (also for the SM-like Higgs h_4), but

is not possible for h_1. The latter can decay to right-handed neutrino plus light neutrino, but with a very small BR.

5.5 Conclusions

We performed a dedicated analysis of the parameter space of the $\mu\nu$SSM, in the light of the increasing data about the properties of the SM-like Higgs boson. For sampling the Higgs sector, we used a powerful likelihood data-driven method based on the algorithm `Multinest`. The states of the Higgs sector crucial for our analysis are the two Higgs doublets and the three right sneutrinos, which are mixed among themselves. After determining the relevant parameters related to this sector (see Eq. (5.2)), we performed scans to search for points compatible with the latest experimental data on Higgs physics. For constraining the predictions of our extended Higgs sector, we interfaced `HiggsBounds` with `Multinest`, and to address whether a given Higgs scalar of the $\mu\nu$SSM is in agreement with the signals observed by ATLAS and CMS we also interfaced `HiggsSignals` with `Multinest`. In addition, we demanded the compatibility with observables such as B and μ decays.

In this framework, we performed the three scans described in Table 5.1, which are determined by the range of λ couplings mixing Higgses and right sneutrinos. In particular, we considered $\lambda \in (0.01, 0.2)$, $(0.2, 0.5)$, and $(0.5, 1.2)$. Perturbativity up to the GUT scale is not imposed, and that is why we allow λ values larger than 0.4. Neither we imposed perturbativity up to the GUT scale for κ couplings among right sneutrinos, considering therefore the range $\kappa \in (0.01, 2)$. The results are summarized in Figs. 5.4, 5.8, and 5.12 for the three scans. Clearly, we find viable solutions in almost the entire $\kappa - \lambda$ plane with the exception of the scan S_3 in Fig. 5.12, which is more constrained. This is due to the large values of $\lambda \in (0.5, 1.2)$ that can give rise to tachyons originated in the mixing between the two Higgs doublets.

We have obtained therefore that the parameter space of our model contains many viable solutions, including also many different phenomenological possibilities. For example, there are solutions where the SM-like Higgs is the lightest scalar (red and light-red points in the figures), but also solutions where it is not (blue and light-blue points). In the latter case, it is even possible to have the other (singlet-like) scalars with masses $\lesssim m_{\rm Higgs}/2$. In addition, we also find solutions where several scalars are degenerated with masses close to 125 GeV, and can have their signals rates superimposed contributing to the resonance observed at 125 GeV.

Given these results, it is then important to study in detail the collider phenomenology of the solutions found. In particular, the impact of the new states, not only the right but also the left sneutrinos, and the neutralinos containing right-handed neutrinos. Novel signals associated to them might help to probe the $\mu\nu$SSM at the LHC. These analyses will be carried out in a fortcoming publication [105].

Chapter 6

Sampling the $\mu\nu$SSM for displaced tau left sneutrino LSP at the LHC

In the previous chapter we thoroughly analyzed the neutral scalar Higgs sector of the $\mu\nu$SSM in the light of the current experimental data, arguing that the parameters controlling Higgs physics can be decoupled from those of the neutrino sector. As a consequence, the relevant parameters for neutrino physics were fixed. In this chapter, which is based on our work of Ref. [57], we fix the relevant parameters that determine Higgs physics and analyse the parameter space of the neutrino sector of the model. In addition, since the left sneutrino mass and couplings are determined by neutrino physics, we analyse the phenomenology at the LHC of the displaced dilepton signal from the decay of a tau left sneutrino as the LSP with a mass in the range $45 - 100$ GeV. We compare the predictions of this scenario with the ATLAS search for long-lived particles using displaced lepton pairs in pp collisions, and investigate the regions of the parameter space of the model that can be probed at the current and future runs of the LHC.

6.1 Introduction

The search for low-energy SUSY is one of the main goals of the LHC. This search has been focused mainly on signals with MET inspired in RPC models, such as the MSSM [3, 6, 43]. There, significant bounds on sparticle masses have been obtained [96], especially for strongly interacting sparticles whose masses must be above about 1 TeV [106, 107]. Less stringent bounds of about 100 GeV have been obtained for weakly interacting sparticles, and even the bino-like neutralino is basically not constrained due to its small pair production cross section. Qualitatively similar results have also been obtained in

the analysis of simplified RPV scenarios with trilinear lepton- or baryon-number violating terms [19], assuming a single channel available for the decay of the LSP into leptons. However, this assumption is not possible in other RPV scenarios, such as the $\mu\nu$SSM, where the several decay branching ratios (BRs) of the LSP significantly decrease the signal. This implies that the extrapolation of the usual bounds on sparticle masses to the $\mu\nu$SSM is not applicable.

The most recent analyses of signals at the LHC for LSP candidates in the $\mu\nu$SSM have been dedicated to the left sneutrino [20, 21], and to the bino-like neutralino [74].[1] In the latter case, it was shown that only a small region of the parameter space of the $\mu\nu$SSM was excluded [74] when the left sneutrino is the next-to-LSP (NLSP) and hence a suitable source of binos. In particular, the region of bino (sneutrino) masses $110 - 150$ $(110 - 160)$ GeV.

Concerning the left sneutrino LSP, in Ref. [20] the prospects for detection of signals with di-photon plus leptons or MET from neutrinos, and multi-leptons, from the pair production of left sneutrinos/sleptons and their prompt decays ($c\tau \lesssim 0.1$ mm), were analyzed. A significant evidence is expected only in the mass range of about 100 to 300 GeV. The mass range of 45 to 100 GeV (with the lower limit imposed not to disturb the decay width of the Z) was covered in Ref [21] for the tau left sneutrino ($\widetilde{\nu}_\tau$) LSP. First, it was checked that no constraint on the $\widetilde{\nu}_\tau$ mass is obtained from previous searches. In particular, since the sneutrino has several relevant decay modes, the LEP lower bound on its mass mass of about 90 GeV [108–113] obtained under the assumption of BR one to leptons, via trilinear RPV couplings, is not applicable in the $\mu\nu$SSM. Similar conclusions were obtained from LEP mono-photon search (gamma+MET) [114], and LHC mono-photon and mono-jet (jet+MET) searches [115, 116]. Concerning LEP searches for staus [108–113], in the $\mu\nu$SSM the left stau does not decay directly but through an off-shell W and a $\widetilde{\nu}_\tau$, and therefore searches for its direct decay are not relevant in this model. Although the sneutrino mass can in principle be constrained using searches for final states as those of the $\mu\nu$SSM from the production of a pair of $\widetilde{\nu}_\tau$ from staus, it was also checked in Ref [21] that this is not the case. Then, the displaced-vertex decays of the $\widetilde{\nu}_\tau$ LSP producing signals with di-lepton pairs was studied. Using the present data set of the ATLAS 8-TeV dilepton search [73], the conclusion was that one can constrain the sneutrino in some regions of the parameter space of the $\mu\nu$SSM, especially when the Yukawa couplings and mass scale of neutrinos are rather small. In order to improve the

[1] The phenomenology of a neutralino LSP was analyzed in the past in Refs. [52, 53, 60, 62].

sensitivity of this search, it was proposed an optimization of the trigger requirements exploited in ATLAS based on a high level trigger that utilizes the tracker information.

The above analyses were carried out in the simplest case of the $\mu\nu$SSM with one right-handed neutrino superfield. Thus only one of the light neutrinos gets a nonvanishing tree-level contribution to its mass, whereas the other two masses rely on loop corrections. Basically, the only experimental constraint imposed in those works was that the heavier neutrino mass should be in the range $m_\nu \sim [0.05, 0.23]$ eV, i.e. below the upper bound on the sum of neutrino masses ~ 0.23 eV [117], and above the square root of the mass-squared difference $\Delta m^2_{\rm atm} \sim 2.42 \times 10^{-3}{\rm eV}^2$ [118]. Although these analyses were useful to get a first idea of the accelerator constraints on the left sneutrino LSP, the lack of experimental bounds on the masses of the superpartners in the $\mu\nu$SSM makes it peremptory a detailed study reproducing the whole neutrino physics. This is the aim of this chapter. We will reconsider the analysis of Ref. [21], but in the context of the $\mu\nu$SSM with three families of right-handed neutrino superfields where all the neutrinos get contributions to their masses at tree level. In particular, we will study the constraints on the parameter space by sampling the model to get the $\widetilde{\nu}_\tau$ LSP in the range of masses $45 - 100$ GeV, with a decay length of the order of the millimeter. We will pay special attention to reproduce the experimental neutrino masses and mixing angles [10–13]. The different values of the neutrino Yukawas will imply that certain regions of the parameter space are excluded by the LEP analysis, unlike the result of Ref [21]. In addition, we will impose on the resulting parameters to be in agreement with Higgs data and other observables.

The chapter is organized as follows. In Sections 6.2 and 6.3, we will discuss the relevant parameters of the $\mu\nu$SSM for our analysis of the neutrino/sneutrino sector, emphasizing the special role of the sneutrino in this scenario since its couplings have to be chosen so that the neutrino oscillation data are reproduced. In Section 6.4, we will introduce the phenomenology of the $\widetilde{\nu}_\tau$ LSP, studying its pair production channels at the LHC, as well as the signals. These consist of two dileptons or a dilepton plus MET from the sneutrino decays. Then, we will consider the existing dilepton displaced-vertex searches, and discuss its feasibility and significance on $\widetilde{\nu}_\tau$ searches. In Section 6.5, we will discuss the strategy that we employed to perform scans searching for points of the parameter space of our scenario compatible with current experimental data on neutrino and Higgs physics, as well as flavor observables. The input parameters used and the results of the scans will be presented in Sections 6.6 and 6.7, respectively, and applied to show the current reach of the LHC search on the parameter space of the $\widetilde{\nu}_\tau$ LSP based on the ATLAS 8-TeV result [73],

and the prospects for the 13-TeV searches. Finally, our conclusions are left for Section 6.8.

6.2 Neutrino/sneutrino physics

Since reproducing neutrino data is an important asset of the $\mu\nu$SSM, as explained above, we will try to establish here qualitatively what regions of the parameter space are the best in order to be able to obtain correct neutrino masses and mixing angles. In particular, we will determine natural hierarchies among neutrino Yukawas, and among left sneutrino VEVs.

In addition, left sneutrinos are special in the $\mu\nu$SSM with respect to other SUSY models. This is because, as discussed in Eq. (3.67), their masses are determined by the minimization equations with respect to v_i. Thus, they depend not only on left sneutrino VEVs but also on neutrino Yukawas, and as a consequence neutrino physics is very relevant. In particular, if we work with Eq. (3.69) using Eq. (3.4), we can write

$$m^2_{\widetilde{\nu}^{\mathcal{R}}_{iL}} = m^2_{\widetilde{\nu}^{\mathcal{I}}_{iL}} \approx \frac{Y_{\nu_i} v_u}{v_i} \frac{v_{iR}}{\sqrt{2}} \left(-A_{\nu_i} - \frac{\mathcal{M}_i}{2} + \frac{\mu}{\tan\beta} \right). \tag{6.1}$$

Assuming the simplest situation that all the A_{ν_i} are naturally of the order of the TeV, neutrino physics determines sneutrino masses through the prefactor $Y_{\nu_i} v_u / v_i$. Note that for simplicity of notation we will use v_i for the left sneutrino VEVs instead of v_{iL} thorough this chapter. Considering the normal ordering (NO) for the neutrino mass spectrum, which is nowadays favored by the analyses of neutrino data [10–13], representative solutions for neutrino/sneutrino physics using diagonal neutrino Yukawas in this scenario are summarized below. Note that these solutions take advantage of the dominance of the gaugino seesaw for some of the three neutrino families.

1) $M < 0$, with $Y_{\nu_1} < Y_{\nu_2}, Y_{\nu_3}$, and $v_1 > v_2, v_3$.

As explained in Refs. [54, 80], a negative value for M is useful in order to reproduce neutrino data with Y_{ν_1} the smallest Yukawa and v_1 the largest VEV. Essentially, this is because a small tuning in Eq. (3.32) between the gaugino seesaw and the ν_R-Higgsino seesaw is necessary in order to obtain the correct mass of the first family. Here the contribution of the gaugino seesaw is always the largest one. On the contrary, for the other two neutrino families, the contribution of the ν_R-Higgsino seesaw is the most important one and that of the gaugino seesaw is less relevant for the tuning. Following the above discussion about the prefactor of Eq. (6.1), these hierarchies of Yukawas and VEVs determine that $m_{\widetilde{\nu}_1}$ is the smallest of all the sneutrino masses.

2) $M > 0$, with $Y_{\nu_3} < Y_{\nu_1} < Y_{\nu_2}$, and $v_1 < v_2 \sim v_3$.

In this case, it is easy to find solutions with the gaugino seesaw as the dominant one for the third family. Then, v_3 determines the corresponding neutrino mass and Y_{ν_3} can be small. On the other hand, the NO for neutrinos determines that the first family dominates the lightest mass eigenstate implying that $Y_{\nu_1} < Y_{\nu_2}$ and $v_1 < v_2, v_3$, with both ν_R-Higgsino and gaugino seesaws contributing significantly to the masses of the first and second family. Taking also into account that the composition of these two families in the second mass eigenstate is similar, we expect $v_2 \sim v_3$. Now for this solution we will have $m_{\widetilde{\nu}_3}$ as the smallest of all the sneutrino masses.

3) $M > 0$, with $Y_{\nu_2} < Y_{\nu_1} < Y_{\nu_3}$, and $v_1 < v_2 \sim v_3$.

These solutions can be deduced from the previous ones in 2) interchanging the values of the third family, Y_{ν_3} and v_3, with the corresponding ones of the second family, Y_{ν_2} and v_2. A small adjust in the parameters will lead again to a point in the parameter space satisfying neutrino data. This is clear from the fact that θ_{13} and θ_{12} are not going to be significantly altered, whilst θ_{23} may require a small tuning in the parameters. If the gaugino seesaw dominates for the second family, v_2 determines the corresponding neutrino mass and Y_{ν_2} can be small. Then, $m_{\widetilde{\nu}_2}$ will be the smallest of all sneutrino masses.

We will see in the next subsection that solutions of type 2) are the ones interesting for our analysis.

Let us finally point out that when off-diagonal neutrino Yukawas are allowed, it is not possible to arrive to a general conclusion regarding the hierarchy in sneutrinos masses, specially when the gaugino seesaw is sub-dominant. This is because one can play with the hierarchies among v_i with enough freedom in the neutrino Yukawas in order to reproduce the experimental results. Therefore, there is no a priori knowledge of the hierarchies in the sneutrino masses, and carrying out an analysis case by case turns out to be necessary.

6.3 $\widetilde{\nu}_\tau$ LSP

In the $\mu\nu$SSM, because of RPV any SUSY particle can be a candidate for the LSP. Nevertheless, the case of the $\widetilde{\nu}_\tau$ LSP turns out to be particularly interesting because of the large value of the tau Yukawa coupling, which can give rise to significant BRs for decays to[2] $\tau\tau$ and $\tau\ell$, once the sneutrinos are dominantly pair-produced via a Drell-Yan process mediated by a virtual W, Z or γ, as we will discuss in the next section.

There is enough freedom in the parameter space of the $\mu\nu$SSM in order to get light

[2]In what follows, the symbol ℓ will be used for an electron or a muon, $\ell = e, \mu$, and charge conjugation of fermions is to be understood where appropriate.

left sneutrinos. Assuming as discussed above that the A_{ν_i} are naturally of the order of the TeV, values of the prefactor of Eq. (6.1) $Y_{\nu_i} v_u / v_i$ in the range of about $0.01 - 1$, i.e. $Y_{\nu_i} \sim 10^{-8} - 10^{-6}$, will give rise to left sneutrino masses in the range of about $100 - 1000$ GeV. Thus, with the hierarchy of neutrino Yukawas $Y_{\nu_3} \sim 10^{-8} - 10^{-7} < Y_{\nu_{1,2}} \sim 10^{-6}$, we can obtain a $\widetilde{\nu}_\tau$ LSP with a mass around 100 GeV whereas the masses of $\widetilde{\nu}_{e,\mu}$ are of the order of the TeV. Clearly, we are in the case of solutions for neutrino physics of type 2) discussed in Subsection 6.2. Actually this type of hierarchy, with significant values for $Y_{\nu_{1,2}}$, increases the dilepton BRs of the $\widetilde{\nu}_\tau$ LSP producing signals that can be probed at the LHC, as the analysis of the next sections will show.

It is worth noticing here that in this scenario the left stau can be naturally the NLSP, since it is only a little heavier than the $\widetilde{\nu}_\tau$ because they are in the same $SU(2)$ doublet, with the mass splitting mainly due to the usual small D-term contribution, $-m_W^2 \cos 2\beta$. As we will see in the next section, this has implications for the production of the left sneutrino LSP at the LHC, because the direct production of sleptons and their decays is a significant source of sneutrinos.

6.4 Searching for $\widetilde{\nu}_\tau$ LSP at the LHC

To probe the $\widetilde{\nu}_\tau$ LSP, the dilepton displaced-vertex searches are found to be the most promising. Following the strategy of Ref. [21], we will compare the predictions of our current scenario with three right-handed neutrinos with the ATLAS search [73] for long-lived particles using displaced ($\gtrsim$ 1 mm) lepton pairs $\ell\ell$ in pp collisions at $\sqrt{s} = 8$ TeV, as well as the prospects for the 13-TeV searches.

The direct production of $\widetilde{\nu}_\tau$ occurs via a Z channel giving rise to a pair of scalar and pseudoscalar left sneutrinos, as shown in Fig. 6.1(a). Note that they are co-LSPs since they have essentially degenerate masses, as explained in the previous section. On the other hand, since the left stau is typically the NLSP its direct production and decay is another important source of the $\widetilde{\nu}_\tau$ LSP. In particular, pair production can be obtained through a γ or Z decaying into two staus, as shown in Fig. 6.1(b), with the latter having a dominant RPC prompt decay into a (scalar or pseudoscalar) sneutrino plus an off-shell W producing a soft meson or a pair of a charged lepton and a neutrino. Note that although RPV decays of the stau are possible, e.g. stau into a tau plus a neutrino, they are extremely supressed compared to the RPC one. Numerically, the stau has partial decay widths through RPV diagrams $\sim 10^{-14} - 10^{-13}$ GeV, while the ones corresponding to the RPC three-body decays are $\sim 10^{-7}$ GeV. Therefore, its proper decay length is $\sim 10^{-9}$

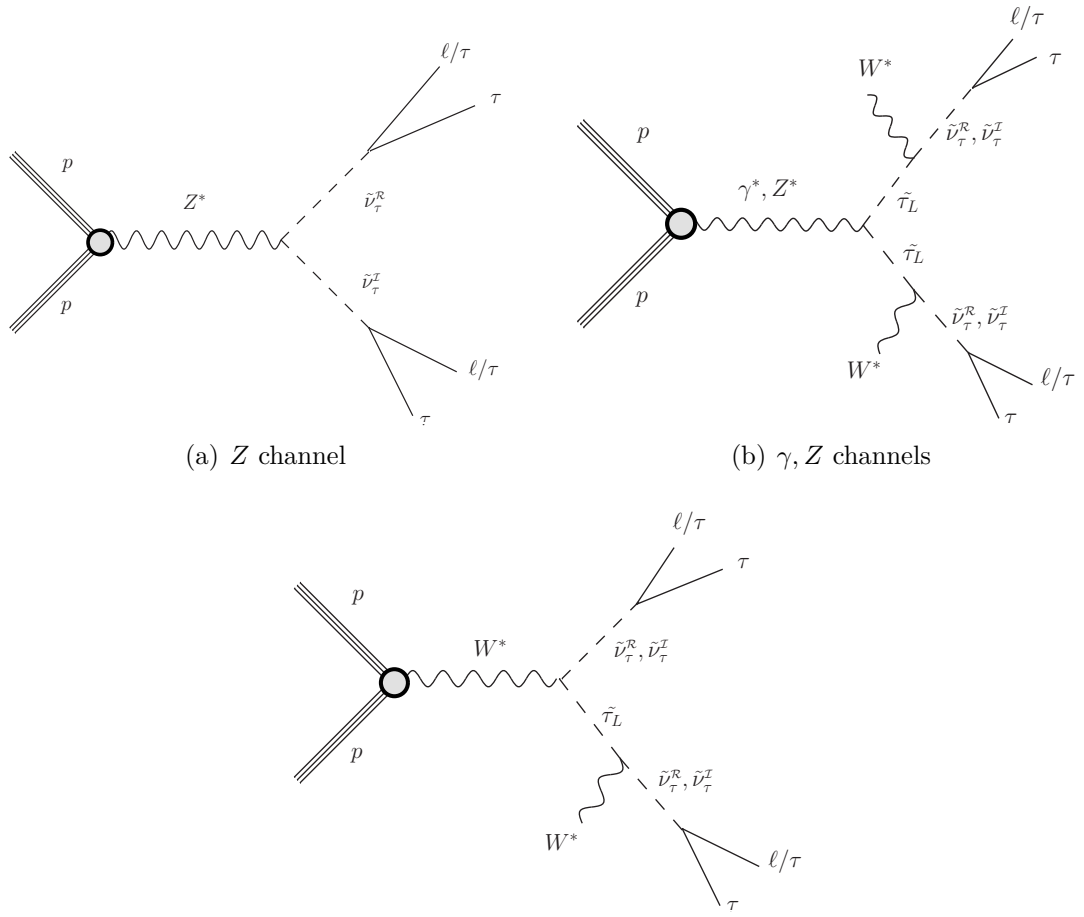

(a) Z channel

(b) γ, Z channels

(c) W channel

Figure 6.1: Decay channels into two $\tau\,\ell/\tau$, from a pair production at the LHC of scalar and pseudoscalar tau left sneutrinos co-LSPs. Decay channels into one $\tau\,\ell/\tau$ plus neutrinos are the same but substituting in (a), (b) and (c) one of the two vertices by a two-neutrino vertex.

m, with the BRs corresponding to the RPV decays $< 10^{-6}$. Sneutrinos can also be pair produced through a W decaying into a stau and a (scalar or pseudoscalar) sneutrino as shown in Fig. 6.1(c), with the stau decaying as before.

Subsequently, the pair-produced $\widetilde{\nu}_\tau$ can decay into $\tau\,\ell/\tau$. As a result of the mixing between left sneutrinos and Higgses, the sizable decay of $\widetilde{\nu}_\tau$ into $\tau\tau$ is possible because of the large value of the tau Yukawa coupling. Other sizable decays into $\tau\,\ell/\tau$ can occur through the Yukawa interaction of $\widetilde{\nu}_\tau$ with τ and charged Higgsinos, via the mixing between the latter and ℓ or τ. To analyze these processes we can write approximate formulas for the partial decay widths of the scalar/pseudoscalar tau left sneutrino. The

one into $\tau\tau$ is given by:

$$\Gamma\left(\widetilde{\nu}_\tau \to \tau\tau\right) \approx \frac{m_{\widetilde{\nu}_\tau}}{16\pi}\left(Y_\tau Z^{H/A}_{\widetilde{\nu}_\tau H_d} - Y_{\nu_\tau}\frac{Y_\tau}{3\lambda}\right)^2, \tag{6.2}$$

where $Y_\tau \equiv Y_{e_{33}}$, and $Z^{H/A}$ is the matrix which diagonalizes the mass matrix for the neutral scalars/pseudoscalars. The latter is determined by the neutrino Yukawas, which are the order parameters of the RPV. The contribution of λ in the second term of Eq. (6.2) is due to the charged Higgsino mass that can be approximated by the value of $\mu = 3\lambda\frac{v_R}{\sqrt{2}}$. The partial decay width into $\tau\ell$ can then be approximated for both sneutrino states by the second term of Eq. (6.2) with the substitution $Y_{\nu_\tau} \to Y_{\nu_\ell}$:

$$\Gamma\left(\widetilde{\nu}_\tau \to \tau\ell\right) \approx \frac{m_{\widetilde{\nu}_\tau}}{16\pi}\left(Y_{\nu_\ell}\frac{Y_\tau}{3\lambda}\right)^2. \tag{6.3}$$

On the other hand, the gauge interactions of $\widetilde{\nu}_\tau$ with neutrinos and binos (winos) can produce a large decay width into neutrinos, via the gauge mixing between these gauginos and neutrinos. This partial decay width can be approximated for scalar and pseudoscalar sneutrinos as

$$\sum_i \Gamma(\widetilde{\nu}_\tau \to \nu_\tau\nu_i) \approx \frac{m_{\widetilde{\nu}_\tau}}{16\pi}\sum_i\left|\frac{g'}{2}U^V_{i4} - \frac{g}{2}U^V_{i5}\right|^2, \tag{6.4}$$

where U^V is the matrix which diagonalizes the mass matrix for the neutral fermions, and the above entries can be approximated as

$$\begin{aligned} U^V_{i4} &\approx \frac{-g'}{\sqrt{2}M_1}\sum_l v_l U^{PMNS}_{il}, \\ U^V_{i5} &\approx \frac{g}{\sqrt{2}M_2}\sum_l v_l U^{PMNS}_{il}. \end{aligned} \tag{6.5}$$

Here U^{PMNS}_{il} are the entries of the PMNS matrix, with i and l neutrino physical and flavor indices, respectively. The relevant diagrams for $\widetilde{\nu}_\tau$ searches that include this decay mode are the same as in Fig. 6.1, but substituting one of the $\tau\,\ell/\tau$ vertices by a two-neutrino vertex.

Let us remark that other decay channels of the $\widetilde{\nu}_\tau$ can be present and have been taken into account in our numerical computation, but they turn out to be negligible for the sneutrino masses that we are interested in this work.

Given the above results valid for three families of right-handed neutrino superfields, we can now follow the prescription of Ref. [21] for improving and recasting the ATLAS search [73] to the case of the $\widetilde{\nu}_\tau$. One of the problems with the existing searches [73, 119–

121] is that they are designed for a generic purpose and therefore not optimized for light metastable particles such as the $\widetilde{\nu}_\tau$; we thus proposed in Ref. [21] a strategy of improving these searches by lowering trigger thresholds, relying on a high level trigger that utilizes tracker information. This optimization turned out to be quite feasible and considerably improves the sensitivity of the displaced-vertex searches to long-lived $\widetilde{\nu}_\tau$. In particular, in the ATLAS 8-TeV analysis, the events must satisfy the following trigger requirements [73]:

- One muon with $p_{\rm T} > 50$ GeV and $|\eta| < 1.07$, one electron with $p_{\rm T} > 120$ GeV or two electrons with $p_{\rm T} > 40$ GeV each,

and off-line selection requirements:

- One pair e^+e^-, $\mu^+\mu^-$ or $e^\pm\mu^\mp$ with $p_{\rm T} > 10$ GeV and $0.02 < |\eta| < 2.5$ for each particle.

As shown in Ref. [21], the trigger requirement for electrons is so restrictive that it makes the selection efficiency for the dielectron channel be a few percent level, while for the $\mu^+\mu^-$ and $e^\pm\mu^\mp$ channels the efficiency can be a few tens of percent. We can however overcome this difficulty by optimizing the trigger requirements for left sneutrino searches by relaxing the momentum thresholds [21]. In fact, it is possible to reduce momentum thresholds for triggers by means of established techniques. For instance, the `mu24i` trigger used in the ATLAS experiment [122] only requires $p_{\rm T} > 24$ GeV; such a low threshold can be achieved thanks to the information from the inner detector. This information can also improve the trigger performance in a wider range of the pseudorapidity of tracks, and thus we can also relax the requirement on η; from $|\eta| < 1.07$ to $|\eta| < 2.5$ [122]. It is then argued in Ref. [21] that we can still consider the number of background events to be zero even after we relax the momentum threshold. Consequently, to exploit this trigger instead of that used in Ref. [73] can significantly enhance the sensitivity to light sneutrinos, since the typical momentum of muons from the sneutrino decays is a few tens of GeV. After all, one can use the following criteria for the optimized 8-TeV analysis:[3]

- At least one muon with $p_{\rm T} > 24$ GeV.
- One pair $\mu^+\mu^-$ or $e^\pm\mu^\mp$ with $p_{\rm T} > 10$ GeV and $0.02 < |\eta| < 2.5$ for each particle.

[3]We could have required a lower threshold for the electron trigger as well, but we do not consider this optimization since we are unable to estimate the increase in the number of background events caused by the relaxation in the trigger requirement [21].

We can also assume an optimization of the trigger requirements in the 13-TeV searches. It is again discussed in Ref. [21] that one can use the following criteria for the 13-TeV analysis:

- At least one electron or muon with $p_{\rm T} > 26$ GeV.
- One pair $\mu^+\mu^-$, e^+e^-, or $e^\pm\mu^\mp$ with $p_{\rm T} > 10$ GeV and $0.02 < |\eta| < 2.5$ for each particle.

Since we do not have the 13-TeV result for dilepton displaced-vertex searches for the moment, we just assume the expected number of background events to be zero, which should be validated in the future experiments. It is worth noticing that unlike the previous two trigger requirements, in this case the p_T threshold of 26 GeV is for both muons and electrons. The improvement of the selection efficiencies, $\epsilon_{\rm sel}$, for different masses, for the three production processes, and for the $\mu\mu$, μe, and ee channels, can be found in Tables III-IX of Ref. [21]. As pointed out also in that work, this possible improvement is not only for the ATLAS analysis but also for the CMS one [119].

We can now discuss how to obtain the limits for light sneutrinos. Throughout our analysis, we assume that the number of both background and signal events to be zero, as in the ATLAS 8-TeV search result [122]. The limits from the ATLAS search can be translated into a vertex-level efficiency, taking into account the lack of observation of events for any value of the decay length. Therefore, $\epsilon_{\rm vert}(c\tau)$ can be obtained as the ratio of the number of signal events compatible with zero observed events (which in this case is 3 as we assume zero background) and that corresponding to the upper limits given in Ref. [73] with an appropriate modification described in Ref. [21]; for example, we can use the purple-shaded solid line of Fig. 3 in the later work to obtain the vertex-level efficiency $\epsilon^{\mu\mu}_{\rm vert}(c\tau)$ for the dimuon channel. It is found that the efficiency decreases significantly for $c\tau \lesssim 1$ mm, which has important implications for the prospects of the $\widetilde{\nu}_\tau$ searches as we will see below. By multiplying the number of the events passing the trigger and event selection criteria with this vertex-level efficiency, we can estimate the total number of signal events; for the 8-TeV case, this is given for the $\mu\mu$ channel by

$$\begin{aligned} \#\text{Dimuons} &= \left[\sigma(pp \to Z \to \widetilde{\nu}_\tau\widetilde{\nu}_\tau)\epsilon^Z_{\rm sel} + \sigma(pp \to W \to \widetilde{\nu}_\tau\widetilde{\tau})\epsilon^W_{\rm sel} + \sigma(pp \to \gamma, Z \to \widetilde{\tau}\widetilde{\tau})\epsilon^{\gamma,Z}_{\rm sel}\right] \\ &\times \mathcal{L} \times \left[\text{BR}(\widetilde{\nu}^{\mathcal{R}}_\tau \to \mu\mu)\ \epsilon^{\mu\mu}_{\rm vert}(c\tau^{\mathcal{R}}) + \text{BR}(\widetilde{\nu}^{\mathcal{I}}_\tau \to \mu\mu)\ \epsilon^{\mu\mu}_{\rm vert}(c\tau^{\mathcal{I}})\right], \end{aligned} \tag{6.6}$$

where

$$\mathrm{BR}(\widetilde{\nu}_\tau \to \mu\mu) \equiv \mathrm{BR}(\widetilde{\nu}_\tau \to \tau\mu) \times 0.1739 + \mathrm{BR}(\widetilde{\nu}_\tau \to \tau\tau) \times (0.1739)^2\,, \tag{6.7}$$

with 0.1739 the BR of the τ decay into muons (plus neutrinos), and we use an integrated luminosity of $\mathcal{L} = 20.3$ fb^{-1} [73] (300 fb^{-1} when studying the 13-TeV prospects). The same formula can be applied for the other two channels. If the predicted number of signal events is above 3 the corresponding parameter point of the model is excluded so that this is compatible with zero number of events.

Let us finally remark that in our analysis below, we scan the parameter space of the model and therefore $m_{\widetilde{\nu}_\tau}$ can be regarded as a continuous variable, unlike Ref [21] where the sneutrino masses used were 50, 60, 80 and 100 GeV. For the selection efficiency we used a polynomial fitting from the discrete values of $\epsilon_{\rm sel}$ given in Ref. [21] for each production mode, whereas for the vertex-level efficiency, the fitting function is of the form $e^{P[\log(c\tau)]}$, where $P[x]$ is a polynomial in the variable x.

6.5 Sampling the $\mu\nu$SSM for $\widetilde{\nu}_\tau$ LSP

In this section we describe the likelihood we use in the scans to search for points in the parameter space that are compatible with neutrino and Higgs physics, as well as $\widetilde{\nu}_\tau$ LSP with a mass in the range of $45 - 100$ GeV. To carry out this analysis, we employ the method described in Chapter 4 to sample the $\mu\nu$SSM.

In order to concentrate the sampling in the area in which the mass of the tau left sneutrino $m_{\widetilde{\nu}_\tau} \in (45, 100)$ GeV, in addition to the observables presented in Subsection 4.4, we construct a likelihood function $\mathcal{L}_{\widetilde{\nu}_\tau}$ which is a Gaussian with mean value $\mu_{m_{\widetilde{\nu}_\tau}} = 70$ GeV and width $\sigma_{m_{\widetilde{\nu}_\tau}} = 10$ GeV, and included it in the combined likelihood. In sum, the joint likelihood function we use in this work is

$$\mathcal{L}_{\rm tot} = \mathcal{L}_{\widetilde{\nu}_\tau} \times \mathcal{L}_{\rm neutrino} \times \mathcal{L}_{\rm Higgs} \times \mathcal{L}_{\rm B\ physics} \times \mathcal{L}_{\mu\ \rm decay} \times \mathcal{L}_{m_{\widetilde{\chi}^\pm}}\,. \tag{6.8}$$

The likelihoods were defined in Chapter 4, but we repeat them here. $\mathcal{L}_{\widetilde{\nu}_\tau}$ is basically the prior we impose on the tau left sneutrino mass, $\mathcal{L}_{\rm neutrino}$ represents measurements of neutrino observables, $\mathcal{L}_{\rm Higgs}$ Higgs observables, $\mathcal{L}_{\rm B\ physics}$ B-physics constraints, $\mathcal{L}_{\mu\ \rm decay}$ μ decays constraints and $\mathcal{L}_{m_{\widetilde{\chi}^\pm}}$ constraints on the chargino mass. Note that neutrino data in this case is taken from Table 4.1.

6.6 Input parameters

In order to efficiently scan for the $\widetilde{\nu}_\tau$ LSP in the $\mu\nu$SSM with a mass in the range $45 - 100$ GeV, it is important to identify first the parameters to be used, and optimize their number and their ranges of values. This is what we carry out here, where we discuss the most relevant parameters for obtaining correct neutrino and Higgs physics, providing at the same time the $\widetilde{\nu}_\tau$ as the LSP with the mass in the desired range.

The relevant parameters in the neutrino sector of the $\mu\nu$SSM are $\lambda, \kappa, v_R, v_i, Y_{\nu_i}, \tan\beta$ and M (see Eq. (3.43)). Since λ, κ and v_R are crucial for Higgs physics, we will fix first them to appropriate values. The parameter $\tan\beta$ is also important for both, Higgs and neutrino physics, thus we will consider a narrow range of possible values to ensure good Higgs physics. Concerning M, which is a kind of average of bino and wino soft masses (see Eq. (3.34)), inspired by GUTs we will assume $M_2 = 2M_1$, and scan over M_2. On the other hand, sneutrino masses introduce in addition the parameters T_{ν_i} (see Eq. (3.67)). In particular, T_{ν_3} is the most relevant one for our discussion of the $\widetilde{\nu}_\tau$ LSP, and we will scan it in an appropriate range of small values. Since the left sneutrinos of the first two generations must be heavier, we will fix $T_{\nu_{1,2}}$ to a larger value.

Summarizing, we will perform scans over the 9 parameters $Y_{\nu_i}, v_i, T_{\nu_3}, \tan\beta, M_2$, as shown in Table 6.1, using log priors (in logarithmic scale) for all of them, except for $\tan\beta$ which is taken to be a flat prior (in linear scale). The ranges of v_i and Y_{ν_i} are natural in the context of the electroweak-scale seesaw of the $\mu\nu$SSM. The range of T_{ν_3} is also natural if we follow the usual assumption based on the supergravity framework discussed in Eq. (3.69) that the trilinear parameters are proportional to the corresponding Yukawa couplings, i.e. in this case $T_{\nu_3} = A_{\nu_3} Y_{\nu_3}$ implying $-A_{\nu_3} \in (1, 10^4)$ GeV. Concerning M_2, its range of values is taken such that a bino at the bottom of the neutralino spectrum leaves room to accommodate a $\widetilde{\nu}_\tau$ LSP with a mass below 100 GeV. Scans 1 (S_1) and 2 (S_2) correspond to different values of $\tan\beta$, and other benchmark parameters as shown in Table 6.2.

In Table 6.2 we choose first two values of λ, covering a representative region of this parameter. From a small/moderate value, $\lambda \approx 0.1$ (S_1), to a large value, $\lambda \approx 0.4$ (S_2), in the border of perturbativity up to the GUT scale [50]. For scan S_1, since λ is small we are in a similar situation as in the MSSM, and moderate/large values of $\tan\beta$, $|T_{u_3}|$, and soft stop masses, are necessary to obtain the correct SM-like Higgs mass. In addition, if we want to avoid the chargino mass bound of RPC SUSY, the value of λ also force us to choose a moderate/large value of v_R to obtain a large enough value of $\mu = 3\lambda\frac{v_R}{\sqrt{2}}$. In

Scan 1 (S_1)	**Scan 2** (S_2)
$\tan\beta \in (10, 16)$	$\tan\beta \in (1, 4)$
$Y_{\nu_i} \in (10^{-8}, 10^{-6})$	
$v_i \in (10^{-6}, 10^{-3})$	
$-T_{\nu_3} \in (10^{-6}, 10^{-4})$	
$M_2 \in (150, 2000)$	

Table 6.1: Range of low-energy values of the input parameters that are varied in the two scans, where Y_{ν_i}, v_i, T_{ν_3} and M_2 are log priors while $\tan\beta$ is a flat prior. The VEVs v_i, and the soft parameters T_{ν_3} and M_2, are given in GeV.

Parameter	**Scan 1** (S_1)	**Scan 2** (S_2)
λ	0.102	0.42
κ	0.4	0.46
v_R	1750	421
T_λ	340	350
$-T_\kappa$	390	108
$-T_{u_3}$	4140	1030
$m_{\widetilde{Q}_{3L}}$	2950	1972
$m_{\widetilde{u}_{3R}}$	1140	1972
M_3	2700	
$m_{\widetilde{Q}_{1,2L}}, m_{\widetilde{u}_{1,2R}}, m_{\widetilde{e}_{1,2,3R}}$	1000	
$T_{u_{1,2}}$	0	
$T_{d_{1,2}}$, T_{d_3}	0, 100	
$T_{e_{1,2}}$, T_{e_3}	0, 40	
$-T_{\nu_{1,2}}$	10^{-3}	

Table 6.2: Low-energy values of the input parameters that are fixed in the two scans. The VEV v_R and the soft trilinear parameters, soft gluino masses and soft scalar masses are given in GeV.

particular, we choose $v_R = 1750$ GeV giving rise to $\mu \approx 379$ GeV. The latter parameters, λ and v_R, together with κ and T_λ are also relevant to obtain the correct values of the off-diagonal terms of the mass matrix mixing the right sneutrinos with Higgses. As explained in Eqs. (3.44) and (3.45), the parameters κ and v_R (together with T_κ) are also crucial to determine the mass scale of the right sneutrinos. In scan S_1, where we choose $T_\kappa = -390$ GeV to have heavy pseudoscalar right sneutrinos (of about 1190 GeV), the value of κ has to be large enough in order to avoid too light (even tachyonic) scalar right sneutrinos. Choosing $\kappa = 0.4$, we get masses for the latter of about $700 - 755$ GeV.

For scan S_2, where we choose a large value for λ, we are in a similar situation as in the NMSSM, and a small value of $\tan\beta$, and moderate values of $|T_{u_3}|$ and soft stop masses, are sufficient to reproduce the correct SM-like Higgs mass. Now, a moderate value of v_R is sufficient to obtain a large enough value of μ. In particular, we choose $v_R = 421$ GeV giving rise to $\mu \approx 375$ GeV. This value of v_R implies that $|T_\kappa|$ cannot be as large as for scan S_1 because then a too large value of κ would be needed to avoid tachyonic scalar right sneutrinos. Thus we choose $T_\kappa = -108$ GeV, and $\kappa = 0.42$, which produces scalar and pseudoscalar sneutrinos lighter than in scan S_1 but still heavier than $\widetilde{\nu}_\tau$ LSP and left stau NLSP. In particular, their masses are in the ranges $225 - 256$ GeV and $345 - 355$ GeV, respectively.

The values of the parameters shown below $m_{\widetilde{u}_{3R}}$ in Table 6.2, concerning gluino, and squark and slepton masses, and quark and lepton trilinear parameters, are not specially relevant for our analysis, and we choose for each of them the same values for both scans. Finally, compared to the values of T_{ν_3}, the values chosen for $T_{\nu_{1,2}}$ are natural within our framework $T_{\nu_{1,2}} = A_{\nu_{1,2}} Y_{\nu_{1,2}}$, since larger values of the Yukawa couplings are required for similar values of A_{ν_i}. In the same way, the values of T_{d_3} and T_{e_3} have been chosen taking into account the corresponding Yukawa couplings.

6.7 Results

By using the methods described in the previous sections, we evaluate now the current and potential limits on the parameter space of our scenario from the displaced-vertex searches with the 8-TeV ATLAS result [73], and discuss the prospects for the 13-TeV searches.

To find regions consistent with experimental observations we have performed about 72 million of spectrum evaluations in total and the total amount of computer required for this was approximately 380 CPU years.

To carry this analysis out, we follow several steps. First, we select points from the scan that lie within $\pm 3\sigma$ of all neutrino physics observables, namely the mixing angles and mass squared differences. Second, we put $\pm 3\sigma$ cuts from $b \to s\gamma$, $B_s \to \mu^+\mu^-$ and $B_d \to \mu^+\mu^-$. The points that pass these cuts are required to satisfy also the upper limits of $\mu \to e\gamma$ and $\mu \to eee$. The third step in the selection of our points is to ensure a tau left sneutrino LSP with $m_{\widetilde{\nu}_\tau} \in (45, 100)$ GeV, and the left stau as the NLSP. In the fourth step we impose that Higgs physics is realized. As already mentioned, we use `HiggsBounds` and `HiggsSignals` taking into account the constraints from the latest 13-TeV results. In particular, we require that the p-value reported by `HiggsSignals` be larger than 5 %. It is worth noticing here that, with the help of Vevacious [104], we have also checked that the EWSB vacua corresponding to the previous allowed points are stable.

The final set of cuts is related to $\widetilde{\nu}_\tau$ LSP searches with displaced vertices. From the points left above, we select those with decay length $c\tau > 0.1$ mm in order to be constrained by the current experimental results, as mentioned in previous sections. Finally, since the number of signal events compatible with zero observed events is 3, we look for points with a number of signal events above 3.

6.7.1 Constraints from neutrino/sneutrino physics.

Reproducing neutrino physics is very important in the $\mu\nu$SSM. Therefore we analyze first the constraints imposed by this requirement on the relevant parameter space of the model when the $\widetilde{\nu}_\tau$ is the LSP.

Imposing all the cuts discussed above, with the exception of the one associated to the number of signal events, we show in Fig. 6.2 the values of the parameter A_{ν_3} versus the prefactor in Eq. (3.69), $Y_{\nu_3} v_u / v_3$, giving rise to a mass of the $\widetilde{\nu}_\tau$ in the desired range $45 - 100$ GeV. The colours indicate different values of this mass. Scan S_1 (S_2) is shown in the left (right)-hand side of the figure. Let us remark that these plots have been obtained using the full numerical computation including loop corrections, although the tree-level mass in Eq. (3.69) gives a good qualitative idea of the results. In particular, in scan S_1 we can see that the allowed range of $-A_{\nu_3}$ is $779 - 1820$ GeV, corresponding to $-T_{\nu_3}$ in the range $8.3 \times 10^{-6} - 3.5 \times 10^{-5}$ GeV. We can also see, as can be deduced from Eq. (3.69), that for a fixed value of $-A_{\nu_3}$ ($Y_{\nu_3} v_u / v_3$) the greater $Y_{\nu_3} v_u / v_3$ ($-A_{\nu_3}$) is, the greater $m_{\widetilde{\nu}_\tau}$ becomes. For scan S_2, the allowed range of $-A_{\nu_3}$ turns out to be $67 - 3764$ GeV, corresponding to $-T_{\nu_3}$ in the range $2.1 \times 10^{-6} - 4.9 \times 10^{-5}$ GeV. The differences in the range of allowed values for A_{ν_3} and $Y_{\nu_3} v_u / v_3$ of the scan S_1 with respect to S_2, are

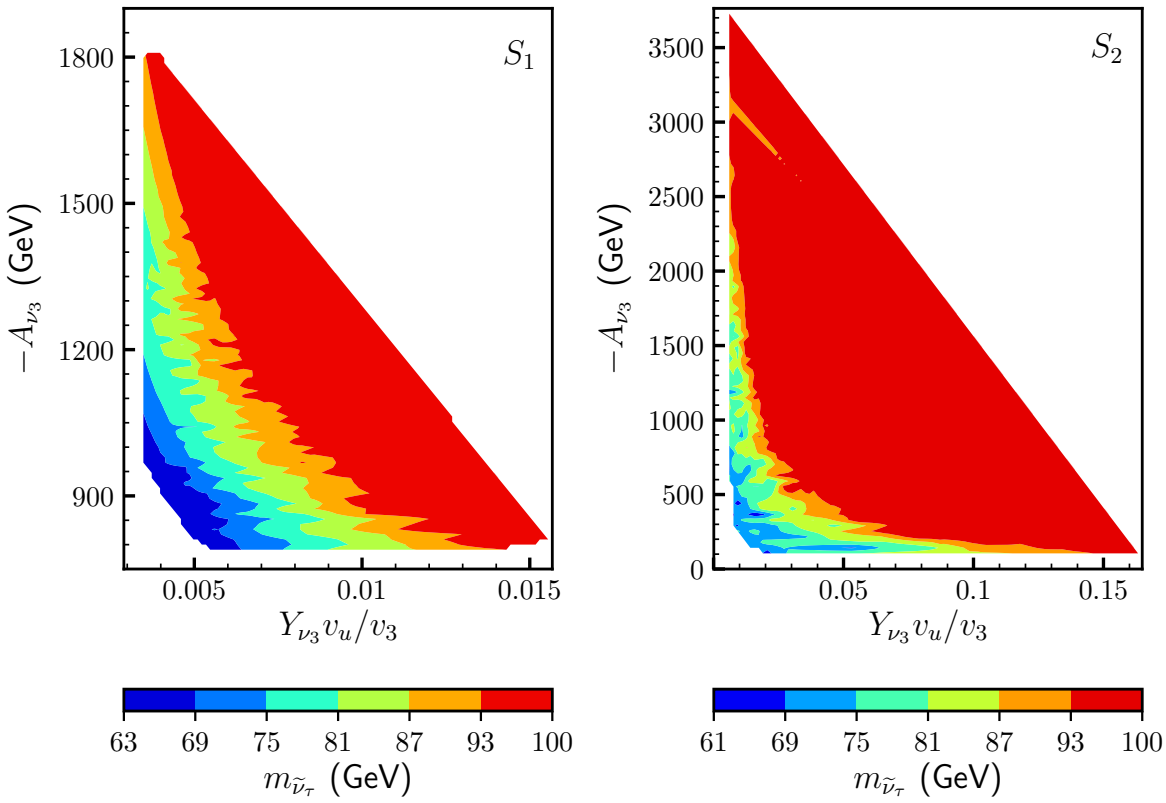

Figure 6.2: $-A_{\nu_3}$ versus $Y_{\nu_3} v_u / v_3$ for scan S_1 (left) and scan S_2 (right). The colours indicate different values of the tau left sneutrino LSP mass.

due to the negative vs. the positive contribution of the sum of the second and third terms in the bracket of Eq. (3.69), respectively, as well as to the different values of v_R which appears also as a prefactor in that equation.

Let us finally note that $m_{\tilde{\nu}_\tau}$ is always larger than about 61 GeV, which corresponds to half of the mass of the SM-like Higgs (remember that we allow a ± 3 GeV theoretical uncertainty on its mass). For smaller masses, the latter would dominantly decay into sneutrino pairs, leading to an inconsistency with Higgs data.[4]

In Fig. 6.3, we show v_3 vs. Y_{ν_3} for scan S_1 (left) and scan S_2 (right), with the colours indicating now different values of M. There we can see that the greater v_3 is, the greater M becomes. In addition, for a fixed value of v_3, M is quite independent of the variation in Y_{ν_3}. This confirms that, as explained in solution 2) of Subsection 6.2, the gaugino seesaw is the dominant one for the third neutrino family. From the figure, we can see that the

[4]In this scenario the SM-like Higgs decays into pairs of scalar/pseudoscalar tau left sneutrinos via gauge interactions, mostly from D-terms $\sim \frac{1}{4}(g^2 + g'^2)\tilde{\nu}_i \tilde{\nu}_i^* H_u^0 H_u^{0*}$, since its largest component is H_u^0.

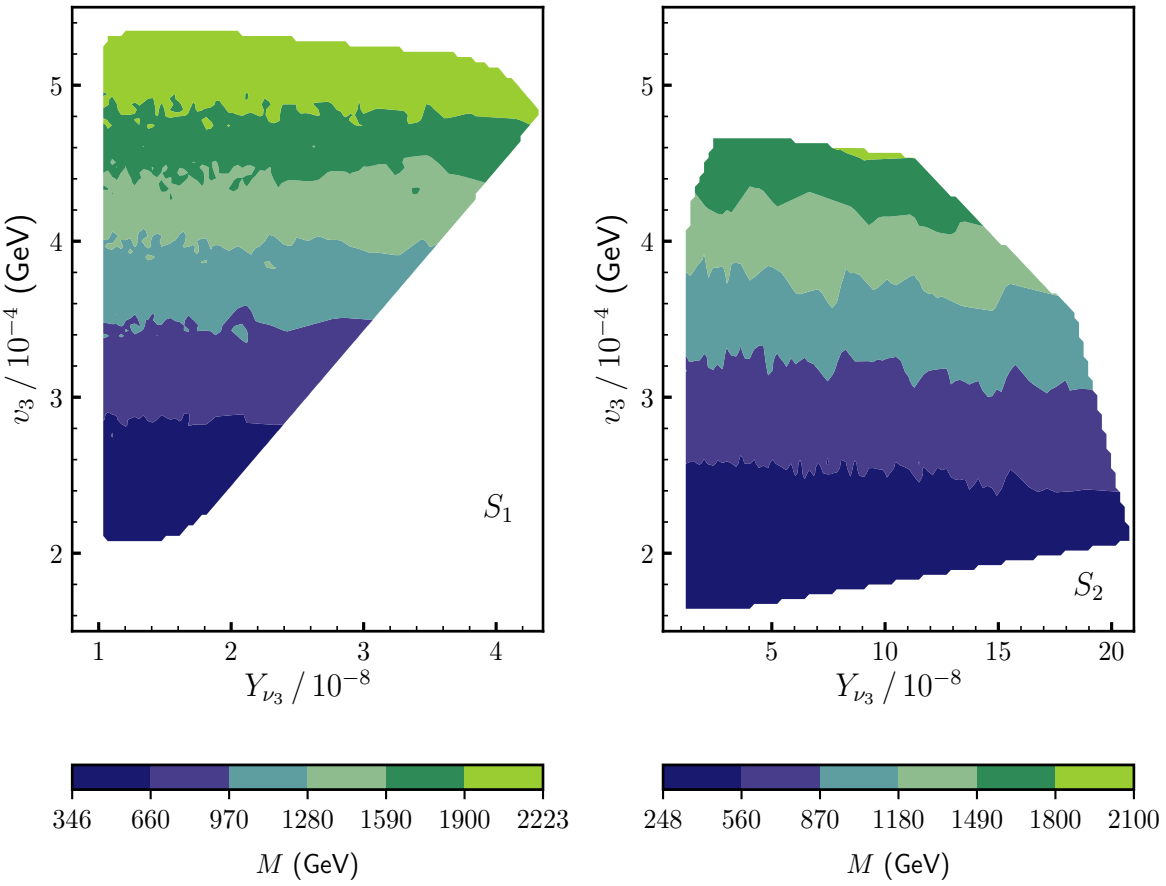

Figure 6.3: v_3 versus Y_{ν_3} for scan S_1 (left) and scan S_2 (right). The colours indicate different values of the gaugino mass parameter M defined in Eq. (3.34).

range of M reproducing the correct neutrino physics is $346 - 2223$ GeV for scan S_1 and $248 - 2100$ GeV for S_2, corresponding to M_2 in the range $236 - 1515$ GeV and $169 - 1431$ GeV, respectively. Note that for a fixed value of v_3, when Y_{ν_3} is sufficiently large the $\widetilde{\nu}_\tau$ becomes heavier than 100 GeV, and these points are not shown in the figure. As can also be seen, Y_{ν_3} acquires larger values in scan S_2 than in S_1, in agreement with the discussion of Fig. 6.2.

The values of Y_{ν_3} and v_3 used in order to obtain a $\widetilde{\nu}_\tau$ LSP in turn constrain the values of $Y_{\nu_{1,2}}$ and $v_{1,2}$ producing a correct neutrino physics. This is shown in Fig. 6.4, where δm^2 vs. Y_{ν_i} and v_i is plotted. As we can see, we obtain the hierarchy qualitatively discussed in solution 2) of Subsection 6.2, i.e. $Y_{\nu_3} < Y_{\nu_1} < Y_{\nu_2}$, and $v_1 < v_2 \lesssim v_3$. The values of the Yukawas $Y_{\nu_{1,2}}$ in scan S_2 are smaller than the corresponding ones in S_1 because for these two families the ν_R-Higgsino seesaw contributes significantly to the neutrino

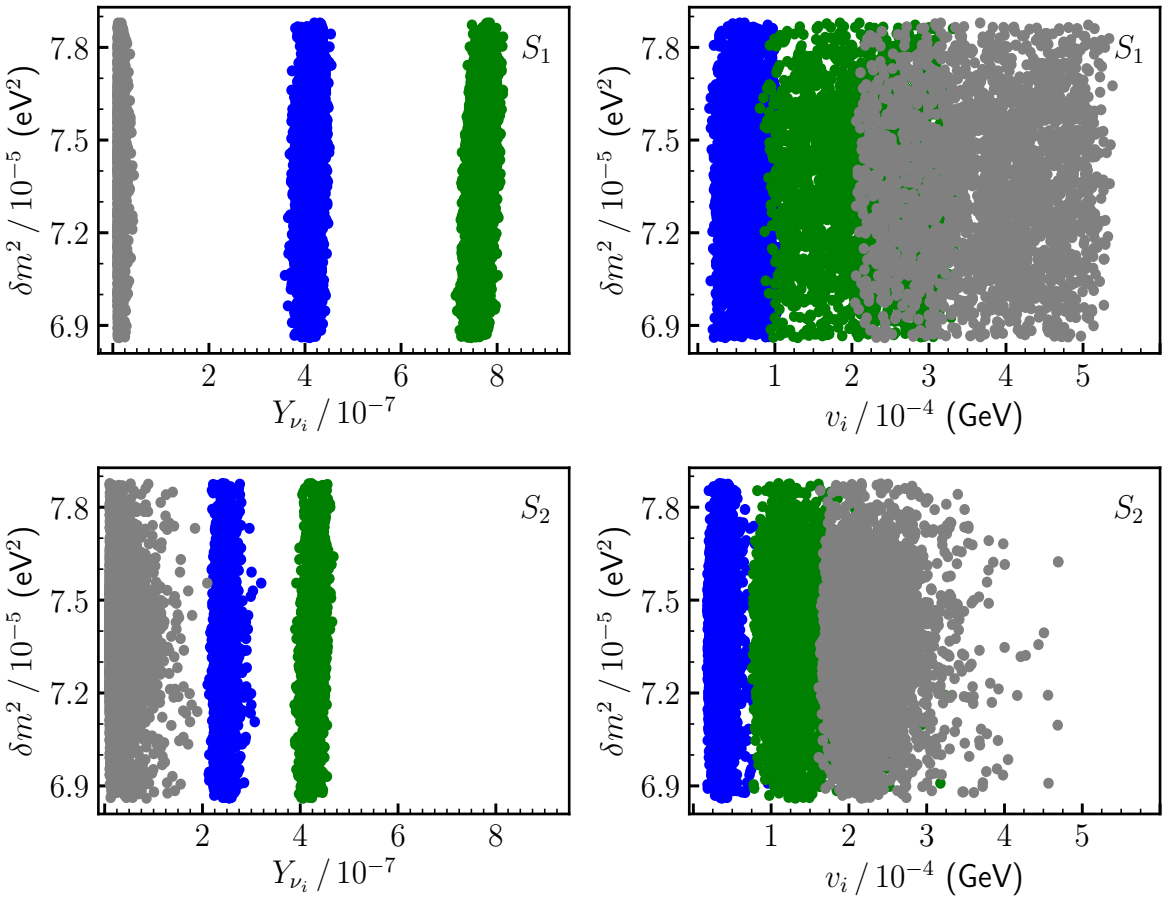

Figure 6.4: δm^2 versus neutrino Yukawas (left) and left sneutrino VEVs (right) for scan S_1 (top) and S_2 (bottom). Colors blue, green and grey correspond to $i = 1, 2, 3$, respectively.

masses, and v_R is smaller for scan S_2. Concerning the absolute value of neutrino masses, we obtain $m_{\nu_1} \sim 0.002$ eV, $m_{\nu_2} \sim 0.008$ eV, and $m_{\nu_3} \sim 0.05$ eV, fulfilling the cosmological upper bound on the sum of neutrino masses of 0.12 eV mentioned in Subsection 6.6. The predicted value of the sum of the neutrino masses can be tested in future CMB experiments such as CMB-S4 [123]. It is also worth noticing here that these hierarchies of neutrino Yukawas and left sneutrino VEVS, give rise to a $\widetilde{\nu}_\mu$ mass in the range $766 - 1568$ GeV for scan S_1 and $466 - 945$ GeV for S_2, producing the contributions $a_\mu^{\rm SUSY} \sim 3 \times 10^{-10}$ and $\sim 1 \times 10^{-10}$, respectively, which are within the SM uncertainty of the muon anomalous magnetic moment as mentioned in Subsection 4.4.5.

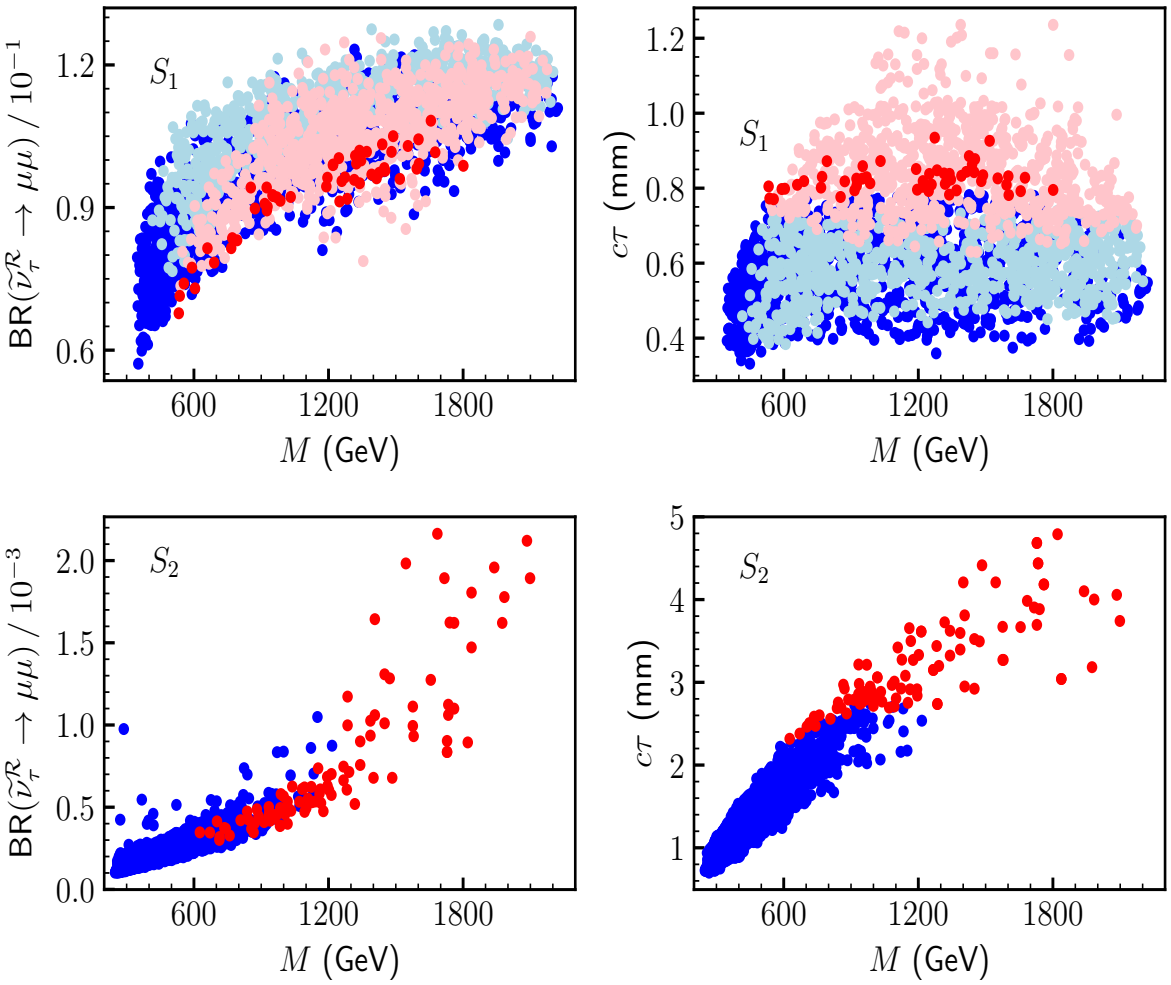

Figure 6.5: (Left) Branching ratio versus M for the decay of a scalar $\widetilde{\nu}_\tau$ LSP with $m_{\widetilde{\nu}_\tau} \in (61-100)$ GeV into $\mu\mu$ for scan S_1 (top) and S_2 (bottom). (Right) Proper decay length $c\tau$ of the scalar $\widetilde{\nu}_\tau$ LSP versus M for scan S_1 (top) and S_2 (bottom). In all plots, the dark-red points indicate that the number of signal events is above 3 analyzing the prospects for the 13-TeV search with an integrated luminosity of 300 fb^{-1}, combining the $\mu\mu$, $e\mu$ and ee channels, and considering also the optimization of the trigger requirements discussed in the text. The light-red points in scan S_1 although have a number of signal events above 3, are already excluded by the LEP result, as discussed in the text. The dark-blue points indicate that the number of signal events is below 3 and therefore inaccessible. The light-blue points in scan S_1 have also a number of signal events below 3, and, in addition, are already excluded by the LEP result.

6.7.2 Constraints from accelerator searches

Once the neutrino (and sneutrino) physics has determined the relevant regions of the parameter space of the $\widetilde{\nu}_\tau$ LSP in the $\mu\nu$SSM, we are ready to analyze the reach of the

LHC search.

Given that for each scan the largest neutrino Yukawa is Y_{ν_2}, the most important contribution to the dilepton BRs comes from the channel $\widetilde{\nu}_\tau \to \tau\mu$. We also expect that the BR($\widetilde{\nu}_\tau \to \mu\mu$) is larger for scan S_1 than for S_2, as can be checked in Fig. 6.5 (left plots),[5] where BR($\widetilde{\nu}_\tau^{\mathcal{R}} \to \mu\mu$) is plotted vs. M, for the points fulfilling all constraints from neutrino/sneutrino physics (although not shown here, a similar figure is obtained in the case of the pseudoscalar $\widetilde{\nu}_\tau^{\mathcal{I}}$). The main reason is the smaller (larger) value of λ ($\tan\beta$) for scan S_1 with respect to S_2, which are crucial parameters in Eq. (6.3) for the partial decay width. Although $\tan\beta$ does not appear explicitly in that equation, note that $Y_\tau = (\sqrt{2}m_\tau/v)\sqrt{\tan^2\beta + 1}$. In addition, as shown in Fig. 6.4, the value of Y_{ν_2} is larger for scan S_1 than for S_2, contributing therefore to larger BRs. We can also observe in both plots of Fig. 6.5 for the BRs that they increase with larger values of M. This can be understood from Eq. (6.4) showing that larger values of M decrease the decay width to neutrinos. In Fig. 6.5 (right plots), we show the proper decay length of the $\widetilde{\nu}_\tau^{\mathcal{R}}$ vs. M. Clearly, this is larger for scan S_2 than for S_1 because the BRs into charged leptons are smaller in the former case, as discussed before. Let us finally remember that the lower and upper bounds on M in the figure, have their origin in the analysis of the previous section reproducing neutrino (sneutrino) physics.

It is apparent that in scan S_2 for M larger than about 1000 GeV, the points that we find fulfilling all constraints are not uniformly distributed. This happens essentially because the value of v_R is smaller than in scan S_1 modifying the relevant contribution of the ν_R-Higgsino seesaw for the first two families, in such a way that is more difficult to reproduce neutrino physics unless more accurate values of the neutrino Yukawas are input in the computation. As obtained in Subsection 6.7.1, and can be seen in Fig. 6.4, the allowed values of Y_{ν_3} are larger for S_2. This makes more complicated to obtain the correct mixing, producing a tuning in the parameters. To obtain these more accurate values, we would have had to run Multinest a much longer time making the task very computer resources demanding. This is not really necessary since it is not going to affect the shape of the figure, and therefore neither the conclusions obtained. In addition, let us point out that we could have also modified the values of the parameters used for scan S_2 reproducing more easily neutrino physics, e.g. increasing v_R and modifying accordingly

[5]Notice that the partial decay widths into neutrinos for the S_1 and S_2 cases are similar in size for a given value of M, as can be seen from Eq. (6.4) and Fig. 6.4. Therefore, a larger partial decay width of the $\widetilde{\nu}_\tau \to \mu\tau$ channel for scan S_1 implies a larger value of BR($\widetilde{\nu}_\tau^{\mathcal{R}} \to \mu\mu$), compared with that for scan S_2.

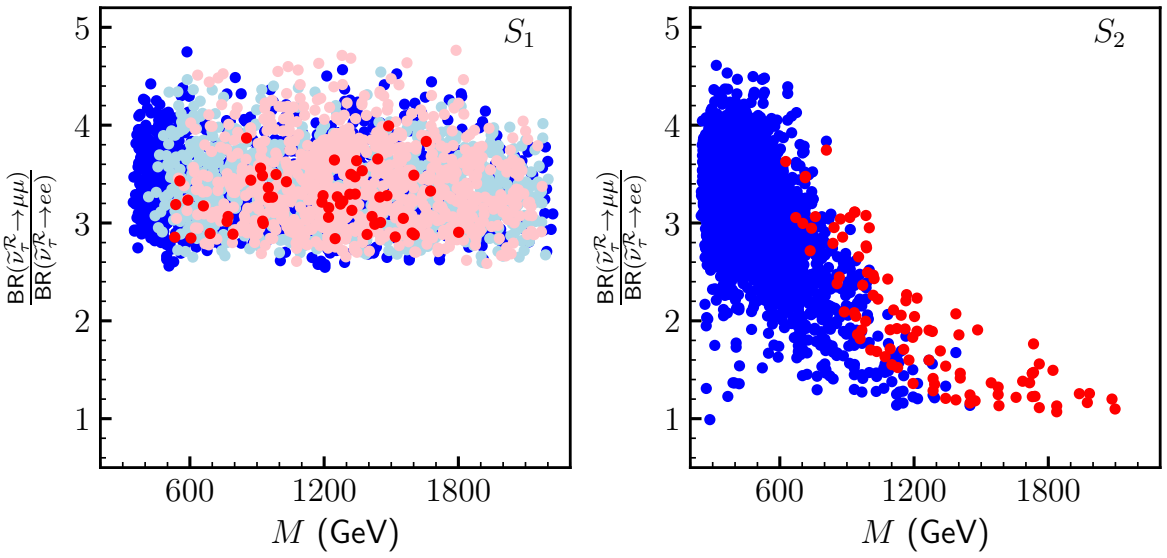

Figure 6.6: Ratios of the branching fractions of $\widetilde{\nu_\tau} \to \mu\mu$ and $\widetilde{\nu_\tau} \to ee$ for scan S_1 (left) and scan S_2 (right). The color code is the same as in Fig. 6.5.

the other parameters to keep the good Higgs physics.

In all plots of Fig 6.5, the (light- and dark-)red points correspond to regions of the parameter space where the number of signal events is above 3. Note that this only occurs for the 13-TeV analysis with an integrated luminosity of $\mathcal{L} = 300$ fb^{-1}. For the 8-TeV analysis, even considering the optimization of the trigger requirements, no points have a number of signal events larger than 3. However, we have checked that the light-red points in scan S_1 are already excluded by the LEP bound on left sneutrino masses [108–113]. To carry out this analysis, one can consider e.g. Fig. 6a of Ref. [111], where the cross section upper limit for tau sneutrinos decaying directly to $\ell\ell\tau\tau$ via a dominant $\hat{L}\hat{L}\hat{e}^c$ operator is shown. Assuming BR = 1, a lower bound on the sneutrino mass was obtained through the comparison with the MSSM cross section for pair production of tau sneutrinos. To recast this result we multiplied this cross section by the factor $\mathrm{BR}(\widetilde{\nu}_\tau^{\mathcal{R}} \to \tau\mu) \times \mathrm{BR}(\widetilde{\nu}_\tau^{\mathcal{I}} \to \tau\mu)$ for each of our points. For an average value of $\mathrm{BR}(\widetilde{\nu}_\tau \to \mu\mu) = 0.1$ as we can see in Fig 6.5, the cross section must be multiplied then by a factor of ~ 0.33, lowering the bound on the sneutrino mass from about 90 GeV in the case of trilinear RPV to about 74 GeV in our case (see Fig. 6.7 below). This result turns out to be qualitatively different from the one of Ref. [21], where no bound on the sneutrino mass was obtained from recasting the LEP result. This is due to the simplified assumption made in that work that all neutrino Yukawas have the same value and therefore democratic BRs, implying a smaller value for

the above factor. On the other hand, using Table II of Ref. [21] with the BRs modified appropriately, we have checked that the lack of constraint on the sneutrino mass from the production of a pair of left staus at LEP obtained in that work, is still valid. We have arrived at the same conclusion for LEP mono-photon search and LHC mono-photon and mono-jet searches, taking also into account the most recent results [124,125]. Let us finally remark that the (light- and dark-)blue points correspond to regions where the number of signal events is below 3, and therefore inaccessible. In addition, we have checked that the light-blue points on top of the dark-blue ones are already excluded by the LEP result.

Concerning scan S_2, we can see in Fig 6.5 that the BRs into charged leptons are about two orders of magnitude smaller than for S_1, and therefore following the above discussion we have checked that no points are excluded by LEP results in this case. Note that although these BRs are smaller, still a significant number of points with signal events above 3 can be obtained when M increases because of the larger value of the decay length, which gives rise to a larger vertex-level efficiency.

Figure 6.5 also shows that the sensitivity of the dilepton displaced-vertex searches to $\widetilde{\nu}_\tau$ is limited by their small efficiency for $c\tau \lesssim 1$ mm, especially for the S_1 case. It is, however, worth noticing that we may even probe such a short lifetime region by optimizing the search strategy for the sub-millimeter displaced vertices, as discussed in Refs. [126, 127]. Our result highly motivates a dedicated work for such an optimization, which we defer to another occasion.

As discussed in Section 6.4, the value of Y_{ν_1} is rather large in our scenario, and therefore we expect a sizable branching fraction for the $\widetilde{\nu}_\tau \to ee$ channel. In fact, the ratio of the branching fractions for the $\widetilde{\nu}_\tau \to ee$ and $\widetilde{\nu}_\tau \to \mu\mu$ channels has important implications for our scenario since it reflects the information from the neutrino data via the neutrino Yukawa couplings (see Fig. 6.4). To see this, we plot it against the parameter M in Fig. 6.6. It is found that for the S_1 case, the ratios $R_{\mu/e} \equiv \mathrm{BR}(\widetilde{\nu}_\tau^{\mathcal{R}} \to \mu\mu)/\mathrm{BR}(\widetilde{\nu}_\tau^{\mathcal{R}} \to ee)$ are in the range $3 \lesssim R_{\mu/e} \lesssim 5$, while for the S_2 case they are more widely distributed: $1 \lesssim R_{\mu/e} \lesssim 4.6$. This different behaviour can be understood if we realize that for scan S_1 the second term of $\mathrm{BR}(\widetilde{\nu}_\tau \to \mu\mu)$ in Eq. (6.7) is negligible with respect to the first one, and the same for the corresponding terms of $\mathrm{BR}(\widetilde{\nu}_\tau \to ee)$. Thus, with the approximation in Eq. (6.3) one gets $R_{\mu/e} \approx (Y_{\nu_\mu}/Y_{\nu_e})^2$, which using the results for the neutrino Yukawas in Fig. 6.4 gives rise to the above range around 3.5. However, for scan S_2 the term of $\mathrm{BR}(\widetilde{\nu}_\tau \to ee)$ proportional to $\mathrm{BR}(\widetilde{\nu}_\tau \to \tau\tau)$ is not negligible with respect to the one proportional to $\mathrm{BR}(\widetilde{\nu}_\tau \to \tau e)$, which is much smaller than in scan S_1, due to the

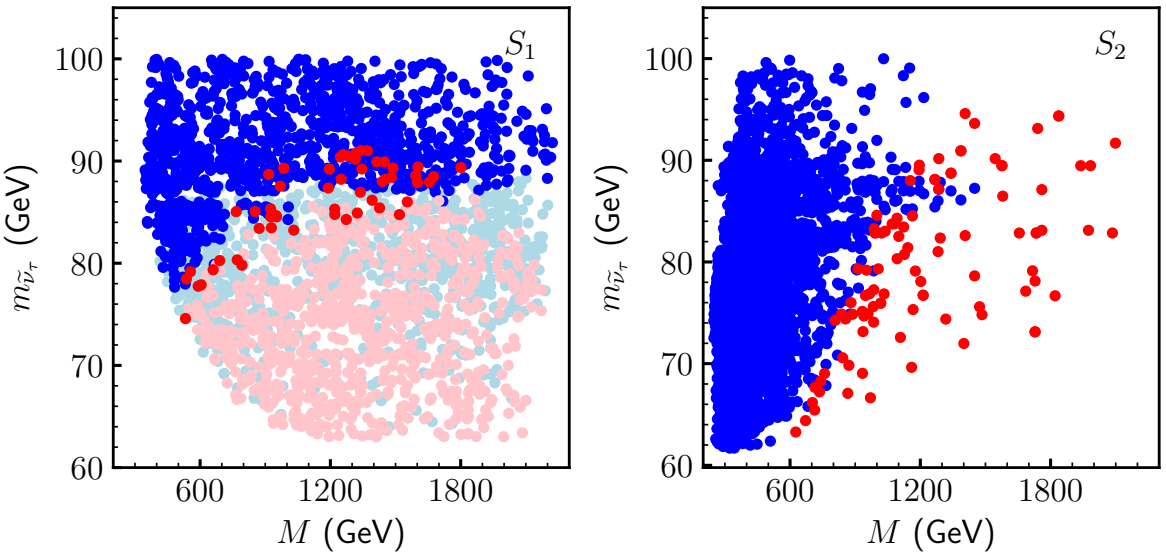

Figure 6.7: Tau left sneutrino LSP mass versus M for scan S_1 (left) and scan S_2 (right). The color code is the same as in Fig. 6.5.

contribution of the first term in Eq. (6.2). This implies that the ratio $R_{\mu/e}$ in scan S_2 can be smaller than in S_1, as can be seen in the figure. Now, if we particularly focus on the parameter points that can be probed at the 13-TeV LHC, the S_2 case predicts $R_{\mu/e} \lesssim 3.6$, and thus we can in principle distinguish this case from the S_1 case by measuring this ratio in the future LHC experiments such as the high-luminosity LHC.

Finally, we show in Fig. 6.7 $m_{\widetilde{\nu}_\tau}$ vs. M. For scan S_1 (left plot), tau left sneutrino masses in the range 74−91 GeV can be probed, corresponding to a gaugino mass parameter M in the range $532-1801$ GeV, i.e. $M_2 \in (363-1228)$ GeV. Clearly, red points appear in these regions because smaller sneutrino masses produce larger decay lengths. Since decay lengths are larger for scan S_2, the range of sneutrino masses that can be probed is also larger than for S_1. In particular, we can see in the right plot that the range of sneutrino masses is $63-95$ GeV. In this scenario, M is in the range $625-2100$ GeV, correspoding to $M_2 \in (427-1431)$ GeV. Let us finally mention that points with sneutrino masses slightly larger than 100 GeV, and with $c\tau > 0.1$ mm, exist, but since they are not constrained by the number of signals events and therefore cannot be probed at the LHC run 3, we do not show them in the figures. In any cases, if we actually detect the $\widetilde{\nu}_\tau$ signal and measure its mass[6] and lifetime in future experiments, we can considerably narrow down the allowed

[6] As discussed in Ref. [21], we can in principle measure the mass of $\widetilde{\nu}_\tau$ by using hadronically decaying tau leptons.

parameter region, which plays an important role in testing the $\mu\nu$SSM.

6.8 Conclusions

In the framework of the $\mu\nu$SSM, where there is RPV and the several decay BRs of the LSP significantly decrease the signals, there is a lack of experimental bounds on the masses of the sparticles. To fill this gap in SUSY searches, it is then crucial to analyze the recent experimental results that can lead to limits on sparticle masses in this model, and the prospects for the searches with a higher energy and luminosity.

With this purpose, we recast the result of the ATLAS 8-TeV displaced dilepton search from long-lived particles [73], to obtain the potential limits on the parameter space of the tau left sneutrino LSP in the $\mu\nu$SSM with a mass in the range $45 - 100$ GeV. A crucial point of the analysis, which differentiates the $\mu\nu$SSM from other SUSY models is that neutrino masses and mixing angles are predicted by the generalized electroweak scale seesaw of the $\mu\nu$SSM once the parameters of the model are fixed. This is obtained at tree level when three generations of right-handed neutrinos are considered. Therefore, the sneutrino couplings have to be chosen so that the neutrino oscillation data are reproduced, which has important implications for the sneutrino decay properties.

The sneutrino LSP is produced via the Z-boson mediated Drell-Yan process or through the W- and γ/Z-mediated process accompanied with the production and decay of the left stau NLSP, as shown in Fig. 6.1. Due to the RPV term present in the $\mu\nu$SSM, the left sneutrino LSP becomes metastable and eventually decays into the SM leptons. Because of the large value of the tau Yukawa coupling, a significant fraction of the sneutrino LSP decays into a pair of tau leptons or a tau lepton and a light charged lepton, while the rest decays into a pair of neutrinos. A tau sneutrino LSP implies in our scenario that the tau neutrino Yukawa is the smallest coupling, driving neutrino physics to dictate that the muon neutrino Yukawa is the largest of the neutrino Yukawas. As a consequence, the most important contribution to the dilepton BRs comes from the channel $\widetilde{\nu}_\tau \to \tau\mu$. It is found then that the decay distance of the left sneutrino tends to be as large as $\gtrsim 1$ mm, which thus can be a good target of displaced vertex searches.

The strategy that we employed to search for these points was the same as in Chapter 5, but in this case performing the two scans of the parameter space related to neutrino/sneutrino physics described in Table 6.1, imposing compatibility with current experimental data on neutrino and Higgs physics, as well as flavor observables.

The final result of our analysis for the 8-TeV case is that no points of the parameter

space of the $\mu\nu$SSM can be probed. This is also true even considering the optimization of the trigger requirements proposed in Ref. [21]. Nevertheless, important regions can be probed at the LHC run 3 with the trigger optimization, as summarized in Fig. 6.7. We in particular emphasize that a trigger optimization for muons has more significant impact on the search ability than that for electrons because of the larger muon neutrino Yukawa coupling in our scenario. Our observation, therefore, suggests that optimizing only the muon trigger already has great benefit. In addition, searching for "sub-millimeter" dilepton displaced vertices is also promising. We thus highly motivate both the ATLAS and CMS collaborations to take account of these options seriously.

If the metastable $\widetilde{\nu}_\tau$ signature is actually found in the future LHC experiments, we may also measure the mass, lifetime, and decay branching fractions of $\widetilde{\nu}_\tau$ through the detailed analysis of this signature. We can then include these physical observables into our scan procedure as well in order to further narrow down the allowed parameter space. For instance, we can distinguish the S_1 and S_2 cases by measuring the ratio $\mathrm{BR}(\widetilde{\nu}_\tau^{\mathcal{R}} \to \mu\mu)/\mathrm{BR}(\widetilde{\nu}_\tau^{\mathcal{R}} \to ee)$ as shown in Fig. 6.6. We can also restrict the parameter M through the measurements of the mass and decay length of $\widetilde{\nu}_\tau$, which allows us to infer the gaugino mass scale and thus gives important implications for future high energy colliders.

Chapter 7

Explaining muon anomalous $(g-2)$ in the $\mu\nu$SSM

In the previous chapters, we have shown that the parameter space of the $\mu\nu$SSM can simultaneously accommodate massive neutrino and reproduce Higgs physics. We have also shown that important part of it can host light electroweak gauginos and left sneutrinos (and sleptons). The presence of these light states can enhance the model contribution to the anomalous magnetic moment of the muon, $a_\mu = (g-2)_\mu/2$. Motivated by this, in this chapter based on our work of Ref. [128], we want to identify the parts of the viable regions of the parameter space that lead to a sizable contribution to a_μ in order to reproduce the measured value.

7.1 Introduction

One of the long standing problems of the SM is the deviation between its prediction and the measured value of the muon anomalous magnetic dipole moment. This discrepancy, $\Delta a_\mu = a_\mu^{\rm exp} - a_\mu^{\rm SM}$, has survived over decades even after improving the theoretical calculations within the SM and performing accurate experimental measurements. The latest value of Δa_μ reported by [96],

$$\Delta a_\mu = 26.8 \pm 6.3 \pm 4.3 \times 10^{-10}\,, \tag{7.1}$$

represents 3.5σ discrepancy between the measured value and the SM prediction and hence could be the manifestation of NP beyond the SM. Also, the muon $g-2$ experiments at Fermilab (E989) [129] and at J-PARC (E34) [130] are planned to reduce the experimental uncertainty of a_μ by a factor of four [131, 132] and this could raise this deviation up to

7.0σ [133] which would be a very strong evidence of NP.

On the one hand, if SUSY is responsible of this deviation, then at least some SUSY particles are expected to be in the vicinity of the electroweak scale, namely, muon left sneutrino, smuon and electroweak gauginos $\widetilde{B}$ and $\widetilde{W}$. On the other hand, the search for SUSY at colliders, inspired by RPC models puts significant bounds on sparticles masses' [96], especially for strongly interacting sparticles whose masses must be above about 1 TeV [106, 107]. Nevertheless, less stringent bounds of about 100 GeV have been obtained for weakly interacting sparticles. Qualitatively similar results have also been obtained in the analysis of simplified RPV scenarios with trilinear lepton- or baryon-number violating terms [19], assuming a single channel available for the decay of the LSP into leptons. However, this assumption is not possible in the $\mu\nu$SSM, where the decay BRs of the LSP can significantly decrease the signals. This means that the extrapolation of the usual bounds on sparticles masses' to the $\mu\nu$SSM is not directly applicable. As a result, very light sparticles are still possible, making the model very interesting for addressing Δa_μ. For instance, we have shown in Chapter 6 that the electroweak gauginos whose masses are controlled by $M_{i=1,2}$, are very important for reproducing neutrino physics in the model and that the left sneutrinos whose masses and couplings are directly connected to neutrino physics, can naturally be light depending on the choice of the parameters. As a consequence, SUSY contributions to a_μ can naturally be sizeable to accommodate Eq. (7.1).

In this Chapter we analyze the parameter space of the $\mu\nu$SSM that reproduces simultaneously neutrino and Higgs physics and explains the discrepancy Δa_μ. To achieve this, we sample the model for Δa_μ using the likelihood method described in Chapter 4 and we focus on the scenarios with light/moderate $\widetilde{\nu}_\mu$, $\widetilde{\mu}$, $\widetilde{B}$ and $\widetilde{W}$.

7.2 SUSY contribution to a_μ in the $\mu\nu$SSM

The contributions to the a_μ in supersymmetric models are known to essentially come from the chargino-sneutrino and neutralino-smuon loops, and have been intensively studied. For example in the case of the MSSM, the one-loop contributions can be found in [134–137] and at two-loop in [138–140]. In the singlet(s) extension(s) of the MSSM, the contribution to a_μ would have same expressions provided that the mixing matrices are appropriately taken into account. Nevertheless, as was pointed out in Ref. [141, 142], the numerical results in these models can differ from the ones in the MSSM. Depending on the parameters of the concerned model, very light neutral scalars (few GeV) can appear

at the bottom of the spectrum and the presence of such very light eigenstates can have an impact on a_μ. This scenario has been also addressed in [143–145] in the context of two-Higgs-doublet-models. Note that light neutralinos with leading singlino composition are possible but their contributions are small, owning to their weak couplings to the MSSM sector.

Concerning the $\mu\nu$SSM, which is a singlets extension of the MSSM, assuming that the singlets scalars and pseudoscalars (as well as singlinos) are heavy, their contributions is very small and the expressions of the SUSY contributions to the a_μ can be translated from the MSSM. It follows that the dominants one-loop contributions to a_μ from the chargino-sneutrino and neutralino-smuon loop, can be respectively appropriated as [134],

$$\Delta a_\mu^C \approx \frac{\alpha_2 m_\mu^2}{4\pi}\frac{\mu M_2 \tan\beta}{m^2_{\widetilde{\nu}_\mu}}\left[\frac{F_C(M_2^2/m^2_{\widetilde{\nu}_\mu}) - F_C(\mu^2/m^2_{\widetilde{\nu}_\mu})}{M_2^2-\mu^2}\right] \tag{7.2}$$

and

$$\Delta a_\mu^N \approx \frac{\alpha_1 m_\mu^2}{4\pi}\frac{\mu M_1 \tan\beta}{(m^2_{\widetilde{\mu}_R} - m^2_{\widetilde{\mu}_L})}\left[\frac{F_N(M_1^2/m^2_{\widetilde{\mu}_R})}{m^2_{\widetilde{\mu}_R}} - \frac{F_N(M_1^2/m^2_{\widetilde{\mu}_L})}{m^2_{\widetilde{\mu}_L}}\right], \tag{7.3}$$

where the loop functions are given by

$$F_C(k) = \frac{3-4k+k^2+2\ln k}{(1+k)^3}, \quad F_N(k) = \frac{-1+k^2-2k\ln k}{(1+k)^3}. \tag{7.4}$$

Notice that m_μ and $m_{\widetilde{\mu}_L}$ ($m_{\widetilde{\mu}_R}$) are muon and left- (right-)handed smuon masses respectively and $\alpha_i = g_i^2/(4\pi)$.

It is well known that the chargino contribution Δa_μ^C is much larger compared with the neutralino contribution Δa_μ^N. Thus, in the following we discuss the Eq. (7.4) in order to draw some important conclusions on the SUSY contributions to a_μ that we will check with our numerical results.

In the light of Eq. (7.1), decreasing the values of M_2, μ or $m_{\widetilde{\nu}_\mu}$ leads to an enhancement in Δa_μ^C. Also, the sign of Δa_μ^C is given by the sign of the product μM_2 since the factor in brackets of Eq. (7.4) is positive in general [136]. In the present work, we assume that M_2 and μ are positive and thus we expect a positive contribution to a_μ. In contrast, the Δa_μ^C increases with increasing $\tan\beta$. Thus, the parameters controlling the SUSY contributions to a_μ in the scenario we consider are

$$M_2,\ \mu,\ m_{\widetilde{\nu}_\mu},\ \tan\beta, \tag{7.5}$$

and they have to be appropriately chosen to satisfy the constraints we impose and to explain the experimental discrepancy of Eq. (7.1). Recall that, from Subsection 3.6.3, the muon left sneutrino mass is mainly determined by T_{ν_2}, Y_{ν_2} and v_2.

To qualitatively understand the behaviour of the dominant contribution to a_μ, we show in Fig. 7.1, Δa_μ^C versus $m_{\widetilde{\nu}_\mu}$ for different values of other relevant parameters. It can be deduced, assuming that the SUSY contributions to muon anomalous magnetic moment is determined by the Eq. (7.2) that, to explain the $\pm 2\sigma$ discrepancy of Eq. (7.1), for $\mu = 380$ GeV and $\tan\beta = 14$, excludes $m_{\widetilde{\nu}_\mu} \gtrsim 600$ (100) GeV corresponding to $M_2 = 150$ (900) GeV. In these regions the contribution to a_μ is too small. Another point to note is that this contribution can become very large for small values of $m_{\widetilde{\nu}_\mu}$ and M_2. Concretely, this scenario corresponds to $M_2 = 150$ GeV and $m_{\widetilde{\nu}_\mu} \lesssim 200$ GeV (blue triangles in the white area above the yellow colored band). We will check these features with the numerical results presented in Section 7.5.

7.3 Sampling the $\mu\nu$SSM for a_μ

In this section we describe the likelihood that we use to search for benchmark points of the parameter space that are compatible with the current experimental data from neutrino and Higgs physics as well as that from the measurement of Δa_μ. To this end, we performed a scan over the parameter space of the model, with the input parameters optimally chosen as will be subsequently discussed in Section 7.4.

For the sampling of the $\mu\nu$SSM, we used the method described in Chapter 4. The goal is to find regions of the parameter space of the $\mu\nu$SSM that are compatible with the discrepancy of Eq. 7.1. For that we have constructed the likelihood,

$$\mathcal{L}_{\rm tot} = \mathcal{L}_{a_\mu} \times \mathcal{L}_{\rm neutrino} \times \mathcal{L}_{\rm Higgs} \times \mathcal{L}_{\rm B\ physics} \times \mathcal{L}_{\mu\ \rm decay} \times \mathcal{L}_{m_{\widetilde{\chi}^\pm}}, \tag{7.6}$$

where different pieces in the right hand side are described in Section 4.4.

7.4 Input parameters

The optimal setup to address the anomalous muon a_μ, is to focus on the scenarios involving light moun left sneutrinos (and smuon) and Wino (Bino). Thus we follow the same strategy for the choice of the parameters as in Chapter 6 but in this case instead of tau left sneutrino as the LSP, we are interested in the muon left sneutrino. Consequently, we scan over T_{ν_2} and fix T_{ν_3}.

Concerning how to get light/moderate $\widetilde{\nu}_\mu$, we have seen from the previous chapters

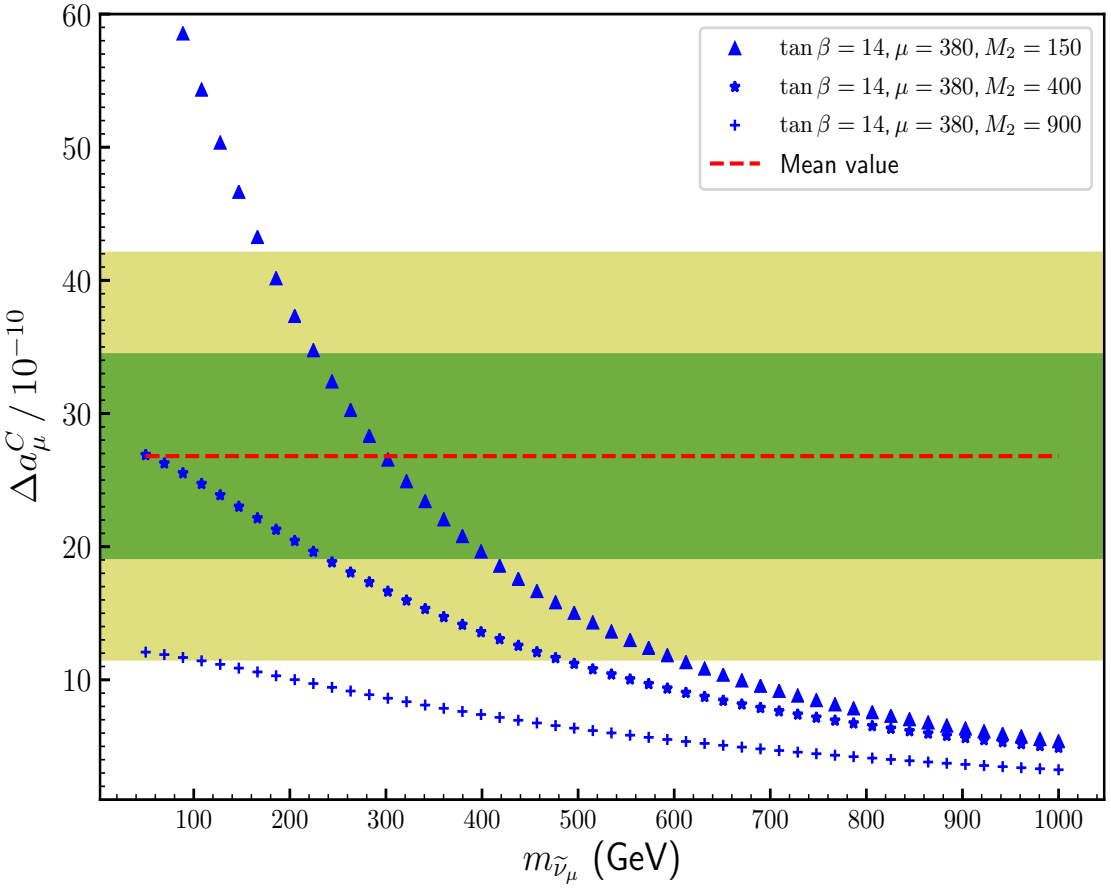

Figure 7.1: Δa_μ^C versus $m_{\widetilde{\nu}_\mu}$ for different values of M_2. The green and yellow bands represent the $\pm 1\sigma$ and $\pm 2\sigma$ regions of Δa_μ respectively and the red dashed line the best fit value. Recall that μ and M_2 are in GeV.

that we have the freedom in the parameter space of the $\mu\nu$SSM. For example, with the assumption that the A_{ν_2} is naturally of the order of the TeV, values of the prefactor of Eq. (3.69) $Y_{\nu_2} v_u / v_2$ in the range of about $0.01 - 1$, i.e. $Y_{\nu_2} \sim 10^{-8} - 10^{-6}$, will give rise to muon left sneutrino mass in the range of about $100 - 1000$ GeV. Thus, with the hierarchy of neutrino $Y_{\nu_2} \sim 10^{-8} - 10^{-7} < Y_{\nu_{1,3}} \sim 10^{-6}$, we can obtain a $\widetilde{\nu}_\mu$ light with a mass around 100 GeV whereas the masses of $\widetilde{\nu}_{e,\tau}$ are of the order of the TeV. Clearly, we are in the case of solutions for neutrino physics of type 3) discussed in Subsection 6.2. It is worth noticing here that in this scenario, the left smuon would be naturally light and this has an interesting implication since light smuon are also relevant for reproducing the anomalous muon magnetic moment. For getting light gauginos, the parameters M_1 and M_2 can be taken as small as of the order of 100 GeV without spoiling neutrino physics depending

on the choice of other parameters of the model. Thus, assuming the GUT inspired low energy relation $M_2 = 2\,M_1$. This also allows to get light Bino although not being so relevant for Δa_μ .

As discussed in Eq. (3.43), the relevant parameters in the neutrino sector of the $\mu\nu$SSM are $\lambda, \kappa, v_R, v_i, Y_{\nu_i}, \tan\beta$ and $M_{1,2}$. Since λ, κ and v_R are crucial for Higgs physics, we fix them to appropriate values. The parameter $\tan\beta$ is also important for both, Higgs and neutrino physics, thus we will consider a narrow range of possible values to ensure good Higgs physics.

Summarizing, we perform a scan over the 9 parameters $Y_{\nu_i}, v_i, T_{\nu_2}, \tan\beta, M_2$, as shown in Table 7.1, using log priors (in logarithmic scale) for all of them, except for $\tan\beta$ which is taken to be a flat prior (in linear scale). The ranges of parameters are same as those in Chapter 6 except for M_2. In the present work, we decrease the upper bound of M_2 to 1000 GeV because we do not expect sizable contribution to a_μ for larger values. The other parameters are same as these of Table 6.2.

Scan (S)
$\tan\beta \in (10, 16)$
$Y_{\nu_i} \in (10^{-8}, 10^{-6})$
$v_i \in (10^{-6}, 10^{-3})$
$-T_{\nu_2} \in (10^{-6}, 10^{-4})$
$M_2 \in (150, 1000)$

Table 7.1: Range of low-energy values of the input parameters that are varied in the two scans, where Y_{ν_i}, v_i, T_{ν_2} and M_2 are log priors while $\tan\beta$ is a flat prior. The VEVs v_i, and the soft parameters T_{ν_3} and M_2, are given in GeV.

7.5 Results

To find regions consistent with experimental observations we have performed about 36 million of spectrum evaluations in total and the total amount of computer required for this was approximately 190 CPU years.

To carry out this analysis, we select points from the scan that lie within $\pm 3\sigma$ of all neutrino physics observables [13] summarized in Table 4.2. Second, we put $\pm 3\sigma$ cuts from $b \to s\gamma$, $B_s \to \mu^+\mu^-$ and $B_d \to \mu^+\mu^-$ and require them to satisfy also the upper limits of $\mu \to e\gamma$ and $\mu \to eee$. In the third step, we impose that Higgs physics is realized. In

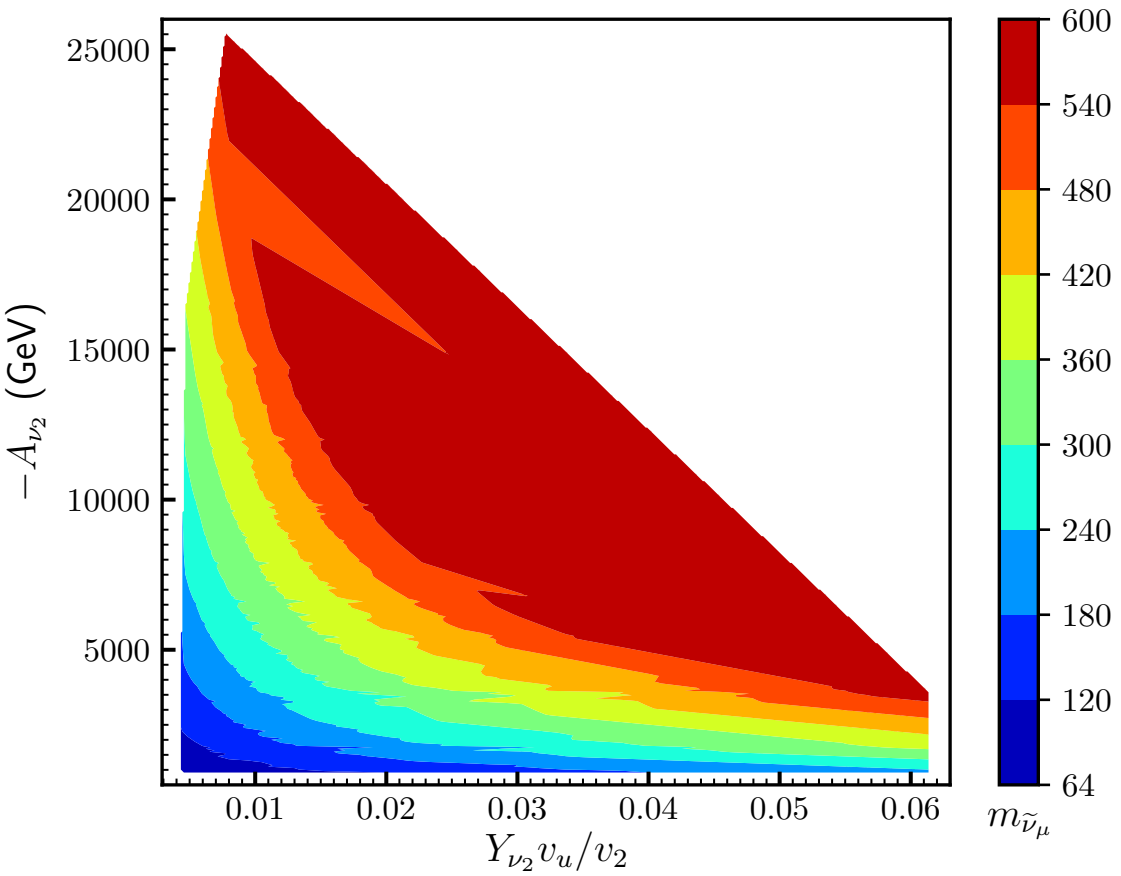

Figure 7.2: $-A_{\nu_2}$ versus $Y_{\nu_2} v_u / v_2$. The colours indicate different values of the muon left sneutrino mass.

particular, we require that the p-value reported by `HiggsSignals` be larger than 5 %. We also check with Vevacious [104] that the EWSB vacua corresponding to the previous allowed points are stable. Finally, since we want to explain the Δa_μ, of the allowed points, we select those within $\pm 2\sigma$ of Δa_μ. The resulting points with this last selection cut are presented in Section 7.5.2.

7.5.1 Constraints from neutrino and light $\tilde{\nu}_\mu$ physics.

Imposing all the cuts discussed above, we show in Fig. 7.2 the values of the parameter A_{ν_2} versus the prefactor in Eq. (3.69), $Y_{\nu_2} v_u / v_2$, giving rise to different values for the mass of the $\tilde{\nu}_\mu$. Let us remark that the plot has been obtained using the full numerical computation including loop corrections, although the tree-level mass in Eq. (3.69) gives a good qualitative idea of the results. In particular, we can see that the allowed range

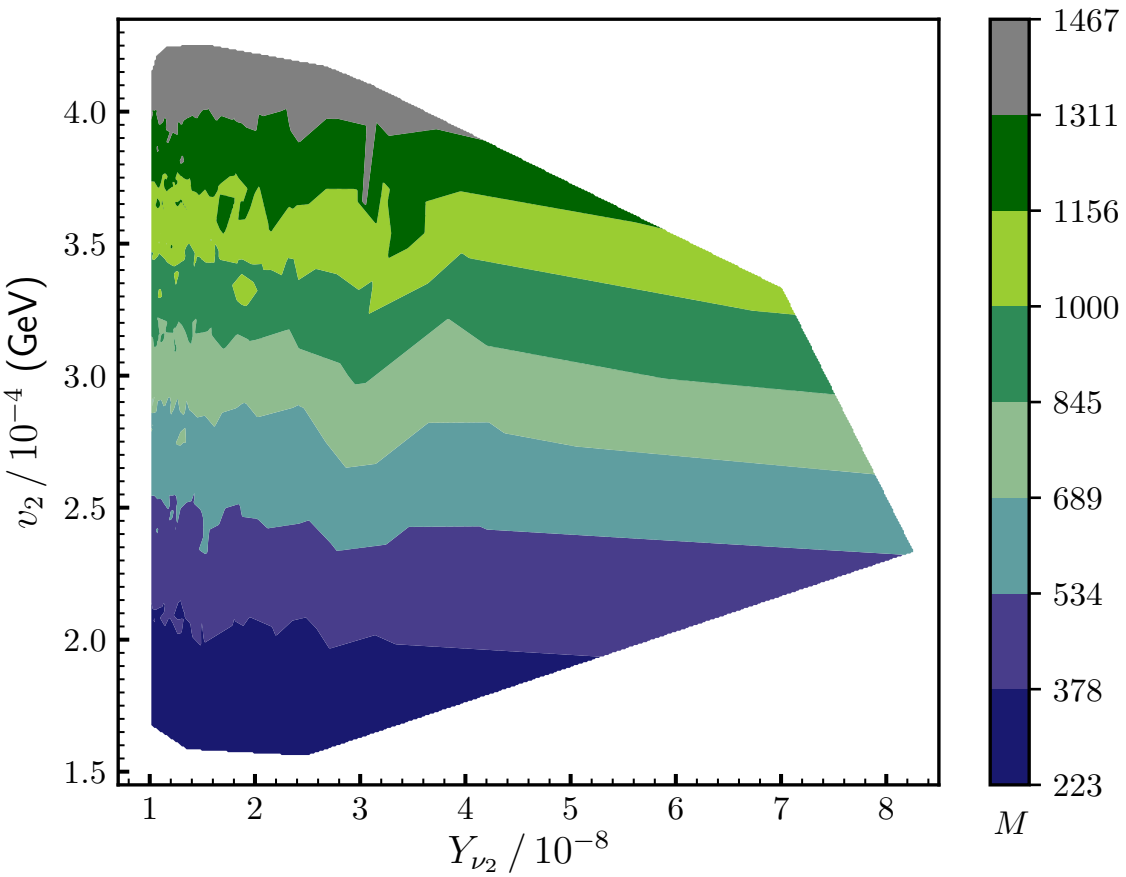

Figure 7.3: v_2 versus Y_{ν_2} for the scan. The colours indicate different values of the gaugino mass parameter M defined in Eq. (3.34).

of $-A_{\nu_2}$ is $861 - 25500$ GeV, corresponding to $-T_{\nu_2}$ in the range $8.8 \times 10^{-6} - 3.8 \times 10^{-4}$ GeV. We can also see, as can be deduced from Eq. (3.69), that for a fixed value of $-A_{\nu_2}$ ($Y_{\nu_2} v_u/v_2$) the greater $Y_{\nu_2} v_u/v_2$ ($-A_{\nu_2}$) is, the greater $m_{\tilde{\nu}_\mu}$ becomes. Let us finally note that $m_{\tilde{\nu}_\mu}$ is always larger than 64 GeV, which corresponds to about half of the mass of the SM-like Higgs. The reason is same as in the case of tau left sneutrino LSP, that is, for smaller masses, the SM-like Higgs would dominantly decay into sneutrino pairs, leading to an inconsistency with Higgs data.

In Fig. 7.3, we show v_2 vs. Y_{ν_2}, with the colours indicating different values of M. There we can see that the greater v_2 is, the greater M becomes. In addition, for a fixed value of v_2, M is quite independent of the variation in Y_{ν_2}. This confirms that, as explained in solution 3) of Subsection 6.2, the gaugino seesaw is the dominant one for the second neutrino family. From the figure, we can see that the range of M reproducing the correct

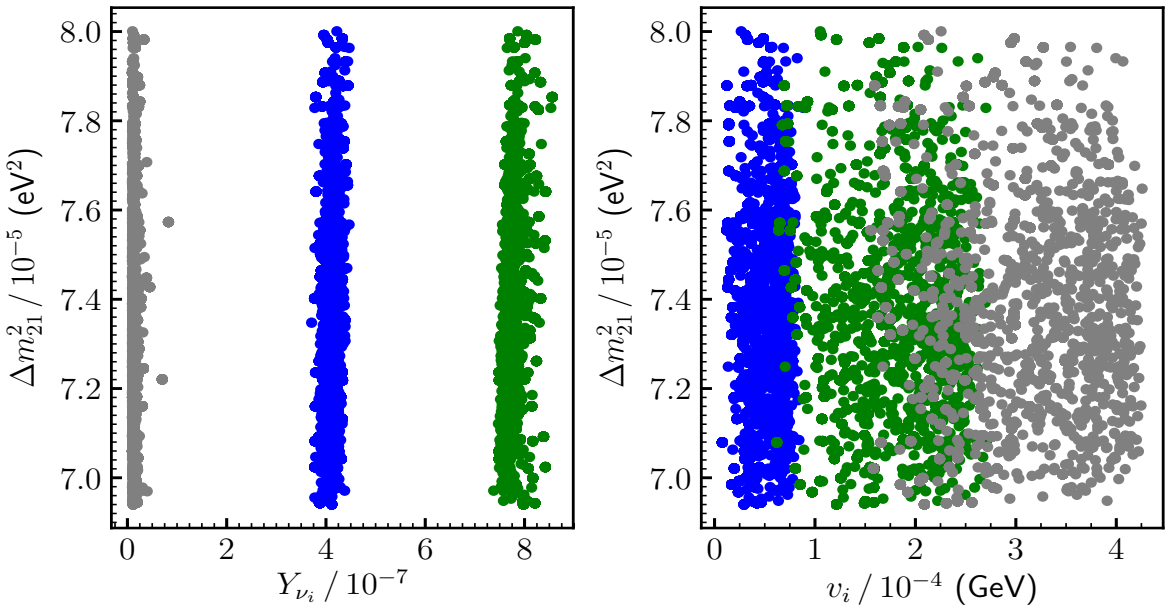

Figure 7.4: Δm^2_{21} versus neutrino Yukawas (left) and left sneutrino VEVs (right). Colors blue, grey and green correspond to $i = 1, 2, 3$, respectively.

neutrino physics is $223 - 1467$ GeV corresponding to M_2 in the range $152 - 1000$ GeV.

The values of Y_{ν_2} and v_2 used in order to obtain a $\widetilde{\nu}_\mu$ light in turn constrain the values of $Y_{\nu_{1,3}}$ and $v_{1,3}$ producing a correct neutrino physics. This is shown in Fig. 7.4, where Δm^2_{21} vs. Y_{ν_i} and v_i is plotted. As we can see, we obtain the hierarchy qualitatively discussed in solution 3) of Subsection 6.2, i.e. $Y_{\nu_2} < Y_{\nu_1} < Y_{\nu_3}$, and $v_1 < v_3 \lesssim v_2$.

Concerning the absolute value of neutrino masses, we obtain $m_{\nu_1} \sim 0.001$ - 0.002 eV, $m_{\nu_2} \sim 0.008$ - 0.009 eV, and $m_{\nu_3} \sim 0.05$ eV, fulfilling the cosmological upper bound on the sum of neutrino masses of 0.12 eV.

7.5.2 Constraints from muon a_μ

Once the neutrino physics has determined the relevant regions of the parameter space of the $\mu\nu$SSM for getting left muon sneutrino mass as light as possible but consistent with Higgs physics, we are ready to analyze the regions of the parameter space that can explain the deviation between the SM prediction and the experimental value of the anomalous magnetic moment of muon.

In our scenario μ is fixed to ≈ 379 GeV, thus, from Eq. (7.2) the parameters that determine the chargino-sneutrino contribution to a_μ are M_2, $m_{\widetilde{\nu}_\mu}$ and $\tan\beta$. In the following we discuss the Δa_μ constraint on these parameters.

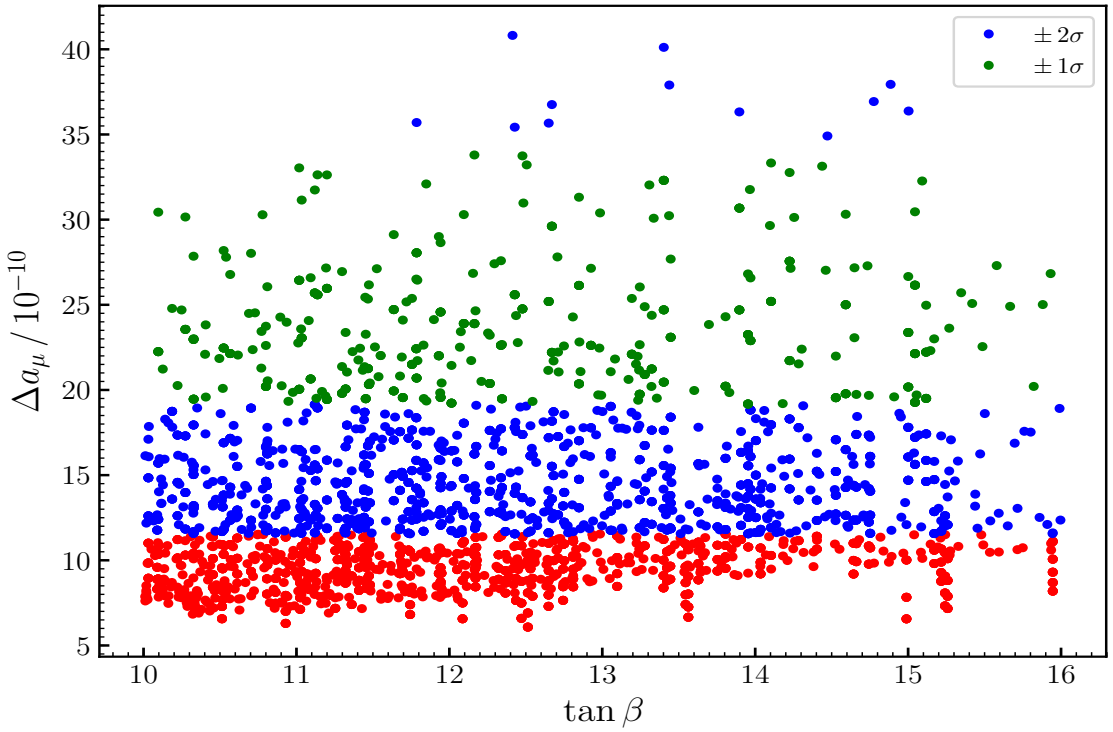

Figure 7.5: Δa_μ versus $\tan\beta$. The green and blue colors represent the 1σ and 2σ on Δa_μ. Notice that the green points are part of the blue points. The red points are not within the 2σ cut on Δa_μ.

We expect $\tan\beta$ to not have notable effects on the SUSY contribution to a_μ considering its narrow range we chose. This is shown in Fig. 7.5 where it can be seen that Δa_μ is independent of $\tan\beta$. However, the effects are expected to be sizable with the variations of M_2 and $m_{\tilde{\nu}_\mu}$ and we discuss them subsequently.

In Figs. 7.6 and 7.7, we show Δa_μ versus M_2 and $m_{\tilde{\nu}_\mu}$ respectively. The white regions in the upper right sides are excluded by the size of the SUSY contribution to a_μ, for increasing $m_{\tilde{\nu}_\mu}$ or M_2 it is hard to get large values for Δa_μ. Being illustrative, on the one hand for $M_2 \sim 200$ (800) GeV, and on the other hand, for $m_{\tilde{\nu}_\mu} \sim 100$ (500) GeV, the contribution to Δa_μ is less about 40 (13). In addition, to explain the $1\,\sigma$ (green) and $2\,\sigma$ (blue) regions of Δa_μ require values smaller than about 520 GeV and 920 GeV for M_2 and below 320 GeV and 540 GeV for $m_{\tilde{\nu}_\mu}$ respectively. In sum, this result agrees with the features of Fig. 7.1 and confirms that in our scenario the approximation of Eq. (7.2) can be qualitatively used to describe the SUSY contribution to a_μ in the $\mu\nu$SSM.

In Fig. 7.8 which can be regarded as the summary plot of the scan, we show $m_{\tilde{\nu}_\mu}$ versus M_2 parameter space. The viable points (green and blue) are classified in three

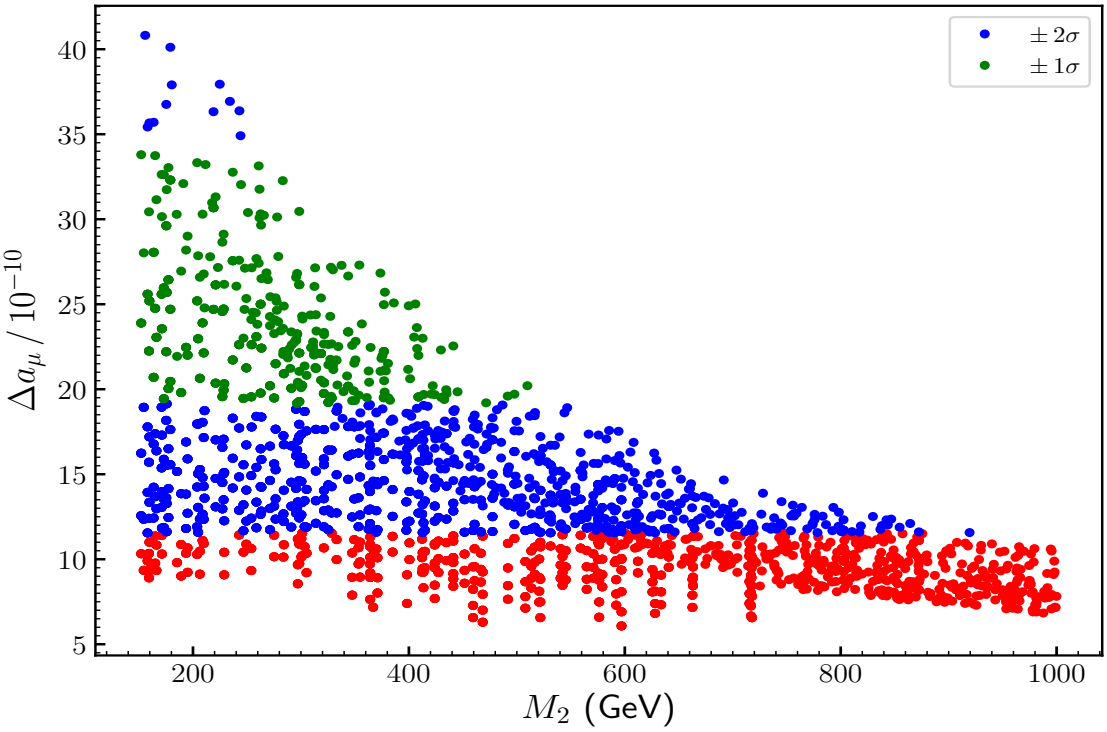

Figure 7.6: Δa_μ versus M_2. The colors are same as in Fig. 7.5.

different categories: the *dot* symbol corresponds to the case where $m_{\widetilde{\nu}_\mu}$ is smaller than the mass of Bino. Notice that $M_2 = 2M_1$ and hence, Bino will always be lighter than Wino. The *plus* symbol represents the case where the $m_{\widetilde{\nu}_\mu}$ is between the mass of Bino and the mass of Wino. The *triangle* represent the case where the left muon sneutrino is heavier than the Wino. This categorization will be important when the constraints from the LHC searches will be taken into account. For instance, the presence of light left muon sneutrino, Bino and Wino of order of 100 GeV and long-lived could be constrained by LHC searches long-lived particles decaying into an oppositely charged lepton pair, $\mu\mu$, ee, or $e\mu$, for example Refs. [73, 146]. But for the moment we focus on the constraint of Δa_μ on the $M_2 - m_{\widetilde{\nu}_\mu}$ parameter space of the $\mu\nu$SSM.

Imposing 2σ on the Δa_μ excludes regions with $M_2 \gtrsim 900$ GeV, for $m_{\widetilde{\nu}_\mu} \sim 65$ GeV and $m_{\widetilde{\nu}_\mu} \gtrsim 550$ GeV for $M_2 \sim 150$ GeV. Notice that, none of the points we found has Δa_μ larger than the 2σ upper bound. Larger SUSY contributions are found for $M_2 \sim 150$ GeV, when left muon sneutrino is as light as 100 GeV. However pushing the lower bound on M_2 to smaller values about 100 GeV would lead to very large Δa_μ.

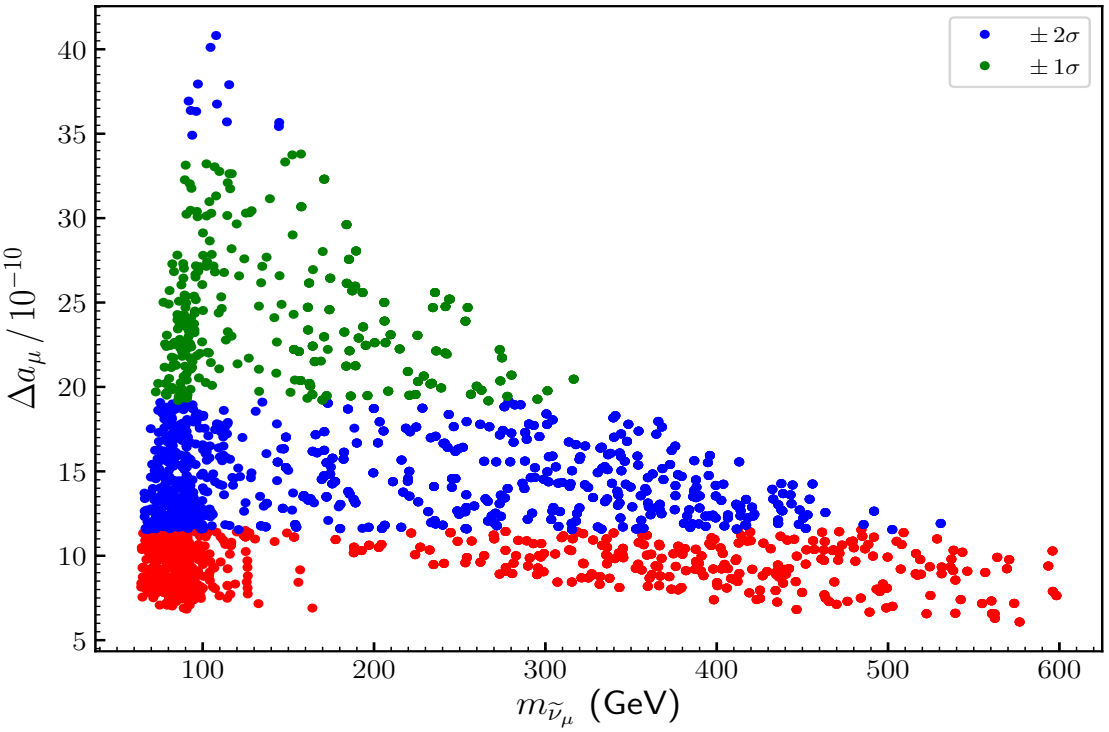

Figure 7.7: Δa_μ versus M_2. The colors are same as in Fig. 7.5.

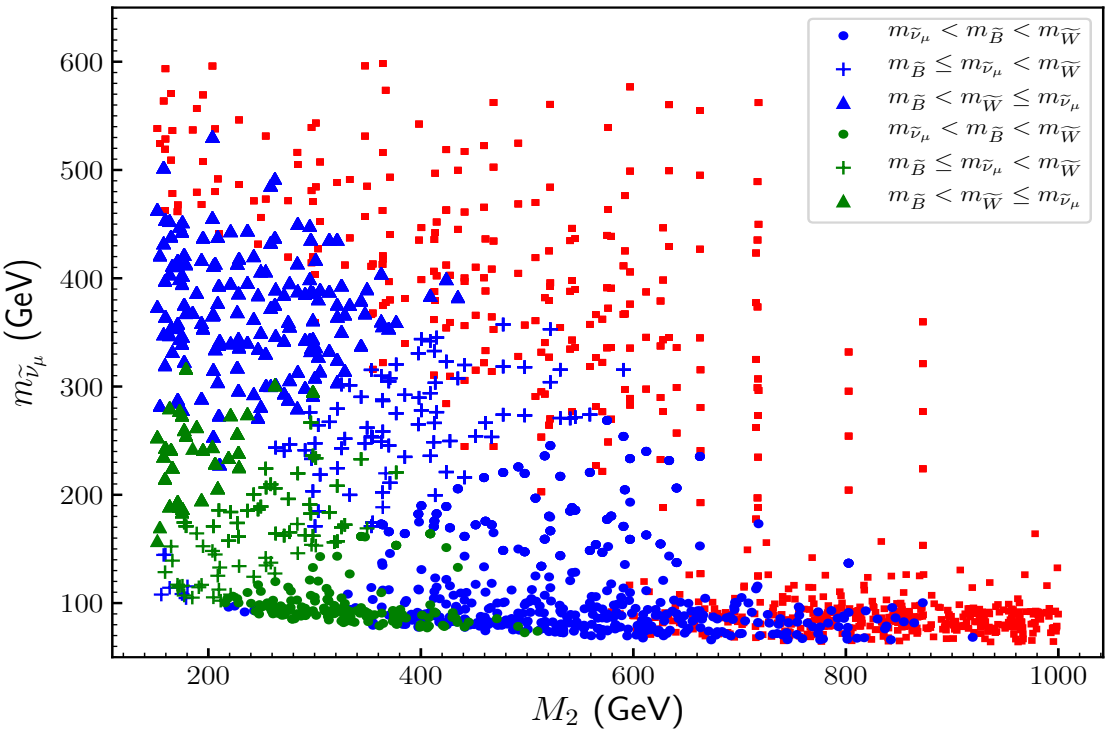

Figure 7.8: $m_{\widetilde{\nu}_\mu}$ versus M_2. The colors are same as in Fig. 7.5. The viable points are classified in three categories: The *dot* symbol corresponds to the case where $m_{\widetilde{\nu}_\mu}$ is smaller than the mass of Bino (M_1). Notice that $M_2 = M_1$. The *plus* symbol represents the case where the $m_{\widetilde{\nu}_\mu}$ is between the mass of Bino and the mass of Wino (M_2). The *triangle* is left for case where the left muon sneutrino is heavier than the Wino.

7.6 Conclusions

We have analyzed within the framework of the $\mu\nu$SSM, the parameter space that can explain the about 3.5σ deviation of the measured value of the anomalous magnetic moment of the muon with respect to the prediction of the SM. Unlike in the RPC SUSY models, like the MSSM, where it seems hard to explain Δa_μ while satisfying the existing experimental bounds on the masses of sparticles, in the $\mu\nu$SSM, with the breaking of the R-parity, these bounds can be relaxed. Besides, the $\mu\nu$SSM can naturally predict light left sneutrinos as well as electroweak gauginos that are consistent with Higgs and neutrino data. In addition, the presence of these light sparticles in the spectrum is known to enhance the supersymmetric contribution to the anomalous magnetic moment of the muon and thus are very important for accommodating the discrepancy between the experimental and the SM values.

In this work, we sampled the $\mu\nu$SSM to reproduce the latest value of Δa_μ given in Eq. (7.1) and to achieve that we focused on the regions of the parameter space that lead to light/moderate electroweak gauginos (Wino and Bino) and muon left sneutrino (and smuon) and at the same time are compatible with the latest Higgs and neutrino data. We found that important regions of the parameter space of the model can easily reproduce Δa_μ. For instance, in our scenario, for $\pm 1\sigma$ of Δa_μ, the allowed ranges for M_2 and $m_{\tilde{\nu}_\mu}$ are respectively $150 - 520$ GeV and $75 - 320$ GeV. Note that, at $\pm 2\sigma$ the upper bounds on these parameters are pushed upwards to around 920 GeV and 540 GeV respectively.

Nevertheless, we are also aware that the LHC searches of electroweakinos could further constrain the allowed regions of our scenario. For instance, the presence of light left muon sneutrino or gaugino of order of 100 GeV could be constrained by LHC searches for long-lived particles decaying into charged leptons, for example, the analyses of Refs. [73, 146]. But in this work, we did not consider yet the potential exclusion power of these searches in our scenario. The next step will be to check whether the allowed regions we found survive with constraints from the colliders searches.

Chapter 8

Conclusiones y perspectivas de futuro/Conclusions and future perspectives

En este capítulo resumimos los principales resultados de esta tesis, en la que hemos analizado a fondo el espacio de parámetros del $\mu\nu$SSM a la luz de los datos experimentales existentes y de las perspectivas de las exploraciones futuras del LHC.

El hecho de que no se haya descubierto todavía nueva física BSM en los colisionadores de partículas, junto con la cantidad creciente de datos experimentales, están poniendo restricciones severas sobre los modelos supersimétricos. Por tanto, son necesarios estudios especializados en el espacio de parámetros de las teorías BSM. En este contexto, en el trabajo empleamos un método muy potente para escanear el espacio de parámetros del $\mu\nu$SSM con el fin de encontrar las regiones que son compatibles con los datos experimentales existentes. Como se explica en el texto, el $\mu\nu$SSM es un modelo supersimétrico bien motivado que de forma natural ofrece una solución al problema μ y al mismo tiempo aborda el origen delas masas y los ángulos de mezclas de los neutrinos. Debido a los nuevos términos introducidos para resolver estos problemas, conteniendo tres familias de supercampos de neutrinos *right-handed*, se produce RPV, con el tamaño de la violación controlada por los pequeños acoplos de Yukawa de los neutrinos. Como consecuencia de esta pequeña RPV y de que el espectro de partículas es mayor, se producen señales nuevas características del modelo tales como estados finales desplazados, multileptones o nuevas canales de decaimiento de las partículas y esto hace que la fenomenología en los colisionadores sea muy rica y diversa.

Tras haber descrito los aspectos teóricos del $\mu\nu$SSM en el Capítulo 3, en el Capítulo 4 presentamos la metodología utilizada en esta tesis para estudiar el espacio de parámetros del modelo y también para buscar escenarios fenomenológicos que puedan ser testados en el funcionamiento actual y futuro del LHC. En concreto, usamos un algoritmo basado en datos y probabilidades llamado `Multinest` para muestrear el $\mu\nu$SSM. Este método nos permitió llevar a cabo escaneos en diferentes subconjuntos del espacio de parámetros y derivar aquellos que están de acuerdo con una clase de datos dada. Para el cálculo del espectro usamos `SARAH` para generar una versión `SPheno` de nuestro modelo. Posteriormente, conectamos SPheno con MultiNest. Es de destacar, que para encontrar regiones consistentes con las observaciones experimentales en todos los estudios realizados en esta tesis, hemos llevado a cabo alrededor de 268 millones de evaluaciones de espectro en total. La cantidad total de tiempo de computación requerida para esto fue de aproximadamente 1680 años de CPU.

En el Capítulo 5, que está basado en nuestro trabajo de la Ref. [98], hemos aplicado este método para escanear el sector Higgs del $\mu\nu$SSM. Hemos analizado minuciosamente las regiones del espacio de parámetros a la luz de los datos crecientes sobre las propiedades del bosón de Higgs del SM. Para llevar a cabo este estudio de manera eficiente, optimizamos el tiempo y los recursos de computación identificando, en primero lugar, los parámetros más relevantes que determinan la física del Higgs del $\mu\nu$SSM. Para restringir las predicciones del sector de Higgs extendido, donde los dobletes de Higgs se mezclan con los sneutrinos, hemos conectado `HiggsBounds` con Multinest y para saber si un determinado escalar del $\mu\nu$SSM está de acuerdo con las señales observadas por ATLAS y CMS, también hemos conectado `HiggsSignals` con Multinest. Además, exigimos la compatibilidad con observables tales como los decaimientos del B y del muon. En este marco, hemos realizado los tres escaneos $S_{1,2,3}$ descritos en la Tabla 5.1, que están determinados por el rango de los acoplos λ que mezclan Higgses y *right sneutrinos*. En concreto, hemos considerado $\lambda \in (0.01,\, 0.2)$, $(0.2,\, 0.5)$ y $(0.5,\, 1.2)$. No imponemos de partida perturbatividad hasta la escala GUT y por eso permitimos valores de λ mayores de 0.4. Tampoco imponemos perturbatividad hasta la escala GUT a los acoplamientos κ entre los *right sneutrinos*, considerando por lo tanto el rango $\kappa \in (0.01,\, 2)$. Los resultados se resumen en las Figs. 5.4, 5.8 y 5.12 para los tres escans. Claramente, encontramos soluciones viables en casi todo el plano $\kappa - \lambda$ con la excepción del escan S_3 en la Fig. 5.12, que está más restringido. Esto se debe a los valores grandes de $\lambda \in (0.5,\, 1.2)$ que pueden dar lugar a taquiones originados en la mezcla entre los dos dobletes de Higgs.

Hemos obtenido por tanto que el espacio de parámetros de nuestro modelo contiene muchas soluciones viables, incluyendo también muchas posibilidades fenomenológicas distintas. Por ejemplo, hay soluciones en las que el Higgs del SM es el escalar más ligero (puntos rojos y rojos claro en las figuras), pero también soluciones donde no lo es (puntos azules y azules claro). En este último caso, es incluso posible tener los otros escalares (tipo singlete) con masas $\lesssim m_{\rm Higgs}/2$. Además, también encontramos soluciones en las que varios escalares están degenerados con masas cercanas a 125 GeV y pueden tener sus señales superpuestas contribuyendo a la resonancia observada a 125 GeV.

Dados estos resultados, es importante estudiar en detalle en el futuro la fenomenología en colisionadores de las soluciones encontradas. En concreto, el impacto de los nuevos estados, no solo los *right sneutrinos* sino también los *left sneutrinos*, y los neutralinos que contienen los *right-handed neutrinos*. Las nuevas señales asociadas a ellos pueden verificar si el $\mu\nu$SSM es el modelo supersimétrico adecuado.

En el Capítulo 6, que está basado en nuestro trabajo de la Ref. [57], primero señalamos que en el marco del $\mu\nu$SSM, donde hay RPV y la existencia de varios BRs de decaimiento de la LSP disminuyen significativamente las señales, no hay básicamente límites experimentales sobre las masas de las partículas supersimétricas. Para llenar este vacío en las búsquedas de SUSY, es crucial analizar los resultados experimentales recientes que puedan conducir a límites en las masas de las partículas SUSY en nuestro modelo, así como las perspectivas para las búsquedas con energía y luminosidad más grandes.

Con este propósito, hemos reutilizado el resultado de la búsqueda de ATLAS a 8 TeV de dileptones desplazados debidos a partículas de vidas medias grandes [73], para obtener los límites potenciales en el espacio de parámetros del *sneutrino tauónico left* como LSP en el $\mu\nu$SSM, con la masa en el rango $45 - 100$ GeV. Un punto crucial del análisis, que diferencia al $\mu\nu$SSM de otros modelos SUSY, es que las masas y los ángulos de mezclas de los neutrinos se pueden predecir debido al *seesaw* generalizado a la escala EW del $\mu\nu$SSM, una vez se fijan los parámetros del modelo. Esto se obtiene a *nivel árbol* cuando se consideran tres generaciones de *neutrinos rigt-handed*. Por lo tanto, los acoplos de los sneutrinos deben ser elegidos de forma que los datos de las oscilaciones de los neutrinos se reproduzcan, lo cual tiene implicaciones importantes para las propiedades de decaimiento del sneutrino.

El sneutrino LSP se produce a través del proceso Drell-Yan mediado por el bosón Z, o a través del proceso mediado por W y γ/Z acompañado con la producción y decaimiento del *left stau* NLSP, como se muestra en la Fig. 6.1. Debido al término RPV presente en el

$\mu\nu$SSM, el *left sneutrino* LSP es metaestable y eventualmente decae en leptones del SM. Debido al valor grande del acoplo de Yukawa del lepton tau, una fracción significativa del sneutrino LSP decae en un par de leptones tau o un leptón tau y un leptón ligero, mientras que el resto decae en un par de neutrinos. El *left sneutrino* LSP implica en nuestro escenario que el Yukawa del neutrino tauónico es el acoplo más pequeño, llevando a la física de neutrinos a dictar que el Yukawa del neutrino muónico es el más grande de los Yukawas de los neutrinos. Como consecuencia, la contribución más importante a los BRs de dileptones proviene del canal $\widetilde{\nu}_\tau \to \tau\mu$. Se encuentra entonces que la longitud de decaimiento del *left sneutrino* tiende a ser tan grande como $\gtrsim 1$ mm, lo que puede ser un buen objetivo para las búsquedas de vértices desplazados. Para estimar la sensibilidad de este análisis, las muestras de eventos simulados se generaron usando `MadGraph` y `PYTHIA`.

La estrategia que hemos empleado para buscar estos puntos ha sido la misma que en el Capítulo 5, pero en este caso realizando los dos escaneos $S_{1,2}$ del espacio de parámetros relacionados con la física de neutrinos/sneutrinos descritos en la Table 6.1, y requiriendo la compatibilidad con los datos experimentales actuales sobre la física de neutrinos y de Higgs, así como con los observables de sabor.

El resultado final de nuestro análisis para el caso de 8 TeV es que, en nuestro escenario, no se puede testar ningún punto del espacio de parámetros del $\mu\nu$SSM. Esto también se cumple incluso si se considera la optimización de los requisitos del *trigger* propuesta en la Ref. [21]. Sin embargo, regiones importantes pueden ser testadas en el *run 3* del LHC con la optimización del *trigger*, como se resume en la Fig. 6.7. En concreto, enfatizamos que una optimización del *trigger* de muones tiene un mayor impacto en la capacidad de búsqueda que la del de electrones, debido al mayor tamaño del acoplo de Yukawa del neutrino muónico en nuestro escenario. Nuestra observación, por lo tanto, sugiere que optimizar sólo el *trigger* de muones es ya muy beneficioso. Además, la búsqueda de vértices de dileptones desplazados del orden del sub-milímetro es también prometedora. Por tanto, consideramos que hemos motivado fuertemente a las colaboraciones ATLAS y CMS para que tengan en cuenta seriamente estas opciones.

Si se encuentra la señal del $\widetilde{\nu}_\tau$ metaestable en los futuros experimentos del LHC, también se podría medir la masa, la vida media y las BRs de decaimiento del $\widetilde{\nu}_\tau$ a través del análisis detallado de la misma. Entonces, podemos incluir estos observables físicos en nuestro procedimiento de escaneo también para reducir aún más el espacio de parámetros permitido. Por ejemplo, podemos distinguir entre los casos S_1 y S_2 midiendo la relación $\mathrm{BR}(\widetilde{\nu}_\tau^{\mathcal{R}} \to \mu\mu)/\mathrm{BR}(\widetilde{\nu}_\tau^{\mathcal{R}} \to ee)$ como se muestra en la Fig. 6.6. También podemos restringir

el parámetro M de los gauginos a través de las mediciones de la masa y la longitud de decaimiento del $\widetilde{\nu}_\tau$, lo que nos permite inferir la escala de masa del gaugino y, por lo tanto, da lugar a importantes implicaciones para futuros colisionadores de particulas.

En el capítulo Chapter 7, que está basado en nuestro trabajo de la Ref. [128], analizamos las regiones del espacio de parámetros del $\mu\nu$SSM que satisfacen a las físicas del Higgs y de los neutrinos y que explican uno de los rompecabezas más antiguos y desafiantes del SM, la discrepancia a 3.5σ entre la predicción del SM y el valor medido experimentalmente del momento magnético anómalo del muón. La presencia de partículas supersimétricas ligeras como los *left sneutrinos* y los gauginos en el $\mu\nu$SSM, que aún son viables a pesar de las restricciones de los datos experimentales y que potencialmente pueden escapar a una clase de búsquedas del LHC, hacen que el modelo sea muy interesante en este sentido. Hemos encontrado que regiones importantes del espacio de parámetros del modelo pueden explicar fácilmente esta discrepancia. Los resultados de nuestro escenario indican que, a 1σ, se espera que el parámetro M_2 y la masa del muón *left sneutrino* sean respectivamente sobre de $150-520$ GeV y $65-320$ GeV. En 2σ, los límites superiores son empujados hacia arriba a alrededor de 920 GeV y 540 GeV respectivamente. Esto tiene una implicación muy importante para las búsquedas en los colisionadores en el futuro. Si esta desviación persiste en el futuro, entonces la predicción del $\mu\nu$SSM puede ser usada para determinar la masa del muón *left sneutrino* y reducir la escala de masa para un descubrimiento potencial de particulas supersimétricas asociadas a los bosones del SM.

Debemos ser también conscientes de que las búsquedas del LHC de *electroweakinos* podrían acotar también las regiones permitidas de nuestro escenario. Las perspectivas de futuro para nuestro análisis son tener en cuenta las búsquedas en el LHC de partículas de vidas medias grandes que decaen a leptones cargados para limitar aún más las actuales regiones viables del $\mu\nu$SSM que hemos encontrado.

Por último, cabe resaltar que los estudios realizados en esta tesis abren nuevos caminos para muchos otros trabajos interesantes en el futuro. Varios de ellos ya han sido sugeridos en la discusión anterior. Claramente, el sector escalar neutro del $\mu\nu$SSM ofrece escenarios ricos y muy variados, tales como varios Higgses contribuyendo a la señal observada, de forma que un estudio exhaustivo de los mismos en el futuro será necesario. Otro ejemplo es el reanálisis de las búsquedas del LHC de partículas de vida media grande. Hemos demostrado que es muy útil para testar el $\mu\nu$SSM. Por tanto, análisis similares para otras partículas SUSY como LSPs, tales como *stops*, *right sleptons*, etc., constituyen un nuevo paso interesante para restringir el espacio de parámetros del $\mu\nu$SSM. Por todo lo

anterior, podemos decir que la metodología empleada en esta tesis es una herramienta muy poderosa para estudiar no sólo el espacio de parámetros del $\mu\nu$SSM, sino también para futuras investigaciones de otras teorías BSM.

Conclusions and future perspectives

In this chapter, we summarize the main results of this thesis, in which we have thoroughly analyzed the parameter space of the $\mu\nu$SSM in the light of current data and the prospects for explorations at future runs of the LHC.

The lack of discovery of new physics BSM at particles colliders together with the increasingly amount of experimental data, are putting severe constraints on supersymmetric models. Therefore, dedicated analyses of the parameter space of theories BSM are becoming necessary. In this context, we employed a powerful approach to scan the parameter space of the $\mu\nu$SSM in order to find the regions that are compatible with given existing experimental data. As explained in the text, the $\mu\nu$SSM is a well motivated supersymmetric model that naturally offers a solution to the μ problem and simultaneously addresses the origin of non-zero masses and mixing angles for neutrinos. Due to the new terms introduced to solve these challenges, containing three families of right-handed neutrino superfields, there is RPV with the amount of violation controlled by the small Yukawa couplings for neutrinos. As a consequence of this small RPV and the enlarged particle spectrum, novel signatures such as displaced final states, multileptons, or new decay chains for particles are characteristic of the model, and this renders the collider phenomenology very rich and diverse.

After describing the theoretical aspects of the $\mu\nu$SSM in Chapter 3, in Chapter 4 we presented the methodology used in this thesis to study the parameter space of this model, and also to look for phenomenological scenarios that can be probed in the current and future runs of the LHC. In particular, we used a likelihood data-driven method algorithm based on `Multinest` to sample the $\mu\nu$SSM. This method allowed us to perform scans on subsets of the parameter space and to derive those that are in agreement with a given class of data. For the computation of the spectrum, we used `SARAH` to generate a `SPheno` version for our model. Then, we interface SPheno with MultiNest. It is worth noticing here, that to find regions consistent with experimental observations for all the studies carried out in this thesis, we had to perform about 268 million of spectrum evaluations in total, and the total amount of computer required for this was approximately 1680 CPU

years.

In Chapter 5, which is based on our work of Ref. [98], we applied this method to scan the Higgs sector of the $\mu\nu$SSM. We thoroughly analyzed the regions of the parameter space in the light of the increasing data about the properties of the SM-like Higgs boson. To efficiently conduct this study, we optimized the computing time and resources by first identifying the most relevant parameters that determine the Higgs physics of the $\mu\nu$SSM. For constraining the predictions of the extended Higgs sector, where the Higgs doublets are mixed with the sneutrinos, we interfaced `HiggsBounds` with Multinest, and to address whether a given Higgs scalar of the $\mu\nu$SSM is in agreement with the signals observed by ATLAS and CMS, we also interfaced `HiggsSignals` with Multinest. In addition, we demanded the compatibility with observables such as B and μ decays. In this framework, we performed the three scans $S_{1,2,3}$ described in Table 5.1, which are determined by the range of λ couplings mixing Higgses and right sneutrinos. In particular, we considered $\lambda \in$ (0.01, 0.2), (0.2, 0.5), and (0.5, 1.2). Perturbativity up to the GUT scale is not imposed, and that is why we allow λ values larger than 0.4. Neither we imposed perturbativity up to the GUT scale for κ couplings among right sneutrinos, considering therefore the range $\kappa \in (0.01, 2)$. The results are summarized in Figs. 5.4, 5.8, and 5.12 for the three scans. Clearly, we find viable solutions in almost the entire $\kappa - \lambda$ plane with the exception of the scan S_3 in Fig. 5.12, which is more constrained. This is due to the large values of $\lambda \in$ (0.5, 1.2) that can give rise to tachyons originated in the mixing between the two Higgs doublets.

We have, therefore, obtained that the parameter space of our model contains many viable solutions, including also many different phenomenological possibilities. For example, there are solutions where the SM-like Higgs is the lightest scalar (red and light-red points in the figures), but also solutions where it is not (blue and light-blue points). In the latter case, it is even possible to have the other (singlet-like) scalars with masses $\lesssim m_{\rm Higgs}/2$. In addition, we also find solutions where several scalars are degenerated with masses close to 125 GeV, and can have their signal rates superimposed contributing to the resonance observed at 125 GeV.

Given these results, it is then important to study in detail in the future the collider phenomenology of the solutions found. In particular, the impact of the new states, not only the right but also the left sneutrinos, and the neutralinos containing right-handed neutrinos. Novel signals associated to them might check whether the $\mu\nu$SSM is the adequate SUSY model.

In Chapter 6, which is based on our work of Ref. [57], we pointed out first that in the framework of the $\mu\nu$SSM, where there is RPV and the several decay BRs of the LSP significantly decrease the signals, there is a lack of experimental bounds on the masses of the sparticles. To fill this gap in SUSY searches, it is then crucial to analyze the recent experimental results that can lead to limits on sparticle masses in this model, and the prospects for the searches with a higher energy and luminosity.

With this purpose, we recast the result of the ATLAS 8-TeV displaced dilepton search from long-lived particles [73], to obtain the potential limits on the parameter space of the tau left sneutrino LSP in the $\mu\nu$SSM with a mass in the range $45 - 100$ GeV. A crucial point of the analysis, which differentiates the $\mu\nu$SSM from other SUSY models, is that neutrino masses and mixing angles are predicted by the generalized electroweak scale seesaw of the $\mu\nu$SSM once the parameters of the model are fixed. This is obtained at tree level when three generations of right-handed neutrinos are considered. Therefore, the sneutrino couplings have to be chosen so that the neutrino oscillation data are reproduced, which has important implications for the sneutrino decay properties.

The sneutrino LSP is produced via the Z-boson mediated Drell-Yan process or through the W- and γ/Z-mediated process accompanied with the production and decay of the left stau NLSP, as shown in Fig. 6.1. Due to the RPV term present in the $\mu\nu$SSM, the left sneutrino LSP becomes metastable and eventually decays into the SM leptons. Because of the large value of the tau Yukawa coupling, a significant fraction of the sneutrino LSP decays into a pair of tau leptons or a tau lepton and a light charged lepton, while the rest decays into a pair of neutrinos. A tau sneutrino LSP implies in our scenario that the tau neutrino Yukawa is the smallest coupling, driving neutrino physics to dictate that the muon neutrino Yukawa is the largest of the neutrino Yukawas. As a consequence, the most important contribution to the dilepton BRs comes from the channel $\widetilde{\nu}_\tau \to \tau\mu$. It is found then that the decay distance of the left sneutrino tends to be as large as $\gtrsim 1$ mm, which thus can be a good target of displaced vertex searches. To estimate the sensitivity of this analysis, samples of simulated events were generated using `MadGraph` and `PYTHIA`.

The strategy that we employed to search for these points was the same as in Chapter 5, but in this case performing the two scans $S_{1,2}$ of the parameter space related to neutrino/sneutrino physics described in Table 6.1, imposing compatibility with current experimental data on neutrino and Higgs physics, as well as flavor observables.

The final result of our analysis for the 8-TeV case is that no points of the parameter space of the $\mu\nu$SSM can be probed. This is also true even considering the optimization

of the trigger requirements proposed in Ref. [21]. Nevertheless, important regions can be probed at the LHC run 3 with the trigger optimization, as summarized in Fig. 6.7. We in particular emphasize that a trigger optimization for muons has more significant impact on the search ability than that for electrons because of the larger muon neutrino Yukawa coupling in our scenario. Our observation, therefore, suggests that optimizing only the muon trigger already has great benefit. In addition, searching for "sub-millimeter" dilepton displaced vertices is also promising. We thus highly motivate both the ATLAS and CMS collaborations to take account of these options seriously.

If the metastable $\widetilde{\nu}_\tau$ signature is actually found in the future LHC experiments, we may also measure the mass, lifetime, and $\widetilde{\nu}_\tau$ decay BRs through the detailed analysis of this signature. We can then include these physical observables into our scan procedure as well in order to further narrow down the allowed parameter space. For instance, we can distinguish the S_1 and S_2 cases by measuring the ratio $\mathrm{BR}(\widetilde{\nu}_\tau^{\mathcal{R}} \to \mu\mu)/\mathrm{BR}(\widetilde{\nu}_\tau^{\mathcal{R}} \to ee)$ as shown in Fig. 6.6. We can also restrict the gaugino parameter M through the measurements of the mass and decay length of $\widetilde{\nu}_\tau$, which allows us to infer the gaugino mass scale and thus gives important implications for future high energy colliders.

In Chapter 7, which is based on our work of Ref. [128], we analyzed the regions of the parameter space of the $\mu\nu$SSM that satisfy Higgs and neutrino physics and explain one of the long standing and challenging puzzles of the SM, the 3.5σ discrepancy between the SM prediction and the experimental measured value of the anomalous magnetic moment of the muon. The presence of light supersymmetric particles such as the left sneutrinos and electroweak gauginos in the $\mu\nu$SSM, that still survive despite the strong constraints from the neutrino and Higgs data and that potentially can escape a class of the LHC searches, make the model very suitable in this regard. We found that important regions of the parameter space of the model can easily explain this discrepancy. The results of our scenario indicate that, at 1σ, the parameter M_2 and the mass of the muon left sneutrino are expected to be respectively in the range $150 - 520$ GeV and $65 - 320$ GeV. At 2σ, the upper bounds are pushed upwards to around 920 GeV and 540 GeV respectively. This has important implications for future colliders searches. If this deviation persists in the future, then the prediction of the $\mu\nu$SSM can be used for pinning down the mass of the muon left sneutrino and narrowing down the mass scale for a potential discovery of electroweak supersymmetric partners of the SM gauge bosons.

We were also aware that the LHC searches of electroweakinos could further constrain the allowed regions of our scenario. The future prospects for our analysis is to take into

account the LHC searches for long-lived particles decaying into charged leptons to further constrain the current viable regions of the $\mu\nu$SSM that we found.

Let us finally remark that the studies carried out in this thesis open up new pathways for many other interesting works for the future. Several of them have already been suggested above. Clearly, the neutral scalar sector of the $\mu\nu$SSM offers rich and a variety of scenarios, such as several Higgses contributing to the observed signal, and a thorough study of them in future will be necessary. Another example is the recasting of LHC searches for long-lived particles. It has shown up to be very useful for probing the $\mu\nu$SSM. Thus, similar analyses for other SUSY particles as LSPs such as stops, right sleptons, etc., constitute an interesting next step for constraining the parameter space of the $\mu\nu$SSM. Because of all this, we can say that the methodology employed in this thesis is a very powerful tool for studying not only the parameter space of the $\mu\nu$SSM, but also for future investigations of other theories BSM.

Appendix A

Mass Matrices

We review below the tree-level mass matrices generated in the $\mu\nu$SSM. Upon EWSB, fields with the same color, electric charge and spin mix. To name them we follow the convention of using for the eigenstates the names of detected particles: Higgs, neutrinos, leptons. In what follows we use i, j, k, l, m, n as family indexes, and a, b as the indices for the physical states (mass eigenstates). Note that we are using here the summation convention on repeated indices.

A.1 Scalar Mass Matrices

The scalar mass matrices generated in the $\mu\nu$SSM were computed in Appendix A.1 of Ref. [50] with the assumption of CP conservation for simplicity. In this Appendix, we write those equations and replace the values of the soft masses obtained through the minimization conditions in Eqs. (3.14)-(3.17), assuming that slepton soft mass matrices are diagonal in flavor space.

A.1.1 Mass Matrix for Higgses

Higgses mix with left and right sneutrinos. In the basis $S^T = (H_d^{\mathcal{R}}, H_u^{\mathcal{R}}, \tilde{\nu}_{iR}^{\mathcal{R}}, \tilde{\nu}_{jL}^{\mathcal{R}})$, one obtains the following mass terms for scalar Higgses in the Lagrangian:

$$-\frac{1}{2} S^T m_h^2 S \,, \tag{A.1}$$

where m_h^2 is the 8×8 (symmetric) matrix obtained computing the second derivative of the scalar potential of Eq. (3.5) with respect to the fields

$$m_h^2 = \begin{pmatrix} m^2_{H_d^{\mathcal{R}} H_d^{\mathcal{R}}} & m^2_{H_d^{\mathcal{R}} H_u^{\mathcal{R}}} & m^2_{H_d^{\mathcal{R}} \widetilde{\nu}_{jR}^{\mathcal{R}}} & m^2_{H_d^{\mathcal{R}} \widetilde{\nu}_{jL}^{\mathcal{R}}} \\ m^2_{H_u^{\mathcal{R}} H_d^{\mathcal{R}}} & m^2_{H_u^{\mathcal{R}} H_u^{\mathcal{R}}} & m^2_{H_u^{\mathcal{R}} \widetilde{\nu}_{jR}^{\mathcal{R}}} & m^2_{H_u^{\mathcal{R}} \widetilde{\nu}_{jL}^{\mathcal{R}}} \\ m_{\widetilde{\nu}_{iR}^{\mathcal{R}} H_d^{\mathcal{R}}} & m_{\widetilde{\nu}_{iR}^{\mathcal{R}} H_u^{\mathcal{R}}} & m^2_{\widetilde{\nu}_{iR}^{\mathcal{R}} \widetilde{\nu}_{jR}^{\mathcal{R}}} & m^2_{\widetilde{\nu}_{iR}^{\mathcal{R}} \widetilde{\nu}_{jL}^{\mathcal{R}}} \\ m^2_{\widetilde{\nu}_{iL}^{\mathcal{R}} H_d^{\mathcal{R}}} & m^2_{\widetilde{\nu}_{iL}^{\mathcal{R}} H_u^{\mathcal{R}}} & m^2_{\widetilde{\nu}_{iL}^{\mathcal{R}} \widetilde{\nu}_{jR}^{\mathcal{R}}} & m^2_{\widetilde{\nu}_{iL}^{\mathcal{R}} \widetilde{\nu}_{jL}^{\mathcal{R}}} \end{pmatrix} , \tag{A.2}$$

$$\begin{aligned} m^2_{H_d^{\mathcal{R}} H_d^{\mathcal{R}}} &= m^2_{H_d} + \frac{1}{8}(g^2+g'^2)(3v_d^2 - v_u^2 + v_{iL}v_{iL}) + \frac{1}{2}\lambda_i\lambda_j v_{iR}v_{jR} + \frac{1}{2}\lambda_i\lambda_i v_u^2 \\ &= \frac{1}{4}(g^2+g'^2)v_d^2 + v_{iR}\tan\beta\left(\frac{1}{\sqrt{2}}T_{\lambda_i} + \frac{1}{2}\lambda_j\kappa_{ijk}v_{kR}\right) + Y_{\nu_{ij}}\frac{v_{iL}}{2v_d}\left(\lambda_k v_{jR}v_{kR} + \lambda_j v_u^2\right) \end{aligned} \tag{A.3}$$

$$\begin{aligned} m^2_{H_u^{\mathcal{R}} H_u^{\mathcal{R}}} &= m^2_{H_u} + \frac{1}{8}(g^2+g'^2)(-v_d^2 + 3v_u^2 - v_{iL}v_{iL}) + \frac{1}{2}\lambda_i\lambda_j v_{iR}v_{jR} + \frac{1}{2}\lambda_i\lambda_i v_d^2 \\ &\quad -Y_{\nu_{ij}}\lambda_j v_d v_{iL} + \frac{1}{2}Y_{\nu_{ik}}Y_{\nu_{ij}}v_{jR}v_{kR} + \frac{1}{2}Y_{\nu_{ik}}Y_{\nu_{jk}}v_{iL}v_{jL} \\ &= \frac{1}{4}(g^2+g'^2)v_u^2 + v_{iR}\frac{1}{\tan\beta}\left(\frac{1}{\sqrt{2}}T_{\lambda_i} + \frac{1}{2}\lambda_j\kappa_{ijk}v_{kR}\right) \\ &\quad -\frac{v_{iL}}{v_u}\left(\frac{1}{\sqrt{2}}T_{\nu_{ij}}v_{jR} + \frac{1}{2}Y_{\nu_{ij}}\kappa_{ljk}v_{lR}v_{kR}\right) , \end{aligned} \tag{A.4}$$

$$m^2_{H_u^{\mathcal{R}} H_d^{\mathcal{R}}} = -\frac{1}{4}(g^2+g'^2)v_d v_u - \frac{1}{\sqrt{2}}T_{\lambda_i}v_{iR} - \frac{1}{2}\lambda_k\kappa_{ijk}v_{iR}v_{jR} + v_d v_u\lambda_i\lambda_i - Y_{\nu_{ij}}\lambda_j v_u v_{iL} , \tag{A.5}$$

$$m^2_{\widetilde{\nu}_{iR}^{\mathcal{R}} H_d^{\mathcal{R}}} = -\frac{1}{\sqrt{2}}T_{\lambda_i}v_u - \lambda_k\kappa_{ijk}v_u v_{jR} + \lambda_i\lambda_j v_d v_{jR} - \frac{1}{2}Y_{\nu_{ji}}\lambda_k v_{jL}v_{kR} - \frac{1}{2}Y_{\nu_{jk}}\lambda_i v_{jL}v_{kR} , \tag{A.6}$$

$$m^2_{\widetilde{\nu}_{iR}^{\mathcal{R}} H_u^{\mathcal{R}}} = -\frac{1}{\sqrt{2}}T_{\lambda_i}v_d + \frac{1}{\sqrt{2}}T_{\nu_{ji}}v_{jL} - \lambda_k\kappa_{ilk}v_d v_{lR} + \lambda_i\lambda_j v_u v_{jR} + Y_{\nu_{jk}}\kappa_{ilk}v_{jL}v_{lR} + Y_{\nu_{jk}}Y_{\nu_{ji}}v_u v_{kR} \tag{A.7}$$

$$\begin{aligned} m^2_{\widetilde{\nu}_{iR}^{\mathcal{R}} \widetilde{\nu}_{jR}^{\mathcal{R}}} &= \left(m^2_{\widetilde{\nu}_R}\right)_{ij} + \sqrt{2}T_{\kappa_{ijk}}v_{kR} - \lambda_k\kappa_{ijk}v_d v_u + \kappa_{ijk}\kappa_{lmk}v_{lR}v_{mR} + 2\kappa_{ilk}\kappa_{jmk}v_{lR}v_{mR} \\ &\quad +\frac{1}{2}\lambda_i\lambda_j(v_d^2+v_u^2) + Y_{\nu lk}\kappa_{ijk}v_u v_{lL} - \frac{1}{2}(Y_{\nu_{kj}}\lambda_i + Y_{\nu_{ki}}\lambda_j)v_d v_{kL} + \frac{1}{2}Y_{\nu_{ki}}Y_{\nu_{kj}}v_u^2 + \frac{1}{2}Y_{\nu_{ki}}Y_{\nu_{lj}}v_{kL}v_{lL} \\ &= \sqrt{2}T_{\kappa_{ijk}}v_{kR} - \lambda_k\kappa_{ijk}v_d v_u + \kappa_{ijk}\kappa_{lmk}v_{lR}v_{mR} + 2\kappa_{ilk}\kappa_{jmk}v_{lR}v_{mR} + \frac{1}{2}\lambda_i\lambda_j(v_d^2+v_u^2) \\ &\quad -Y_{\nu lk}\kappa_{ijk}v_u v_{lL} - \frac{1}{2}\left(Y_{\nu_{kj}}\lambda_i + Y_{\nu_{ki}}\lambda_j\right)v_d v_{kL} + \frac{1}{2}Y_{\nu_{ki}}Y_{\nu_{kj}}v_u^2 + \frac{1}{2}Y^{\nu}_{li}Y_{\nu_{kj}}v_{kL}v_{lL} \\ &\quad +\frac{\delta_{ij}}{v_{jR}}\left[-\frac{1}{\sqrt{2}}T_{\nu_{ki}}v_{kL}v_u + \frac{1}{\sqrt{2}}T_{\lambda_i}v_u v_d - \frac{1}{\sqrt{2}}T^{\kappa}_{ilk}v_{lR}v_{kR} + \lambda_l\kappa_{ilk}v_d v_u v_{kR}\right. \\ &\quad -\kappa_{lim}\kappa_{lnk}v_{mR}v_{nR}v_{kR} - \frac{1}{2}\lambda_i\lambda_l(v_d^2+v_u^2)v_{lR} - Y_{\nu lk}\kappa_{ikm}v_u v_{lL}v_{mR} \\ &\quad \left.+\frac{1}{2}\left(Y^{\nu}_{kl}\lambda_i + Y_{\nu_{ki}}\lambda_l\right)v_d v_{kL}v_{lR} - \frac{1}{2}Y_{\nu_{ki}}Y^{\nu}_{kl}v_u^2 v_{lR} - \frac{1}{2}Y_{\nu_{ki}}Y^{\nu}_{lm}v_{kL}v_{lL}v_{mR}\right] , \end{aligned} \tag{A.8}$$

$$m^2_{\widetilde{\nu}^{\mathcal{R}}_{iL} H^{\mathcal{R}}_d} = \frac{1}{4}(g^2+g'^2)v_d v_{iL} - \frac{1}{2}Y_{\nu_{ij}}\lambda_j v_u^2 - \frac{1}{2}Y_{\nu_{ij}}\lambda_k v_{kR} v_{jR}\,, \tag{A.9}$$

$$m^2_{\widetilde{\nu}^{\mathcal{R}}_{iL} H^{\mathcal{R}}_u} = -\frac{1}{4}(g^2+g'^2)v_u v_{iL} + \frac{1}{\sqrt{2}}T_{\nu_{ij}} v_{jR} + \frac{1}{2}Y_{\nu_{ik}}\kappa_{ljk} v_{lR} v_{jR} - Y_{\nu_{ij}}\lambda_j v_d v_u + Y_{\nu_{ij}} Y_{\nu_{kj}} v_u v_{kL}, \tag{A.10}$$

$$\begin{aligned} m^2_{\widetilde{\nu}^{\mathcal{R}}_{iL}\widetilde{\nu}^{\mathcal{R}}_{jR}} &= \frac{1}{\sqrt{2}}T_{\nu_{ij}} v_u - \frac{1}{2}Y_{\nu_{ij}}\lambda_k v_d v_{kR} - \frac{1}{2}Y_{\nu_{ik}}\lambda_j v_d v_{kR} + Y_{\nu_{ik}}\kappa_{jlk} v_u v_{lR} + \frac{1}{2}Y_{\nu_{ij}} Y_{\nu_{kl}} v_{kL} v_{lR} \\ &\quad + \frac{1}{2}Y_{\nu_{il}} Y_{\nu_{kj}} v_{kL} v_{lR}\,, \end{aligned} \tag{A.11}$$

$$\begin{aligned} m^2_{\widetilde{\nu}^{\mathcal{R}}_{iL}\widetilde{\nu}^{\mathcal{R}}_{jL}} &= \left(m^2_{\widetilde{L}_L}\right)_{ij} + \frac{1}{4}(g^2+g'^2)v_{iL}v_{jL} + \frac{1}{8}(g^2+g'^2)(v_{kL}v_{kL} + v_d^2 - v_u^2)\delta_{ij} \\ &\quad + \frac{1}{2}Y_{\nu_{ik}} Y_{\nu_{jk}} v_u^2 + \frac{1}{2}Y_{\nu_{ik}} Y^{\nu}_{jl} v_{kR} v_{lR} \\ &= \frac{1}{4}(g^2+g'^2)v_{iL}v_{jL} + \frac{1}{2}Y_{\nu_{ik}} Y_{\nu_{jk}} v_u^2 + \frac{1}{2}Y_{\nu_{ik}} Y^{\nu}_{jl} v_{kR} v_{lR} + \frac{\delta_{ij}}{v_{jL}}\left[-\frac{1}{\sqrt{2}}T_{\nu_{ik}} v_u v_{kR}\right. \\ &\quad \left. + \frac{1}{2}Y_{\nu_{ik}}\left(\lambda_l v_d v_{kR} v_{lR} + \lambda_k v_d v_u^2 - \kappa_{klm} v_u v_{lR} v_{mR} - Y_{\nu_{mk}} v_{mL} v_u^2 - Y_{\nu_{ml}} v_{mL} v_{lR} v_{kR}\right)\right]. \end{aligned} \tag{A.12}$$

This matrix is diagonalized by an orthogonal matrix Z^H:

$$Z^H m_h^2 \; {Z^H}^T = \left(m_h^2\right)^{\text{dia}}\,, \tag{A.13}$$

with

$$S = {Z^H}^T h\,, \tag{A.14}$$

where the 8 entries of the matrix h are the 'Higgs' mass eigenstate fields. In particular,

$$H_d^{\mathcal{R}} = Z^H_{b1} h_b\,, \quad H_u^{\mathcal{R}} = Z^H_{b2} h_b\,, \quad \tilde{\nu}_{iR}^{\mathcal{R}} = Z^H_{bi} h_b\,, \quad \tilde{\nu}_{jL}^{\mathcal{R}} = Z^H_{bj} h_b\,. \tag{A.15}$$

A.1.2 Mass Matrix for Pseudoscalar Higgses

Following similar arguments as above, in the basis $P^T = (H_d^{\mathcal{I}}, H_u^{\mathcal{I}}, \tilde{\nu}_{iR}^{\mathcal{I}}, \tilde{\nu}_{jL}^{\mathcal{I}})$, one obtains the following mass terms for pseudoscalar Higgses in the Lagrangian:

$$-\frac{1}{2}P^T m^2_{A^0} P\,, \tag{A.16}$$

where $m^2_{A^0}$ is the 8×8 (symmetric) matrix

$$m^2_{A^0} = \begin{pmatrix} m^2_{H_d^{\mathcal{I}} H_d^{\mathcal{I}}} & m^2_{H_d^{\mathcal{I}} H_u^{\mathcal{I}}} & m^2_{H_d^{\mathcal{I}} \widetilde{\nu}^{\mathcal{I}}_{jR}} & m^2_{H_d^{\mathcal{I}} \widetilde{\nu}^{\mathcal{I}}_{jL}} \\ m^2_{H_u^{\mathcal{I}} H_d^{\mathcal{I}}} & m^2_{H_u^{\mathcal{I}} H_u^{\mathcal{I}}} & m^2_{H_u^{\mathcal{I}} \widetilde{\nu}^{\mathcal{I}}_{jR}} & m^2_{H_u^{\mathcal{I}} \widetilde{\nu}^{\mathcal{I}}_{jL}} \\ m_{\widetilde{\nu}^{\mathcal{I}}_{iR} H_d^{\mathcal{I}}} & m_{\widetilde{\nu}^{\mathcal{I}}_{iR} H_u^{\mathcal{I}}} & m^2_{\widetilde{\nu}^{\mathcal{I}}_{iR} \widetilde{\nu}^{\mathcal{I}}_{jR}} & m^2_{\widetilde{\nu}^{\mathcal{I}}_{iR} \widetilde{\nu}^{\mathcal{I}}_{jL}} \\ m^2_{\widetilde{\nu}^{\mathcal{I}}_{iL} H_d^{\mathcal{I}}} & m^2_{\widetilde{\nu}^{\mathcal{I}}_{iL} H_u^{\mathcal{I}}} & m^2_{\widetilde{\nu}^{\mathcal{I}}_{iL} \widetilde{\nu}^{\mathcal{I}}_{jR}} & m^2_{\widetilde{\nu}^{\mathcal{I}}_{iL} \widetilde{\nu}^{\mathcal{I}}_{jL}} \end{pmatrix} , \tag{A.17}$$

$$m^2_{H_d^{\mathcal{I}} H_d^{\mathcal{I}}} = m^2_{H_d^{\mathcal{R}} H_d^{\mathcal{R}}} - \frac{1}{4}(g^2 + g'^2) v_d^2 \tag{A.18}$$

$$m^2_{H_u^{\mathcal{I}} H_u^{\mathcal{I}}} = m^2_{H_u^{\mathcal{R}} H_u^{\mathcal{R}}} - \frac{1}{4}(g^2 + g'^2) v_u^2 \ , \tag{A.19}$$

$$m^2_{H_u^{\mathcal{I}} H_d^{\mathcal{I}}} = \frac{1}{\sqrt{2}} T_{\lambda_i} v_{iR} + \frac{1}{2} \lambda_k \kappa_{ijk} v_{iR} v_{jR} \ , \tag{A.20}$$

$$m^2_{\widetilde{\nu}^{\mathcal{I}}_{iR} H_d^{\mathcal{I}}} = \frac{1}{\sqrt{2}} T_{\lambda_i} v_u - \lambda_k \kappa_{ijk} v_u v_{jR} - \frac{1}{2} Y_{\nu_{ji}} \lambda_k v_{jL} v_{kR} + \frac{1}{2} Y_{\nu_{jk}} \lambda_i v_{jL} v_{kR} \ , \tag{A.21}$$

$$m^2_{\widetilde{\nu}^{\mathcal{I}}_{iR} H_u^{\mathcal{I}}} = \frac{1}{\sqrt{2}} T_{\lambda_i} v_d - \frac{1}{\sqrt{2}} T_{\nu_{ji}} v_{jL} - \lambda_k \kappa_{ilk} v_d v_{lR} + Y_{\nu_{jk}} \kappa_{ilk} v_{jL} v_{lR} \ , \tag{A.22}$$

$$m^2_{\widetilde{\nu}^{\mathcal{I}}_{iR} \widetilde{\nu}^{\mathcal{I}}_{jR}} = m^2_{\widetilde{\nu}^{\mathcal{R}}_{iR} \widetilde{\nu}^{\mathcal{R}}_{jR}} - 2 \left(\sqrt{2} T_{\kappa_{ijk}} v_{kR} - \lambda_k \kappa_{ijk} v_d v_u + \kappa_{ijk} \kappa_{lmk} v_{lR} v_{mR} \right) \ , \tag{A.23}$$

$$m^2_{\widetilde{\nu}^{\mathcal{I}}_{iL} H_d^{\mathcal{I}}} = -\frac{1}{2} Y_{\nu_{ij}} \lambda_j v_u^2 - \frac{1}{2} Y_{\nu_{ij}} \lambda_k v_{kR} v_{jR} \ , \tag{A.24}$$

$$m^2_{\widetilde{\nu}^{\mathcal{I}}_{iL} H_u^{\mathcal{I}}} = -\frac{1}{\sqrt{2}} T_{\nu_{ij}} v_{jR} - \frac{1}{2} Y_{\nu_{ik}} \kappa_{ljk} v_{lR} v_{jR} \ , \tag{A.25}$$

$$\begin{aligned} m^2_{\widetilde{\nu}^{\mathcal{I}}_{iL} \widetilde{\nu}^{\mathcal{I}}_{jR}} = & -\frac{1}{\sqrt{2}} T_{\nu_{ij}} v_u + \frac{1}{2} Y_{\nu_{ij}} \lambda_k v_d v_{kR} - \frac{1}{2} Y_{\nu_{ik}} \lambda_j v_d v_{kR} + Y_{\nu_{il}} \kappa_{jlk} v_u v_{kR} \\ & - \frac{1}{2} Y_{\nu_{ij}} Y_{\nu_{lk}} v_{lL} v_{kR} + \frac{1}{2} Y_{\nu_{ik}} Y_{\nu_{lj}} v_{lL} v_{kR} \ , \end{aligned} \tag{A.26}$$

$$m^2_{\widetilde{\nu}^{\mathcal{I}}_{iL} \widetilde{\nu}^{\mathcal{I}}_{jL}} = m^2_{\widetilde{\nu}^{\mathcal{R}}_{iL} \widetilde{\nu}^{\mathcal{R}}_{jL}} - \frac{1}{4}(g^2 + g'^2) v_{iL} v_{jL} \ , \tag{A.27}$$

and, in order to simplify some of these formulas, the entries of the mass matrix for Higgses are used when appropriate. The matrix of Eq. (A.17) is diagonalized by an orthogonal matrix Z^A:

$$Z^A m^2_{A^0} \ {Z^A}^T = \left(m^2_{A^0} \right)^{\text{dia}} \ , \tag{A.28}$$

with

$$P = Z^{A^T} A^0 \,, \tag{A.29}$$

where the 8 entries of the matrix A^0 are the 'pseudoscalar Higgs' mass eigenstate fields. In particular,

$$H_d^{\mathcal{I}} = Z^A_{b1} h_b \,, \quad H_u^{\mathcal{I}} = Z^A_{b2} h_b \,, \quad \tilde{\nu}_{iR}^{\mathcal{I}} = Z^A_{bi} h_b \,, \quad \tilde{\nu}_{jL}^{\mathcal{I}} = Z^A_{bj} h_b \,. \tag{A.30}$$

A.1.3 Mass Matrix for Charged Higgses

Charged Higgses mix with left and right sleptons. In the basis $C^T = (H_d^{-*}, H_u^+, \widetilde{e}^*_{iL}, \widetilde{e}^*_{jR})$, one obtains the following mass terms in the Lagrangian:

$$- C^{*T} m^2_{H^+} C \,, \tag{A.31}$$

where $m^2_{H^+}$ is the 8×8 (symmetric) matrix

$$m^2_{H^+} = \begin{pmatrix} m^2_{H_d^- H_d^{-*}} & m^2_{H_d^- H_u^+} & m^2_{H_d^- \widetilde{e}^*_{jL}} & m^2_{H_d^- \widetilde{e}^*_{jR}} \\ m^2_{H_u^{+*} H_d^{-*}} & m^2_{H_u^{+*} H_u^+} & m^2_{H_u^{+*} \widetilde{e}^*_{jL}} & m^2_{H_u^{+*} \widetilde{e}^*_{jR}} \\ m^2_{\widetilde{e}_{iL} H_d^{-*}} & m^2_{\widetilde{e}_{iL} H_u^+} & m^2_{\widetilde{e}_{iL} \widetilde{e}^*_{jL}} & m^2_{\widetilde{e}_{iL} \widetilde{e}^*_{jR}} \\ m^2_{\widetilde{e}_{iR} H_d^{-*}} & m^2_{\widetilde{e}_{iR} H_u^+} & m^2_{\widetilde{e}_{iR} \widetilde{e}^*_{jL}} & m^2_{\widetilde{e}_{iR} \widetilde{e}^*_{jR}} \end{pmatrix} , \tag{A.32}$$

$$m^2_{H_d^- H_d^{-*}} = m^2_{H_d^{\mathcal{R}} H_d^{\mathcal{R}}} - \frac{1}{4}(g^2 + g'^2) v_d^2 + \frac{g^2}{4}(v_u^2 - v_{iL} v_{iL}) - \frac{1}{2}\lambda_i \lambda_j v_u^2 + \frac{1}{2} Y_{e_{ik}} Y_{e_{jk}} v_{iL} v_{jL} \,, \tag{A.33}$$

$$\begin{aligned} m^2_{H_u^{+*} H_u^+} &= m^2_{H_u^{\mathcal{R}} H_u^{\mathcal{R}}} - \frac{1}{4}(g^2 + g'^2) v_u^2 + \frac{g^2}{4}(v_d^2 + v_{iL} v_{iL}) - \frac{1}{2}\lambda_i \lambda_i v_d^2 + Y_{\nu_{ij}} \lambda_j v_d v_{iL} \\ &\quad - \frac{1}{2} Y_{\nu_{ik}} Y_{\nu_{jk}} v_{iL} v_{jL} \,, \end{aligned} \tag{A.34}$$

$$m^2_{H_u^{+*} H_d^{-*}} = \frac{g^2}{4} v_d v_u + \frac{1}{\sqrt{2}} T_{\lambda_i} v_{iR} + \frac{1}{2} \lambda_k \kappa_{ijk} v_{iR} v_{jR} - \frac{1}{2} \lambda_i \lambda_i v_d v_u + \frac{1}{2} Y_{\nu_{ij}} \lambda_j v_u v_{iL} \,, \tag{A.35}$$

$$m^2_{\widetilde{e}_{iL} H_d^{-*}} = \frac{g^2}{4} v_d v_{iL} - \frac{1}{2} Y_{\nu_{ij}} \lambda_k v_{kR} v_{jR} - \frac{1}{2} Y_{e_{ij}} Y_{e_{kj}} v_d v_{kL} \,, \tag{A.36}$$

$$m^2_{\widetilde{e}_{iL} H_u^+} = \frac{g^2}{4} v_u v_{iL} - \frac{1}{\sqrt{2}} T_{\nu_{ij}} v_{jR} - \frac{1}{2} Y_{\nu_{ij}} \kappa_{ljk} v_{lR} v_{kR} + \frac{1}{2} Y_{\nu_{ij}} \lambda_j v_d v_u - \frac{1}{2} Y_{\nu_{ik}} Y_{\nu_{kj}} v_u v_{jL} \,, \tag{A.37}$$

$$m^2_{\widetilde{e}_{iR}H_d^{-*}} = -\frac{1}{\sqrt{2}}T_{e_{ji}}v_{jL} - \frac{1}{2}Y_{e_{ki}}Y_{\nu_{kj}}v_u v_{jR} \,, \tag{A.38}$$

$$m^2_{\widetilde{e}_{iR}H_u^{+}} = -\frac{1}{2}Y_{e_{ki}}(\lambda_j v_{kL}v_{jR} + Y_{\nu_{kj}}v_d v_{jR}) \,, \tag{A.39}$$

$$m^2_{\widetilde{e}_{iL}\widetilde{e}^*_{jR}} = \frac{1}{\sqrt{2}}T_{e_{ij}}v_d - \frac{1}{2}Y_{e_{ij}}\lambda_k v_u v_{kR} \,, \tag{A.40}$$

$$m^2_{\widetilde{e}_{iR}\widetilde{e}^*_{jR}} = \left(m^2_{\widetilde{e}_R}\right)_{ij} + \frac{g'^2}{4}(v_u^2 - v_d^2 - v_{kL}v_{kL})\delta_{ij} + \frac{1}{2}Y_{e_{ki}}Y_{e_{kj}}v_d^2 \,, \tag{A.41}$$

$$\begin{aligned} m^2_{\widetilde{e}_{iL}\widetilde{e}^*_{jL}} = {} & m^2_{\widetilde{\nu}^{\mathcal{R}}_{iL}\widetilde{\nu}^{\mathcal{R}}_{jL}} - \frac{1}{4}(g^2+g'^2)v_{iL}v_{jL} + \frac{g^2}{4}(v_u^2 - v_d^2 - v_{kL}v_{kL})\delta_{ij} + \frac{g^2}{4}v_{iL}v_{jL} \\ & -\frac{1}{2}Y_{\nu_{ik}}Y_{\nu_{jk}}v_u^2 + \frac{1}{2}Y_{e_{il}}Y_{e_{jl}}v_d^2 \,, \end{aligned} \tag{A.42}$$

and, in order to simplify some of these formulas, the entries of the mass matrix for Higgses are used when appropriate. Matrix of Eq. (A.32) is diagonalized by an orthogonal matrix Z^+:

$$Z^+ m^2_{H^+} \; {Z^+}^T = \left(m^2_{H^+}\right)^{\text{dia}} \,, \tag{A.43}$$

with

$$C = {Z^+}^T H^+ \,, \tag{A.44}$$

where the 8 entries of the matrix H^+ are the 'charged Higgs' mass eigenstate fields. In particular,

$$H_d^- = Z^+_{b1}H_b^- \,, \quad H_u^+ = Z^+_{b2}H_b^+ \,, \quad \widetilde{e}_{iL} = Z^+_{bi}H_b^- \,, \quad \widetilde{e}_{jR} = Z^+_{bj}H_b^- \,. \tag{A.45}$$

A.1.4 Mass Matrix for Down-Squarks

Left and right down-squarks are mixed. In the basis $\widetilde{d}^T = \left(\widetilde{d}_{iL}, \widetilde{d}_{jR}\right)$, one obtains the following mass terms in the Lagrangian:

$$-\,\widetilde{d}^T m^2_{\widetilde{d}}\,\widetilde{d}^* \,, \tag{A.46}$$

where $m^2_{\widetilde{d}}$ is the 6×6 (symmetric) matrix

$$m^2_{\widetilde{d}} = \begin{pmatrix} m^2_{\widetilde{d}_{iL}\widetilde{d}^*_{jL}} & m^2_{\widetilde{d}_{iL}\widetilde{d}^*_{jR}} \\ m^2_{\widetilde{d}_{iR}\widetilde{d}^*_{jL}} & m^2_{\widetilde{d}_{iR}\widetilde{d}^*_{jR}} \end{pmatrix} , \tag{A.47}$$

$$m^2_{\widetilde{d}_{iL}\widetilde{d}^*_{jL}} = \left(m^2_{\widetilde{Q}_L}\right)_{ij} - \frac{1}{24}\left(3g^2 + g'^2\right)\left(v_d^2 - v_u^2 + v_{kL}v_{kL}\right) + \frac{1}{2}Y_{d_{ik}}Y_{d_{jk}}v_d^2 , \tag{A.48}$$

$$m^2_{\widetilde{d}_{iR}\widetilde{d}^*_{jR}} = \left(m^2_{\widetilde{d}_R}\right)_{ij} - \frac{g'^2}{12}\left(v_d^2 - v_u^2 + v_{kL}v_{kL}\right) + \frac{1}{2}Y_{d_{ki}}Y_{d_{kj}}v_d^2 , \tag{A.49}$$

$$m^2_{\widetilde{d}_{iL}\widetilde{d}^*_{jR}} = m^2_{\widetilde{d}_{jR}\widetilde{d}^*_{iL}} = \frac{1}{\sqrt{2}}T_{d_{ij}}v_d - \frac{1}{2}Y_{d_{ij}}\lambda_k v_u v_{kR} . \tag{A.50}$$

Matrix of Eq. (A.47) is diagonalized by an orthogonal matrix Z^D:

$$Z^D m^2_{\tilde{d}}\, {Z^D}^T = \left(m^2_{\tilde{d}}\right)^{\text{dia}} , \tag{A.51}$$

with

$$\tilde{d} = {Z^D}^T \tilde{D} , \tag{A.52}$$

where the 6 entries of the matrix $\tilde{D}$ are the down-squark mass eigenstate fields. In particular,

$$\tilde{d}_{iL} = Z^D_{bi}\tilde{D}_b , \quad \tilde{d}_{jR} = Z^D_{bj}\tilde{D}_b . \tag{A.53}$$

A.1.5 Mass Matrix for Up-Squarks

Left and right up-squarks are mixed. In the basis $\widetilde{u}^T = (\widetilde{u}_{iL}, \widetilde{u}_{jR})$, one obtains the following mass terms in the Lagrangian:

$$-\,\widetilde{u}^T m^2_{\widetilde{u}}\, \widetilde{u}^* , \tag{A.54}$$

where $m^2_{\widetilde{u}}$ is the 6×6 (symmetric) matrix

$$m^2_{\widetilde{u}} = \begin{pmatrix} m^2_{\widetilde{u}_{iL}\widetilde{u}^*_{jL}} & m^2_{\widetilde{u}_{iL}\widetilde{u}^*_{jR}} \\ m^2_{\widetilde{u}_{iR}\widetilde{u}^*_{jL}} & m^2_{\widetilde{u}_{iR}\widetilde{u}^*_{jR}} \end{pmatrix} , \tag{A.55}$$

$$m^2_{\widetilde{u}_{iL}\widetilde{u}^*_{jL}} = \left(m^2_{\widetilde{Q}_L}\right)_{ij} + \frac{1}{24}\left(3g^2 - g'^2\right)\left(v_d^2 - v_u^2 + v_{kL}v_{kL}\right) + \frac{1}{2}Y_{u_{ik}}Y_{u_{jk}}v_u^2 \ , \quad \text{(A.56)}$$

$$m^2_{\widetilde{u}_{iR}\widetilde{u}^*_{jR}} = \left(m^2_{\widetilde{u}_R}\right)_{ij} + \frac{g'^2}{6}\left(v_d^2 - v_u^2 + v_{kL}v_{kL}\right) + \frac{1}{2}Y_{u_{ki}}Y_{u_{kj}}v_u^2 \ , \quad \text{(A.57)}$$

$$m^2_{\widetilde{u}_{iL}\widetilde{u}^*_{jR}} = m^2_{\widetilde{u}_{jR}\widetilde{u}^*_{iL}} = \frac{1}{\sqrt{2}}T_{u_{ij}}v_u - \frac{1}{2}Y_{u_{ij}}\lambda_k v_d v_{kR} + \frac{1}{2}Y_{u_{ij}}Y_{\nu_{lk}}v_{lL}v_{kR} \ . \quad \text{(A.58)}$$

Matrix of Eq. (A.55) is diagonalized by an orthogonal matrix Z^U:

$$Z^U m^2_{\tilde{u}}\ {Z^U}^T = \left(m^2_{\tilde{u}}\right)^{\rm dia} \ , \quad \text{(A.59)}$$

with

$$\tilde{u} = {Z^U}^T \tilde{U} \, , \quad \text{(A.60)}$$

where the 6 entries of the matrix $\tilde{U}$ are the up-squark mass eigenstate fields. In particular,

$$\tilde{u}_{iL} = Z^U_{bi}\tilde{U}_b \, , \quad \tilde{u}_{jR} = Z^U_{bj}\tilde{U}_b \, . \quad \text{(A.61)}$$

A.2 Fermion Mass Matrices

The neutrino and lepton mass matrices were computed in Appendix A.2 of Ref. [50] with the assumption of CP conservation. In this Appendix we write the general fermion mass matrices, including the quarks matrices, without assuming CP conservation. To obtain the results, we apply the standard rotation in the gauge sector:

$$\begin{pmatrix} \widetilde{W}_1 \\ \widetilde{W}_2 \\ \widetilde{W}_3 \end{pmatrix} = Z^{\widetilde{W}} \begin{pmatrix} \widetilde{W}^- \\ \widetilde{W}^+ \\ \widetilde{W}^0 \end{pmatrix} \ ,$$

where the mixing matrix $Z^{\widetilde{W}}$ is parametrized by

$$Z^{\widetilde{W}} = \begin{pmatrix} \frac{1}{\sqrt{2}} & \frac{1}{\sqrt{2}} & 0 \\ \frac{-i}{\sqrt{2}} & \frac{i}{\sqrt{2}} & 0 \\ 0 & 0 & 1 \end{pmatrix} \ ,$$

and $\widetilde{W}_{1,2,3}$ are the 2–component wino fields in the soft Lagrangian of Eq. (3.2).

A.2.1 Mass Matrix for Neutrinos

The usual left-handed neutrinos of the SM mix with the right-handed neutrinos and the neutral gauginos and higgsinos. Working in the basis of 2–component spinors[1], $(\chi^0)^T = \left(\varphi_{\nu_i}, \widetilde{B}^0, \widetilde{W}^0, \widetilde{H}^0_d, \widetilde{H}^0_u, \eta_{\nu_j}\right)$, one obtains the following neutral fermion mass terms in the Lagrangian:

$$-\frac{1}{2}(\chi^0)^T m_\nu \chi^0 + \text{h.c.}\,, \tag{A.62}$$

where m_ν is the 10×10 (symmetric) matrix

$$m_\nu = \begin{pmatrix} 0_{3\times3} & -\frac{1}{\sqrt{2}}g'\langle\widetilde{\nu}_{iL}\rangle^* & \frac{1}{\sqrt{2}}g\langle\widetilde{\nu}_{iL}\rangle^* & 0_{3\times1} & Y_{\nu_{ik}}\langle\widetilde{\nu}_{kR}\rangle^* & \langle H^0_u\rangle Y_{\nu_{ij}} \\ -\frac{1}{\sqrt{2}}g'\langle\widetilde{\nu}_{jL}\rangle^* & M_1 & 0 & -\frac{1}{\sqrt{2}}g'\langle H^0_d\rangle^* & \frac{1}{\sqrt{2}}g'\langle H^0_u\rangle^* & 0_{1\times3} \\ \frac{1}{\sqrt{2}}g\langle\widetilde{\nu}_{jL}\rangle^* & 0 & M_2 & \frac{1}{\sqrt{2}}g\langle H^0_d\rangle^* & -\frac{1}{\sqrt{2}}g\langle H^0_u\rangle^* & 0_{1\times3} \\ 0_{1\times3} & -\frac{1}{\sqrt{2}}g'\langle H^0_d\rangle^* & \frac{1}{\sqrt{2}}g\langle H^0_d\rangle^* & 0 & -\lambda_k\langle\widetilde{\nu}_{kR}\rangle^* & -\lambda_j\langle H^0_u\rangle \\ Y_{\nu_{jk}}\langle\widetilde{\nu}_{kR}\rangle^* & \frac{1}{\sqrt{2}}g'\langle H^0_u\rangle^* & -\frac{1}{\sqrt{2}}g\langle H^0_u\rangle^* & -\lambda_k\langle\widetilde{\nu}_{kR}\rangle^* & 0 & -\lambda_j\langle H^0_d\rangle + Y_{\nu_{kj}}\langle\widetilde{\nu}_{kL}\rangle \\ \langle H^0_u\rangle(Y_{\nu_{ij}})^T & 0_{3\times1} & 0_{3\times1} & -\lambda_i\langle H^0_u\rangle & -\lambda_i\langle H^0_d\rangle + Y_{\nu_{ki}}\langle\widetilde{\nu}_{kL}\rangle & 2\kappa_{ijk}\langle\widetilde{\nu}_{kR}\rangle^* \end{pmatrix}. \tag{A.63}$$

This is diagonalized by an unitary matrix U^V:

$$U^{V^*} m_\nu \, U^{V^\dagger} = m_\nu^{\text{dia}}\,, \tag{A.64}$$

with

$$\chi^0 = U^{V^\dagger}\lambda^0\,, \tag{A.65}$$

where the 10 entries of the matrix λ^0 are the 2-component 'neutrino' mass eigenstate fields. In particular,

$$\begin{aligned} \nu_{iL} &= U^{V^*}_{bi}\lambda^0_b\,, \quad \widetilde{B}^0 = U^{V^*}_{b4}\lambda^0_b\,, \quad \widetilde{W}^0 = U^{V^*}_{b5}\lambda^0_b\,, \\ \widetilde{H}^0_d &= U^{V^*}_{b6}\lambda^0_b\,, \quad \widetilde{H}^0_u = U^{V^*}_{b7}\lambda^0_b\,, \quad (\nu_{jR})^{c^*} = U^V_{bj}\lambda^{0^*}_b\,. \end{aligned} \tag{A.66}$$

[1]Since both helicities are present for neutrinos, it is convenient to introduce here the notation where φ_α is a left-handed spinor and $\overline{\eta}^{\dot\alpha}$ a right-handed spinor. Thus we are using in $(\chi^0)^T$, $\varphi^\alpha_{\nu_i} \equiv (\nu_{iL})^{c^*}$ and $\eta^\alpha_{\nu_j} \equiv \nu^*_{jR}$, and in χ^0, $\varphi_{\nu_i\,\alpha} \equiv \nu_{iL}$ and $\eta_{\nu_j\,\alpha} \equiv (\nu_{jR})^c$.

A.2.2 Mass Matrix for Leptons

The usual leptons of the SM mix with charged gauginos and higgsinos. In the basis of 2–component spinors[2], $(\chi^-)^T = \left(\varphi_{e_i}, \widetilde{W}^-, \widetilde{H}_d^-\right)$ and $(\chi^+)^T = \left(\eta_{e_j}, \widetilde{W}^+, \widetilde{H}_u^+\right)$, one obtains the following charged fermion mass terms in the Lagrangian:

$$-(\chi^-)^T m_e \chi^+ + \text{h.c.}\,, \tag{A.67}$$

where m_e is the 5×5 matrix

$$m_e = \begin{pmatrix} \langle H_d^0 \rangle Y_{ij}^e & g\langle \widetilde{\nu}_{iL} \rangle^* & -Y_{\nu_{ik}} \langle \widetilde{\nu}_{kR} \rangle^* \\ 0_{1\times 3} & M_2 & g\langle H_u^0 \rangle^* \\ -Y_{e_{kj}} \langle \widetilde{\nu}_{kL} \rangle & g\langle H_d^0 \rangle^* & \lambda_k \langle \widetilde{\nu}_{kR} \rangle^* \end{pmatrix}. \tag{A.68}$$

This is diagonalized by two unitary matrices U_L^e and U_R^e:

$$U_R^{e\,*} m_e U_L^{e\,\dagger} = m_e^{\text{dia}}\,, \tag{A.69}$$

with

$$\chi^+ = U_L^{e\,\dagger} \lambda^+\,, \tag{A.70}$$

$$\chi^- = U_R^{e\,\dagger} \lambda^-\,, \tag{A.71}$$

where the 5 entries of the matrices λ^+, λ^-, are the 2-component 'lepton' mass eigenstate fields. In particular,

$$\begin{aligned} (e_{jR})^{c^*} &= U_{Lb4}^e \lambda_b^{+\,*}\,, \quad \widetilde{W}^+ = U_{Lb4}^{e\,*} \lambda_b^+\,, \quad \widetilde{H}_u^+ = U_{Lb5}^{e\,*} \lambda_b^+\,, \\ e_{iL} &= U_{Rbi}^{e\,*} \lambda_b^-\,, \quad \widetilde{W}^- = U_{Rb4}^{e\,*} \lambda_b^-\,, \quad \widetilde{H}_d^- = U_{Rb5}^{e\,*} \lambda_b^-\,. \end{aligned} \tag{A.72}$$

A.2.3 Mass Matrix for Down-Quarks

In the basis of 2–components spinors $(d_L^*)^T = (d_{iL}^*)$, $(d_R)^T = (d_{jR})$, one obtains the following down-quark mass terms in the Lagrangian:

$$-(d_L^*)^T m_d d_R + \text{h.c.}\,, \tag{A.73}$$

[2]Following the convention of the previous footnote, we have in this case $\varphi_{e_i}^\alpha \equiv (e_{iL})^{c^*}$ and $\eta_{e_j\,\alpha} \equiv (e_{jR})^c$.

where m_d is the 3×3 matrix

$$m_d = \left(\langle H_d^0 \rangle^* Y_{d_{ij}}^* \right) . \tag{A.74}$$

This is diagonalized by two unitary matrices U_L^d and U_R^d:

$$U_L^{d^\dagger} m_d U_R^d = m_d^{\rm dia} , \tag{A.75}$$

with

$$d_R = U_R^d D_R , \tag{A.76}$$

$$d_L = U_L^d D_L . \tag{A.77}$$

where the 3 entries of the matrices D_L, D_R are the 2-component down-quark mass eigenstate fields. In particular,

$$\begin{aligned} d_{jR} &= U_{Rjb}^d D_{bR} , \\ d_{iL} &= U_{Rib}^d D_{bL} . \end{aligned} \tag{A.78}$$

A.2.4 Mass Matrix for Up-Quarks

In the basis of 2–components spinors $(u_L^*)^T = (u_{iL}^*)$, $(u_R)^T = (u_{jR})$, one obtains the following up-quark mass terms in the Lagrangian:

$$-(u_L^*)^T m_u u_R + \text{h.c.} , \tag{A.79}$$

where m_u is the 3×3 matrix

$$m_u = \left(\langle H_u^0 \rangle^* Y_{u_{ij}}^* \right) . \tag{A.80}$$

This is diagonalized by two unitary matrices U_L^u and U_R^u:

$$U_L^{u^\dagger} m_u U_R^u = m_u^{\rm dia} , \tag{A.81}$$

with

$$u_R = U_R^u U_R , \tag{A.82}$$

$$u_L = U_L^u U_L . \tag{A.83}$$

where the 3 entries of the matrices U_L, U_R are the 2-component up-quark mass eigenstate fields. In particular,

$$\begin{aligned} u_{jR} &= U^u_{Rjb} U_{bR}\,, \\ u_{iL} &= U^u_{Rib} U_{bL}\,. \end{aligned} \tag{A.84}$$

Appendix B

Higgs-right sneutrino mass submatrices

Using the parameters of Eq. (3.25) in the equations of Appendices A.1.1 and A.1.2, and neglecting terms suppressed by the small $Y_{\nu_{ij}}$ and v_{iL}, the tree-level entries of the 5×5 Higgs-right sneutrino submatrices [20, 50, 52, 53, 64] can be approximated as follows:

B.1 Scalars

$$m^2_{H_d^{\mathcal{R}} H_d^{\mathcal{R}}} = \tan\beta \sum_i \frac{v_{iR}}{\sqrt{2}} \left(T_{\lambda_i} + \lambda_i \frac{\mathcal{M}_i}{2} \right) + \left(\frac{v}{\sqrt{2}} \right)^2 \frac{1}{1+\tan^2\beta} \, \frac{1}{2}(g^2 + g'^2), \tag{B.1}$$

$$m^2_{H_u^{\mathcal{R}} H_u^{\mathcal{R}}} = \frac{1}{\tan\beta} \sum_i \frac{v_{iR}}{\sqrt{2}} \left(T_{\lambda_i} + \lambda_i \frac{\mathcal{M}_i}{2} \right) + \left(\frac{v}{\sqrt{2}} \right)^2 \frac{\tan^2\beta}{1+\tan^2\beta} \, \frac{1}{2}(g^2 + g'^2), \tag{B.2}$$

$$m^2_{H_d^{\mathcal{R}} H_u^{\mathcal{R}}} = -\sum_i \frac{v_{iR}}{\sqrt{2}} \left(T_{\lambda_i} + \lambda_i \frac{\mathcal{M}_i}{2} \right) + \left(\frac{v}{\sqrt{2}} \right)^2 \frac{\tan\beta}{1+\tan^2\beta} \left[-\frac{1}{2}(g^2 + g'^2) + 2\sum_i \lambda_i^2 \right], \tag{B.3}$$

$$m^2_{\widetilde{\nu}_{iR}^{\mathcal{R}} H_u^{\mathcal{R}}} = -\frac{v}{\sqrt{2}} \frac{1}{\sqrt{1+\tan^2\beta}} \left[T_{\lambda_i} \; + \lambda_i \left(\mathcal{M}_i - 2\mu \tan\beta \right) \right], \tag{B.4}$$

$$m^2_{\widetilde{\nu}_{iR}^{\mathcal{R}} H_d^{\mathcal{R}}} = -\frac{v}{\sqrt{2}} \frac{\tan\beta}{\sqrt{1+\tan^2\beta}} \left[T_{\lambda_i} \; + \lambda_i \left(\mathcal{M}_i - \frac{2\mu}{\tan\beta} \right) \right], \tag{B.5}$$

$$\begin{aligned} m^2_{\widetilde{\nu}_{iR}^{\mathcal{R}} \widetilde{\nu}_{jR}^{\mathcal{R}}} = \delta_{ij} \Bigg\{ & \left(\frac{T_{\kappa_i}}{\kappa_i} + 2\mathcal{M}_i \right) \frac{\mathcal{M}_i}{2} + \frac{\lambda_i \mu}{v_{iR}/\sqrt{2}} \left(\frac{v}{\sqrt{2}} \right)^2 \left(\frac{1}{\mu} \frac{T_{\lambda_i}}{\lambda_i} \frac{\tan\beta}{1+\tan^2\beta} - 1 \right) \\ & - T_{\nu_i} \frac{v}{\sqrt{2}} \frac{\tan\beta}{\sqrt{1+\tan^2\beta}} \Bigg\} + \lambda_i \lambda_j \left(\frac{v}{\sqrt{2}} \right)^2, \end{aligned} \tag{B.6}$$

where $\mu = \sum_i \lambda_i \frac{v_{iR}}{\sqrt{2}}$ and $\mathcal{M}_i = 2\kappa_i \frac{v_{iR}}{\sqrt{2}}$.

B.2 Pseudoscalars

$$m^2_{H_d^{\mathcal{I}} H_d^{\mathcal{I}}} = \tan\beta \sum_i \frac{v_{iR}}{\sqrt{2}} \left(T_{\lambda_i} + \lambda_i \frac{\mathcal{M}_i}{2} \right) \tag{B.7}$$

$$m^2_{H_u^{\mathcal{I}} H_u^{\mathcal{I}}} = \frac{1}{\tan\beta} \sum_i \frac{v_{iR}}{\sqrt{2}} \left(T_{\lambda_i} + \lambda_i \frac{\mathcal{M}_i}{2} \right) \tag{B.8}$$

$$m^2_{H_d^{\mathcal{I}} H_u^{\mathcal{I}}} = \sum_i \frac{v_{iR}}{\sqrt{2}} \left(T_{\lambda_i} + \lambda_i \frac{\mathcal{M}_i}{2} \right) \tag{B.9}$$

$$m^2_{\widetilde{\nu}^{\mathcal{I}}_{iR} H_u^{\mathcal{I}}} = \frac{v}{\sqrt{2}} \frac{1}{\sqrt{1+\tan^2\beta}} \left(T_{\lambda_i} - \lambda_i \mathcal{M}_i \right), \tag{B.10}$$

$$m^2_{\widetilde{\nu}^{\mathcal{I}}_{iR} H_d^{\mathcal{I}}} = \frac{v}{\sqrt{2}} \frac{\tan\beta}{\sqrt{1+\tan^2\beta}} \left(T_{\lambda_i} - \lambda_i \mathcal{M}_i \right), \tag{B.11}$$

$$\begin{aligned} m^2_{\widetilde{\nu}^{\mathcal{I}}_{iR} \widetilde{\nu}^{\mathcal{I}}_{jR}} = \delta_{ij} \Bigg\{ & -\frac{3}{2} \frac{T_{\kappa_i}}{\kappa_i} \mathcal{M}_i + \frac{\lambda_i \mu}{v_{iR}/\sqrt{2}} \left(\frac{v}{\sqrt{2}} \right)^2 \left[\frac{1}{\mu} \left(\frac{T_{\lambda_i}}{\lambda_i} + 2\mathcal{M}_i \right) \frac{\tan\beta}{1+\tan^2\beta} - 1 \right] \\ & - T_{\nu_i} \frac{v}{\sqrt{2}} \frac{\tan\beta}{\sqrt{1+\tan^2\beta}} \Bigg\} + \lambda_i \lambda_j \left(\frac{v}{\sqrt{2}} \right)^2 . \end{aligned} \tag{B.12}$$

Appendix C

Results from the $\lambda - \kappa$ plane

Here we show several figures for each scan, where the viable points of the parameter space can be seen in the $\kappa - \lambda$ plane for different values of the other parameters.

C.1 *Scan 1* $(0.01 \leq \lambda < 0.2)$

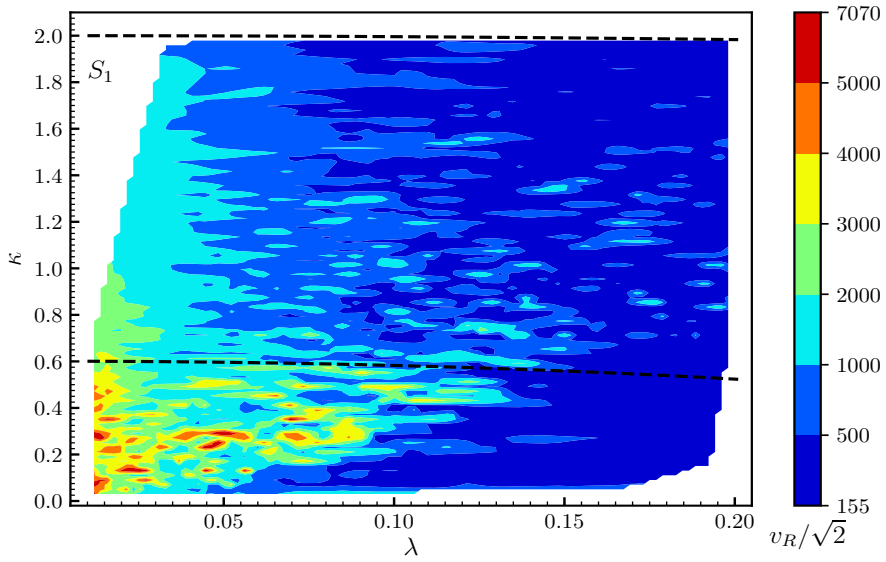

Figure C.1: Viable points of the parameter space for S_1 in the $\kappa - \lambda$ plane. The points below the lower black dashed line fulfill the condition of Eq. (3.41), where perturbativity is assumed up to the GUT scale. All points below the upper dashed line fulfill the condition of Eq. (3.42), where perturbativity is relaxed up to 10 TeV. The colours indicate different values of the right sneutrino VEVs $v_R/\sqrt{2}$.

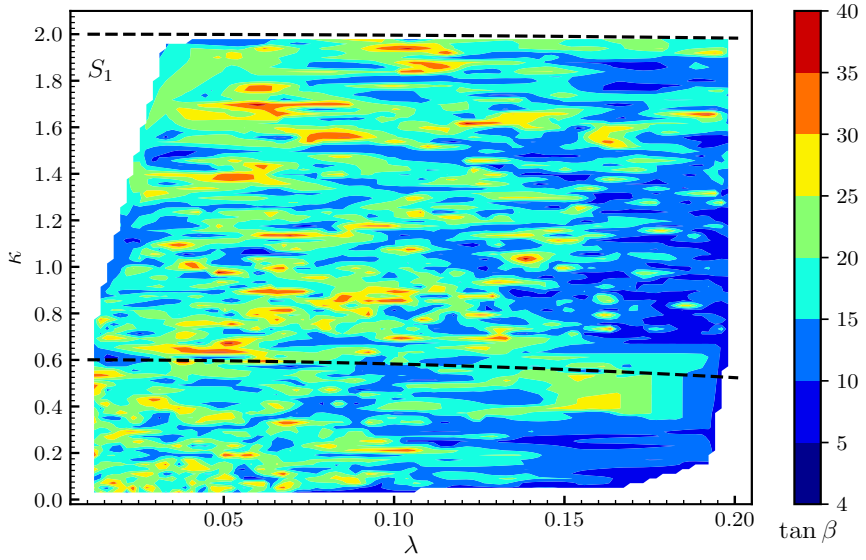

Figure C.2: The same as in Fig. C.1, but the colours indicate different values of $\tan\beta$.

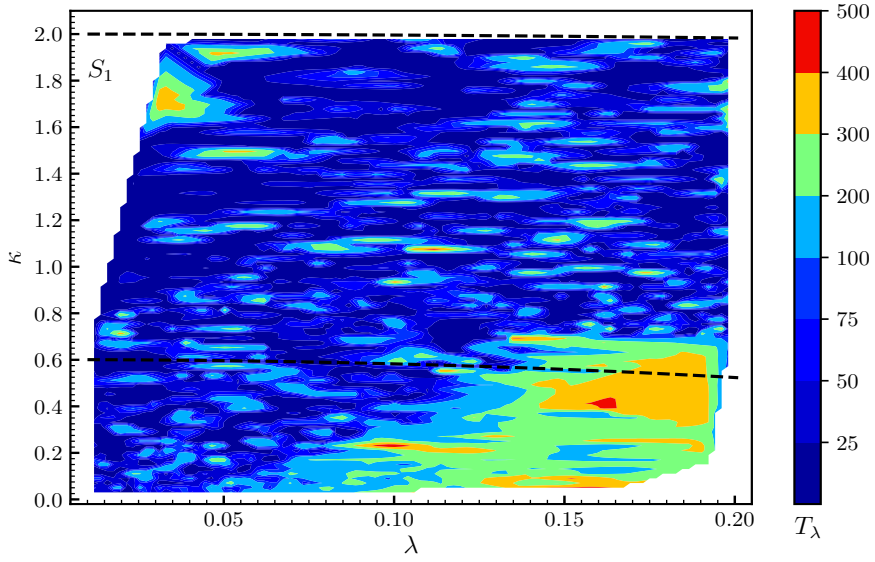

Figure C.3: The same as in Fig. C.1, but the colours indicate different low-energy values of the trilinear soft terms T_λ.

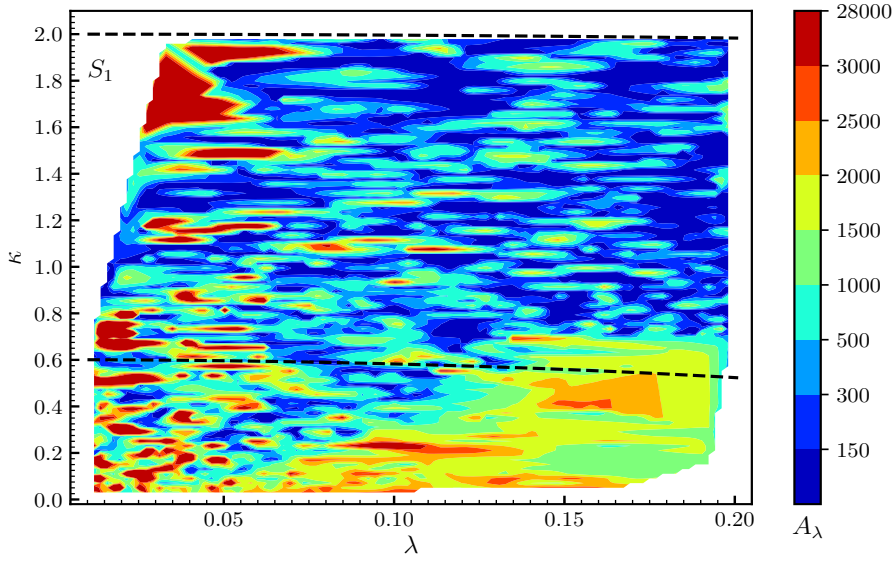

Figure C.4: The same as in Fig. C.1, but the colours indicate different low-energy values of the trilinear soft terms A_λ, assuming the supergravity relation $A_\lambda = T_\lambda/\lambda$.

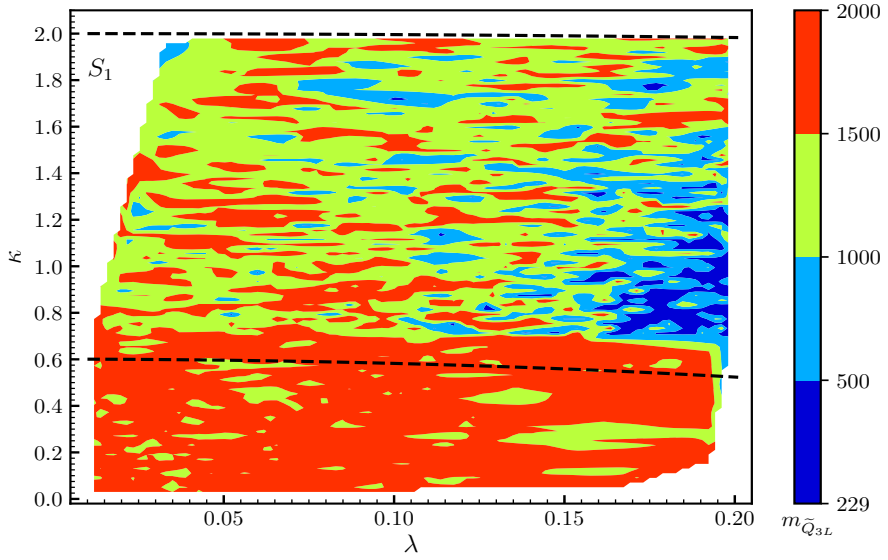

Figure C.5: The same as in Fig. C.1, but the colours indicate different low-energy values of the soft masses $m_{\widetilde{Q}_{3L}}$.

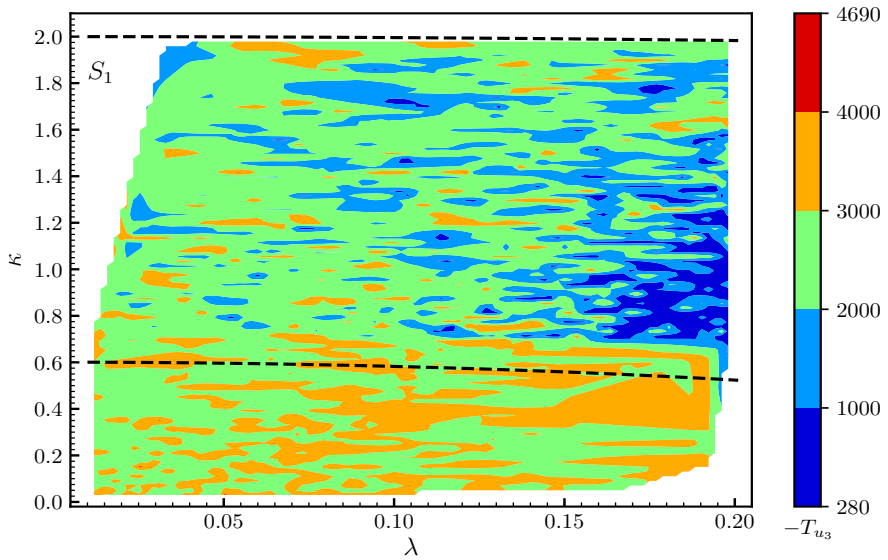

Figure C.6: The same as in Fig. C.1, but the colours indicate different low-energy values of the trilinear soft term T_{u_3}.

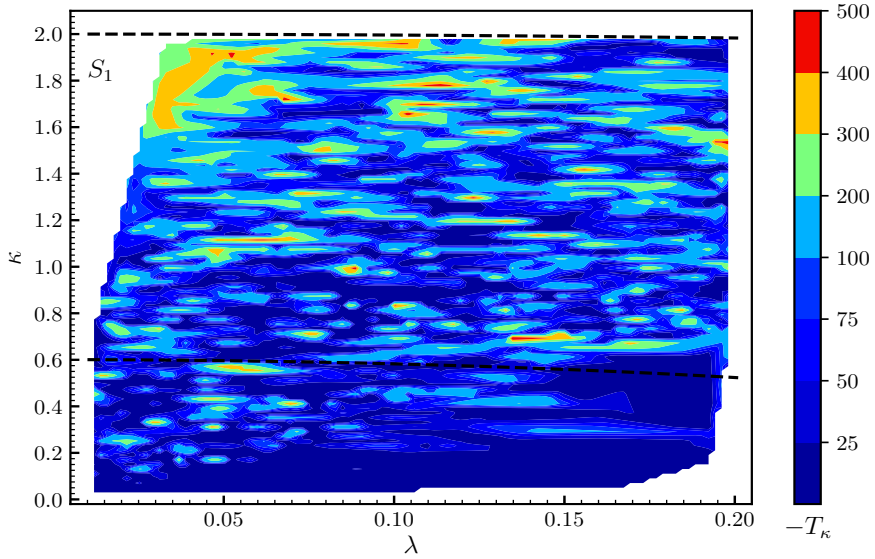

Figure C.7: The same as in Fig. C.1, but the colours indicate different low-energy values of the trilinear soft terms T_κ.

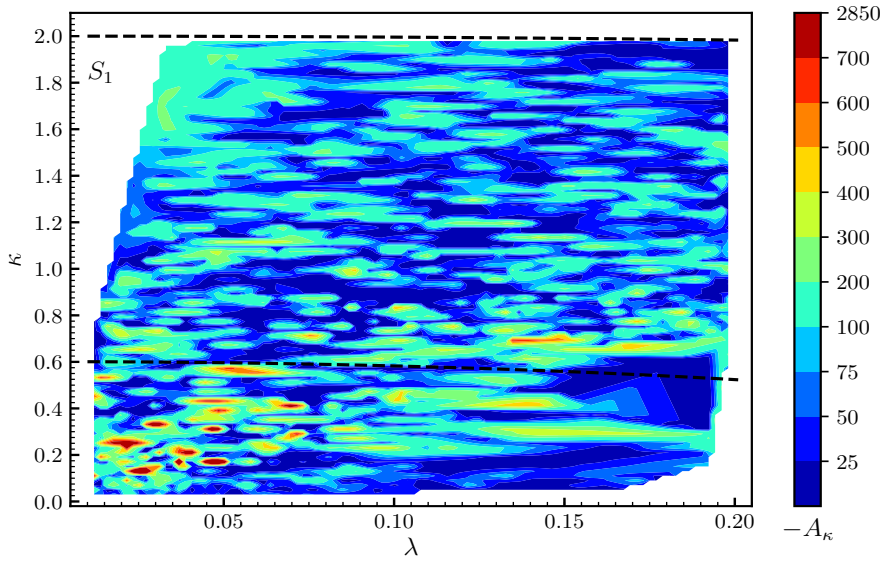

Figure C.8: The same as in Fig. C.1, but the colours indicate different low-energy values of the trilinear soft terms A_κ, assuming the supergravity relation $A_\kappa = T_\kappa/\kappa$.

C.2 *Scan 2* ($0.2 \leq \lambda < 0.5$)

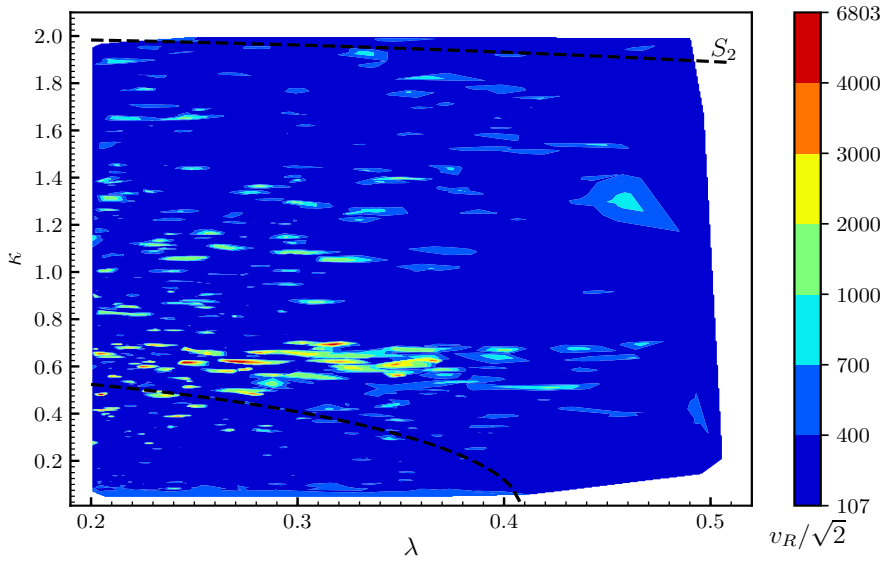

Figure C.9: Viable points of the parameter space for S_2 in the $\kappa - \lambda$ plane. The points below the lower black dashed line fulfill the condition of Eq. (3.41), where perturbativity is assumed up to the GUT scale. All points below the upper dashed line fulfill the condition of Eq. (3.42), where perturbativity is relaxed up to 10 TeV. The colours indicate different values of the right sneutrino VEVs $v_R/\sqrt{2}$.

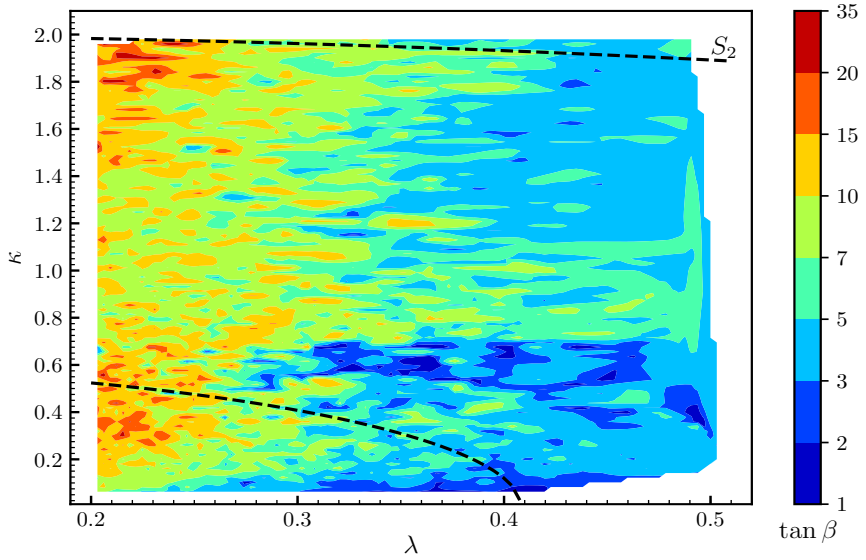

Figure C.10: The same as in Fig. C.9, but the colours indicate different values of $\tan\beta$.

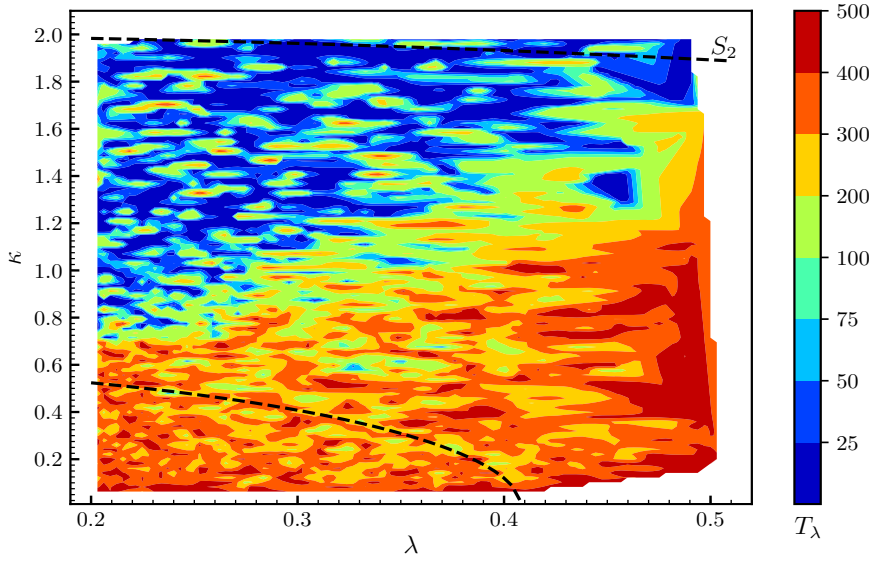

Figure C.11: The same as in Fig. C.9, but the colours indicate different low-energy values of the trilinear soft terms T_λ.

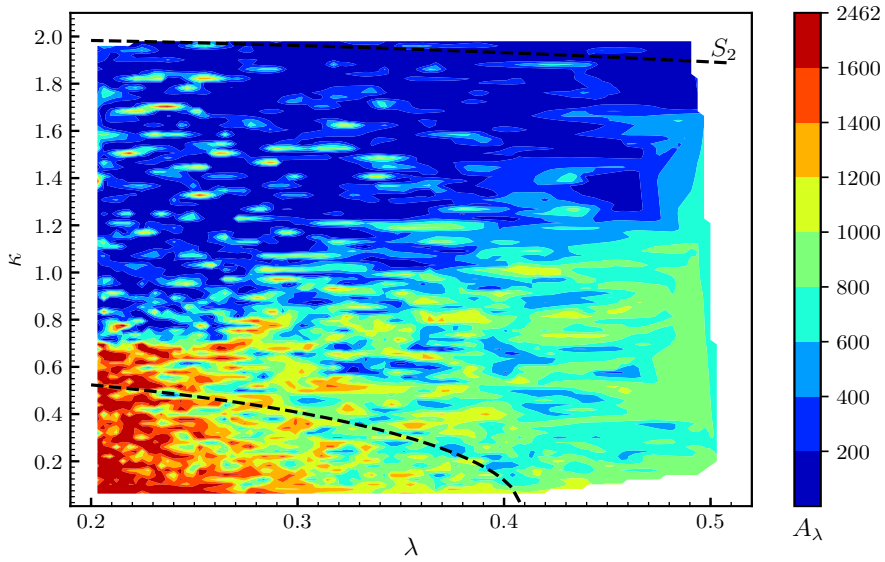

Figure C.12: The same as in Fig. C.9, but the colours indicate different low-energy values of the trilinear soft terms A_λ, assuming the supergravity relation $A_\lambda = T_\lambda/\lambda$.

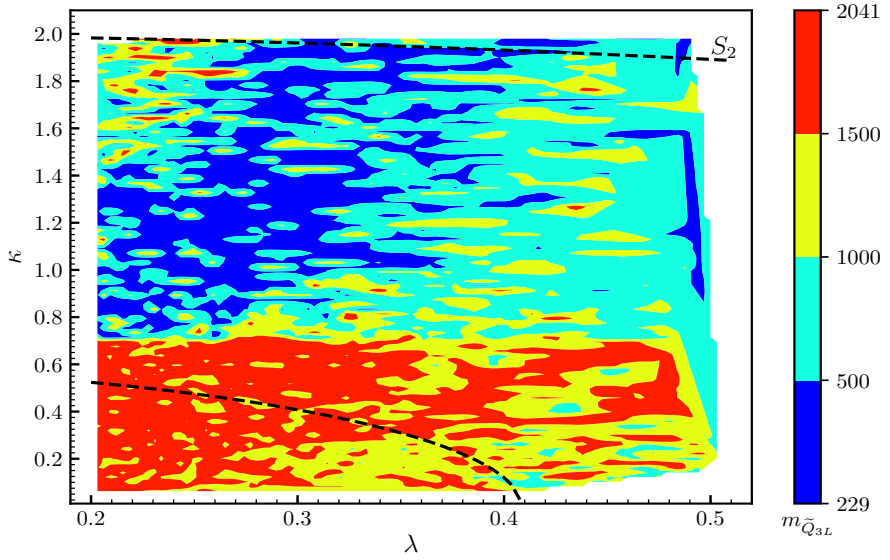

Figure C.13: The same as in Fig. C.9, but the colours indicate different low-energy values of the soft masses $m_{\widetilde{Q}_{3L}}$.

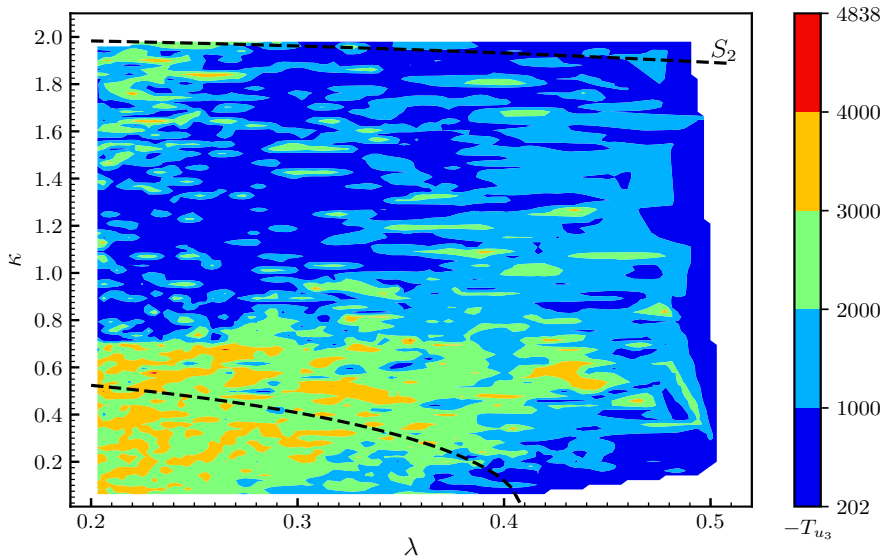

Figure C.14: The same as in Fig. C.9, but the colours indicate different low-energy values of the trilinear soft term T_{u_3}.

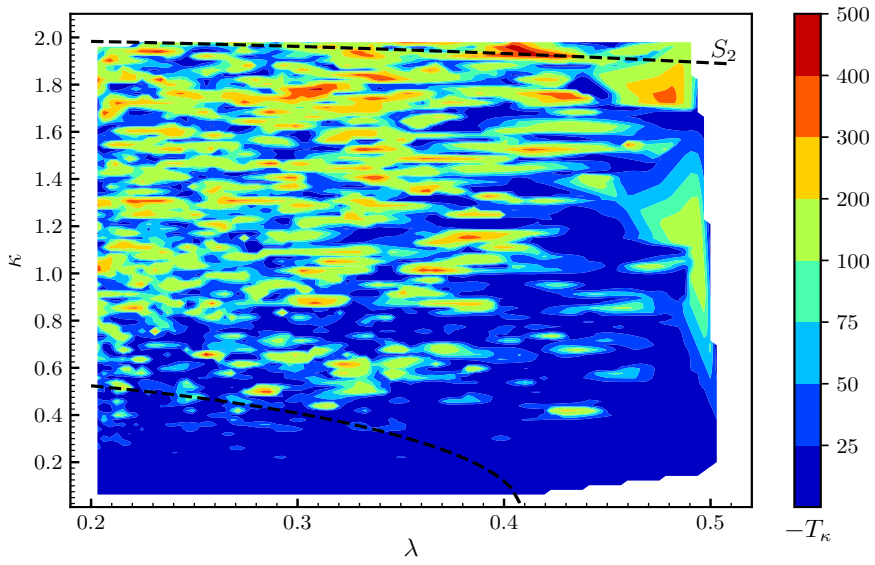

Figure C.15: The same as in Fig. C.9, but the colours indicate different low-energy values of the trilinear soft terms T_κ.

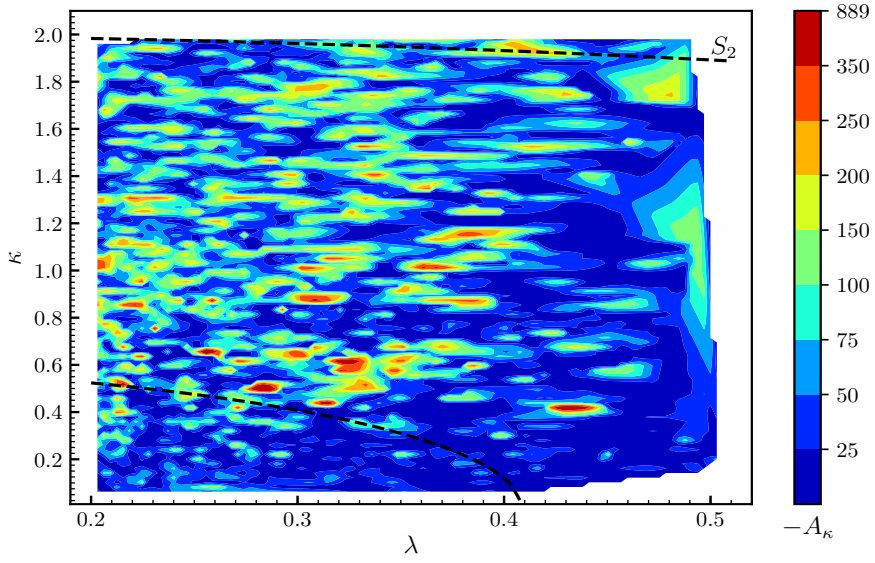

Figure C.16: The same as in Fig. C.9, but the colours indicate different low-energy values of the trilinear soft terms A_κ, assuming the supergravity relation $A_\kappa = T_\kappa/\kappa$.

C.3 *Scan 3* ($0.5 \leq \lambda < 1.2$)

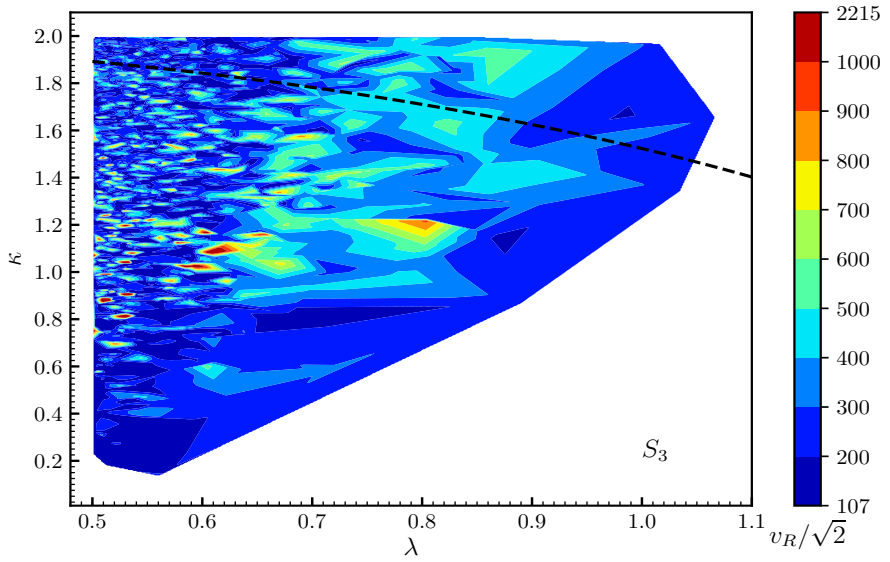

Figure C.17: Viable points of the parameter space for S_3 in the $\kappa - \lambda$ plane. The points below the dashed line fulfill the condition of Eq. (3.42), where perturbativity is relaxed up to 10 TeV. The colours indicate different values of the right sneutrino VEVs $v_R/\sqrt{2}$.

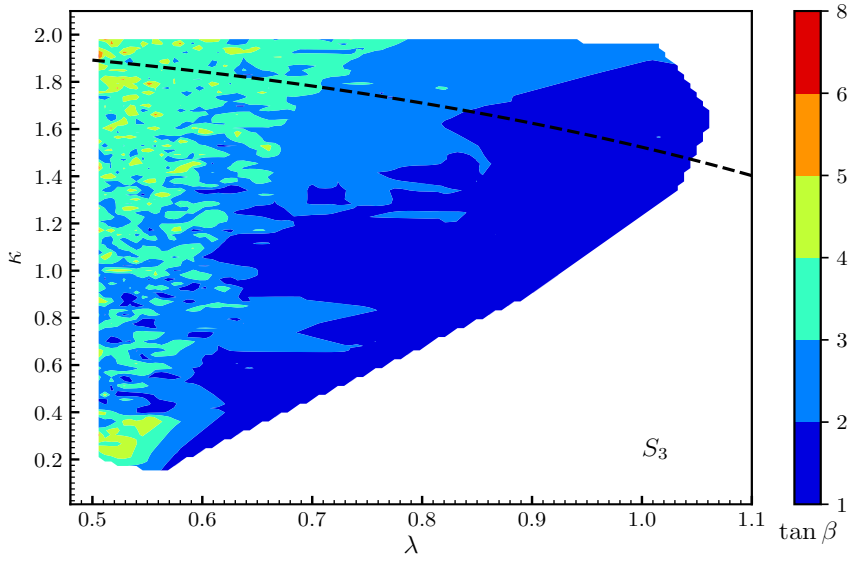

Figure C.18: The same as in Fig. C.17, but the colours indicate different values of $\tan\beta$.

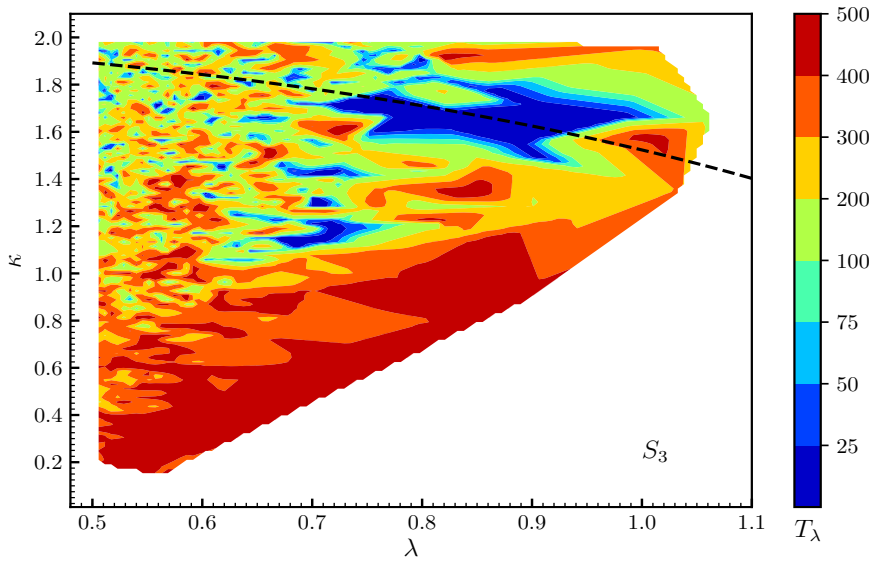

Figure C.19: The same as in Fig. C.17, but the colours indicate different low-energy values of the trilinear soft terms T_λ.

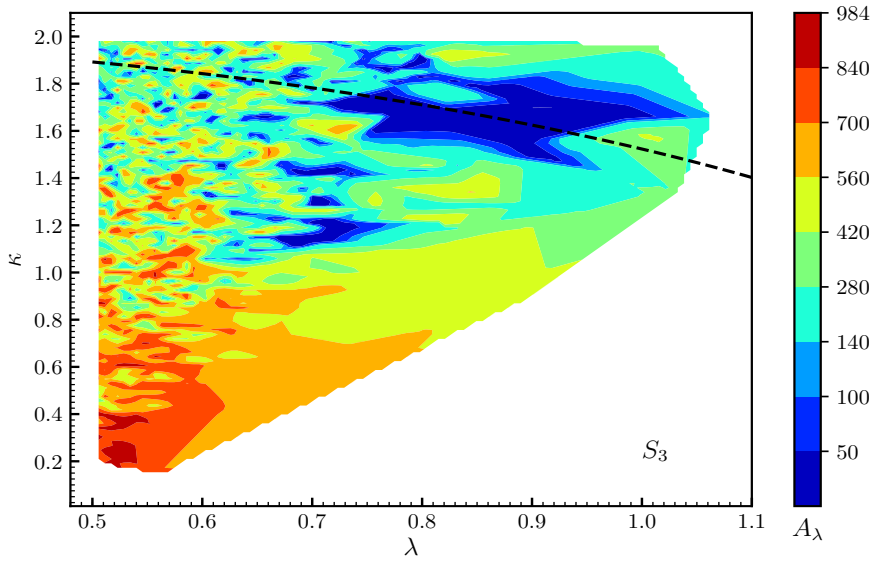

Figure C.20: The same as in Fig. C.17, but the colours indicate different low-energy values of the trilinear soft terms A_λ, assuming the supergravity relation $A_\lambda = T_\lambda/\lambda$.

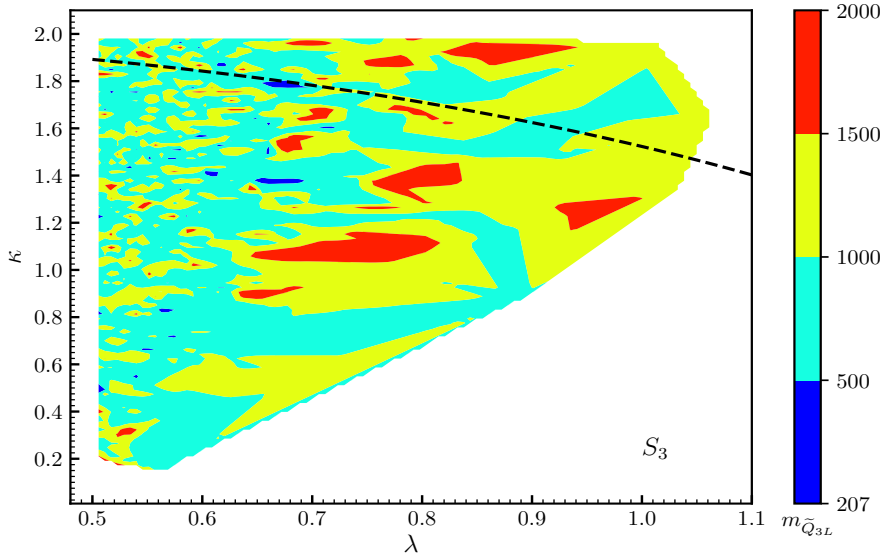

Figure C.21: The same as in Fig. C.17, but the colours indicate different low-energy values of the soft masses $m_{\widetilde{Q}_{3L}}$.

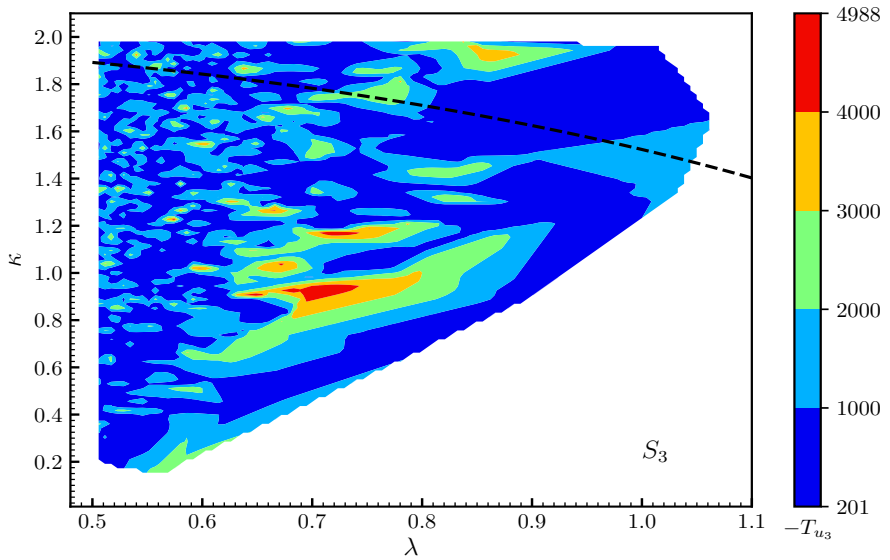

Figure C.22: The same as in Fig. C.17, but the colours indicate different low-energy values of the trilinear soft term T_{u_3}.

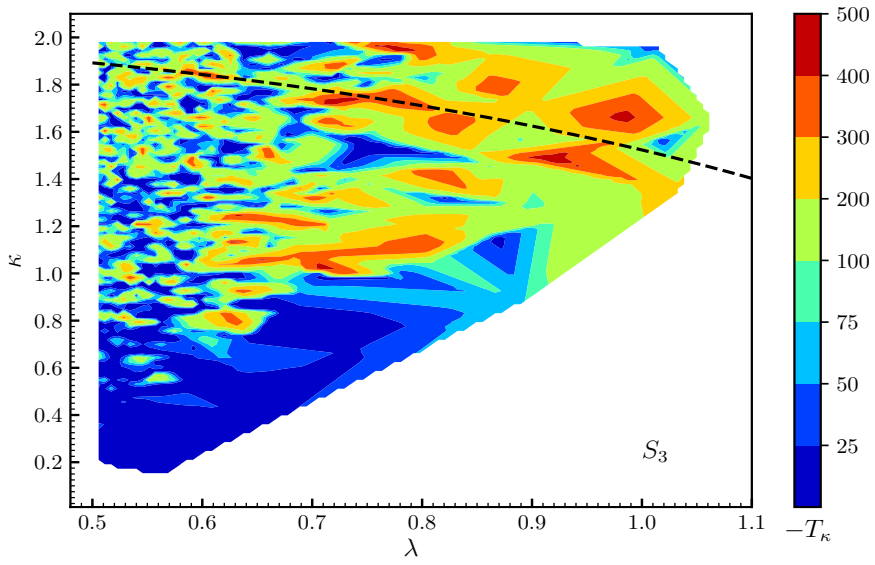

Figure C.23: The same as in Fig. C.17, but the colours indicate different low-energy values of the trilinear soft terms T_κ.

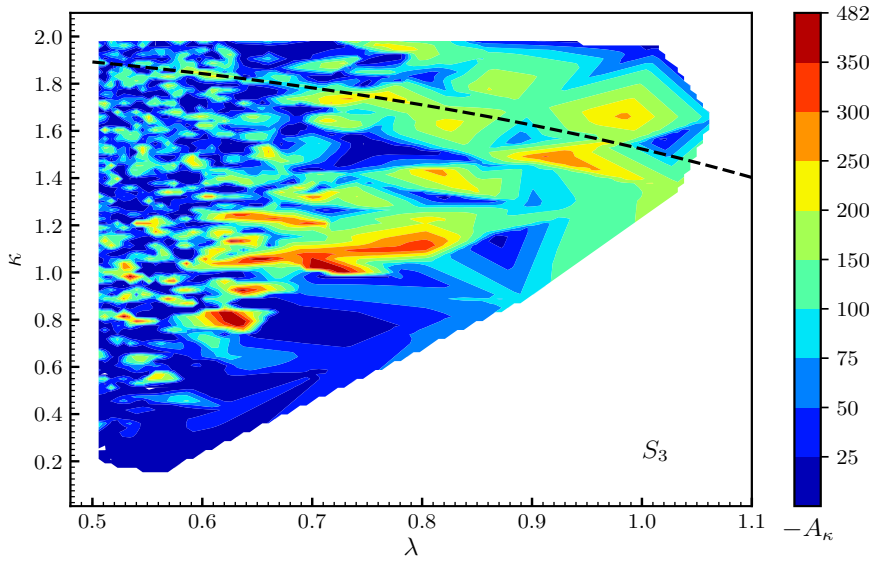

Figure C.24: The same as in Fig. C.17, but the colours indicate different low-energy values of the trilinear soft terms A_κ, assuming the supergravity relation $A_\kappa = T_\kappa/\kappa$.

Appendix D

Benchmark points

Here we show for each scan several benchmark points discussed in the text.

D.1 *Scan 1* ($0.01 \leq \lambda < 0.2$)

S1-ss1
$\lambda = 0.02,\ \ \kappa = 0.036,\ \ v_R/\sqrt{2} = 1799.28\ (\mu = 107.95,\ \mathcal{M} = 129.54)$ $\tan\beta = 32.54,\ \ T_\lambda = 60.70,\ -T_\kappa = 1.46,\ \ -T_{u_3} = 2632.61,\ \ m_{\widetilde{Q}_{3L}} = 1604.33$
$m_{h_1}(\widetilde{\nu}_R^{\mathcal{R}}) = 119.69,\ \ m_{h_2}(\widetilde{\nu}_R^{\mathcal{R}}) = 122.54,\ \ m_{h_3}(H_u^{\mathcal{R}}) = 124.81,\ \ m_{h_4}(\widetilde{\nu}_R^{\mathcal{R}}) = 125.56$ $m_{h_5}(\widetilde{\nu}_{\tau L}^{\mathcal{R}}) = 488.88,\ \ m_{h_6}(\widetilde{\nu}_{\mu L}^{\mathcal{R}}) = 1034.75,\ \ m_{h_7}(\widetilde{\nu}_{eL}^{\mathcal{R}}) = 1693.70,\ \ m_{h_8}(H_d^{\mathcal{R}}) = 3290.47$
$m_{A_2}(\widetilde{\nu}_R^{\mathcal{I}}) = 87.95,\ \ m_{A_3}(\widetilde{\nu}_R^{\mathcal{I}}) = 87.952,\ \ m_{A_4}(\widetilde{\nu}_R^{\mathcal{I}}) = 88.75$ $m_{A_5}(\widetilde{\nu}_{\tau L}^{\mathcal{I}}) = 488.88,\ \ m_{A_6}(\widetilde{\nu}_{\mu L}^{\mathcal{I}}) = 1034.75,\ \ m_{A_7}(\widetilde{\nu}_{eL}^{\mathcal{I}}) = 1693.70,\ \ m_{A_8}(H_d^{\mathcal{I}}) = 3290.46$
$m_{H_2^-}(\widetilde{\tau}_L) = 495.75,\ \ m_{H_3^-}(\widetilde{e}_R) = 1003.31,\ \ m_{H_4^-}(\widetilde{\mu}_R) = 1003.31$ $m_{H_5^-}(\widetilde{\tau}_R) = 1003.53,\ \ m_{H_6^-}(\widetilde{\mu}_L) = 1038.37,\ \ m_{H_7^-}(\widetilde{e}_L) = 1695.31,\ \ m_{H_8^-}(H_d^-) = 3291.45$
$\lvert Z^H_{h_1\widetilde{\nu}_{eR}^{\mathcal{R}}}\rvert^2 = 99.24\,\%,\ \lvert Z^H_{h_1\widetilde{\nu}_{\mu R}^{\mathcal{R}}}\rvert^2 = 0.44\,\%,\ \ \lvert Z^H_{h_1\widetilde{\nu}_{\tau R}^{\mathcal{R}}}\rvert^2 = 0.1\,\%,\ \ \lvert Z^H_{h_1 H_d^{\mathcal{R}}}\rvert^2 = 0.000027\,\%,\ \ \lvert Z^H_{h_1 H_u^{\mathcal{R}}}\rvert^2 = 0.2\,\%$ $\lvert Z^H_{h_2\widetilde{\nu}_{eR}^{\mathcal{R}}}\rvert^2 = 0.35\,\%,\ \lvert Z^H_{h_2\widetilde{\nu}_{\mu R}^{\mathcal{R}}}\rvert^2 = 98.15\,\%,\ \ \lvert Z^H_{h_2\widetilde{\nu}_{\tau R}^{\mathcal{R}}}\rvert^2 = 0.43\,\%,\ \ \lvert Z^H_{h_2 H_d^{\mathcal{R}}}\rvert^2 = 0.0005\,\%,\ \ \lvert Z^H_{h_2 H_u^{\mathcal{R}}}\rvert^2 = 1.04\,\%$ $\lvert Z^H_{h_3\widetilde{\nu}_{eR}^{\mathcal{R}}}\rvert^2 = 0.061\,\%,\ \lvert Z^H_{h_3\widetilde{\nu}_{\mu R}^{\mathcal{R}}}\rvert^2 = 0.25\,\%,\ \ \lvert Z^H_{h_3\widetilde{\nu}_{\tau R}^{\mathcal{R}}}\rvert^2 = 28.56\,\%,\ \ \lvert Z^H_{h_3 H_d^{\mathcal{R}}}\rvert^2 = 0.07\,\%,\ \ \lvert Z^H_{h_3 H_u^{\mathcal{R}}}\rvert^2 = 71.00\,\%$ $\lvert Z^H_{h_4\widetilde{\nu}_{eR}^{\mathcal{R}}}\rvert^2 = 0.34\,\%,\ \lvert Z^H_{h_4\widetilde{\nu}_{\mu R}^{\mathcal{R}}}\rvert^2 = 1.15\,\%,\ \ \lvert Z^H_{h_4\widetilde{\nu}_{\tau R}^{\mathcal{R}}}\rvert^2 = 70.89\,\%,\ \ \lvert Z^H_{h_4 H_d^{\mathcal{R}}}\rvert^2 = 0.03\,\%,\ \ \lvert Z^H_{h_4 H_u^{\mathcal{R}}}\rvert^2 = 27.58\,\%$
$\mathrm{BR}(h_1 \to bb) = 0.186,\ \ \mathrm{BR}(h_1 \to \tau\tau) = 0.031,\ \ \mathrm{BR}(h_1 \to WW) = 0.39$ $\mathrm{BR}(h_1 \to ZZ) = 0.0354,\ \ \mathrm{BR}(h_1 \to \gamma\gamma) = 0.00899,\ \mathrm{BR}(h_1 \to gg) = 0.285$
$\mathrm{BR}(h_2 \to bb) = 0.38,\ \ \mathrm{BR}(h_2 \to \tau\tau) = 0.063,\ \ \mathrm{BR}(h_2 \to WW) = 0.312$ $\mathrm{BR}(h_2 \to ZZ) = 0.0315,\ \ \mathrm{BR}(h_2 \to \gamma\gamma) = 0.0049,\ \ \mathrm{BR}(h_2 \to gg) = 0.171$
$\mathrm{BR}(h_3 \to bb) = 0.49,\ \ \mathrm{BR}(h_3 \to \tau\tau) = 0.0813,\ \ \mathrm{BR}(h_3 \to WW) = 0.258$ $\mathrm{BR}(h_3 \to ZZ) = 0.0279,\ \ \mathrm{BR}(h_3 \to \gamma\gamma) = 0.003,\ \ \mathrm{BR}(h_3 \to gg) = 0.114$
$\mathrm{BR}(h_4 \to bb) = 0.51,\ \ \mathrm{BR}(h_4 \to \tau\tau) = 0.0846,\ \ \mathrm{BR}(h_4 \to WW) = 0.250$ $\mathrm{BR}(h_4 \to ZZ) = 0.0275,\ \ \mathrm{BR}(h_4 \to \gamma\gamma) = 0.00265,\ \ \mathrm{BR}(h_4 \to gg) = 0.1$
$\Gamma^{\mathrm{tot}}_{h_1} = 2.32 \times 10^{-6},\ \ \Gamma^{\mathrm{tot}}_{h_2} = 2.09 \times 10^{-5},\ \ \Gamma^{\mathrm{tot}}_{h_3} = 2.18 \times 10^{-3},\ \ \Gamma^{\mathrm{tot}}_{h_4} = 10^{-3}$

Table D.1: Benchmark point (S1-ss1) from scan S_1, with several scalars of masses close to the mass of the SM-like Higgs. Input parameters at the low scale M_{EWSB} are given in the first box, where we also show for completeness $\mu = 3\lambda v_R/\sqrt{2}$ and $\mathcal{M} = 2\kappa v_R/\sqrt{2}$ since their values determine Higgsino and right-handed neutrino masses. Scalar, pseudoscalar and charged Higgs masses are shown in the second, third and fourth boxes, respectively. Scalar mass eigenstates are denoted by $h_{1,\ldots,8}$, pseudoscalars by $A_{2,\ldots,8}$ and charged Higgses by $H^-_{2,\ldots,8}$ associating the first states to the Goldstone bosons eaten by the Z and $W^\pm$. Their dominant composition is written in brackets. For the case of the SM-like Higgs and singlet-like scalars their main compositions are broken down in the fifth box. Their branching ratios are shown in the sixth-nineth boxes. Their decay widths are shown in the tenth box. VEVs, soft parameters, sparticle masses and decay widths are given in GeV.

D.2 *Scan 2* $(0.2 \leq \lambda < 0.5)$

S2-R1
$\lambda = 0.25,\ \ \kappa = 0.56,\ \ v_R/\sqrt{2} = 203.73\ (\mu = 152.79,\ \mathcal{M} = 228.17)$ $\tan\beta = 2.31,\ \ T_\lambda = 82.2,\ \ -T_\kappa = 0.56,\ \ -T_{u_3} = 1515,\ \ m_{\widetilde{Q}_{3L}} = 1700$
$m_{h_1}(H_u^{\mathcal{R}}) = 125.17,\ \ m_{h_2}(\widetilde{\nu}_{\tau L}^{\mathcal{R}}) = 159.82,\ m_{h_3}(\widetilde{\nu}_R^{\mathcal{R}}) = 227.54,\ \ m_{h_4}(\widetilde{\nu}_R^{\mathcal{R}}) = 232.34$ $m_{h_5}(\widetilde{\nu}_R^{\mathcal{R}}) = 239.13,\ \ m_{h_6}(\widetilde{\nu}_{\mu L}^{\mathcal{R}}) = 340.90,\ \ m_{h_7}(H_d^{\mathcal{R}}) = 433.89,\ \ m_{h_8}(\widetilde{\nu}_{eL}^{\mathcal{R}}) = 557.08$
$m_{A_2}(\widetilde{\nu}_R^{\mathcal{I}}) = 91.61,\ \ m_{A_3}(\widetilde{\nu}_R^{\mathcal{I}}) = 92.45,\ \ m_{A_4}(\widetilde{\nu}_R^{\mathcal{I}}) = 110.37$ $m_{A_5}(\widetilde{\nu}_{\tau L}^{\mathcal{I}}) = 159.82,\ \ m_{A_6}(\widetilde{\nu}_{\mu L}^{\mathcal{I}}) = 340.90,\ \ m_{A_7}(H_d^{\mathcal{I}}) = 424.37,\ \ m_{A_8}(\widetilde{\nu}_{eL}^{\mathcal{I}}) = 557.08$
$m_{H_2^-}(\widetilde{\tau}_L) = 173.21,\ \ m_{H_3^-}(\widetilde{\mu}_L) = 346.13,\ \ m_{H_4^-}(H_d^-) = 426.77$ $m_{H_5^-}(\widetilde{e}_L) = 558.46,\ \ m_{H_6^-}(\widetilde{\tau}_R) = 1003.45,\ \ m_{H_7^-}(\widetilde{\mu}_R) = 1003.51,\ \ m_{H_8^-}(\widetilde{e}_R) = 1003.51$
$\lvert Z^H_{h_1\widetilde{\nu}_{eR}^{\mathcal{R}}}\rvert^2 = 2.85\,\%,\ \lvert Z^H_{h_1\widetilde{\nu}_{\mu R}^{\mathcal{R}}}\rvert^2 = 2.76\,\%,\ \lvert Z^H_{h_1\widetilde{\nu}_{\tau R}^{\mathcal{R}}}\rvert^2 = 2.68\,\%,\ \ \lvert Z^H_{h_1 H_d^{\mathcal{R}}}\rvert^2 = 19.36\,\%,\ \ \lvert Z^H_{h_1 H_u^{\mathcal{R}}}\rvert^2 = 72.32\,\%$ $\lvert Z^H_{h_3\widetilde{\nu}_{eR}^{\mathcal{R}}}\rvert^2 = 84.34\,\%,\ \lvert Z^H_{h_3\widetilde{\nu}_{\mu R}^{\mathcal{R}}}\rvert^2 = 12.37\,\%,\ \lvert Z^H_{h_3\widetilde{\nu}_{\tau R}^{\mathcal{R}}}\rvert^2 = 2.44\,\%,\ \ \lvert Z^H_{h_3 H_d^{\mathcal{R}}}\rvert^2 = 0.016\,\%,\ \ \lvert Z^H_{h_3 H_u^{\mathcal{R}}}\rvert^2 = 0.83\,\%$ $\lvert Z^H_{h_4\widetilde{\nu}_{eR}^{\mathcal{R}}}\rvert^2 = 4.50\,\%,\ \lvert Z^H_{h_4\widetilde{\nu}_{\mu R}^{\mathcal{R}}}\rvert^2 = 66.66\,\%,\ \lvert Z^H_{h_4\widetilde{\nu}_{\tau R}^{\mathcal{R}}}\rvert^2 = 27.59\,\%,\ \ \lvert Z^H_{h_4 H_d^{\mathcal{R}}}\rvert^2 = 0.03\,\%,\ \ \lvert Z^H_{h_4 H_u^{\mathcal{R}}}\rvert^2 = 1.20\,\%$ $\lvert Z^H_{h_5\widetilde{\nu}_{eR}^{\mathcal{R}}}\rvert^2 = 6.88\,\%,\ \lvert Z^H_{h_5\widetilde{\nu}_{\mu R}^{\mathcal{R}}}\rvert^2 = 16.70\,\%,\ \lvert Z^H_{h_5\widetilde{\nu}_{\tau R}^{\mathcal{R}}}\rvert^2 = 65.72\,\%,\ \ \lvert Z^H_{h_5 H_d^{\mathcal{R}}}\rvert^2 = 0.4\,\%,\ \ \lvert Z^H_{h_5 H_u^{\mathcal{R}}}\rvert^2 = 10.29\,\%$
$\mathrm{BR}(h_1 \to bb) = 0.5548,\ \ \mathrm{BR}(h_1 \to \tau\tau) = 0.0926,\ \ \mathrm{BR}(h_1 \to WW) = 0.219$ $\mathrm{BR}(h_1 \to ZZ) = 0.0239,\ \ \mathrm{BR}(h_1 \to \gamma\gamma) = 0.00235,\ \ \mathrm{BR}(h_1 \to gg) = 0.088$
$\Gamma^{\mathrm{tot}}_{h_1} = 3.48 \times 10^{-3}$

Table D.2: Benchmark point (S2-R1) from scan S_2, with the scalar h_1 as the SM-like Higgs. Input parameters at the low scale M_{EWSB} are given in the first box, where we also show for completeness $\mu = 3\lambda v_R/\sqrt{2}$ and $\mathcal{M} = 2\kappa v_R/\sqrt{2}$ since their values determine Higgsino and right-handed neutrino masses. Scalar, pseudoscalar and charged Higgs masses are shown in the second, third and fourth boxes, respectively. Scalar mass eigenstates are denoted by $h_{1,\ldots,8}$, pseudoscalars by $A_{2,\ldots,8}$ and charged Higgses by $H^-_{2,\ldots,8}$ associating the first states to the Goldstone bosons eaten by the Z and $W^\pm$. Their dominant composition is written in brackets. For the case of the SM-like Higgs and singlet-like scalars their main compositions are broken down in the fifth box. Relevant branching ratios for h_1 are shown in the sixth box. Its decay width is shown in the seventh box. VEVs, soft parameters, sparticle masses and decay widths are given in GeV.

S2-R2
$\lambda = 0.231,\ \ \kappa = 0.4,\ \ v_R/\sqrt{2} = 775.53\ (\mu = 537.44,\ \mathcal{M} = 620.42)$ $\tan\beta = 1.08,\ \ T_\lambda = 51.0,\ -T_\kappa = 31.93,\ \ -T_{u_3} = 1961.5,\ \ m_{\widetilde{Q}_{3L}} = 1646.89$
$m_{h_1}(H_u^{\mathcal{R}}) = 125.08,\ \ m_{h_2}(\widetilde{\nu}_{\tau L}^{\mathcal{R}}) = 280.48,\ \ m_{h_3}(\widetilde{\nu}_R^{\mathcal{R}}) = 598.58,\ \ m_{h_4}(\widetilde{\nu}_{\mu L}^{\mathcal{R}}) = 609.21$ $m_{h_5}(\widetilde{\nu}_R^{\mathcal{R}}) = 613.25,\ \ m_{h_6}(\widetilde{\nu}_R^{\mathcal{R}}) = 693.20,\ \ m_{h_7}(H_d^{\mathcal{R}}) = 748.88,\ \ m_{h_8}(\widetilde{\nu}_{eL}^{\mathcal{R}}) = 982.96$
$m_{A_2}(\widetilde{\nu}_R^{\mathcal{I}}) = 279.06,\ \ m_{A_3}(\widetilde{\nu}_R^{\mathcal{I}}) = 279.37,\ \ m_{A_4}(\widetilde{\nu}_{\tau L}^{\mathcal{I}}) = 280.48$ $m_{A_5}(\widetilde{\nu}_R^{\mathcal{I}}) = 283.94,\ \ m_{A_6}(\widetilde{\nu}_{\mu L}^{\mathcal{I}}) = 609.21,\ \ m_{A_7}(H_d^{\mathcal{I}}) = 744.60,\ \ m_{A_8}(\widetilde{\nu}_{eL}^{\mathcal{I}}) = 982.96$
$m_{H_2^-}(\widetilde{\tau}_L) = 282.95,\ \ m_{H_3^-}(\widetilde{\mu}_L) = 614.07,\ \ m_{H_4^-}(H_d^-) = 746.13$ $m_{H_5^-}(\widetilde{e}_L) = 981.86,\ \ m_{H_6^-}(\widetilde{\tau}_R) = 1003.57,\ \ m_{H_7^-}(\widetilde{e}_R) = 1003.60,\ \ m_{H_8^-}(\widetilde{\mu}_R) = 1003.60$
$\lvert Z^H_{h_1\widetilde{\nu}_{eR}^{\mathcal{R}}}\rvert^2 = 0.40\,\%,\ \ \lvert Z^H_{h_1\widetilde{\nu}_{\mu R}^{\mathcal{R}}}\rvert^2 = 0.33\,\%,\ \ \lvert Z^H_{h_1\widetilde{\nu}_{\tau R}^{\mathcal{R}}}\rvert^2 = 0.27\,\%\ ,\ \ \lvert Z^H_{h_1 H_d^{\mathcal{R}}}\rvert^2 = 46.66\,\%,\ \ \lvert Z^H_{h_1 H_u^{\mathcal{R}}}\rvert^2 = 52.33\,\%$ $\lvert Z^H_{h_3\widetilde{\nu}_{eR}^{\mathcal{R}}}\rvert^2 = 66.18\,\%,\ \lvert Z^H_{h_3\widetilde{\nu}_{\mu R}^{\mathcal{R}}}\rvert^2 = 30.21\,\%,\ \lvert Z^H_{h_3\widetilde{\nu}_{\tau R}^{\mathcal{R}}}\rvert^2 = 3.6\,\%,\ \ \lvert Z^H_{h_3 H_d^{\mathcal{R}}}\rvert^2 = 0.0048\,\%,\ \ \lvert Z^H_{h_3 H_u^{\mathcal{R}}}\rvert^2 = 0.0055\,\%$ $\lvert Z^H_{h_5\widetilde{\nu}_{eR}^{\mathcal{R}}}\rvert^2 = 5.53\,\%,\ \lvert Z^H_{h_5\widetilde{\nu}_{\mu R}^{\mathcal{R}}}\rvert^2 = 37.14\,\%,\ \lvert Z^H_{h_5\widetilde{\nu}_{\tau R}^{\mathcal{R}}}\rvert^2 = 57.3\,\%,\ \ \lvert Z^H_{h_5 H_d^{\mathcal{R}}}\rvert^2 = 0.0053\,\%,\ \ \lvert Z^H_{h_5 H_u^{\mathcal{R}}}\rvert^2 = 0.0059\,\%$ $\lvert Z^H_{h_6\widetilde{\nu}_{eR}^{\mathcal{R}}}\rvert^2 = 27.87\,\%,\ \lvert Z^H_{h_6\widetilde{\nu}_{\mu R}^{\mathcal{R}}}\rvert^2 = 32.29\,\%,\ \lvert Z^H_{h_6\widetilde{\nu}_{\tau R}^{\mathcal{R}}}\rvert^2 = 38.80\,\%,\ \ \lvert Z^H_{h_6 H_d^{\mathcal{R}}}\rvert^2 = 0.70\,\%,\ \ \lvert Z^H_{h_6 H_u^{\mathcal{R}}}\rvert^2 = 0.31\,\%$
$\mathrm{BR}(h_1 \to bb) = 0.497,\ \ \mathrm{BR}(h_1 \to \tau\tau) = 0.0827,\ \ \mathrm{BR}(h_1 \to WW) = 0.256$ $\mathrm{BR}(h_1 \to ZZ) = 0.0279,\ \ \mathrm{BR}(h_1 \to \gamma\gamma) = 0.00293,\ \ \mathrm{BR}(h_1 \to gg) = 0.109$
$\Gamma^{\mathrm{tot}}_{h_1} = 3.20 \times 10^{-3}$

Table D.3: The same as in Table D.2, but for a different benchmark point.

S2-ss1
$\lambda = 0.39,\ \ \kappa = 0.08,\ \ v_R/\sqrt{2} = 348.75\ (\mu = 408.03,\ \mathcal{M} = 55.8)$ $\tan\beta = 2.25,\ \ T_\lambda = 418,\ -T_\kappa = 0.52,\ \ -T_{u_3} = 294.42,\ \ m_{\widetilde{Q}_{3L}} = 1433.3$
$m_{h_1}(H_u^{\mathcal{R}}) = 123.18,\ \ m_{h_2}(\widetilde{\nu}_R^{\mathcal{R}}) = 125.98,\ \ m_{h_3}(\widetilde{\nu}_R^{\mathcal{R}}) = 126.55,\ \ m_{h_4}(\widetilde{\nu}_R^{\mathcal{R}}) = 139.93$ $m_{h_5}(\widetilde{\nu}_{\tau L}^{\mathcal{R}}) = 212.71,\ \ m_{h_6}(\widetilde{\nu}_{\mu L}^{\mathcal{R}}) = 460.55,\ \ m_{h_7}(\widetilde{\nu}_{eL}^{\mathcal{R}}) = 737.57,\ \ m_{h_8}(H_d^{\mathcal{R}}) = 1088.04$
$m_{A_2}(\widetilde{\nu}_R^{\mathcal{I}}) = 77.24,\ \ m_{A_3}(\widetilde{\nu}_R^{\mathcal{I}}) = 126.19,\ \ m_{A_4}(\widetilde{\nu}_R^{\mathcal{I}}) = 126.41$ $m_{A_5}(\widetilde{\nu}_{\tau L}^{\mathcal{I}}) = 212.71,\ \ m_{A_6}(\widetilde{\nu}_{\mu L}^{\mathcal{I}}) = 460.55,\ \ m_{A_7}(\widetilde{\nu}_{eL}^{\mathcal{I}}) = 737.57,\ \ m_{A_8}(H_d^{\mathcal{I}}) = 1085.45$
$m_{H_2^-}(\widetilde{\tau}_L) = 221.36,\ \ m_{H_3^-}(\widetilde{\mu}_L) = 463.71,\ \ m_{H_4^-}(\widetilde{e}_L) = 737.61$ $m_{H_5^-}(\widetilde{\tau}_R) = 1003.78,\ \ m_{H_6^-}(\widetilde{\mu}_R) = 1003.81,\ \ m_{H_7^-}(\widetilde{e}_R) = 1003.81,\ \ m_{H_8^-}(H_d^-) = 1083.20$
$\lvert Z^H_{h_1\widetilde{\nu}_{eR}^{\mathcal{R}}}\rvert^2 = 5.53\,\%,\ \ \lvert Z^H_{h_1\widetilde{\nu}_{\mu R}^{\mathcal{R}}}\rvert^2 = 1.71\,\%,\ \ \lvert Z^H_{h_1\widetilde{\nu}_{\tau R}^{\mathcal{R}}}\rvert^2 = 0.3\,\%,\ \ \lvert Z^H_{h_1 H_d^{\mathcal{R}}}\rvert^2 = 14.03\,\%,\ \ \lvert Z^H_{h_1 H_u^{\mathcal{R}}}\rvert^2 = 78.40\,\%$ $\lvert Z^H_{h_2\widetilde{\nu}_{eR}^{\mathcal{R}}}\rvert^2 = 59.00\,\%,\ \ \lvert Z^H_{h_2\widetilde{\nu}_{\mu R}^{\mathcal{R}}}\rvert^2 = 36.82\,\%,\ \ \lvert Z^H_{h_2\widetilde{\nu}_{\tau R}^{\mathcal{R}}}\rvert^2 = 3.26\,\%,\ \ \lvert Z^H_{h_2 H_d^{\mathcal{R}}}\rvert^2 = 0.14\,\%,\ \ \lvert Z^H_{h_2 H_u^{\mathcal{R}}}\rvert^2 = 0.76\,\%$ $\lvert Z^H_{h_3\widetilde{\nu}_{eR}^{\mathcal{R}}}\rvert^2 = 5.54\,\%,\ \ \lvert Z^H_{h_3\widetilde{\nu}_{\mu R}^{\mathcal{R}}}\rvert^2 = 30.15\,\%,\ \ \lvert Z^H_{h_3\widetilde{\nu}_{\tau R}^{\mathcal{R}}}\rvert^2 = 63.54\,\%,\ \ \lvert Z^H_{h_3 H_d^{\mathcal{R}}}\rvert^2 = 0.12\,\%,\ \ \lvert Z^H_{h_3 H_u^{\mathcal{R}}}\rvert^2 = 0.63\,\%$ $\lvert Z^H_{h_4\widetilde{\nu}_{eR}^{\mathcal{R}}}\rvert^2 = 29.73\,\%,\ \ \lvert Z^H_{h_4\widetilde{\nu}_{\mu R}^{\mathcal{R}}}\rvert^2 = 31.13\,\%,\ \ \lvert Z^H_{h_4\widetilde{\nu}_{\tau R}^{\mathcal{R}}}\rvert^2 = 32.70\,\%,\ \ \lvert Z^H_{h_4 H_d^{\mathcal{R}}}\rvert^2 = 2.65\,\%,\ \ \lvert Z^H_{h_4 H_u^{\mathcal{R}}}\rvert^2 = 3.77\,\%$
$\mathrm{BR}(h_1 \to bb) = 0.487,\ \ \mathrm{BR}(h_1 \to \tau\tau) = 0.0798,\ \ \mathrm{BR}(h_1 \to WW) = 0.225$ $\mathrm{BR}(h_1 \to ZZ) = 0.0231,\ \ \mathrm{BR}(h_1 \to \gamma\gamma) = 0.0030,\ \ \mathrm{BR}(h_1 \to \widetilde{\chi}^0\widetilde{\chi}^0) = 0.0367,\ \ \mathrm{BR}(h_1 \to gg) = 0.120$
$\mathrm{BR}(h_2 \to bb) = 0.0133,\ \ \mathrm{BR}(h_2 \to \tau\tau) = 0.00218,\ \ \mathrm{BR}(h_2 \to WW) = 0.00791$ $\mathrm{BR}(h_2 \to ZZ) = 0.00087,\ \ \mathrm{BR}(h_2 \to \gamma\gamma) = 0.000084,\ \ \mathrm{BR}(h_2 \to \widetilde{\chi}^0\widetilde{\chi}^0) = 0.971,\ \ \mathrm{BR}(h_2 \to gg) = 0.00324$
$\mathrm{BR}(h_3 \to bb) = 0.0127,\ \ \mathrm{BR}(h_3 \to \tau\tau) = 0.00208,\ \ \mathrm{BR}(h_3 \to WW) = 0.00793$ $\mathrm{BR}(h_3 \to ZZ) = 0.00089,\ \ \mathrm{BR}(h_3 \to \gamma\gamma) = 0.00008,\ \ \mathrm{BR}(h_3 \to \widetilde{\chi}^0\widetilde{\chi}^0) = 0.972,\ \ \mathrm{BR}(h_3 \to gg) = 0.00309$
$\mathrm{BR}(h_4 \to bb) = 0.054,\ \ \mathrm{BR}(h_4 \to \tau\tau) = 0.0089,\ \ \mathrm{BR}(h_4 \to WW) = 0.0447$ $\mathrm{BR}(h_4 \to ZZ) = 0.00588,\ \ \mathrm{BR}(h_4 \to \gamma\gamma) = 0.000115,\ \ \mathrm{BR}(h_4 \to \widetilde{\chi}^0\widetilde{\chi}^0) = 0.88,\ \ \mathrm{BR}(h_4 \to gg) = 0.00436$
$\Gamma^{\mathrm{tot}}_{h_1} = 2.74 \times 10^{-3},\ \ \Gamma^{\mathrm{tot}}_{h_2} = 1.05 \times 10^{-3},\ \ \Gamma^{\mathrm{tot}}_{h_3} = 9.22 \times 10^{-4}\ ,\ \ \Gamma^{\mathrm{tot}}_{h_4} = 5.27 \times 10^{-3}$

Table D.4: The same as in Table D.1, but for a benchmark point (S2-ss1) from scan S_2.

D.3 *Scan 3* ($0.5 \leq \lambda < 1.2$)

S3-ss1
$\lambda = 0.5,\ \ \kappa = 0.23,\ \ v_R/\sqrt{2} = 109.35\ (\mu = 164.02,\ \mathcal{M} = 50.3)$ $\tan\beta = 3.48,\ \ T_\lambda = 309.70,\ \ -T_\kappa = 0.58,\ \ -T_{u_3} = 386.93,\ \ m_{\widetilde{Q}_{3L}} = 1340.97$
$m_{h_1}(\widetilde{\nu}_R^{\mathcal{R}}) = 83.95,\ \ m_{h_2}(\widetilde{\nu}_{\tau L}^{\mathcal{R}}) = 123.06,\ \ m_{h_3}(\widetilde{\nu}_R^{\mathcal{R}}) = 126.32,\ \ m_{h_4}(\widetilde{\nu}_R^{\mathcal{R}}) = 126.76$ $m_{h_5}(H_u^{\mathcal{R}}) = 127.48,\ \ m_{h_6}(\widetilde{\nu}_{\mu L}^{\mathcal{R}}) = 260.06,\ \ m_{h_7}(\widetilde{\nu}_{eL}^{\mathcal{R}}) = 423.60,\ \ m_{h_8}(H_d^{\mathcal{R}}) = 619.46$
$m_{A_2}(\widetilde{\nu}_R^{\mathcal{I}}) = 101.28,\ \ m_{A_3}(\widetilde{\nu}_{\tau L}^{\mathcal{I}}) = 123.06,\ \ m_{A_4}(\widetilde{\nu}_R^{\mathcal{I}}) = 136.48$ $m_{A_5}(\widetilde{\nu}_R^{\mathcal{I}}) = 136.87,\ \ m_{A_6}(\widetilde{\nu}_{\mu L}^{\mathcal{I}}) = 260.67,\ \ m_{A_7}(\widetilde{\nu}_{eL}^{\mathcal{I}}) = 423.67,\ \ m_{A_8}(H_d^{\mathcal{I}}) = 622.49$
$m_{H_2^-}(\widetilde{\tau}_L) = 141.29,\ \ m_{H_3^-}(\widetilde{\mu}_L) = 269.37,\ \ m_{H_4^-}(\widetilde{e}_L) = 425.31$ $m_{H_5^-}(H_d^-) = 601.69,\ \ m_{H_6^-}(\widetilde{\tau}_R) = 1003.12,\ \ m_{H_7^-}(\widetilde{\mu}_L) = 1003.19,\ \ m_{H_8^-}(\widetilde{e}_R) = 1003.19$
$\lvert Z^H_{h_1\widetilde{\nu}_{eR}^{\mathcal{R}}}\rvert^2 = 32.12\,\%,\ \ \lvert Z^H_{h_1\widetilde{\nu}_{\mu R}^{\mathcal{R}}}\rvert^2 = 31.73\,\%,\ \ \lvert Z^H_{h_1\widetilde{\nu}_{\tau R}^{\mathcal{R}}}\rvert^2 = 31.34\,\%,\ \ \lvert Z^H_{h_1 H_d^{\mathcal{R}}}\rvert^2 = 4.78\,\%,\ \ \lvert Z^H_{h_1 H_u^{\mathcal{R}}}\rvert^2 = 1.42\,\%$ $\lvert Z^H_{h_3\widetilde{\nu}_{eR}^{\mathcal{R}}}\rvert^2 = 62.64\,\%,\ \ \lvert Z^H_{h_3\widetilde{\nu}_{\mu R}^{\mathcal{R}}}\rvert^2 = 31.89\,\%,\ \ \lvert Z^H_{h_3\widetilde{\nu}_{\tau R}^{\mathcal{R}}}\rvert^2 = 5.07\,\%,\ \ \lvert Z^H_{h_3 H_d^{\mathcal{R}}}\rvert^2 = 0.027\,\%,\ \ \lvert Z^H_{h_3 H_u^{\mathcal{R}}}\rvert^2 = 0.361\,\%$ $\lvert Z^H_{h_4\widetilde{\nu}_{eR}^{\mathcal{R}}}\rvert^2 = 3.73\,\%,\ \ \lvert Z^H_{h_4\widetilde{\nu}_{\mu R}^{\mathcal{R}}}\rvert^2 = 34.82\,\%,\ \ \lvert Z^H_{h_4\widetilde{\nu}_{\tau R}^{\mathcal{R}}}\rvert^2 = 60.92\,\%,\ \ \lvert Z^H_{h_4 H_d^{\mathcal{R}}}\rvert^2 = 0.035\,\%,\ \ \lvert Z^H_{h_4 H_u^{\mathcal{R}}}\rvert^2 = 0.49\,\%$ $\lvert Z^H_{h_5\widetilde{\nu}_{eR}^{\mathcal{R}}}\rvert^2 = 0.058\,\%,\ \ \lvert Z^H_{h_5\widetilde{\nu}_{\mu R}^{\mathcal{R}}}\rvert^2 = 0.10\,\%,\ \ \lvert Z^H_{h_5\widetilde{\nu}_{\tau R}^{\mathcal{R}}}\rvert^2 = 1.20\,\%,\ \ \lvert Z^H_{h_5 H_d^{\mathcal{R}}}\rvert^2 = 6.19\,\%,\ \ \lvert Z^H_{h_5 H_u^{\mathcal{R}}}\rvert^2 = 92.45\,\%$
$\mathrm{BR}(h_1 \to bb) = 0.858,\ \ \mathrm{BR}(h_1 \to \tau\tau) = 0.14,\ \ \mathrm{BR}(h_1 \to WW) = 3 \times 10^{-8}$ $\mathrm{BR}(h_1 \to ZZ) = 0.0,\ \ \mathrm{BR}(h_1 \to \gamma\gamma) = 0.000038,\ \ \mathrm{BR}(h_1 \to \widetilde{\chi}^0\widetilde{\chi}^0) = 1.2 \times 10^{-9},\ \ \mathrm{BR}(h_1 \to gg) = 0.000324$
$\mathrm{BR}(h_3 \to bb) = 0.00023,\ \ \mathrm{BR}(h_3 \to \tau\tau) = 0.000037,\ \ \mathrm{BR}(h_3 \to WW) = 0.00014$ $\mathrm{BR}(h_3 \to ZZ) = 0.000016,\ \ \mathrm{BR}(h_3 \to \gamma\gamma) = 0.0000014,\ \ \mathrm{BR}(h_3 \to \widetilde{\chi}^0\widetilde{\chi}^0) = 0.99,\ \ \mathrm{BR}(h_3 \to gg) = 0.000058$
$\mathrm{BR}(h_4 \to bb) = 0.000314,\ \ \mathrm{BR}(h_4 \to \tau\tau) = 0.000051,\ \ \mathrm{BR}(h_4 \to WW) = 0.000213$ $\mathrm{BR}(h_4 \to ZZ) = 0.000024,\ \ \mathrm{BR}(h_4 \to \gamma\gamma) = 0.0000021,\ \ \mathrm{BR}(h_4 \to \widetilde{\chi}^0\widetilde{\chi}^0) = 0.99,\ \ \mathrm{BR}(h_4 \to gg) = 0.000082$
$\mathrm{BR}(h_5 \to bb) = 0.37,\ \ \mathrm{BR}(h_5 \to \tau\tau) = 0.060,\ \ \mathrm{BR}(h_5 \to WW) = 0.293$ $\mathrm{BR}(h_5 \to ZZ) = 0.0337,\ \ \mathrm{BR}(h_5 \to \gamma\gamma) = 0.00280,\ \mathrm{BR}(h_5 \to \widetilde{\chi}^0\widetilde{\chi}^0) = 0.115,\ \ \mathrm{BR}(h_5 \to gg) = 0.1$
$\Gamma^{\mathrm{tot}}_{h_1} = 7.85 \times 10^{-4},\ \ \Gamma^{\mathrm{tot}}_{h_3} = 2.58 \times 10^{-2},\ \ \Gamma^{\mathrm{tot}}_{h_4} = 2.42 \times 10^{-2},\ \ \Gamma^{\mathrm{tot}}_{h_5} = 3.64 \times 10^{-3}$

Table D.5: The same as in Table D.1, but for a benchmark point (S3-ss1) from scan S_3.

Bibliography

[1] **ATLAS** Collaboration, G. Aad *et al.*, "Observation of a new particle in the search for the Standard Model Higgs boson with the ATLAS detector at the LHC," *Phys. Lett.* **B716** (2012) 1–29, arXiv:1207.7214 [hep-ex].

[2] **CMS** Collaboration, S. Chatrchyan *et al.*, "Observation of a New Boson at a Mass of 125 GeV with the CMS Experiment at the LHC," *Phys. Lett.* **B716** (2012) 30–61, arXiv:1207.7235 [hep-ex].

[3] H. E. Haber and G. L. Kane, "The Search for Supersymmetry: Probing Physics Beyond the Standard Model," *Phys. Rept.* **117** (1985) 75–263.

[4] I. Simonsen, "A Review of minimal supersymmetric electroweak theory," arXiv:hep-ph/9506369 [hep-ph].

[5] L. Ryder, *Quantum Field Theory*. Cambridge University Press, 1996. https://books.google.es/books$?$id=nnuW_kVJ500C.

[6] S. P. Martin, "A Supersymmetry primer," arXiv:hep-ph/9709356 [hep-ph]. [Adv. Ser. Direct. High Energy Phys.18,1(1998)].

[7] M. Drees, R. Godbole, and P. Roy, *Theory and phenomenology of sparticles: An account of four-dimensional N=1 supersymmetry in high energy physics*. 2004.

[8] D. E. Lopez-Fogliani and C. Muñoz, "Proposal for a Supersymmetric Standard Model," *Phys. Rev. Lett.* **97** (2006) 041801, arXiv:hep-ph/0508297 [hep-ph].

[9] J. E. Kim and H. P. Nilles, "The μ Problem and the Strong CP Problem," *Phys. Lett.* **138B** (1984) 150–154.

[10] F. Capozzi, E. Di Valentino, E. Lisi, A. Marrone, A. Melchiorri, and A. Palazzo, "Global constraints on absolute neutrino masses and their ordering," *Phys. Rev.* **D95** no. 9, (2017) 096014, arXiv:1703.04471 [hep-ph].

[11] P. F. de Salas, D. V. Forero, C. A. Ternes, M. Tortola, and J. W. F. Valle, "Status of neutrino oscillations 2018: 3σ hint for normal mass ordering and improved CP sensitivity," *Phys. Lett.* **B782** (2018) 633–640, arXiv:1708.01186 [hep-ph].

[12] P. F. De Salas, S. Gariazzo, O. Mena, C. A. Ternes, and M. Tórtola, "Neutrino Mass Ordering from Oscillations and Beyond: 2018 Status and Future Prospects," *Front. Astron. Space Sci.* **5** (2018) 36, arXiv:1806.11051 [hep-ph].

[13] I. Esteban, M. C. Gonzalez-Garcia, A. Hernandez-Cabezudo, M. Maltoni, and T. Schwetz, "Global analysis of three-flavour neutrino oscillations: synergies and tensions in the determination of θ_{23}, δ_{CP}, and the mass ordering," *JHEP* **01** (2019) 106, arXiv:1811.05487 [hep-ph].

[14] S. Weinberg, "Supersymmetry at Ordinary Energies. 1. Masses and Conservation Laws," *Phys. Rev.* **D26** (1982) 287.

[15] N. Sakai and T. Yanagida, "Proton Decay in a Class of Supersymmetric Grand Unified Models," *Nucl. Phys.* **B197** (1982) 533.

[16] S. Dimopoulos, S. Raby, and F. Wilczek, "Proton Decay in Supersymmetric Models," *Phys. Lett.* **B112** (1982) 133.

[17] F. Zwirner, "Observable Delta B=2 Transitions Without Nucleon Decay in a Minimal Supersymmetric Extension of the Standard Model," *Phys. Lett.* **B132** (1983) 103–106.

[18] L. J. Hall and M. Suzuki, "Explicit R-Parity Breaking in Supersymmetric Models," *Nucl. Phys.* **B231** (1984) 419–444.

[19] R. Barbier *et al.*, "R-parity violating supersymmetry," *Phys. Rept.* **420** (2005) 1–202, arXiv:hep-ph/0406039 [hep-ph].

[20] P. Ghosh, I. Lara, D. E. López-Fogliani, C. Muñoz, and R. Ruiz de Austri, "Searching for left sneutrino LSP at the LHC," *Int. J. Mod. Phys.* **A33** no. 18n19, (2018) 1850110, arXiv:1707.02471 [hep-ph].

[21] I. Lara, D. E. López-Fogliani, C. Muñoz, N. Nagata, H. Otono, and R. Ruiz De Austri, "Looking for the left sneutrino LSP with displaced-vertex searches," *Phys. Rev.* **D98** no. 7, (2018) 075004, arXiv:1804.00067 [hep-ph].

[22] S. Weinberg, "Implications of Dynamical Symmetry Breaking," *Phys. Rev.* **D13** (1976) 974–996. [Addendum: Phys. Rev.D19,1277(1979)].

[23] E. Gildener, "Gauge Symmetry Hierarchies," *Phys. Rev.* **D14** (1976) 1667.

[24] L. Susskind, "Dynamics of Spontaneous Symmetry Breaking in the Weinberg-Salam Theory," *Phys. Rev.* **D20** (1979) 2619–2625.

[25] D. V. Forero, M. Tortola, and J. W. F. Valle, "Global status of neutrino oscillation parameters after Neutrino-2012," *Phys. Rev.* **D86** (2012) 073012, arXiv:1205.4018 [hep-ph].

[26] M. C. Gonzalez-Garcia, M. Maltoni, J. Salvado, and T. Schwetz, "Global fit to three neutrino mixing: critical look at present precision," *JHEP* **12** (2012) 123, arXiv:1209.3023 [hep-ph].

[27] **Super-Kamiokande** Collaboration, Y. Fukuda *et al.*, "Evidence for oscillation of atmospheric neutrinos," *Phys. Rev. Lett.* **81** (1998) 1562–1567, arXiv:hep-ex/9807003 [hep-ex].

[28] **SNO** Collaboration, Q. R. Ahmad *et al.*, "Direct evidence for neutrino flavor transformation from neutral current interactions in the Sudbury Neutrino Observatory," *Phys. Rev. Lett.* **89** (2002) 011301, arXiv:nucl-ex/0204008 [nucl-ex].

[29] K. Lande, B. T. Cleveland, T. Daily, R. Davis, J. Distel, C. K. Lee, A. Weinberger, P. Wildenhain, and J. Ullman, "Solar neutrino observations with the Homestake ^{37}Cl detector," *AIP Conf. Proc.* **243** (1992) 1122–1133.

[30] **GNO** Collaboration, M. Altmann *et al.*, "Complete results for five years of GNO solar neutrino observations," *Phys. Lett.* **B616** (2005) 174–190, arXiv:hep-ex/0504037 [hep-ex].

[31] **SAGE** Collaboration, J. N. Abdurashitov *et al.*, "Solar neutrino flux measurements by the Soviet-American Gallium Experiment (SAGE) for half the 22 year solar cycle," *J. Exp. Theor. Phys.* **95** (2002) 181–193, arXiv:astro-ph/0204245 [astro-ph]. [Zh. Eksp. Teor. Fiz.122,211(2002)].

[32] **KamLAND** Collaboration, T. Araki *et al.*, "Measurement of neutrino oscillation with KamLAND: Evidence of spectral distortion," *Phys. Rev. Lett.* **94** (2005) 081801, arXiv:hep-ex/0406035 [hep-ex].

[33] **RENO** Collaboration, J. K. Ahn *et al.*, "Observation of Reactor Electron Antineutrino Disappearance in the RENO Experiment," *Phys. Rev. Lett.* **108** (2012) 191802, arXiv:1204.0626 [hep-ex].

[34] **Daya Bay** Collaboration, F. P. An *et al.*, "Spectral measurement of electron antineutrino oscillation amplitude and frequency at Daya Bay," *Phys. Rev. Lett.* **112** (2014) 061801, arXiv:1310.6732 [hep-ex].

[35] **Double Chooz** Collaboration, Y. Abe *et al.*, "First Measurement of θ_{13} from Delayed Neutron Capture on Hydrogen in the Double Chooz Experiment," *Phys. Lett.* **B723** (2013) 66–70, arXiv:1301.2948 [hep-ex].

[36] **BOREXINO** Collaboration, G. Bellini *et al.*, "Neutrinos from the primary proton–proton fusion process in the Sun," *Nature* **512** no. 7515, (2014) 383–386.

[37] **WMAP** Collaboration, D. N. Spergel *et al.*, "Wilkinson Microwave Anisotropy Probe (WMAP) three year results: implications for cosmology," *Astrophys. J. Suppl.* **170** (2007) 377, arXiv:astro-ph/0603449 [astro-ph].

[38] G. Bertone, ed., *Particle Dark Matter: Observations, Models and Searches*. Cambridge Univ. Press, Cambridge, 2010. http://www.cambridge.org/uk/catalogue/catalogue.asp?isbn=9780521763684.

[39] M. Drees and G. Gerbier, "Mini-Review of Dark Matter: 2012," arXiv:1204.2373 [hep-ph].

[40] K. Garrett and G. Duda, "Dark Matter: A Primer," *Adv. Astron.* **2011** (2011) 968283, arXiv:1006.2483 [hep-ph].

[41] F. Takayama and M. Yamaguchi, "Gravitino dark matter without R-parity," *Phys. Lett.* **B485** (2000) 388–392, arXiv:hep-ph/0005214 [hep-ph].

[42] W. Buchmuller, L. Covi, K. Hamaguchi, A. Ibarra, and T. Yanagida, "Gravitino Dark Matter in R-Parity Breaking Vacua," *JHEP* **03** (2007) 037, arXiv:hep-ph/0702184 [HEP-PH].

[43] H. P. Nilles, "Supersymmetry, Supergravity and Particle Physics," *Phys. Rept.* **110** (1984) 1–162.

[44] D. E. Lopez-Fogliani and C. Muñoz, "On a reinterpretation of the Higgs field in supersymmetry and a proposal for new quarks," *Phys. Lett.* **B771** (2017) 136–141, arXiv:1701.02652 [hep-ph].

[45] **Particle Data Group** Collaboration, J. Beringer *et al.*, "Review of Particle Physics (RPP)," *Phys. Rev.* **D86** (2012) 010001.

[46] S. Weinberg, "A New Light Boson?," *Phys. Rev. Lett.* **40** (1978) 223–226.

[47] F. Wilczek, "Problem of Strong p and t Invariance in the Presence of Instantons," *Phys. Rev. Lett.* **40** (1978) 279–282.

[48] H. P. Nilles, M. Srednicki, and D. Wyler, "Weak Interaction Breakdown Induced by Supergravity," *Phys. Lett.* **B120** (1983) 346.

[49] U. Ellwanger, C. Hugonie, and A. M. Teixeira, "The Next-to-Minimal Supersymmetric Standard Model," *Phys. Rept.* **496** (2010) 1–77, arXiv:0910.1785 [hep-ph].

[50] N. Escudero, D. E. Lopez-Fogliani, C. Muñoz, and R. Ruiz de Austri, "Analysis of the parameter space and spectrum of the $\mu\nu$SSM," *JHEP* **12** (2008) 099, arXiv:0810.1507 [hep-ph].

[51] A. Brignole, L. E. Ibanez, and C. Muñoz, "Soft supersymmetry breaking terms from supergravity and superstring models," *Adv. Ser. Direct. High Energy Phys.* **18** (1998) 125–148, arXiv:hep-ph/9707209 [hep-ph].

[52] P. Ghosh and S. Roy, "Neutrino masses and mixing, lightest neutralino decays and a solution to the mu problem in supersymmetry," *JHEP* **04** (2009) 069, arXiv:0812.0084 [hep-ph].

[53] A. Bartl, M. Hirsch, A. Vicente, S. Liebler, and W. Porod, "LHC phenomenology of the $\mu\nu$SSM," *JHEP* **05** (2009) 120, arXiv:0903.3596 [hep-ph].

[54] J. Fidalgo, D. E. Lopez-Fogliani, C. Munoz, and R. Ruiz de Austri, "Neutrino Physics and Spontaneous CP Violation in the mu nu SSM," *JHEP* **08** (2009) 105, arXiv:0904.3112 [hep-ph].

[55] P. Ghosh, P. Dey, B. Mukhopadhyaya, and S. Roy, "Radiative contribution to neutrino masses and mixing in $\mu\nu$SSM," *JHEP* **05** (2010) 087, arXiv:1002.2705 [hep-ph].

[56] F. Gabbiani, E. Gabrielli, A. Masiero, and L. Silvestrini, "A Complete analysis of FCNC and CP constraints in general SUSY extensions of the standard model," *Nucl. Phys.* **B477** (1996) 321–352, arXiv:hep-ph/9604387 [hep-ph].

[57] E. Kpatcha, I. Lara, D. E. López-Fogliani, C. Muñoz, N. Nagata, H. Otono, and R. Ruiz De Austri, "Sampling the $\mu\nu$SSM for displaced decays of the tau left sneutrino LSP at the LHC," arXiv:1907.02092 [hep-ph].

[58] P. Bandyopadhyay, P. Ghosh, and S. Roy, "Unusual Higgs boson signal in R-parity violating nonminimal supersymmetric models at the LHC," *Phys. Rev.* **D84** (2011) 115022, arXiv:1012.5762 [hep-ph].

[59] J. Fidalgo, D. E. Lopez-Fogliani, C. Munoz, and R. Ruiz de Austri, "The Higgs sector of the $\mu\nu$SSM and collider physics," *JHEP* **10** (2011) 020, arXiv:1107.4614 [hep-ph].

[60] P. Ghosh, D. E. Lopez-Fogliani, V. A. Mitsou, C. Munoz, and R. Ruiz de Austri, "Probing the μ-from-ν supersymmetric standard model with displaced multileptons from the decay of a Higgs boson at the LHC," *Phys. Rev.* **D88** (2013) 015009, arXiv:1211.3177 [hep-ph].

[61] P. Ghosh, D. E. López-Fogliani, V. A. Mitsou, C. Muñoz, and R. Ruiz de Austri, "Hunting physics beyond the standard model with unusual $W^{\pm}$ and Z decays," *Phys. Rev.* **D91** no. 3, (2015) 035020, arXiv:1403.3675 [hep-ph].

[62] P. Ghosh, D. E. Lopez-Fogliani, V. A. Mitsou, C. Muñoz, and R. Ruiz de Austri, "Probing the $\mu\nu$SSM with light scalars, pseudoscalars and neutralinos from the decay of a SM-like Higgs boson at the LHC," *JHEP* **11** (2014) 102, arXiv:1410.2070 [hep-ph].

[63] T. Biekötter, S. Heinemeyer, and C. Muñoz, "Precise prediction for the Higgs-boson masses in the $\mu\nu$SSM," *Eur. Phys. J.* **C78** no. 6, (2018) 504, arXiv:1712.07475 [hep-ph].

[64] T. Biekötter, S. Heinemeyer, and C. Muñoz, "Precise prediction for the Higgs-Boson Masses in the $\mu\nu$SSM with three right-handed neutrino superfields," arXiv:1906.06173 [hep-ph].

[65] L. J. Hall, D. Pinner, and J. T. Ruderman, "A Natural SUSY Higgs Near 126 GeV," *JHEP* **04** (2012) 131, arXiv:1112.2703 [hep-ph].

[66] S. Heinemeyer, O. Stal, and G. Weiglein, "Interpreting the LHC Higgs Search Results in the MSSM," *Phys. Lett.* **B710** (2012) 201–206, arXiv:1112.3026 [hep-ph].

[67] P. Draper, P. Meade, M. Reece, and D. Shih, "Implications of a 125 GeV Higgs for the MSSM and Low-Scale SUSY Breaking," *Phys. Rev.* **D85** (2012) 095007, arXiv:1112.3068 [hep-ph].

[68] H. E. Haber, R. Hempfling, and A. H. Hoang, "Approximating the radiatively corrected Higgs mass in the minimal supersymmetric model," *Z. Phys.* **C75** (1997) 539–554, arXiv:hep-ph/9609331 [hep-ph].

[69] R. Barbieri, L. J. Hall, Y. Nomura, and V. S. Rychkov, "Supersymmetry without a Light Higgs Boson," *Phys. Rev.* **D75** (2007) 035007, arXiv:hep-ph/0607332 [hep-ph].

[70] M. Farina, M. Perelstein, and B. Shakya, "Higgs Couplings and Naturalness in λ-SUSY," *JHEP* **04** (2014) 108, arXiv:1310.0459 [hep-ph].

[71] G. Degrassi and P. Slavich, "On the radiative corrections to the neutral Higgs boson masses in the NMSSM," *Nucl. Phys.* **B825** (2010) 119–150, arXiv:0907.4682 [hep-ph].

[72] T. Gherghetta, B. von Harling, A. D. Medina, and M. A. Schmidt, "The Scale-Invariant NMSSM and the 126 GeV Higgs Boson," *JHEP* **02** (2013) 032, arXiv:1212.5243 [hep-ph].

[73] **ATLAS** Collaboration, G. Aad *et al.*, "Search for massive, long-lived particles using multitrack displaced vertices or displaced lepton pairs in pp collisions at $\sqrt{s}$ = 8 TeV with the ATLAS detector," *Phys. Rev.* **D92** no. 7, (2015) 072004, arXiv:1504.05162 [hep-ex].

[74] I. Lara, D. López-Fogliani, and C. Muñoz, "Electroweak superpartners scrutinized at the LHC in events with multi-leptons," *Phys. Lett.* **B790** (2019) 176–183, arXiv:1810.12455 [hep-ph].

[75] **ATLAS** Collaboration, M. Aaboud *et al.*, "Search for chargino-neutralino production using recursive jigsaw reconstruction in final states with two or three charged leptons in proton-proton collisions at $\sqrt{s} = 13$ TeV with the ATLAS detector," *Phys. Rev.* **D98** no. 9, (2018) 092012, arXiv:1806.02293 [hep-ex].

[76] **ATLAS** Collaboration, T. A. collaboration, "Search for chargino-neutralino production with mass splittings near the electroweak scale in three-lepton final states in $\sqrt{s} = 13$ TeV pp collisions with the ATLAS detector,".

[77] K.-Y. Choi, D. E. Lopez-Fogliani, C. Muñoz, and R. Ruiz de Austri, "Gamma-ray detection from gravitino dark matter decay in the mu nu SSM," *JCAP* **1003** (2010) 028, arXiv:0906.3681 [hep-ph].

[78] G. A. Gomez-Vargas, M. Fornasa, F. Zandanel, A. J. Cuesta, C. Munoz, F. Prada, and G. Yepes, "CLUES on Fermi-LAT prospects for the extragalactic detection of munuSSM gravitino Dark Matter," *JCAP* **1202** (2012) 001, arXiv:1110.3305 [astro-ph.HE].

[79] **Fermi-LAT** Collaboration, A. Albert, G. A. Gomez-Vargas, M. Grefe, C. Munoz, C. Weniger, E. D. Bloom, E. Charles, M. N. Mazziotta, and A. Morselli, "Search for 100 MeV to 10 GeV γ-ray lines in the Fermi-LAT data and implications for gravitino dark matter in $\mu\nu$SSM," *JCAP* **1410** no. 10, (2014) 023, arXiv:1406.3430 [astro-ph.HE].

[80] G. A. Gómez-Vargas, D. E. López-Fogliani, C. Muñoz, A. D. Perez, and R. Ruiz de Austri, "Search for sharp and smooth spectral signatures of $\mu\nu$SSM gravitino dark matter with Fermi-LAT," *JCAP* **1703** no. 03, (2017) 047, arXiv:1608.08640 [hep-ph].

[81] R. Trotta, F. Feroz, M. P. Hobson, L. Roszkowski, and R. Ruiz de Austri, "The Impact of priors and observables on parameter inferences in the Constrained MSSM," *JHEP* **12** (2008) 024, arXiv:0809.3792 [hep-ph].

[82] F. Feroz and M. P. Hobson, "Multimodal nested sampling: an efficient and robust alternative to MCMC methods for astronomical data analysis," *Mon. Not. Roy. Astron. Soc.* **384** (2008) 449, arXiv:0704.3704 [astro-ph].

[83] F. Feroz, M. P. Hobson, and M. Bridges, "MultiNest: an efficient and robust Bayesian inference tool for cosmology and particle physics," *Mon. Not. Roy. Astron. Soc.* **398** (2009) 1601–1614, arXiv:0809.3437 [astro-ph].

[84] J. Skilling, "Nested Sampling," in *American Institute of Physics Conference Series*, R. Fischer, R. Preuss, and U. V. Toussaint, eds., vol. 735 of *American Institute of Physics Conference Series*, pp. 395–405. Nov., 2004.

[85] J. Skilling, "Nested sampling for general bayesian computation," *Bayesian Anal.* **1** no. 4, (12, 2006) 833–859.

[86] F. Staub, "SARAH 4 : A tool for (not only SUSY) model builders," *Comput. Phys. Commun.* **185** (2014) 1773–1790, arXiv:1309.7223 [hep-ph].

[87] W. Porod, "SPheno, a program for calculating supersymmetric spectra, SUSY particle decays and SUSY particle production at e+ e- colliders," *Comput. Phys. Commun.* **153** (2003) 275–315, arXiv:hep-ph/0301101 [hep-ph].

[88] W. Porod and F. Staub, "SPheno 3.1: Extensions including flavour, CP-phases and models beyond the MSSM," *Comput. Phys. Commun.* **183** (2012) 2458–2469, arXiv:1104.1573 [hep-ph].

[89] **Planck** Collaboration, N. Aghanim *et al.*, "Planck 2018 results. VI. Cosmological parameters," arXiv:1807.06209 [astro-ph.CO].

[90] P. Bechtle, O. Brein, S. Heinemeyer, G. Weiglein, and K. E. Williams, "HiggsBounds: Confronting Arbitrary Higgs Sectors with Exclusion Bounds from LEP and the Tevatron," *Comput. Phys. Commun.* **181** (2010) 138–167, arXiv:0811.4169 [hep-ph].

[91] P. Bechtle, O. Brein, S. Heinemeyer, O. Stål, T. Stefaniak, G. Weiglein, and K. E. Williams, "HiggsBounds – 4: Improved Tests of Extended Higgs Sectors against Exclusion Bounds from LEP, the Tevatron and the LHC," *Eur. Phys. J.* **C74** no. 3, (2014) 2693, arXiv:1311.0055 [hep-ph].

[92] P. Bechtle, S. Heinemeyer, O. Stal, T. Stefaniak, and G. Weiglein, "Applying Exclusion Likelihoods from LHC Searches to Extended Higgs Sectors," *Eur. Phys. J.* **C75** no. 9, (2015) 421, arXiv:1507.06706 [hep-ph].

[93] P. Bechtle, S. Heinemeyer, O. Stål, T. Stefaniak, and G. Weiglein, "*HiggsSignals*: Confronting arbitrary Higgs sectors with measurements at the Tevatron and the LHC," *Eur. Phys. J.* **C74** no. 2, (2014) 2711, arXiv:1305.1933 [hep-ph].

[94] **Heavy Flavor Averaging Group** Collaboration, Y. Amhis *et al.*, "Averages of B-Hadron, C-Hadron, and tau-lepton properties as of early 2012," arXiv:1207.1158 [hep-ex].

[95] **CMS, LHCb** Collaboration, CMS and L. Collaborations, "Combination of results on the rare decays $B^0_{(s)} \to \mu^+\mu^-$ from the CMS and LHCb experiments,".

[96] **Particle Data Group** Collaboration, M. Tanabashi *et al.*, "Review of Particle Physics," *Phys. Rev.* **D98** no. 3, (2018) 030001.

[97] **CMS** Collaboration, A. M. Sirunyan *et al.*, "Combined search for electroweak production of charginos and neutralinos in proton-proton collisions at $\sqrt{s} = 13$ TeV," *JHEP* **03** (2018) 160, arXiv:1801.03957 [hep-ex].

[98] E. Kpatcha, D. E. Lopez-Fogliani, C. Muñoz, and R. Ruiz De Austri, "Impact of Higgs physics on the parameter space of the $\mu\nu$SSM ," *To be published in EPJC* (2019) .

[99] J.-J. Cao, Z.-X. Heng, J. M. Yang, Y.-M. Zhang, and J.-Y. Zhu, "A SM-like Higgs near 125 GeV in low energy SUSY: a comparative study for MSSM and NMSSM," *JHEP* **03** (2012) 086, arXiv:1202.5821 [hep-ph].

[100] J. Cao, Z. Heng, J. M. Yang, and J. Zhu, "Status of low energy SUSY models confronted with the LHC 125 GeV Higgs data," *JHEP* **10** (2012) 079, arXiv:1207.3698 [hep-ph].

[101] S. F. King, M. Mühlleitner, R. Nevzorov, and K. Walz, "Discovery Prospects for NMSSM Higgs Bosons at the High-Energy Large Hadron Collider," *Phys. Rev.* **D90** no. 9, (2014) 095014, arXiv:1408.1120 [hep-ph].

[102] C. Beskidt, W. de Boer, D. I. Kazakov, and S. Wayand, "Higgs branching ratios in constrained minimal and next-to-minimal supersymmetry scenarios surveyed," *Phys. Lett.* **B759** (2016) 141–148, arXiv:1602.08707 [hep-ph].

[103] H. Zhou, Z. Heng, and D. Li, "The properties of the Higgs bosons and Pair Production of the SM-like Higgs Boson in λ-SUSY at the LHC," arXiv:1601.07288 [hep-ph].

[104] J. E. Camargo-Molina, B. O'Leary, W. Porod, and F. Staub, "**Vevacious**: A Tool For Finding The Global Minima Of One-Loop Effective Potentials With Many Scalars," *Eur. Phys. J.* **C73** no. 10, (2013) 2588, arXiv:1307.1477 [hep-ph].

[105] E. Kpatcha, D. López-Fogliani, C. Muñoz, R. Ruiz de Austri, *et al.*, " in preparation," *in preparation* (2019) .

[106] **ATLAS** Collaboration, M. Aaboud *et al.*, "Search for squarks and gluinos in final states with jets and missing transverse momentum using 36 fb^{-1} of $\sqrt{s} = 13$ TeV pp collision data with the ATLAS detector," *Phys. Rev.* **D97** no. 11, (2018) 112001, arXiv:1712.02332 [hep-ex].

[107] **CMS** Collaboration, A. M. Sirunyan *et al.*, "Search for new phenomena with the M_{T2} variable in the all-hadronic final state produced in proton–proton collisions at $\sqrt{s} = 13$ TeV," *Eur. Phys. J.* **C77** no. 10, (2017) 710, arXiv:1705.04650 [hep-ex].

[108] **DELPHI** Collaboration, P. Abreu *et al.*, "Search for supersymmetry with R-parity violating L L anti-E couplings at S**(1/2) = 183-GeV," *Eur. Phys. J.* **C13** (2000) 591.

[109] **DELPHI** Collaboration, P. Abreu *et al.*, "Search for SUSY with R-parity violating LL anti-E couplings at s**(1/2) = 189-GeV," *Phys. Lett.* **B487** (2000) 36, arXiv:hep-ex/0103006 [hep-ex].

[110] **L3** Collaboration, P. Achard *et al.*, "Search for R parity violating decays of supersymmetric particles in e^+e^- collisions at LEP," *Phys. Lett.* **B524** (2002) 65, arXiv:hep-ex/0110057 [hep-ex].

[111] **ALEPH** Collaboration, A. Heister *et al.*, "Search for supersymmetric particles with R parity violating decays in e^+e^- collisions at $\sqrt{s}$ up to 209 GeV," *Eur. Phys. J.* **C31** (2003) 1, arXiv:hep-ex/0210014 [hep-ex].

[112] **OPAL** Collaboration, G. Abbiendi *et al.*, "Search for R parity violating decays of scalar fermions at LEP," *Eur. Phys. J.* **C33** (2004) 149, arXiv:hep-ex/0310054 [hep-ex].

[113] **DELPHI** Collaboration, J. Abdallah *et al.*, "Search for supersymmetric particles assuming R-parity nonconservation in e+ e- collisions at $\sqrt{s} = 192$ GeV to 208 GeV," *Eur. Phys. J.* **C36** no. 1, (2004) 1, arXiv:hep-ex/0406009 [hep-ex]. [Erratum: Eur. Phys. J.C37,no.1,129(2004)].

[114] **DELPHI** Collaboration, J. Abdallah *et al.*, "Photon events with missing energy in e+ e- collisions at $\sqrt{s} = 130$ to 209 GeV," *Eur. Phys. J.* **C38** (2005) 395, arXiv:hep-ex/0406019 [hep-ex].

[115] **ATLAS** Collaboration, M. Aaboud *et al.*, "Search for new phenomena in events with a photon and missing transverse momentum in pp collisions at $\sqrt{s} = 13$ TeV with the ATLAS detector," *JHEP* **06** (2016) 059, arXiv:1604.01306 [hep-ex].

[116] **ATLAS** Collaboration, M. Aaboud *et al.*, "Search for new phenomena in final states with an energetic jet and large missing transverse momentum in pp collisions at $\sqrt{s}$=13 TeV using the ATLAS detector," *Phys. Rev.* **D94** no. 3, (2016) 032005, arXiv:1604.07773 [hep-ex].

[117] **Planck** Collaboration, P. A. R. Ade *et al.*, "Planck 2015 results. XIII. Cosmological parameters," *Astron. Astrophys.* **594** (2016) A13, arXiv:1502.01589 [astro-ph.CO].

[118] **Daya Bay** Collaboration, F. P. An *et al.*, "New measurement of antineutrino oscillation with the full detector configuration at Daya Bay," *Phys. Rev. Lett.* **115** no. 11, (2015) 111802, arXiv:1505.03456 [hep-ex].

[119] **CMS** Collaboration, V. Khachatryan *et al.*, "Search for long-lived particles that decay into final states containing two electrons or two muons in proton-proton collisions at $\sqrt{s} = 8$ TeV," *Phys. Rev.* **D91** no. 5, (2015) 052012, arXiv:1411.6977 [hep-ex].

[120] **ATLAS** Collaboration, M. Aaboud *et al.*, "Search for long-lived, massive particles in events with displaced vertices and missing transverse momentum in $\sqrt{s} = 13$ TeV pp collisions with the ATLAS detector," *Phys. Rev.* **D97** no. 5, (2018) 052012, arXiv:1710.04901 [hep-ex].

[121] **ATLAS** Collaboration, G. Aad *et al.*, "Search for heavy neutral leptons in decays of W bosons produced in 13 TeV pp collisions using prompt and displaced signatures with the ATLAS detector," arXiv:1905.09787 [hep-ex].

[122] **ATLAS** Collaboration, G. Aad *et al.*, "Performance of the ATLAS muon trigger in pp collisions at $\sqrt{s} = 8$ TeV," *Eur. Phys. J.* **C75** (2015) 120, arXiv:1408.3179 [hep-ex].

[123] **CMB-S4** Collaboration, K. N. Abazajian *et al.*, "CMB-S4 Science Book, First Edition," arXiv:1610.02743 [astro-ph.CO].

[124] **ATLAS** Collaboration, M. Aaboud *et al.*, "Search for dark matter at $\sqrt{s} = 13$ TeV in final states containing an energetic photon and large missing transverse momentum with the ATLAS detector," *Eur. Phys. J.* **C77** no. 6, (2017) 393, arXiv:1704.03848 [hep-ex].

[125] **ATLAS** Collaboration, M. Aaboud *et al.*, "Search for dark matter and other new phenomena in events with an energetic jet and large missing transverse momentum using the ATLAS detector," *JHEP* **01** (2018) 126, arXiv:1711.03301 [hep-ex].

[126] H. Ito, O. Jinnouchi, T. Moroi, N. Nagata, and H. Otono, "Extending the LHC Reach for New Physics with Sub-Millimeter Displaced Vertices," *Phys. Lett.* **B771** (2017) 568–575, arXiv:1702.08613 [hep-ph].

[127] H. Ito, O. Jinnouchi, T. Moroi, N. Nagata, and H. Otono, "Searching for Metastable Particles with Sub-Millimeter Displaced Vertices at Hadron Colliders," *JHEP* **06** (2018) 112, arXiv:1803.00234 [hep-ph].

[128] E. Kpatcha, I. Lara, D. E. López-Fogliani, C. Muñoz, *et al.*, "Explaing the anomalous muon (g − 2) in the $\mu\nu$SSM," *To be published in EPJC* (2019) .

[129] **Muon g-2** Collaboration, J. Grange *et al.*, "Muon (g-2) Technical Design Report," arXiv:1501.06858 [physics.ins-det].

[130] T. M. and, "Newg- 2 experiment at j-PARC," *Chinese Physics C* **34** no. 6, (Jun, 2010) 745–748.

[131] A. Lusiani, "Muon $g - 2$, current experimental status and future prospects," *Acta Physica Polonica. Series B* **49** no. 6, (1, 2018) .

[132] F. Jegerlehner, "The Muon g-2 in Progress," *Acta Phys. Polon.* **B49** (2018) 1157, arXiv:1804.07409 [hep-ph].

[133] A. Keshavarzi, D. Nomura, and T. Teubner, "Muon $g-2$ and $\alpha(M_Z^2)$: A new data-based analysis," *Phys. Rev. D* **97** (Jun, 2018) 114025. https://link.aps.org/doi/10.1103/PhysRevD.97.114025.

[134] T. Moroi, "The Muon anomalous magnetic dipole moment in the minimal supersymmetric standard model," *Phys. Rev.* **D53** (1996) 6565–6575, arXiv:hep-ph/9512396 [hep-ph]. [Erratum: Phys. Rev.D56,4424(1997)].

[135] S. P. Martin and J. D. Wells, "Muon Anomalous Magnetic Dipole Moment in Supersymmetric Theories," *Phys. Rev.* **D64** (2001) 035003, arXiv:hep-ph/0103067 [hep-ph].

[136] D. G. Cerdeno, E. Gabrielli, S. Khalil, C. Muñoz, and E. Torrente-Lujan, "Muon anomalous magnetic moment in supersymmetric scenarios with an intermediate scale and nonuniversality," *Phys. Rev.* **D64** (2001) 093012, arXiv:hep-ph/0104242 [hep-ph].

[137] G. F. Giudice, P. Paradisi, A. Strumia, and A. Strumia, "Correlation between the Higgs Decay Rate to Two Photons and the Muon g - 2," *JHEP* **10** (2012) 186, arXiv:1207.6393 [hep-ph].

[138] G. Degrassi and G. F. Giudice, "QED logarithms in the electroweak corrections to the muon anomalous magnetic moment," *Phys. Rev.* **D58** (1998) 053007, arXiv:hep-ph/9803384 [hep-ph].

[139] S. Heinemeyer, D. Stockinger, and G. Weiglein, "Electroweak and supersymmetric two-loop corrections to (g-2)$_\mu$," *Nucl. Phys.* **B699** (2004) 103–123, arXiv:hep-ph/0405255 [hep-ph].

[140] T.-F. Feng, L. Sun, and X.-Y. Yang, "Electroweak and supersymmetric two-loop corrections to lepton anomalous magnetic and electric dipole moments," *Nucl. Phys.* **B800** (2008) 221–252, arXiv:0805.1122 [hep-ph].

[141] J. F. Gunion, D. Hooper, and B. McElrath, "Light neutralino dark matter in the NMSSM," *Phys. Rev.* **D73** (2006) 015011, arXiv:hep-ph/0509024 [hep-ph].

[142] F. Domingo and U. Ellwanger, "Constraints from the muon g-2 on the parameter space of the NMSSM," *Journal of High Energy Physics* **2008** no. 07, (Jul, 2008) 079–079.

[143] D. Chang, W.-F. Chang, C.-H. Chou, and W.-Y. Keung, "Large two loop contributions to g-2 from a generic pseudoscalar boson," *Phys. Rev.* **D63** (2001) 091301, arXiv:hep-ph/0009292 [hep-ph].

[144] K.-m. Cheung, C.-H. Chou, and O. C. W. Kong, "Muon anomalous magnetic moment, two Higgs doublet model, and supersymmetry," *Phys. Rev.* **D64** (2001) 111301, arXiv:hep-ph/0103183 [hep-ph].

[145] M. Krawczyk, "Precision muon g-2 results and light Higgs bosons in the 2HDM(II)," *Acta Phys. Polon.* **B33** (2002) 2621–2634, arXiv:hep-ph/0208076 [hep-ph].

[146] **ATLAS** Collaboration, G. Aad *et al.*, "Search for displaced vertices of oppositely charged leptons from decays of long-lived particles in pp collisions at $\sqrt{s} = 13$ TeV with the ATLAS detector," arXiv:1907.10037 [hep-ex].